NUCLEAR ENERGY RESEARCH INITIATIVE

U.S. Department of Energy – Nuclear Energy Research Initiative
Contract No. C07-00572
Project No. 06-0945

Powder Metallurgy of Uranium Alloy Fuels for TRU-Burning Reactors

Final Technical Report

2007 to 2010

April 29, 2011

Contacts: Dr. Sean M. McDeavitt, PI
Texas A&M University
Department of Nuclear Engineering
Look College of Engineering
3133 TAMU
College Station, TX 77843-3133
(979) 862–1745 (Phone) (979) 845–6443 (FAX)
mcdeavitt@tamu.edu

Allison Cosgrove, Program Coordinator
Texas A&M University
Department of Nuclear Engineering
Look College of Engineering
3133 TAMU
College Station, TX 77843-3133
(979) 845-4106 (Phone) (979) 845–6443 (FAX)
acosgrove@tamu.edu

Overview

Fast reactors were evaluated to enable the transmutation of transuranic isotopes generated by nuclear energy systems. The motivation for this was that TRU isotopes have high radiotoxicity and relatively long half-lives, making them unattractive for disposal in a long-term geologic repository. Fast reactors provide an efficient means to utilize the energy content of the TRUs while destroying them. An enabling technology that requires research and development is the fabrication metallic fuel containing TRU isotopes using powder metallurgy methods.

This project focused upon developing a powder metallurgical fabrication method to produce U-Zr-transuranic (TRU) alloys at relatively low processing temperatures (500ºC to 600ºC) using either hot extrusion or alpha-phase sintering for charecterization. Researchers quantified the fundamental aspects of both processing methods using surrogate metals to simulate the TRU elements. The process produced novel solutions to some of the issues relating to metallic fuels, such as fuel-cladding chemical interactions, fuel swelling, volatility losses during casting, and casting mold material losses.

Workscope

There were two primary tasks associated with this project:

1. Hot working fabrication using mechanical alloying and extrusion
    - Design, fabricate, and assemble extrusion equipment
    - Extrusion database on DU metal
    - Extrusion database on U-10Zr alloys
    - Extrusion database on U-20xx-10Zr alloys
    - Evaluation and testing of tube sheath metals

2. Low-temperature sintering of U alloys
    - Design, fabricate, and assemble equipment
    - Sintering database on DU metal
    - Sintering database on U-10Zr alloys
    - Liquid assisted phase sintering on U-20xx-10Zr alloys

Appendices Outline

Appendix A contains a Fuel Cycle Research & Development (FCR&D) poster and contact presentation where TAMU made primary contributions. Appendix B contains MSNE theses and final defense presentations by David Garnetti and Grant Helmreich outlining the beginning of the materials processing setup. Also included within this section is a thesis proposal by Jeff Hausaman. Appendix C contains the public papers and presentations introduced at the 2010 American Nuclear Society Winter Meeting.

Appendix A—MSNE theses of David Garnetti and Grant Helmreich and proposal by Jeff Hausaman

- *A.1 December 2009 Thesis by David Garnetti entitled "Uranium Powder Production Via Hydride Formation and Alpha Phase Sintering of Uranium and Uranium-Zirconium Alloys for Advanced Nuclear Fuel Applications"*
- *A.2 September 2009 Presentation by David Garnetti (same title as document in Appendix B.1)*
- *A.3 December 2010 Thesis by Grant Helmreich entitled "Characterization of Alpha-Phase Sintering of Uranium and Uranium-Zirconium Alloys for Advanced Nuclear Fuel Applications"*
- *A.4 October 2010 Presentation by Grant Helmreich (same title as document in Appendix B.3)*
- *A.5 Thesis Proposal by Jeffrey Hausaman entitled "Hot Extrusion of Alpha Phase Uranium-Zirconium Alloys for TRU Burning Fast Reactors"*

Appendix B—External presentations introduced at the 2010 ANS Winter Meeting

- *B.1 J.S. Hausaman, D.J. Garnetti, and S.M. McDeavitt, "Powder Metallurgy of Alpha Phase Uranium Alloys for TRU Burning Fast Reactors," Proceedings of 2010 ANS Winter Meeting, Las Vegas, Nevada, USA, November 7-10, 2010*
- *B.2 PowerPoint Presentation Slides from C.1*
- *B.3 G.W. Helmreich, W.J. Sames, D.J. Garnetti, and S.M. McDeavitt, "Uranium Powder Production Using a Hydride-Dehydride Process," Proceedings of 2010 ANS Winter Meeting, Las Vegas, Nevada, USA, November 7-10, 2010*
- *B.4. PowerPoint Presentation Slides from C.3*
- *B.5 Poster Presentation from C.3*

Appendix C—Fuel cycle research and development undergraduate materials and poster presentation

- *C.1 Poster entitled "Characterization of Alpha-Phase Sintering of Uranium and Uranium-Zirconium Alloys" presented at the Fuel Cycle Technologies Program Annual Meeting*
- *C.2 April 2011 Honors Undergraduate Thesis by William Sames, Research Fellow, entitled "Uranium Metal Powder Production, Particle Distribution Analysis, and Reaction Rate Studies of a Hydride-Dehydride Process"*

APPENDIX A

MSNE theses of David Garnetti and Grant Helmreich and proposal by Jeff Hausaman

URANIUM POWDER PRODUCTION VIA HYDRIDE FORMATION AND ALPHA PHASE SINTERING OF URANIUM AND URANIUM-ZIRCONIUM ALLOYS FOR ADVANCED NUCLEAR FUEL APPLICATIONS

A Thesis

by

DAVID JOSEPH GARNETTI

Submitted to the Office of Graduate Studies of
Texas A&M University
in partial fulfillment of the requirements for the degree of

MASTER OF SCIENCE

December 2009

Major Subject: Nuclear Engineering

URANIUM POWDER PRODUCTION VIA HYDRIDE FORMATION AND ALPHA PHASE SINTERING OF URANIUM AND URANIUM-ZIRCONIUM ALLOYS FOR ADVANCED NUCLEAR FUEL APPLICATIONS

A Thesis

by

DAVID JOSEPH GARNETTI

Submitted to the Office of Graduate Studies of
Texas A&M University
in partial fulfillment of the requirements for the degree of

MASTER OF SCIENCE

Approved by:

Chair of Committee,	Sean M. McDeavitt
Committee Members,	Ibrahim Karaman
	Lin Shao
Head of Department,	Raymond Juzaitis

December 2009

Major Subject: Nuclear Engineering

ABSTRACT

Uranium Powder Production via Hydride Formation and Alpha Phase Sintering of Uranium and Uranium-Zirconium Alloys for Advanced Nuclear Fuel Applications. (December 2009)

David Joseph Garnetti, B.S. Physics, Florida State University

Chair of Advisory Committee: Dr. Sean M. McDeavitt

The research in this thesis covers the design and implementation of a depleted uranium (DU) powder production system and the initial results of a DU-Zr-Mg alloy alpha phase sintering experiment where the Mg is a surrogate for Pu and Am. The powder production system utilized the uranium hydrogen interaction in order to break down larger pieces of uranium into fine powder. After several iterations, a successful reusable system was built. The nominal size of the powder product was on the order of 1 to 3 μm.

The resulting uranium powder was pressed into pellets of various compositions (DU, DU-10Zr, DU-Mg, DU-10Zr-Mg) and heated to approximately 650˚C, just below the alpha-beta phase transition of uranium. The dimensions of the pellets were measured before and after heating and *in situ* dimension changes were measured using a linear variable differential transducer (LVDT).

Post experiment measurement of the pellets proved to be an unreliable indicator of sintering do the cracking of the pellets during cool down. The cracking caused increases in the diameter and height of the samples. The cracks occurred in greater frequency along the edges of the pellets. All of the pellets, except the DU-10Zr-Mg pellet, were slightly conical in shape. This is believed to be an artifact of the powder pressing procedure. A greater

density occurs on one end of the pellet during pressing and thus leads to gradient in the sinter rate of the pellet. The LVDT measurements proved to be extremely sensitive to outside vibration, making a subset of the data inappropriate for analysis.

The pellets were also analyzed using electron microscopy. All pellets showed signs of sintering and an increase in density. The pellets will the greatest densification and lowest porosity were the DU-Mg and DU-10Zr-Mg. The DU-Mg pellet had a porosity of 14 ± 2.%. The DU-10Zr-Mg porosity could not be conclusively determined due to lack of clearly visible pores in the image, however there were very few pores indicating a high degree of sintering. In the DU-10Zr-Mg alloy, large grains of DU were surrounded by Zr. This phenomena was not present in the DU-10Zr pellet where the Zr and DU stayed segregated. There was no indication of alloying between the Zr and DU in pellets.

DEDICATION

I would like to dedicate this thesis to my family. Without their support I would not have been able to make it this far.

ACKNOWLEDGEMENTS

I would like to thank my committee chair, Dr. McDeavitt, for his guidance and support throughout the course of this research.

I would like to thank the Y-12 plant in Oak Ridge Tennessee and Dr. D. Cecala specifically, for their help in procuring the depleted uranium used in this research.

I would like to thank Kevin Hogan for his help on the MatLAB coding and Ryoji Oinuma for his help on the LabView coding.

I would like to thank Grant Helmreich and Julie Borgmeyer for their help on this project and their microscopy work.

I would like to thank Alissa Stafford for her support in the writing and editing of this thesis.

NOMENCLATURE

TRU	Transuranics
DU	Depleted Uranium
EBR II	Experimental Breeder Reactor II
IFR	Integral Fast Reactor
LVDT	Linear Variable Differential Transformer
SEM	Scanning Electron Microscope

.

TABLE OF CONTENTS

Page

LIST OF FIGURES

FIGURE Page

FIGURE Page

FIGURE Page

LIST OF TABLES

1. INTRODUCTION

The renewed interest in using fast reactors as way to burn the transuranics in used nuclear fuel has lead to this examination of U-TRU-Zr fuel fabrication via powder metallurgical methods. Current methods for U-Zr metal fuel fabrication involve melt-casting technologies that are challenged by the volatility of americium (Am) and neptunium (Np) (Fig 1-1). The the inclusion of Am in advanced fuels is important to the successful transmutation of minor actinides in a fast reactor. Losses of Am during casting will lead to an increase cost to the facility as the material will have to be recovered and then handled appropriately as a waste material [1]. This study was initiated as part of an effort to develop an alternative fabrication method that will not involve significant transuranic losses. It is important to note that recent developments at Idaho National Laboratory[1] have shown that TRU volatility may be overcome by increasing the ambient pressure during injection casting, but powder metallurgy still has significant potential as a fuel fabrication technique.

Injection casting has been the preferred method for metal fuel fabrication for previous fast reactor fuels such as the driver fuel for EBR-II and the demonstration IFR fuel pins. A simplified schematic of injection casting is shown in Fig 1-2, which indicates that the molten fuel alloy is created as a liquid pool in the crucible at ~1500°C, quartz injection molds are inserted into the melt, and the system is pressurized to inject the fuel alloy into the molds creating solid pins. After injection, the filled molds are allowed to cool and then are

---

This thesis follows the style of Journal of Nuclear Materials.

broken away liberating the cast fuel pin that may be machined to specification. Past practice has been to use graphite crucibles coated with a stable oxide powder to minimize interactions between the melt and the crucible. The graphite melt crucible had a dual function as a container and as a susceptor for induction heating. Some carbon contamination from the crucible was always present in the molten alloy. The oxide coating on the casting crucible was applied as a slurry typically containing yttrium , zirconium, or thorium oxides [2].

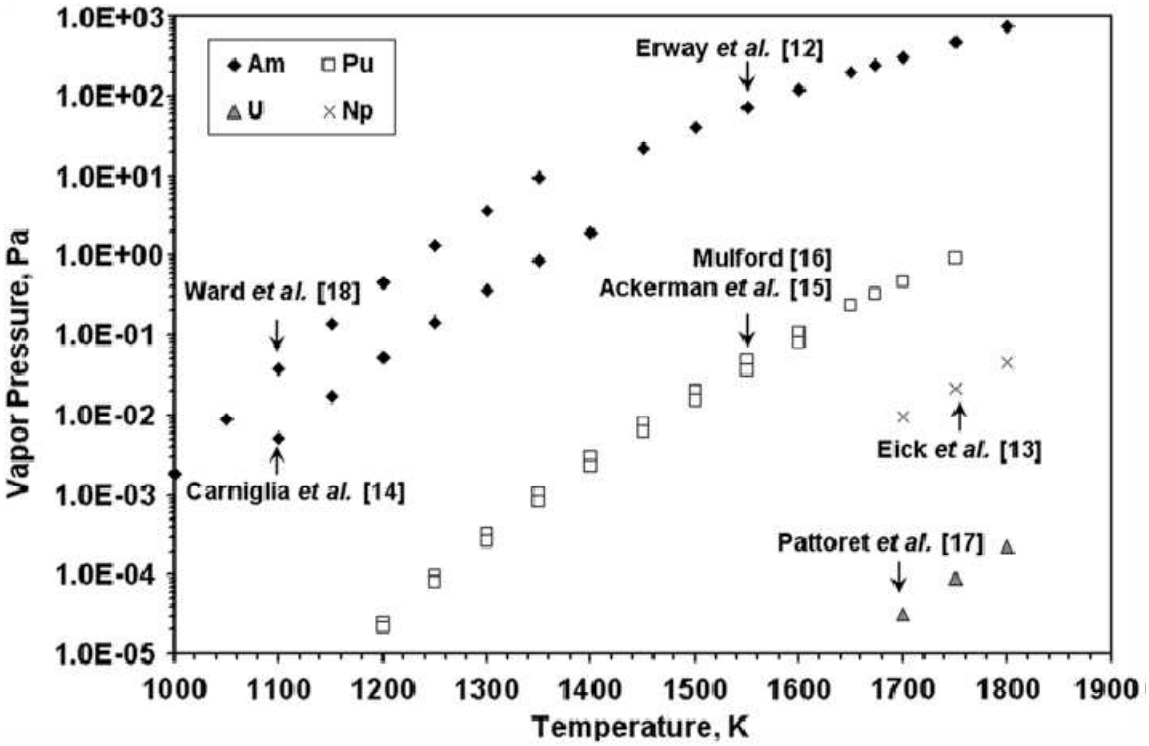

Figure 1-1 Vapor Pressures of the Actinide Metals vs Temperature [1]

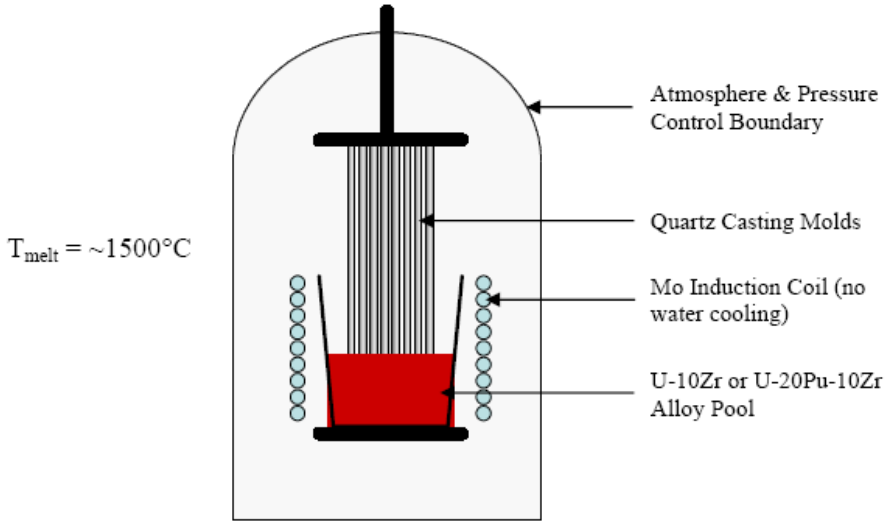

Figure 1-2 Simple schematic of the injection casting process for U-10Zr or U-10Zr-Pu

There are material losses and alloy contamination issues that are inherent in the injection casting process, especially when the higher actinides such as Am are involved in the fuel system. Initial demonstration experiments showed a 40% Am loss from a fuel alloy that had 2.1 wt % Am and 1.3 wt % Np; in this test, the injection casting process was not modified from the nominal U-10Zr methodology [3]. The losses were attributed to evaporation of the volatile contaminates at the casting temperature (1456°C) [3]. Later experiments have shown that these Am losses can be significantly reduced by modifying the casting procedures.

One technique that has been reported involves using a combination of a cover gas and cold trap [1]. A high pressure cover gas was found to reduce Am losses by suppressing Am vaporization. The cold trap is designed to collect any Am that escapes through the high pressure cover gas. This system would be most effective if implemented as a small volume closed system [1]. A small-scale demonstration of this concept was performed with a U-Zr

melt containing 5 wt % Am heated to 1575 K for 5 minutes followed by injection casting. The crucible sides were heated, which made the crucible lid an effective cold trap. Pins were cast with cover gas pressures of 670 Pa and 30 with respective Am losses of 0.3% and 0.006% [1]. This indicates that Am volatility may be overcome and injection casting may be effectively accomplished, but alternative processes are still under development.

The research conducted for this thesis is part of the US Department of Energy's Nuclear Energy Research Initiative (NERI). The goal of NERI is to conduct research that will address key technical issues in the expanding nuclear energy use worldwide. The research in this thesis was conducted under the Advanced Fuel Cycle Initiative (AFCI) category of NERI. The main goal of the research project, which this thesis contributes to, is to develop a method for U-Zr-Pu-Am alloy fabrication that operates at temperatures below 660 °C. The vapor pressures of Am, Np, and Pu are quite low at these temperatures, and therefore volatility losses should not be an issue.

The focus of the research reported in this thesis has been on the development of powder fabrication methods and the initial demonstration of the alpha phase sintering process. Production of fine uranium powder was of the utmost importance for the successful completion of the alpha phase sintering test. A process utilizing the ability to hydride and dehydride uranium was used to produce the uranium powder, 1 to 3 μm sized particles. For reasons of safety and convenience Mg was used as a surrogate in place of Pu. Mg was chosen due to the proximity of its melting point to that of Pu and its relatively high vapor pressure (Mg has a vapor pressure of 0.13 Pa at 500 K). The primary reason for the inclusion of Mg was to simulate the liquid enhanced sintering effect that Pu would have on the pellet. The pellets were made of several different compositions (DU, DU-10Zr, DU-Mg,

and DU-10Zr-Mg). The pellets were all heated to approximately 650 ˚C; some were periodically raised to 700 ˚C and/or 800 ˚C. The pellet dimensions were monitored *in situ* using a linear variable differential transducer (LVDT) as well as physical measurements before and after each experiment. The pellets were cut axially, mounted, and examined using an SEM and digital microscope. Analysis of the LVDT data and SEM imaging indicated sintering of varying degrees in all of the pellets. The research below has created a functioning system and procedures that can produce fine uranium powder for specimen fabrication and it has provided a solid base upon which a larger test matrix can establish the behavior of the sintering and liquid phase sintering methods.

2. BACKGROUND

The focus of this section is to provide a survey of the relevant physical phenomena and technical context that underpins development activities described in the following sections. Section 2.1 provides a brief summary of the mechanisms and models that describe sintering. Section 2.2 provides a summary of the properties of alpha phase uranium and the uranium-zirconium binary system. Section 2.3 summarizes previous work concerning powder production via uranium hydration.

2.1 Sintering

Sintering is the physical process where a form comprised of compacted particles (e.g., powder) is transformed into a dense structure at elevated temperatures through diffusion controlled mechanisms. The process involves the heating of the form and may involve the application of external pressure to the specimen or the addition of a small amount of liquid phase materials [4]. The main driving force of sintering is the reduction of surface area to minimize surface energy within the body. Points of contact between powder particles will initially have a local radius of curvature near zero, which creates a near-infinite driving force for diffusion into that point to form a "neck" or bridge between the particles. There are six different sintering mechanisms outlined in Fig. 2-1 that are typically observed in powder metallurgy and ceramics: surface diffusion; lattice diffusion (from the surface); vapor transport; grain boundary diffusion; lattice diffusion (from the grain boundary); plastic flow [5].

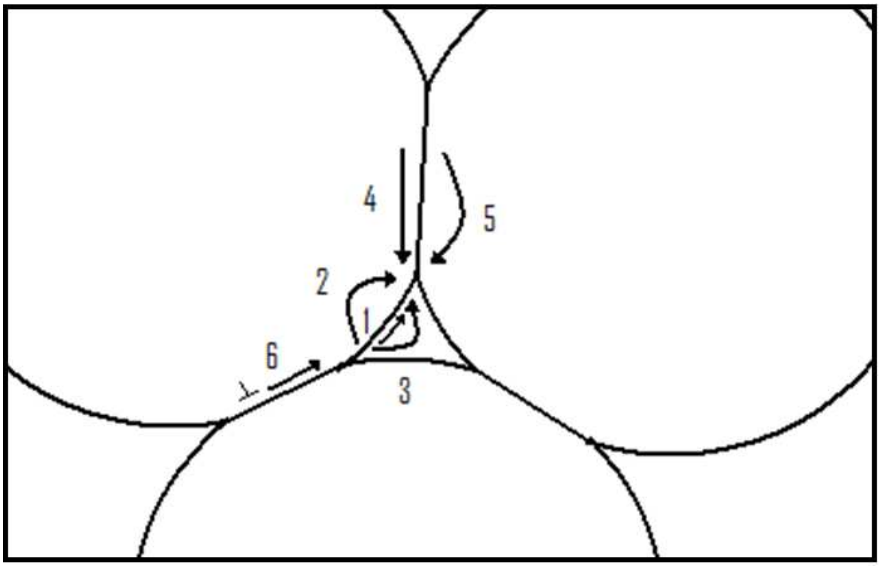

Figure 2-1 Various sinter mechanics: 1 Surface diffusion; 2 Lattice diffusion (from the surface); 3 Vapor transport; 4 Grain Boundary diffusion; 5 Lattice diffusion (from the grain boundary; 6 Plastic flow

As the particles come together by whatever mechanism dominates, the internal void space begins to close and internal porosity is formed. As sintering progresses, there is a significant change in the morphology of this porosity. Initially, pores change from irregular shapes into spherical shapes, again to minimize surface energy effects, and then the volume fraction of the porosity is reduced as the diffusive driving force continues to drive the body toward higher density. Over time, the radius of the pores decreases until an equilibrium condition is reached where the internal pore pressure, p, is balanced by the surface energy "pressure" according to

$$p = \frac{2\gamma}{r}$$

where γ is the surface energy, and r is the radius of curvature for the pore [4]. At this point, shrinkage of the specimen stops. If the external pressure of the body is changed, swelling or densification may occur in order to achieve a new equilibrium [4].

The sintering rate is defined as the rate at which the material densifies and it is often modeled in terms of volumetric strain rate.

$$\text{Sintering Rate} = \frac{d}{dt}\left(\frac{\Delta V}{V_o}\right)$$

where V is the overall volume of the form being sintered. While the total amount of sintering can be easily measured by recording the volume and weight of the specimen before and after heating, it is valuable to know the rate of sintering during the heating process. If the sintering rate is continuingly measured, one can calculate the process activation energy between two different temperatures. The rate of sintering for a powder pressed pellet can be measured in several ways. Two methods which are utilized in this experiment are the measuring of density before and after sintering and the continuous measurement of linear shrinkage [6].

Linear shrinkage was measured using a linear variable differential transducer (LVDT). It is assumed that the volume change in the sample was isotropic, leading to the following equation [6]:

$$\frac{\Delta V}{V_o} = 1 - \left(1 - \frac{\Delta L}{L_o}\right)^3 \approx 3\frac{\Delta L}{L_o}$$

where $\frac{\Delta V}{V_o}$ is the volumetric strain, and $\frac{\Delta L}{L_o}$ is the linear strain. One can also estimate the post sintering volume of the specimen from Y (where $Y = \frac{\Delta L}{L_o}$).[6].

$$V_S = V_G \frac{1}{(1+Y)^3}$$

where V_S is the sintered fractional solid volume and V_G is the green volume.

2.2 Alpha Phase Uranium

2.2.1 Uranium/Alpha Phase Uranium

Uranium may exist in three allotropic phases named α, β, and γ. The alpha phase is stable from low temperatures up to 667°C and has a complex orthorhombic structure [7]. The beta phase has a complex tetragonal structure and is stable in the temperature range of 667 °C to 772 °C. The gamma phase is stable from 772 °C up to the melting point, 1132°C and has a body centered cubic structure. Alpha phase uranium has a theoretical density of 19.04 g/cc at 25 °C [8]. The orthorhombic structure has the following lattice parameter dimensions at 25 °C: a=2.8541 Å, b=5.8541 Å, and c=4.9563 Å [7] [8]. These values are more precise that the older values shown in Fig. 2-2.

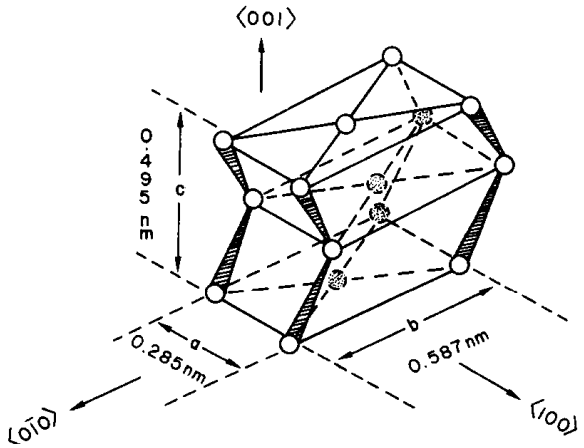

Fig. 2-2 Alpha phase uranium, orthorhombic crystal lattice [7]

At the advent of nuclear energy, pure uranium metal was one of the first fuel forms investigated. Uranium metal has the technical benefits of being of a higher density and having a higher thermal conductivity than oxide fuel. However the well documented swelling of the fuel in the alpha phase of pure uranium metal caused it to be an unusable fuel form [9]. However the swelling issues associated with irradiation "tearing" were overcome through alloying with elements such as zirconium, molybdenum, and other noble metals; uranium zirconium alloys have been used for several fast reactor systems in the past 50 years [10] [11]. During testing of irradiated fuel it has been noted that there is a recovery driven reduction of tearing above 550˚C. The recovery driven reduction has lead to a decrease in the linear shrinkage in some cases [11]. This recovery mechanism has been noted in the work of Burke, Pugh, and McDeavitt [9] [10] [12] [13].

Previous work reported by Chiotti, et al. [14] provides additional relevant experience with uranium powder metallurgy that has been of great benefit to this current project. In this work, a hydride-dehydride process was studied extensively to evaluate the mechanisms of UH_3 formation and decomposition. This work is especially relevant to the powder fabrication method development discussed in Sections 3.1 and 4.1. However, in the midst of this previous study, Chiotti reported the observation of alpha-phase sintering during dehyriding experiments where UH_3 was placed under a vacuum and brought to temperatures above 300°C [14]. As the hydrogen was disassociated from the uranium, loose sintering of the uranium powder was evident because the powder came out of the experiments in solid, but porous "chunks."

All of the observations noted above can be taken together as evidence that uranium has significant diffusive mobility in the alpha phase at temperatures just below the alpha-beta phase transformation temperature.

2.2.2 Alpha Phase Uranium in Uranium Zirconium Alloys

Figure 2-3 shows the binary U-Zr phase diagram [15]. As noted in Section 2.2.1, zirconium is a commonly-used alloying element with uranium in nuclear fuels for fast reactor systems. Pure zirconium exists in two phases: 1) a hexagonal phase stable up to 862˚C (α) and 2) a body center cubic phase stable from 826˚C to the melting point1852˚C (β). In the U-Zr binary system an intermetallic δ-UZr_2 phase is formed bellow 617 ˚C. The δ phase consists nominally of UZr_2 and has a ω-type structure [16] [17]. The U-Zr also contains a γ phase which exhibit full mutual solubility of U and Zr. However the uranium β phase can only dissolve a maximum of 0.4 Wt% of Zr (at 693˚C) and the uranium α phase can dissolve a maximum of 0.2 Wt% of Zr (at 662˚C) [16]. The γ uranium phase has the highest solubility limit for Zr as it shares the same structure, BCC, as the β zirconium phase. Also the alpha beta phase transition line is lowered to 662 ˚C in the U-Zr system.

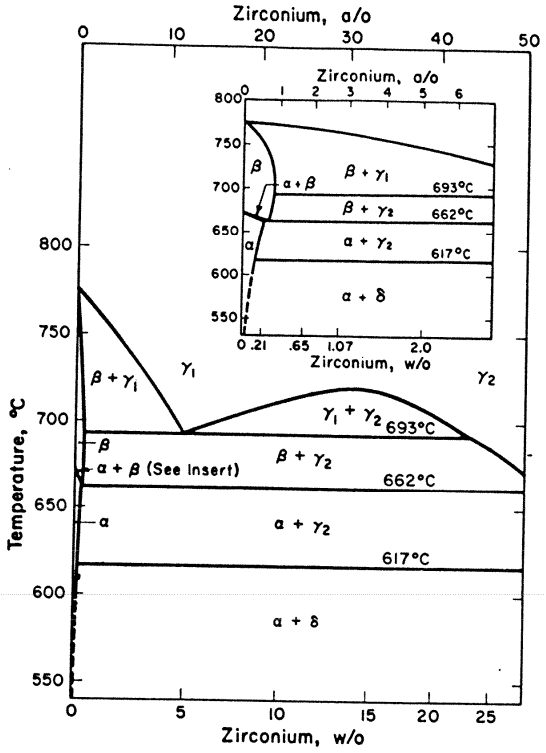

Fig. 2-3 Uranium-Zirconium Phase diagram, with insert [15]

In the previous work of McDeavitt and Solomon [12] [13], the sintering of dehydrided uranium zirconium alloys was observed at temperatures as low as 400°C. and continued until the alpha-beta phase transition line is reached. There was an increase from approximately 44% theoretical density to 49% theoretical density before the alpha beta phase transition line, Fig. 2-4 [12]. The increase is density is evidence of sintering of the specimens during the alpha phase. As the research at the time was not focusing on this phenomenon, it was noted but not thoroughly examined.

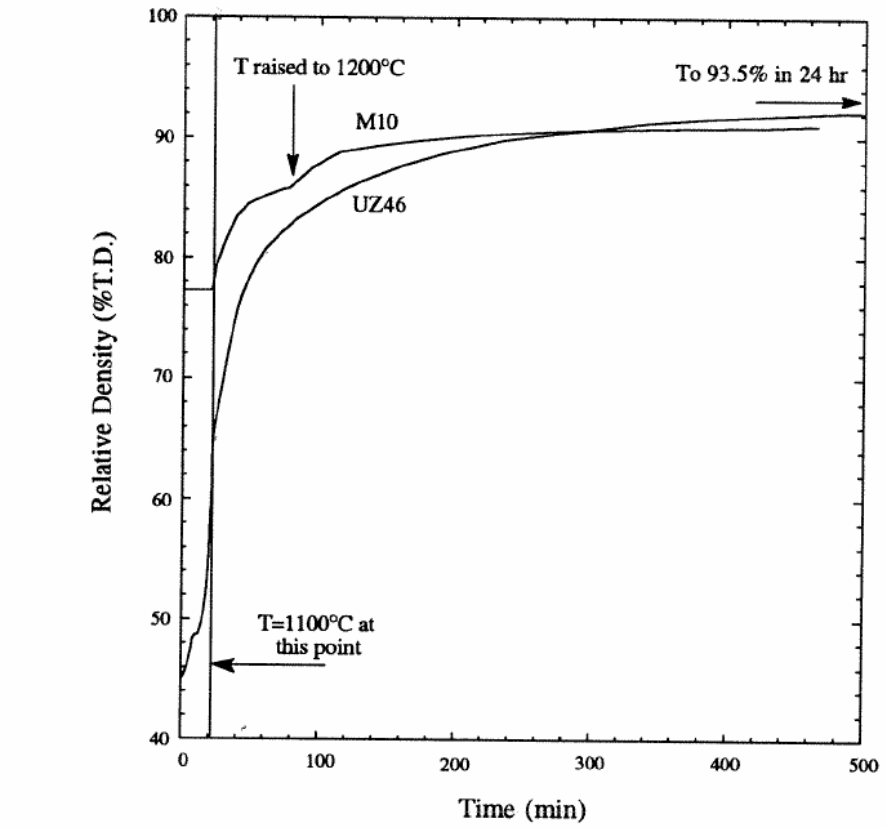

Fig. 2-4 Shows an increase in TD before alpha beta phase transition [12]

2.3 The Uranium Hydride/Dehydride Process

One method that has been previously used to produce fine uranium powder with low oxygen contamination is known as the hydride/dehydride process. This process has the ability to transform pieces of uranium into a high purity fine powder [18].

2.3.1 Uranium Hydride

Uranium Hydride (UH_3) is formed through the following reversible reaction [18]:

$2U + 3H_2 \rightleftharpoons 2UH_3$.

When the reaction takes place with solid uranium metal slugs, it causes the complete destruction of the original structure of the metal [19] due to the large difference in density of uranium metal (19.04 g/cm^3) and UH_3 (10.9 g/ cm^3) [20]. The reaction leaves behind a fine powder that is of black/dark brown color with nominal particle sizes ranging from less than 1 μm up to ~10 μm (approximately -400 mesh) when the reaction is carried out at a temperature of 225 °C [11] [19]. The three principle factors affecting the rate reaction (assuming no oxidation layer is present on the uranium surface) are the surface area of the sample, temperature, and the hydrogen pressure in the reaction chamber [14].

Hydrogen will interact with uranium at temperatures below 150°C, however the reaction reaches maximum efficiency at approximately 225°C, Fig. 2-5 [11] [19]. An induction period has been noticed when hydriding uranium metal at lower temperature. This is most likely caused by the presence of an oxide layer on the uranium metal surface [19]. In cases where there is an oxide layer on the uranium specimens, it has been recommended to initiate the reaction over 300°C; this leads in an increase in the hydrogen diffusion through the oxide layer on the uranium [11]. However, hydriding at temperatures above 300 °C can lead to some sintering of the uranium hydride powder [11].

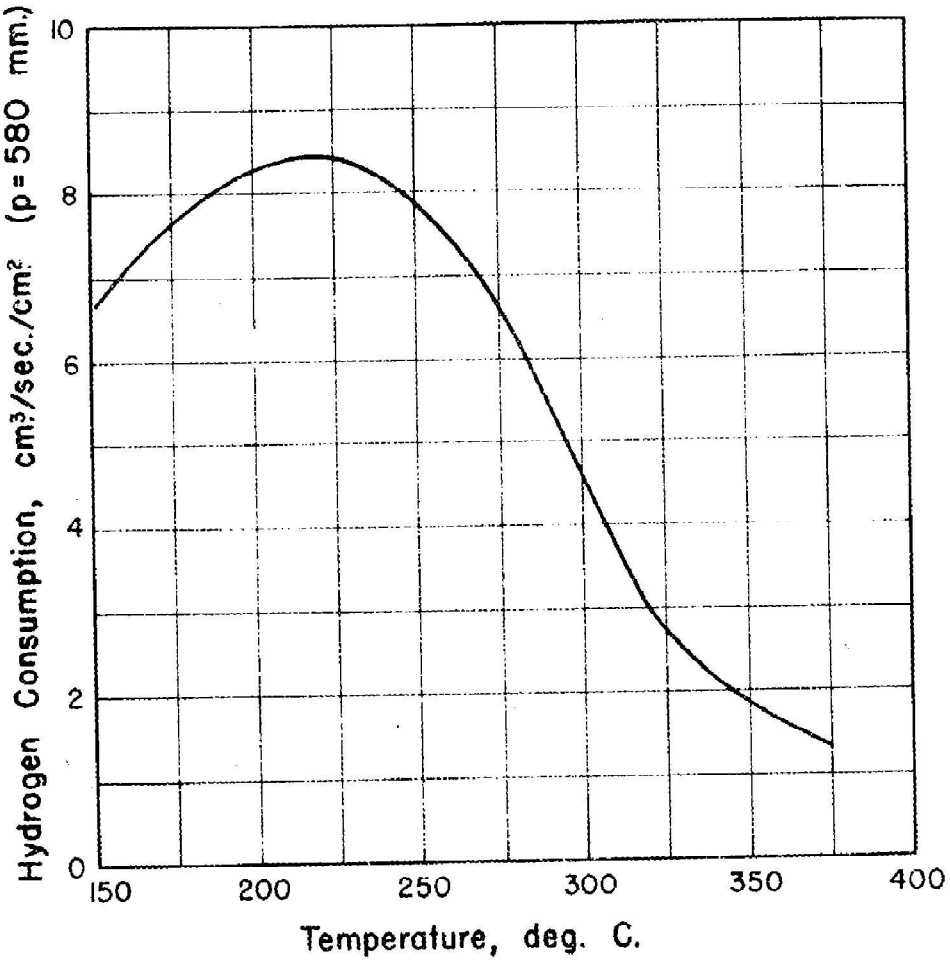

Fig. 2-5 Hydration rate of uranium at constant pressure [14]

2.3.2 Dehydriding Uranium

UH_3 disassociation at atmospheric pressures requires temperatures above 430 °C, Fig. 2-6 [14]. This process can be expedited by heating the uranium hydride in a vacuum. The stabilization of the pressure in the reaction vessel is an indicator that the hydrogen has "completely" disassociated. The uranium metal left behind is in the form of a high purity powder with an average size of a less than 40 μm [11] [18]. During the dehydriding step,

there is a tendency for the powder to sinter into aggregate particles. This sintering becomes noticeable above 300°C. However, these aggregates can be easily broken down by mechanical milling when the dehydriding temperature is kept below ~400°C [14].

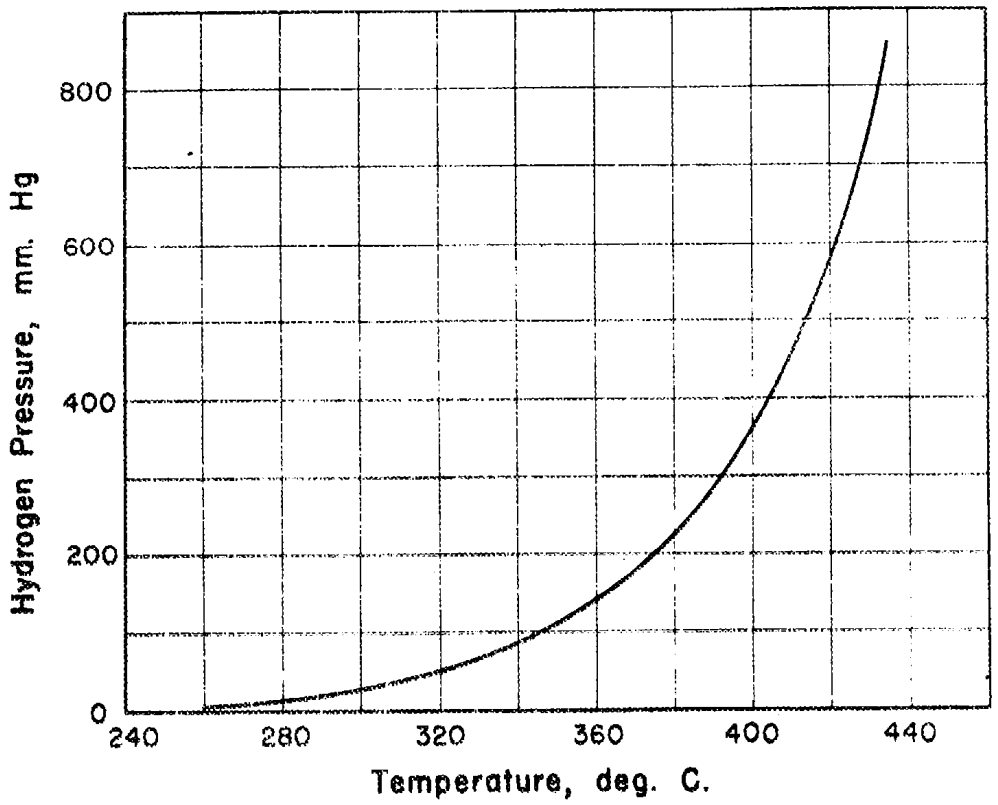

Fig. 2-6 Hydrogen disassociation rate at various temperatures [14]

2.3.3 Uranium Oxide Removal with Nitric Acid

As previously noted, an oxide layer will create a barrier to the diffusion of hydrogen throughout the sample and slow down the hydride formation [19]. An oxide layer may also cause oxygen contamination in the UH_3 and uranium metal powder produced. Therefore it is necessary to remove any oxide layer from the uranium chips as completely as possible.

In order to remove the oxide layer, the uranium chips are placed in a nitric acid solution bath. In previous studies a solution of 25% nitric acid by volume was sufficient for the removal of the oxide layer of 80 mesh uranium metal spheres [12]. The reaction takes places rather quickly, and if the uranium is left in the nitric acid too long the solution will heat up. This will lead to the re-formation of the oxide layer on the uranium [12].

3. EXPERIMENTAL DESIGN AND PROCEDURES

This section describes the three main components of the experimental systems and procedures developed for this thesis. None of the systems described were in existence at the onset of this research, so a major portion of the work reported here was in the establishment of this equipment to the point that the procedures could be performed to meet the research objectives. The three main sections of this section describe the methods and equipment established to perform for the production of uranium metal powder (Section 3.1 & 3.2), the generation of pressed pellets using metal powder mixtures (Section 3.3), and sintering the pressed pellet (Section 3.4 & 3.5). For all three of these operations, great care was required to minimize oxygen contamination of the metal powders. Therefore, nearly all of the experiment takes place in a large inert argon atmosphere glovebox, Fig. 3-1. The operations that were not performed inside of the glovebox are the initial acid washing of the uranium chunks for powder production and the preparation of the experimental samples for SEM and digital microscope analysis. The acid wash step was performed inside of an argon (Ar) atmosphere glovebag and the metallurgical sample preparation was performed in air and both operations were performed in a fume hood.

Fig. 3-1 Inert atmosphere glovebox, primary location of the experiments

3.1 Powder Production Experimental Design

High purity uranium metal powder is highly reactive with air and is not readily available for purchase. Therefore, a reliable uranium powder production method was needed in the laboratory to create the powders required for pressing and sintering. The method selected involves the conversion of uranium metal slugs into uranium hydride powder through vapor phase synthesis and the decomposition of that powder into metal by thermal decomposition; this method is named the hydride/dehyride process. The uranium used in this experiment was obtained from the Y-12 plant at Oak Ridge National Laboratory. The uranium was in the form of rectangular metal chunks weighing approximately 10 to 30 g. The chunks had a black oxide layer which needed to be removed to expose the metal surface

before the uranium could be hydrided. A hydride/dehdyride system was installed in and around the glovebox; a basic schematic of the final system is shown in Fig. 3-2.

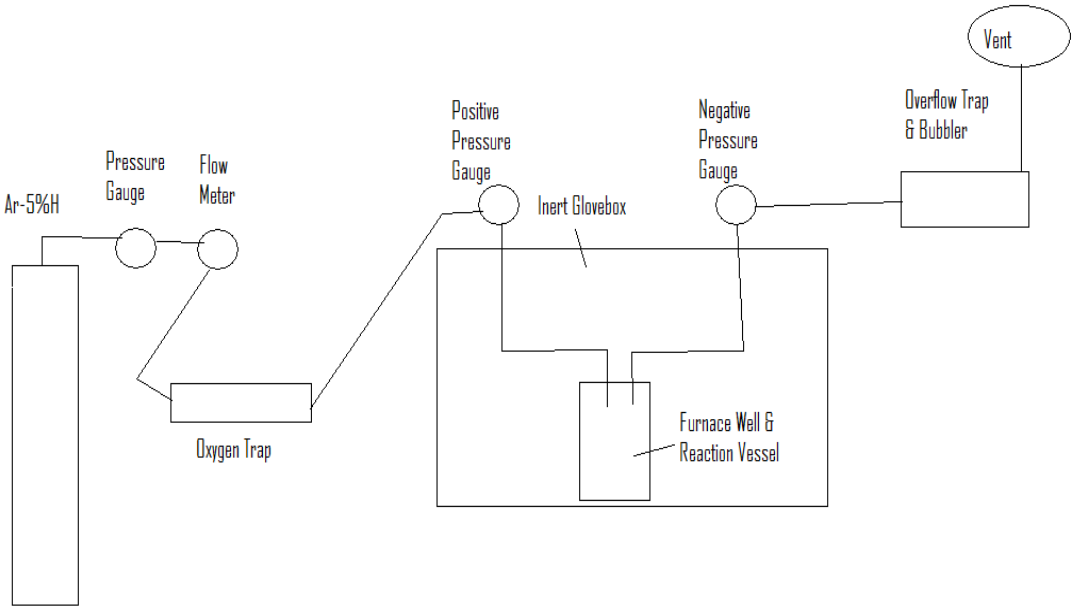

Fig. 3-2 Schematic of the Hydride/Dehydride System

3.1.1 Process Gas Flow

The process gas came from two separate sources, a gas cylinder of welders-grade Ar gas and a gas cylinder of Ar-5%H_2. The gas flow system went through several iterations. Originally the system only used the process gas, Ar-5%H_2, and was monitored by a precession pressure gauge and 10 psi relief valve. The gas line was connected to the east airlock of the glovebox. This design was used for hydride experiments 1 through 4. Later

the gas line was moved from the airlock to the furnace well of the glovebox and attached to a hydride/dehydride reaction vessel that was inserted into a heated furnace well within the glovebox. This design was used for hydride experiments 4 onward. The gas flowed from the furnace well out of the glovebox to an overflow trap and then a silicon oil bubbler. This was done to prevent contaminants from entering the system. The gas then flowed into a fume hood where it was vented to the atmosphere. At this time the gas cylinder containing Ar was added, as it was necessary to fill the furnace well with Ar before removing the reactions vessel. This was done to avoid exposing the glovebox atmosphere to H_2. Next a Ti getter, housed in an alumina tube, was added to the gas flow design. This Ti getter was designed and used in previous Zircaloy hydriding experiments by Adam Parkinson [21]. With the Ti getter a flow meter, pressure gauge and 5 psi relief valve was added to system. In the final iteration the Ti getter was replaced by a commercial bought oxygen and moisture trap. The 5 psi relief valve was removed. All other components of the system remained unchanged. A schematic of the final gas delivery system is shown in Fig. 3-3.

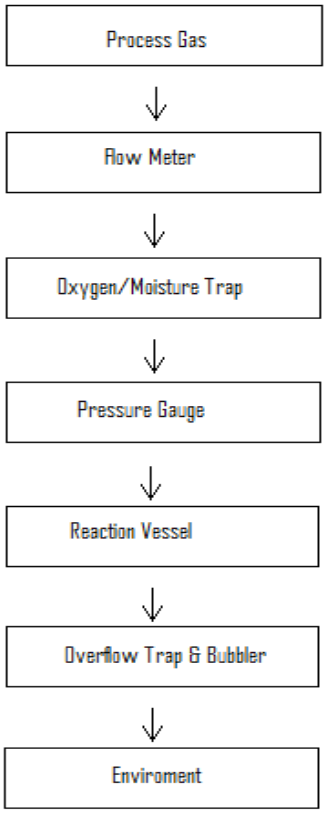

Fig. 3-3 Schematic of the process gas flow path

3.1.2 Titanium Getter/Oxygen and Moisture Trap

The titanium getter, Fig. 3-4, was added during hydride experiment 8, in order to eliminate contaminants from the gas delivery system (N_2, O_2, H_2O). The Ti getter consisted of a 1 5/8 in diameter alumina oxide tube with 350 W Watlow furnace around it. The tube was filled with Ti sponge in the heated region only. This was done to avoid forming TiH_2 on the periphery of the getter furnace [21]. The Ti sponge was kept at a temperature of approximately 1025°C. At this temperature the Ti would not hydride or form a eutectic with the stainless steel cage.

A cage was fabricated to keep the Ti sponge in the heated region. The cage consisted of a 64x64 stainless steel mesh formed into a cylinder with a diameter of approximately 1 3/8 in. On one end of the cylinder a hole was cut to allow an alumina tube to enter the sponge. The alumina tube was used to protect the thermocouple from interacting with the Ti sponge. The cage was then placed in the 1 5/8 diameter alumina tube, filled with Ti sponge, and the thermocouple was inserted.

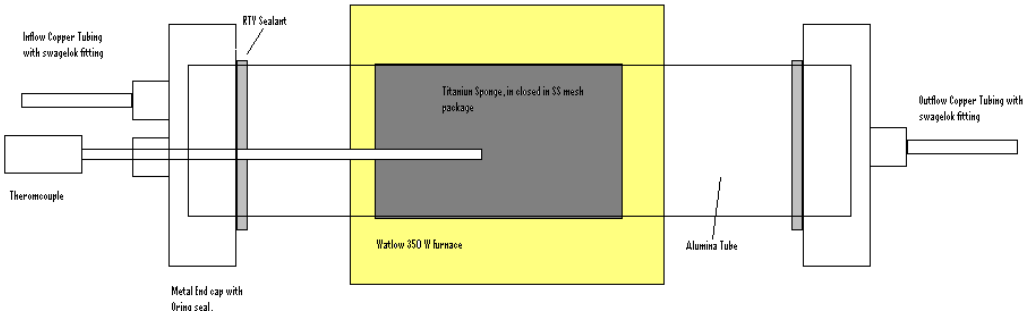

Fig. 3-4, Diagram of Ti Getter

Finally the Ti getter was replaced by an oxygen trap (Alltech Big Oxygen Trap Model 7217) and moisture trap (Alltech Big Moisture Trap Model 7211) during hydride experiment 13. Both of these traps were designed to handle a maximum pressure of 250 psig. The oxygen trap was designed to limit the oxygen to less than 100 ppb and the moisture trap was designed to less than 100 ppb. In practice when placed in series and connected to an Ar gas cylinder with an oxygen level of approximately 14 ppm the traps lowered to the oxygen level to approximately 1.5 ppm and the moisture level was 1 ppm. This oxygen level should have a negligible effect on the hydride system.

3.1.3 Hydride/Dehydride Reaction Vessel

As with the gas delivery system the hydride/dehydride reaction vessel went through several iterations. The original design consisted of a furnace system contained within the east airlock of the glovebox, Fig. 3-5. A 350 W Watlow furnace was placed in the center of a stainless steel pot, diameter 20.32 cm (8 in), with the insulation surrounding it. The samples were contained within a Y_2O_3 crucible which in turn was placed in the furnace. The top gasket of the airlock had a Conax Buffalo feedthrough installed. The feed-through consisted of 6 wires two 12AWG and four 24 AWG thermocouple wire. The 12 AWG wires were used to power the furnace while the thermocouple wiring was attached to two K-type thermocouples. One thermocouple was used to take reading from the Y_2O_3 crucible while the other thermocouple took readings from the insulation region of the system. The furnace reached temperatures upwards of 450°C while the temperature of the airlock walls remained near room temperature. This system was used for hydride experiments 1 through 4. This setup however was found to be inadequate due to O_2 contamination from outside of the system.

Fig. 3-5 Left:Hydride/Dehydride furnace original setup. Right: East airlock with Conax Buffalo electrical feedthrough

The reaction vessel was then moved to inside of the glovebox to eliminate the possibility of contamination from outside the system. The reaction vessel consisted of a dipper device with a rubber stopper on top. A simplified schematic is shown in Fig. 3-6.

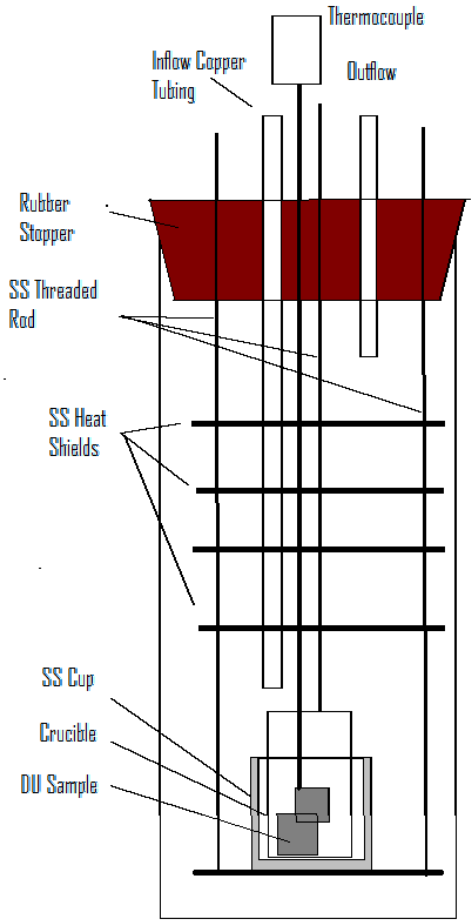

Fig. 3-6 Schematic of Hydride/Dehydride Reaction Vessel

The reaction vessel assembly was fabricated using 1.875 inch diameter 304 stainless steel discs connected by 24 inch long ¼ in diameter 316 stainless steel threaded rod. On the bottom plate a cup was fabricated from 304 stainless steel. The cup had a diameter of 2.3 cm. The cup was affixed to the bottom by a ¼ in screw. An alumina crucible (V=10mL,

OD =22 mm, H = 33mm), which contained the sample, was placed inside of the cup. A high temperature resilient rubber plug was located at the top of the vessel; top diameter 2.48 in, bottom diameter 1.97 in. The opening to the furnace well had a diameter of approximately 2 in. The rubber plug had two sections of ¼ in copper tubing going through it. The center piece of tubing (inflow) ran the length of the dipper while the other piece of tubing (outflow) only protruded approximately 3 cm into the well. The three pieces of threaded rod also protruded from the top of the rubber stopper. The threaded rods and tubing were affixed in place using Torr Seal. This created a gas tight seal with the ability to withstand a rough vacuum, Fig. 3-7. When in use, the gas flow system described above was attached to the inflow and outflow tubing of the reaction vessel. The reaction vessel was kept in place during the experiments by placing weight on top of the stopper to counteract the increase in pressure of the furnace well. This system was used successfully for hydride experiments 5 and onward, but a better design is required for future activities. The Ti getter was used in conjunction with the system for experiment 8 through 12. From experiment 13 onward the oxygen and moisture traps were used in place of the Ti getter.

Fig. 3-7 Hydride/dehydride reaction vessel inside of large glovebox

3.1.4 Nitric Acid Washing of Samples

The depleted uranium samples had an oxide layer which had to be removed before the experiments could take place. The oxide layer was removed through acid washing using a 35% volume nitric acid solution. The nitric acid washing station was setup within a glovebag which was purged with Ar gas. The glovebag (Glas-Col Model X-27-17) was located within a fume hood, Fig. 3-8.

Fig. 3-8 The Depleted Uranium Washing Station

3.2 Powder Production Experimental Procedures

3.2.1 Sample Preparation

The samples were weighed inside of the glovebox using an AL-204 Balance. The due to the fluctuations in glovebox pressure balance had an accuracy of 0.0005 g, the samples were weighed 5 times each given these measurements 0.0002 g accuracy. The samples were then either cut down to a manageable size using a diamond saw and the pieces reweighed individually or taken directly to the nitric acid washing station. The samples were washed in the nitric acid and then rinsed with water over the beaker containing the 35% volume nitric acid solution. The samples were placed in the nitric acid solution for 10-15

minutes or until the oxide layer was removed. There was a visible reaction between the nitric acid solution and the depleted uranium samples. Bubbles would begin to form on the surface of the samples and sometimes the nitric acid solution would change from clear to yellow in color. Once the black oxide layer was removed the depleted uranium sample was a dull silver color with a tinge of gold. The samples were then rinsed with 190 alcohol over a separate beaker. The samples were then immediately taken into the glovebox in order to limit oxidation of the samples post wash.

The samples were reweighed and placed in the crucible of the hydride reaction vessel. The vessel was then placed into the furnace well and connected to the inflow and outflow piping.

3.2.2 Hydride Reaction

After the reaction vessel was connected the gas flow lines the glovebox inlet and overflow trap outlet valve were closed, the vessel was evacuated and a rough vacuum was held for five minutes to remove the original atmosphere in the reaction vessel. The gas flow was changed to Ar-5%H_2 and reaction vessel was pressurized. The sample was kept under Ar-5%H_2 flow while being heated to the set temperature. During the initial experiments the reaction vessel was placed under vacuum for time period of 15-30 minutes periodically after temperature was reached, thus dehydriding the sample. This was done to expose a fresh surface for a hydride reaction and to facilitate the breaking up of the uranium pieces. In later experiments it was determined that this was an extraneous action and therefore was not continued.

After the uranium pieces were sufficiently hydrided the reaction vessel was once again evacuated. The vessel was held at temperature and under vacuum to allow the

hydrogen to completely disassociate for the uranium. The pressure of the system was monitored once the temperature reached 350˚C. During disassociation, the pressure in the vessel would increase for vacuum to approximately 7 Pa and return to vacuum once disassociation was complete. Once the majority of the disassociation reaction was completed the vacuum pressure would return to its previous level. The well was held under vacuum for an additional 15 minutes to insure full disassociation of the hydrogen before cooling began. After the dehydridng was complete and the well sufficiently cooled, the vessel was repressurized using argon gas. The uranium powder was removed from the crucible and then weighed.

Upon removal from the reaction vessel the uranium metal powder was loosely sintered. The sintered pieces were first broken apart by physical shaking the jar the uranium was held in. Then the broken pieces were placed in a stainless steel mortar and pestle were the pieces were ground into a powder. That powder was then place in in a horizontal vibratory mill with the commercial name “Wig-L-Bug” (Model # 3110B) with or without the addition of a stainless steel bearing. The powder was shaken until a fine powder was obtained. The remaining pieces of uranium, which were not hydrided, were removed and used in later hydride experiments. The nominal particle size of the resulting powder was on the order of 1 to 3 μm.

3.3 Pellet Pressing Design and Procedures

The pellets were pressed in a double action punch and die with a pellet diameter of approximately 9.5 mm (0.375 in). The die was fabricated first. Then the punches were fabricated by incrementally turning down the punch radius, to insure a tight fit. Initially the

dies and punches were fabricated from 303 stainless steel, due to the anti-galling and machineable qualities of this alloy. After the first sintering experiment it was determined that the 303 punches could not handle the necessary force without drastically deforming. From sintering experiment 2 the punches were fabricated from H13 tool steel. The H13 punches were heated treated and tempered after fabrication. The pellets were pressed inside the glovebox using a hydraulic press (Caver Laboratory Press Model C).

After weighing the uranium and zirconium powder for the pellet the powders were placed in a stainless steel container. They were then mixed until homogenous using the Wig-L-Bug mixing device. The homogenously mixed powder was then poured into the die with bottom punch in place. The punch and die was then placed on the hydraulic press and the top punch was inserted. In an effort to limit contamination of the pellets no lubrication was used with the punch and die. The pellets were pressed with a maximum load of 15,000 lbs over the 9.5 mm (0.375 in) diameter pellet or approximately 135,000 psi. The pressed pellet was then removed and either placed directly in the furnace well and sintered or placed in sealed container and stored for a later experiment.

3.4 Alpha Phase Sintering Experimental Design

The alpha phase sintering experiments made use of the same furnace as well as the previously mentioned hydride experiments, Fig. 3-9. A reaction vessel was constructed using 316 stainless steel threaded rods, 304 stainless steel heat shields, and a fabricated 304 stainless steel cup, Fig. 3-10. The cup was a fixed to the bottom heat shield via ¼ inch screw. The inner diameter of the cup was 0.90 inches. The alumina crucible was placed inside on the cup and held the pellet during the experiments. The heat shields had a

diameter on 1.875 inches. The heat shields were attached to the threaded rod using hex nuts and each had a ¼ inch hole located in the center. The top plate had a diameter of 2.5 inches. This rested over top of the opening of the furnace well and allowed the rest of the device to hang from that point. Through the center hole a stainless steel rod could be placed. At the top of this rod, the magnet for the LVDT was be affixed to enable monitoring of dimension changes in the specimens. The bottom of the stainless steel rod was covered with a yttrium oxide sheath to prevent interaction with the pellet.

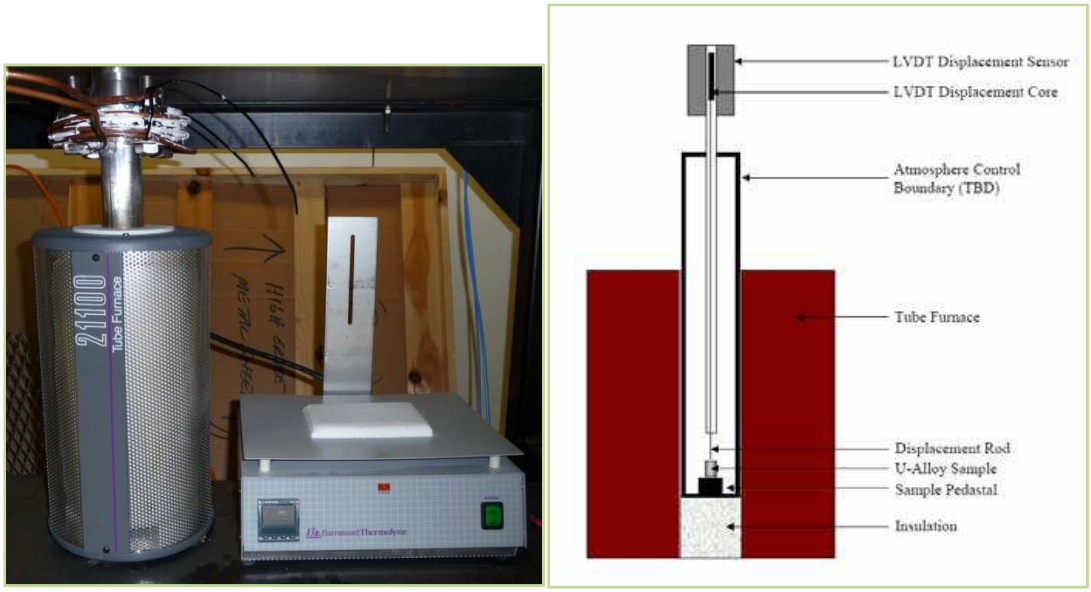

Fig. 3-9 Left: The furnace well and furnace used in the sintering rate and powder production experiments. Right: A simplified schematic of the sintering rate experimental setup

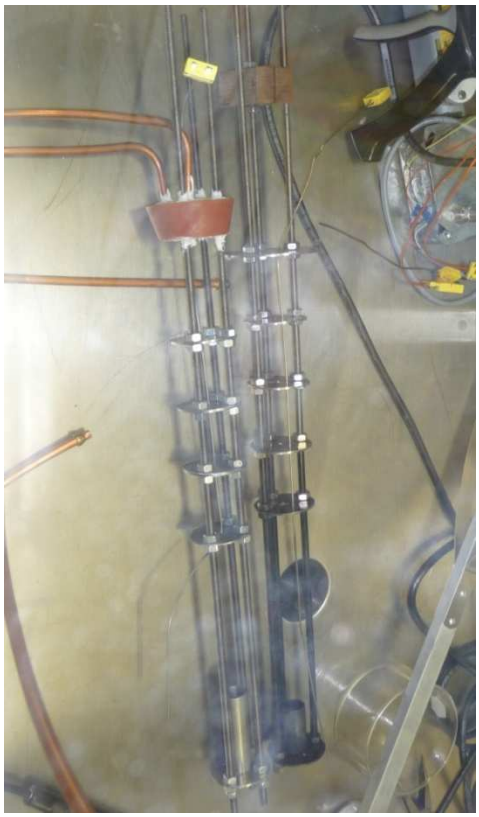

Fig. 3-10 The alpha phase sintering experiment reaction vessel (right) lying next to the hydride reaction vessel (left) on the glovebox floor.

The LVDT was held in place using a carved wooden block which could be tightened or loosened around the LVDT by turning a small screw. The design of the LVDT allows for no interference from frictional forces as it moves freely and does not come into contact with the walls of LVDT, Fig. 3-11.

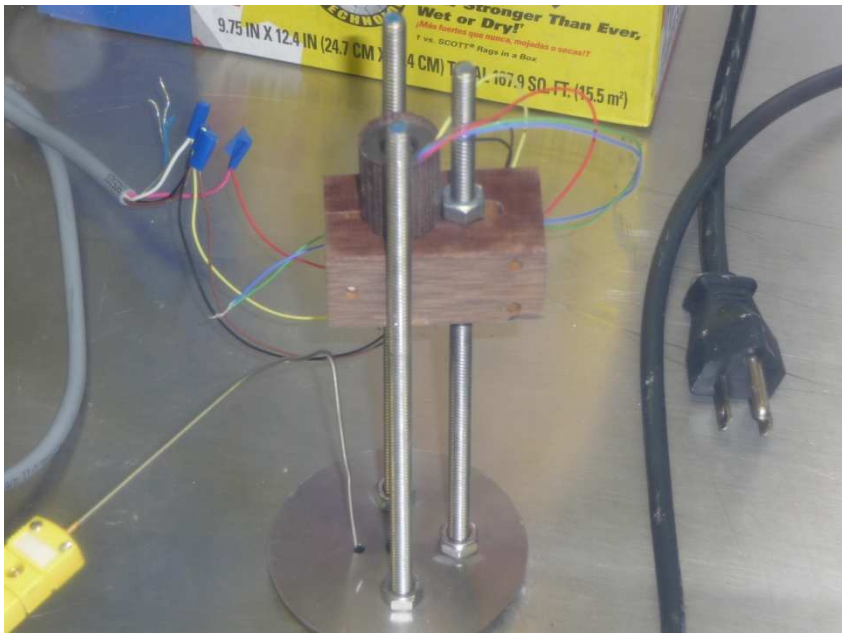

Fig. 3-11 The LVDT with magnet inserted held by the reaction vessel

3.5 Alpha Phase Sintering Experimental Procedures

The pressed pellet was either stored in a sealed container or immediately used in a sintering rate experiment. Before being placed in the furnace well the pellets were weighed using the balance. The diameter and height of the pellets were measured using calipers with an error or 0.0127 mm, the measurements were taken 5 times for each dimension giving a total error for these measurement 00057 mm. The pellets were only handled with tweezers and never came in contact with the gloves in order to prevent contamination of the samples. The pellets were then placed in an alumina crucible which was placed into the cup at the end of the holder.

The LVDT was used to monitor the sintering rate of the pellet. The LVDT magnet was attached to the end of a threaded rod and the rod inserted in the center of the holder. The yttrium oxide sheath was placed over the end of the rod and the sheathed rod was

allowed to rest on top of the pellet. The holder was then placed into the furnace well. The LVDT was then positioned such that the magnet was completely surrounded. Also the magnet was placed towards the upper end of the LVDT so that there would be less chance of the magnet lowering outside the bounds of the LVDT during the experiment, thus stopping the differential voltage signal. The LVDT was then secured by tightening the wooden holder around it.

The k thermocouple and the LVDT were connected to two display units which in turn were connected to a DAQ (National Instrument USB 6029 DAQ). The signals were compiled using the data acquisition program LabView 8.6. The rough data was exported into a Matlab program for analysis.

4. RESULTS

The first section of this section, Section 4.1, describes the results from the uranium hydride/dehydride experiments performed to develop the process to produce clean, fine uranium powder (referred as the powder production experiments). Section 4.2 describes the experiments performed to evaluate the alpha phase sintering of uranium and uranium-zirconium alloys (referred as the sintering rate experiments). The experiments in Section 4.2 depended on the results in Section 4.1 because the hydride/dehydride was necessary to provide the fine uranium powder.

4.1 Powder Production Experiments

The powder production experiments are divided into three groups based on the major stages in the process development equipment described in Section 3. The following section describe the results derived using the "Airlock Setup", the "Initial Furnace Well Setups", and the Successful Furnace Well Setup."

4.1.1 Airlock Setup

Originally the powder production experimental system was placed in the west airlock. This system was used for experiments 1 through 4. The experiments were never successful do to 1) an inability to keep a constant flow of Ar-5%H_2 gas and 2) leaks in the airlock when not under pressure. Even so, small amounts of powder were produced from these experiments (Fig. 4-1), but the initial uranium slugs and the resulting powder appeared to have oxidized during the hydriding portion of the experiment.

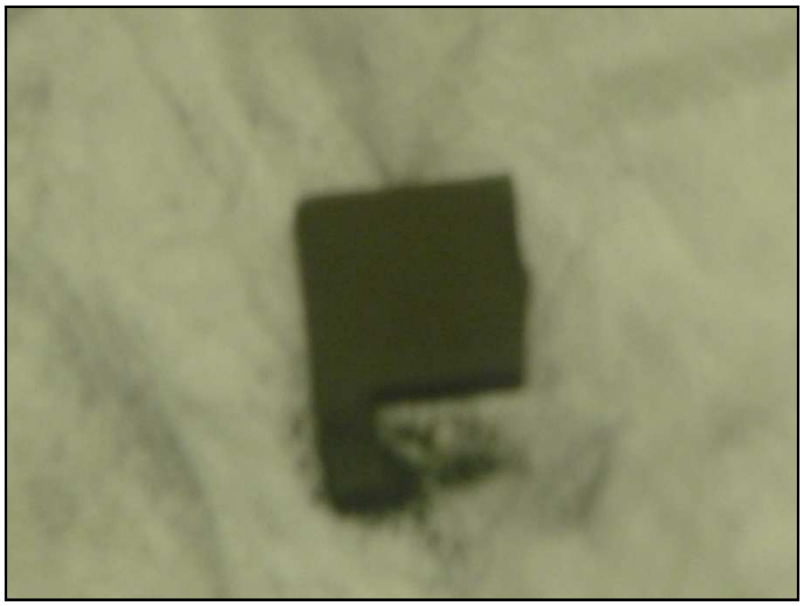

Fig. 4-1 Photo of depleted uranium piece after hydride/dehydride Experiment 3.

Experiment 1 used a depleted uranium (DU) sample with a mass of 28.0829 g. The chamber was evacuated and then filled with Argon gas. The sample was heated to a temperature of 220°C. At this point the airlock was filled with Ar-5%H_2 gas, until the pressure in the airlock reached ambient pressure (~1 atm). The sample was allowed to sit at 220°C in the Ar-5%H_2 atmosphere for 1 hour. Then the chamber was evacuated and heated to 300°C for 1 hour. The sample did not hydride or break down its structure but there was a small amount of black powder around the sample (less than 0.5 g). During the experiment the sample changed in color from silver to dark gray/black.

Experiment 2 used a DU sample with a mass of 35.5965 g. The chamber was evacuated and then filled with Ar gas. The sample was heated to 350˚C. The chamber was then evacuated and filled with Ar-5%H_2 gas. The chamber was then cycled from an Ar-5%H_2 atmosphere 3 times with the dwell time for gas atmosphere being 15, 15, and 25

minutes. The chamber was once again evacuated and brought to a temperature of 450˚C. The sample was held at this temperature for 45 minutes *in vacuo*. The results were similar to the experiment 1 results with only a small amount of black powder produced that was apparently oxidized.

Before Experiment 3 the overpressure valve was removed from the airlock to eliminate a possible source of oxygen contamination. Experiment 3 reused the DU sample from experiment 2. The mass of sample after experiment 2 and a subsequent acid washing was 34.8641g. The chamber was evacuated and then filled with Ar-5%H_2 gas. The sample was then heated to 400 ˚C and allowed to dwell in the Ar-5%H_2 atmosphere for 4.6 hours. At the end of dwell time the sample temperature was 429˚C. The sample was then allowed to cool; no attempt at hydrogen disassociation was made. There was no evidence of hydration or structural breakdown of the sample. The results were similar to the previous experiments with only a small amount of black powder produced that was apparently oxidized.

Before Experiment 4 the pressure gage was removed from the airlock to remove another possible source of oxygen contamination. Experiment 4 reused the DU sample from Experiment 1. The mass of sample post experiment 1 and a subsequent acid washing was 27.9063 g. While the chamber was flooded with Ar-5%H_2 gas, the sample was heated in vacuo to 400˚C. The sample was allowed to sit at a 400 ˚C furnace temperature in the Ar-5%H_2 atmosphere for 2.67 hours. At the end of the dwell period the sample temperature was 465 ˚C. The sample was then allowed to cool in the Ar-5%H_2 atmosphere and no attempt to dehydride was made. There was no evidence of hydration or structural break

down. The results were similar to the previous experiments with only a small amount of black powder produced that was apparently oxidized.

4.1.2 Initial Furnace Well Setups

The reaction vessel was moved into the furnace of the glovebox for the remaining experiments, beginning with Experiment 5. This section will summarize the experimental setups that were never fully successful.

In the initial design the process gas did not flow through an oxygen trap. Small amounts of uranium (~3 grams) were were inserted into the setup described in Section 3 for experiments 5 through 7. During experiment 5 the furnace was heated to 350°C under an Ar-5%H_2 atmosphere for one hour. The temperature was then lowered to 250˚C for 5 hours. No attempt to dehydride was made. After cool down the sample was a dark brown and black in color with no visible hydration or structural breakdown. When the piece was later washed in 35% volume nitric acid solution the sample turned silver, as expected, except for a dark brown line running the length of one face, Fig. 4-2. Experiments 6 and 7 were run under similar circumstances and produced similar results.

Figure 4-2 DU piece structurally intact but discolored after experiment 5

A Ti getter was added to the process gas line for experiments 9 through 12, in order to trap O_2, N_2, moisture, etc. The most successful experiment of this set was experiment 9. During experiment 9 6.2512 g of DU was placed in the reaction vessel. The Ti getter was raised to a temperature above 1000 ˚C before it was exposed to the process gas. The flow rate was kept less than 1 SCFH, and the pressure of the process was kept at approximately 5 psi (the actual pressure in the reaction vessel was most likely lower). The furnace was raised to 275˚C under an Ar-5%H_2 atmosphere and held for 15 hours. A vacuum was established periodically within the reaction vessel during the dwell time in an attempt to promote hydration of the sample. The sample was cooled and removed without attempting to fully dehydride the sample. 1.2094 grams of UH_3, a fine dark brown/black powder, was produced from the sample. The remaining sample and powder were returned to the reaction vessel.

The sample was heated to 275˚C for 24 hours and the chamber was periodically evacuated. A total of 3.1519 g of UH_3 was produced at the end of this process, Fig.4-3.

Fig. 4-3 Powder produce from experiment 9

Experiments 10 and 11 did not produce a significant amount of powder. The results were similar to experiments 5 through 8. During experiment 12 a small amount of powder, approximately 1.5 g was produce over 3 days. However, during the third day a leak in the Ti getter line was discovered. The process gas was immediately shut off and the reaction vessel was sealed off from the system. The powder produced was black in color and did not dehydride when heated under a vacuum. After experiment 12, the bottom third of the copper tubing turned yellow in color, Fig. 4-4. The yellow layer appeared to have been plated and could not be removed with a paper towel. The yellow layer remained on the reaction vessel

for the remainder of the experiments. It had no apparent effects on the experiments. After experiment 12 the Ti getter was abandoned in favor of a commercially made oxygen and moisture trap.

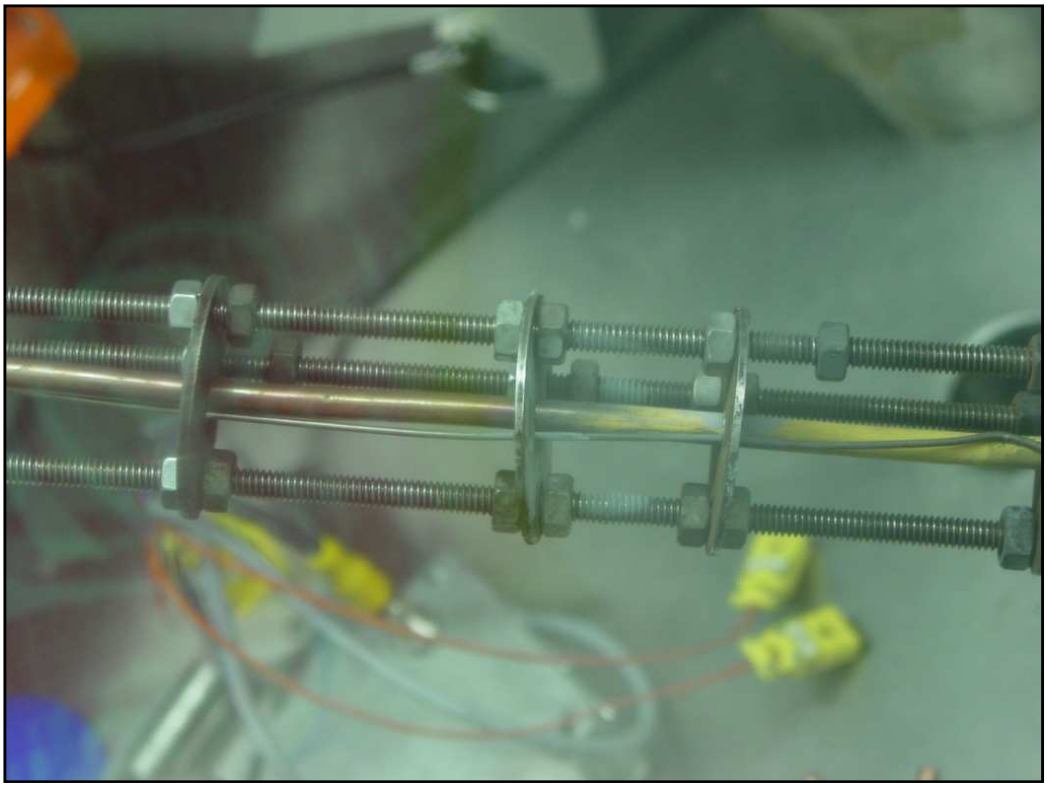

Fig. 4-4 Discoloration of copper tubing after experiment 12

4.1.3 Successful Furnace Well Setup

With the replacement of the Ti getter with the oxygen and moisture trap, Experiment 13 demonstrated a successful and repeatable hydride/dehydride process and therefore represents the final "experiment" in this section; all subsequent hydride/dehydride operations used this procedure for powder production. During experiment 13, 9.6622 grams of uranium metal powder was placed in the reaction vessel. The sample was raised to a

temperature of 265˚C for 24 hours with a flow rate of approximately 2 SCFH and the pressure of the reaction vessel was approximately 2 psi. The sample was cooled with no attempt made to dehydride. A significant amount of dark brown powder, assumed to be UH_3, was visible in the crucible. The non-hydrided portion of the DU sample along with the UH_3 powder was returned to the reaction vessel. The sample was then hydrided for an additional 24 hours under the same conditions. The sample was then place under vacuum and heated to 450 ˚C for 12 hours, this was an extreme amount of time as most literature showed a maximum time of 1 hour when dehydriding 100 grams of UH_3. The entire piece of uranium did not hydride, and the shape of the original uranium sample could be clearly seen in the sintered chunk shown in Fig. 4-5. The piece did not break under light pressure such as pressured applied by tweezers shown in Fig. 4-6, but the piece was broken apart with more applied force and weight. This is consistent with the literature of previous work.

Figure 4-5 Loose and sintered powder produce from experiment 13

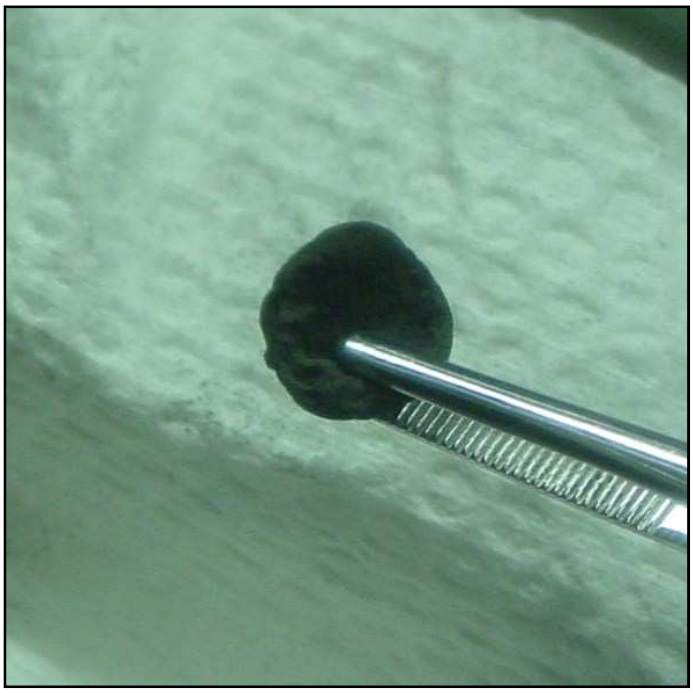

Figure 4-6 Sintered powder from experiment 13

This result was repeated throughout the rest of the experiments. The chunks were loosely sintered and could be mostly broken apart be shaking the chunk in a glass jar. The chunk was further broken apart with a stainless steel mortar and pestle. The pieces were then placed in the Wig-L-Bug and broken down with or without the addition of a stainless steel ball bearing. This process is shown in Fig. 4-7 through 4-10. The uranium, which failed to hydride, can be clearly seen in Fig. 4-11 and 4-12. The loose powder was used in a subsequent sintering experiment.

Figure 4-7 Loose and sintered powder produced post experiment

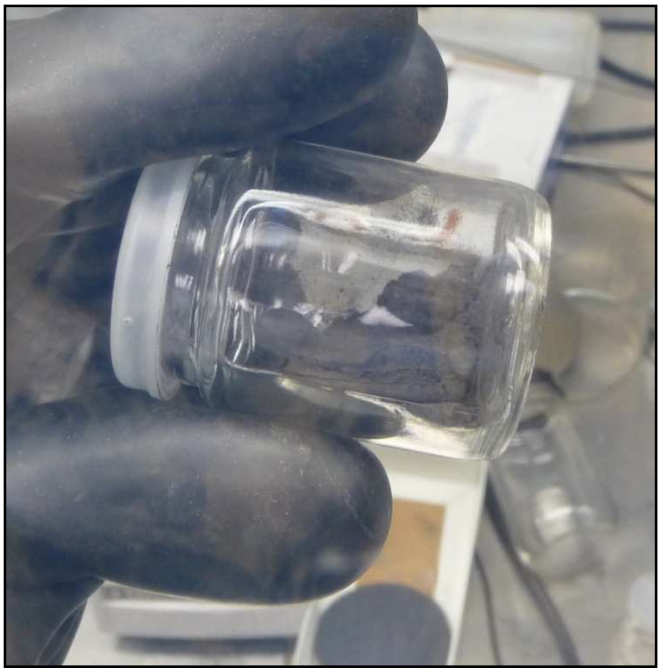

Figure 4-8 Break down of sintered powder after shaking the container

Figure 4-9 Powder, sintered chunks, and non-hydrided DU ground with mortar and pestle

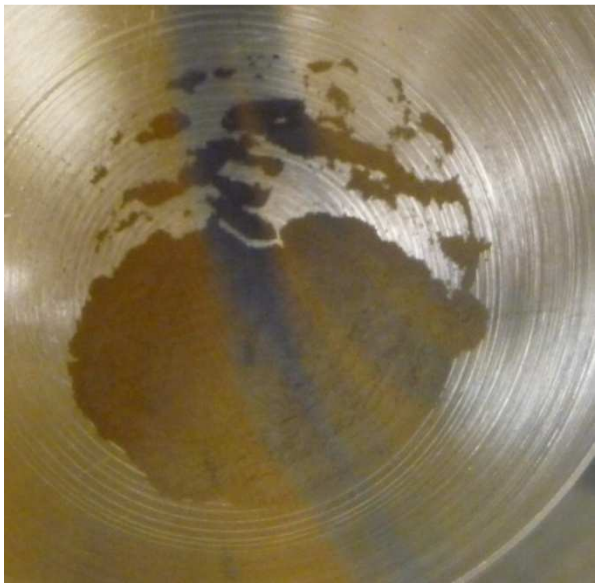

Figure 4-10 Powder after being milled in the Wig-L-Bug (sintered chunks/no hydride DU was removed)

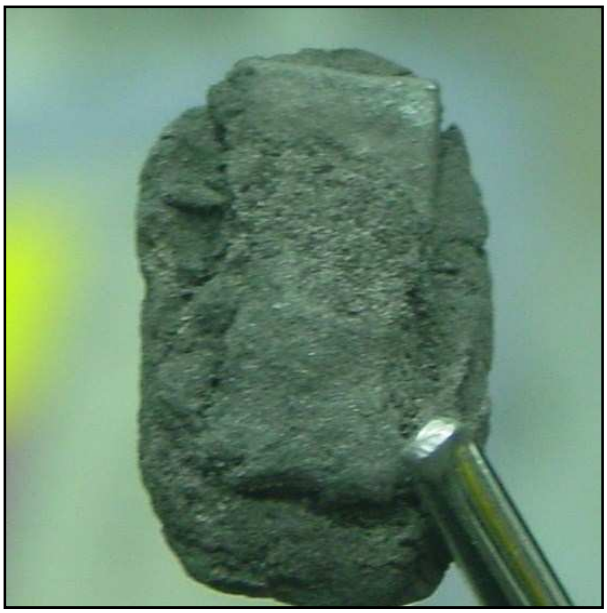

Figure 4-11 Non-hydrided DU visible and surrounded by sintered powder

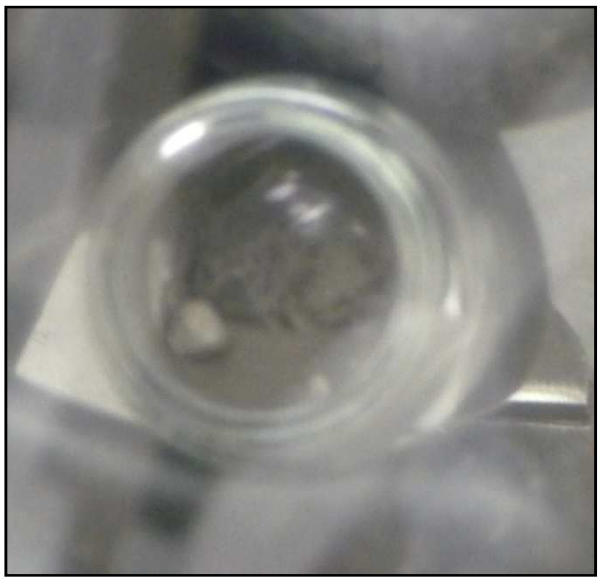

Figure 4-12 Non-hydrided DU with DU powder

The hydrogen disassociation was monitored by observing the pressure change of the reaction vessel during the dehydride phase of the experiment. The well was under a rough vacuum during dehydriding, a pressure of ~0.001 Torr. When the UH_3 would begin to disassociate the pressure on the vacuum gauge would rise. The pressure would continue to rise until a peak value was reached. At this time the pressure would stabilize and then begin to lower, as seen in Figs. 4-13 and 4-14. The dehydride was considered complete after the pressure returned to 0.001 Torr, however the sample remained at temperature *in vacuo* for an additional 15 minutes to insure full hydrogen disassociation.

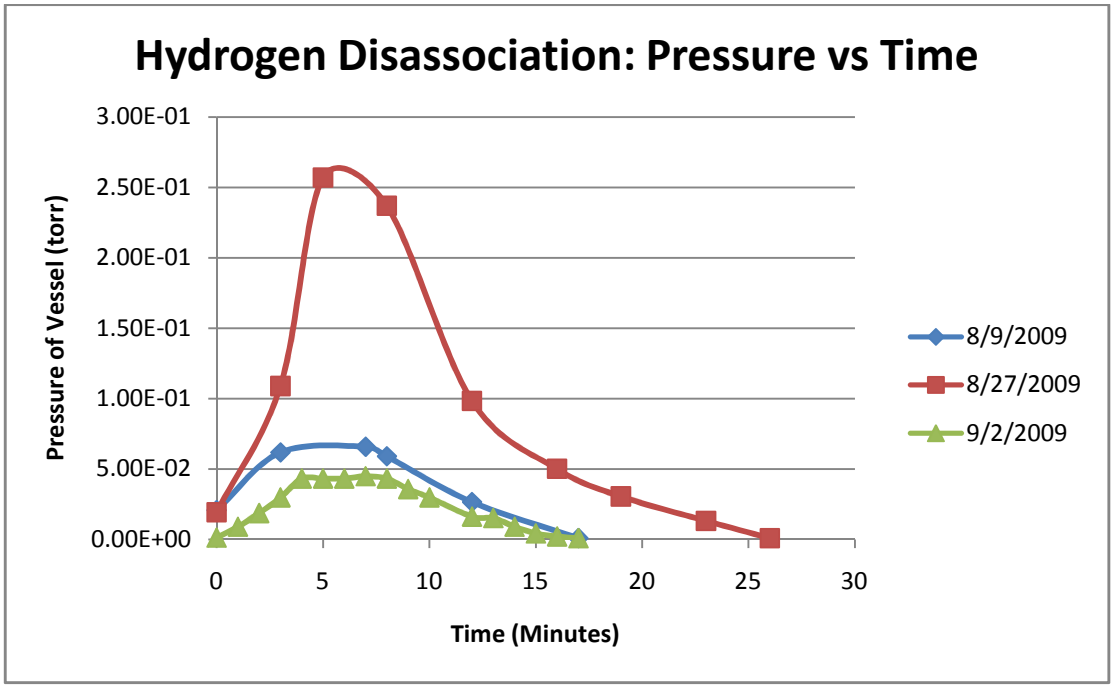

Fig. 4-13 Pressure vs Time during the dehyride step

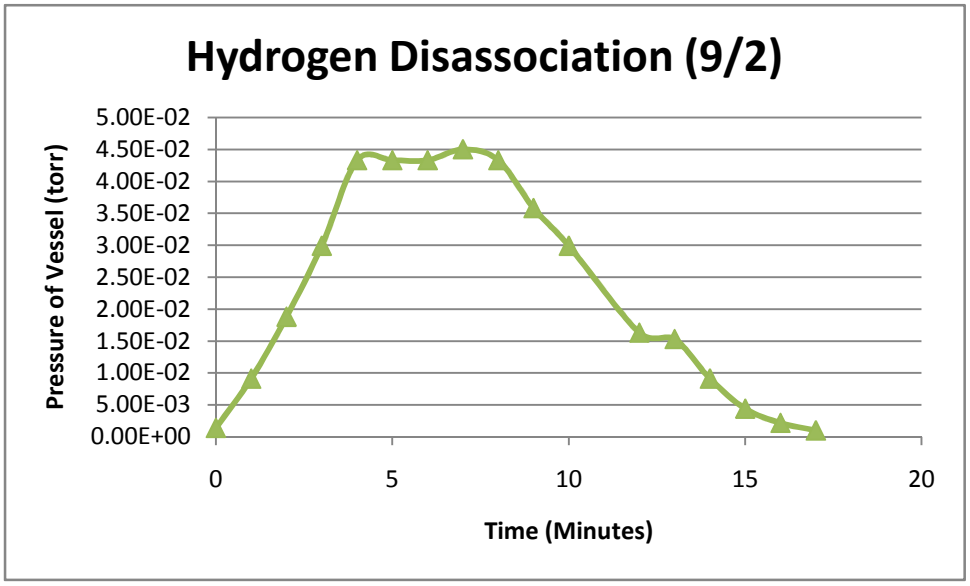

Fig. 4-14 Pressure vs Time during the dehyride step

4.1.4 Digital Microscopy of the DU Powder

A small sample of the DU powder was removed from the glovebox and examined using the KH-1300 microscope. The powder examined was produced during powder production Experiment 13. While the removed powder did oxidize, the images give a good indication of the powder size and characteristics, Fig. 4-15. The larger masses of particles are approximately 100 μm, while the smaller loose powder is on the order of 1 to 3μm. The small particles represent the majority of the powder produced by the methods described here.

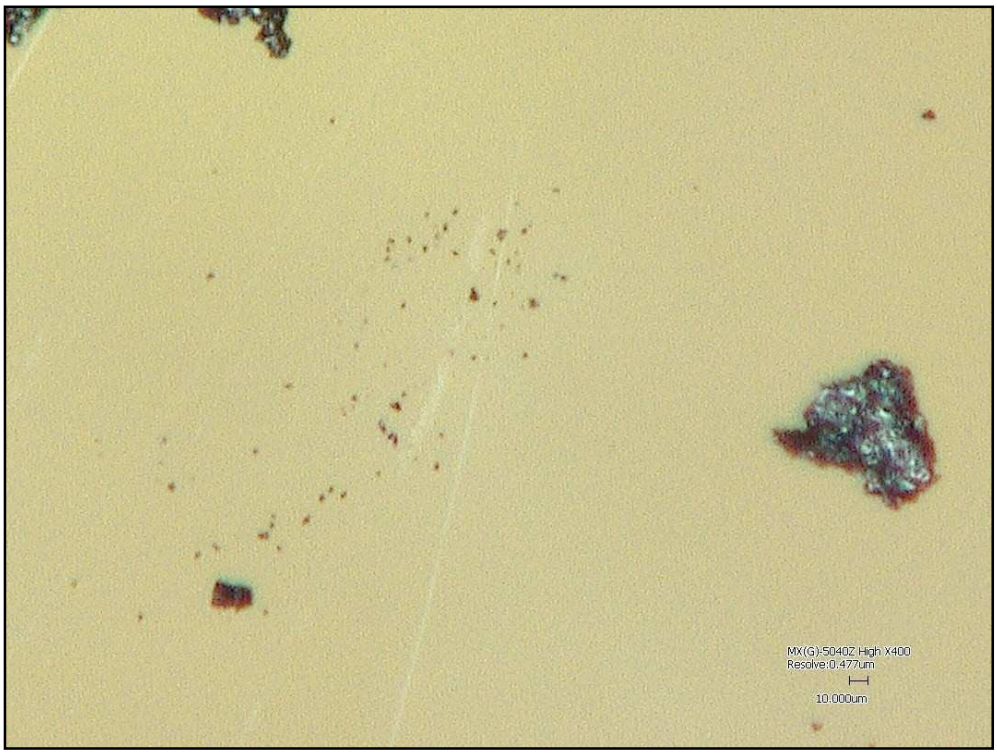

Fig. 4-15 DU at 800X

Also examined with the HIROX KH-1300 was a small piece, approx 1 mm^3, of a sintered DU chunk after the hydrogen disassociation process, Fig. 4-16 through 4-18. The sample was composed of sintered powder and was not a remnant of the original chunk. The sintered portion did not rapidly oxidize during the examination in atmosphere and did not appear to be significantly porous.

Fig. 4-16 DU powder sintered during dehydriding at 50X

Fig. 4-17DU Rough Face at 100X

Fig. 4-18 DU Smooth Face at 100X

4.2 Alpha Phase Sintering Experiments

Once the powder production method was perfected, ten pressed pellets were produced and nine were sintered for evaluation. The pellet powder compositions used in the sintering rate experiments were as follows: 5 pellets of pure DU powder, 2 pellets of DU-10Zr mixture, 1 pellet of DU-1Mg, and 1 pellet of DU-10Zr-2.4Mg (wt%). The pellet radii and heights were measured before and after sintering. In most experiments, the height change was measured during the heating using the LVDT. The samples were also analyzed using a digital microscope (HIROX KH-1300) and an SEM (JOEL-6400).

4.2.1 LVDT Calibration

The LVDT was calibrated using a horizontal motion micrometer. The LVDT magnet was moved at 0.1 in intervals from the bottom of the LVDT to the top and back again. It was determined that the rate of change was 19.1919 volts per inch, Fig 4-19. This

translates to 1.3234 mm per volt (0.0521 inches per volt). Two separate LVDTs and magnets were used during the calibration. No significant change in output was observed.

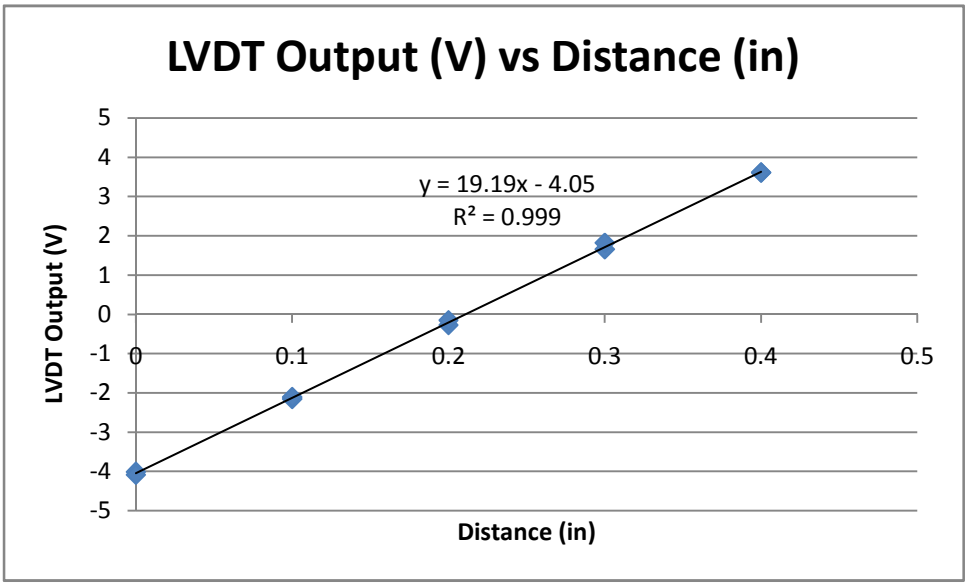

Fig. 4-19 LVDT Output vs Distance

During the sintering experiments the magnet was attached to a steel rod. The steel rod and the vessel well and the assembly hardware thermally expand during heating. In order to quantify this thermal expansion, LVDT output data was recorded without a pellet present in the sintering vessel. This was conducted for an increase from room temperature (~23˚C) to 650˚C, Fig. 4-20, and also for an increase to 700˚C and 795˚C. The data obtained from these calibration experiments were subtracted from the LVDT output obtained from the corresponding sintering experiments. This was done through the use of a data analysis code written in MatLAB.

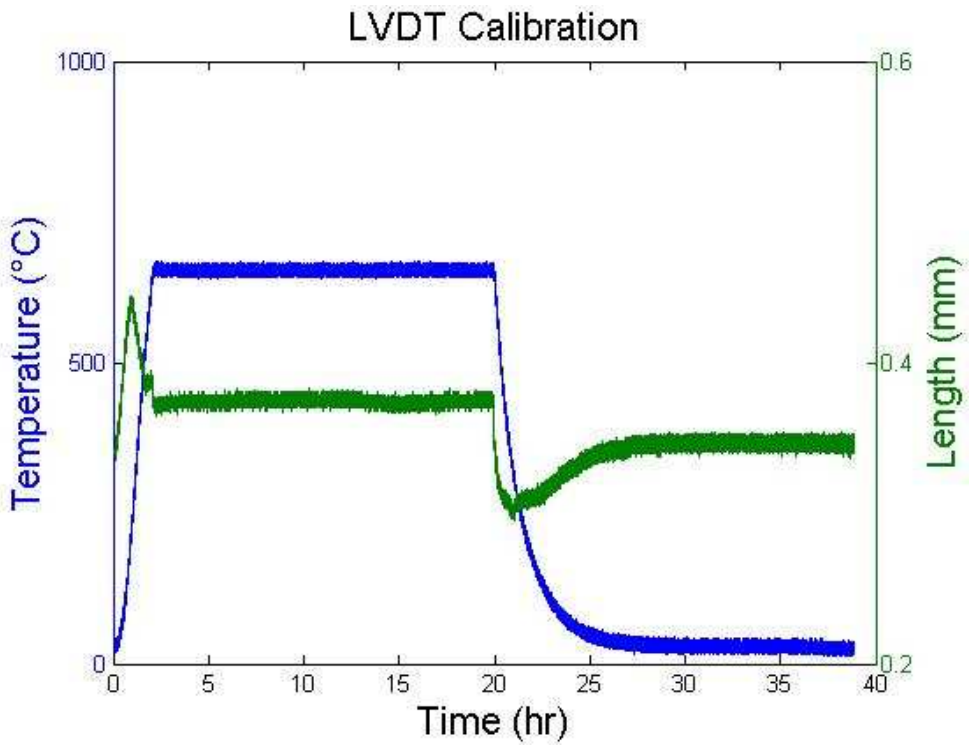

Fig. 4-20 The ramp up and ramp down of the empty system to 650 ˚C, the was an average increase of 0.3753 mm during 650 ˚C dwell time

4.2.2 Physical Observations and LVDT Data of Pellets

The pellet data for all experiments is summarized in Table 4-1 and 4-2.

Table 4-1 Pellet data pre and post experiment

Pellet #	Mass (g)	Pressed Thickness (mm)	Pressed Diameter (mm)	Green Density (% TD)	Post Thickness (mm)	Change (%)
Pellet 2	4.0368	4.3688	9.6215	66.78	4.4704	2.33
Pellet 3	3.3366	4.5288	9.6342	53.11	4.7117	4.04
Pellet 4	2.7656	2.7864	9.6622	71.13	2.8575	2.55
Pellet 5	2.9426	3.556	9.6647	63.47	3.6957	3.93
Pellet 6	2.6417	2.9667	9.6723	64.02	2.9845	0.6
Pellet 8	3.9946	5.0495	9.4234	59.6	5.2705	4.38
Pellet 9	2.9188	3.9472	9.4234	59.63	4.064	2.96
Pellet 10	2.3685	3.5712	9.6139	53.49	3.5687	-0.07

Table 4-2 Pellet data pre and post experiment (continued)

Pellet #	Post Diameter Max (mm)	Change (%)	Post Diameter Min (mm)	Change (%)	ΔL/L (from LVDT data)
Pellet 2	9.9568	3.37	9.8806	2.69	-
Pellet 3	9.8425	2.12	9.6901	0.58	0.0336
Pellet 4	9.8933	2.34	9.7409	0.81	0.0144
Pellet 5	10.1346	4.64	9.8552	1.97	-
Pellet 6	9.4488	-2.37	9.3599	-3.23	0.0506
Pellet 8	9.8171	4.01	9.3599	-0.67	0.0150, 0.0122*
Pellet 9	9.779	3.64	9.525	1.08	-
Pellet 10	9.652	0.39	9.6393	0.26	-

*ΔL/L for Pellet 8 was measured at 24 hours and 34 hours;

- indicates no LVDT was measured for that experiment

The initial pellet, pellet 1, was pressed using a double action punch and die fabricated from 303 stainless steel. The original punches were not strong enough to withstand a great amount of force, pellet 1 was pressed with a maximum force of approximately 5,000 lbs. The green density of pellet 1 was 7.75 g/cm^3 (~40.7% theoretical density). The pellet was a right cylinder with a 6.6802 mm in height and a 9.6266 mm diameter. Pellet 1 had a total mass of 3.7691 g. The pellet was placed in the furnace well and sintered for 48 hours at temperature of 640 °C. While the resulting changes in the LVDT voltage seemed to indicate sintering, the pellet broke into three large pieces inside the well (most likely on cooling). With the large piece, there was also powder in the crucible. This occurrence made any measurement of the post experiment diameter impossible. An attempt was made to measure the height of Pellet 1. While the breakage caused the accuracy of the measurements to be suspect, no shrinkage or swelling was observed.

The second pellet, as well as the rest here forward, was pressed using a 303 stainless steel die and punches fabricated from H13 tool steel which were then heat treated and tempered. This change allowed a much greater force to be applied when pressing the pellets. Pellet 2 was fabricated entirely from DU powder with a maximum pressing force greater than 15,000 lbs. This resulted in a green density of 12.69 g/cm^3 (66.6% theoretical density), Fig. 4-21. The pellet had a total mass of 4.037 g, a height of 4.3688 mm, and a diameter of 9.6266 mm Pellet 2 was sintered for 24 hours at a temperature of 650°C, 4-22. The linear displacement rod was not placed on the pellet for this experiment because it was speculated that it may have been a source of complications in the pellet #1 test. Therefore, there was no real time data of the vertical changes in the pellet. Initially, when pellet #2 was removed from the furnace no change in volume was observed; however on subsequent inspection it

was observed that the pellet had increased slightly in volume and minor cracks were evident. There was a “bump” in the center of the pellet with a maximum height measured at 4.4323 mm. The lowest height measured was 4.3688 mm. The diameter of the pellet was mostly uniform except on one end where it bowed out. The diameter of the non-bowed portion of the pellet was 9.8171 mm. The end portion of the pellet had a measured diameter of 9.9060 mm.

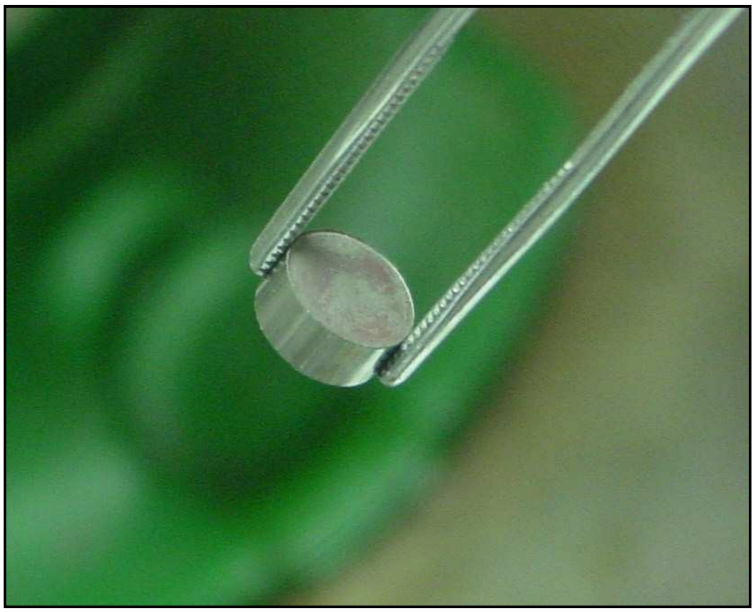

Fig. 4-21 Pellet 2 pre sinter

Fig. 4-22 Pellet 2 post sinter

Pellet 3 was pressed with a maximum load of 15,000 lbs. The green density of this pellet was 10.16 g/cm^3 (53.3% T.D.). Pellet #3 had a total mass of 3.3365 g, a height of 4.5085 mm, and diameter of 9.6266 mm. The pellet was heated to 650˚C for 24 hours, Fig. 4-23. The vertical change in the pellet during the experiment is shown in Figs. 4-24 and 4-25. It is interesting to note that the LVDT data indicates sample shrinkage and the post-test measurements indicate sample growth. Upon completion of the experiment, the final height was measured to be 4.7879 mm, an increase of 6.20%. Also the diameter of the pellet was tapered. A measurement was taken at both ends and in the middle of the pellet. The ends had a diameter of 9.4996 mm and 9.7536 mm. The middle of the pellet was measured at 9.6266 mm, a zero net change in size.

Fig. 4-23 Pellet 3 post sinter rate experiment

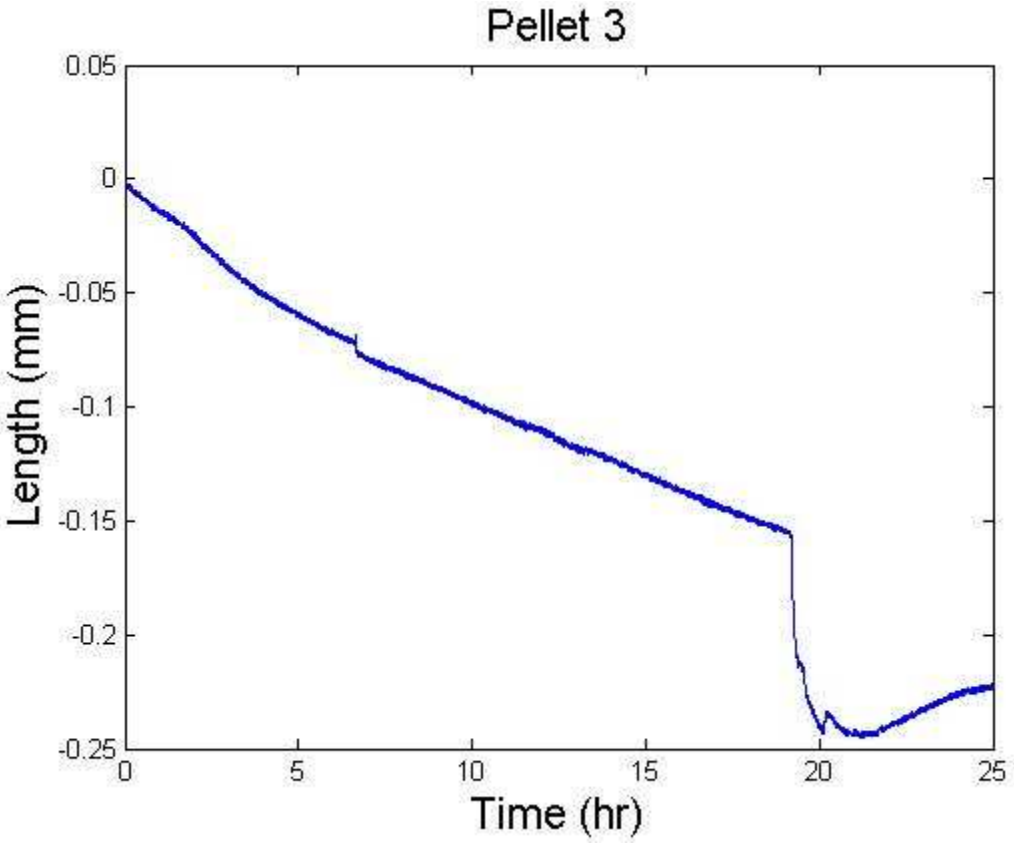

Fig. 4-24 The linear shrinkage of the Pellet 3, with time 0 beginning when the system reached an equilibrium at 650°C

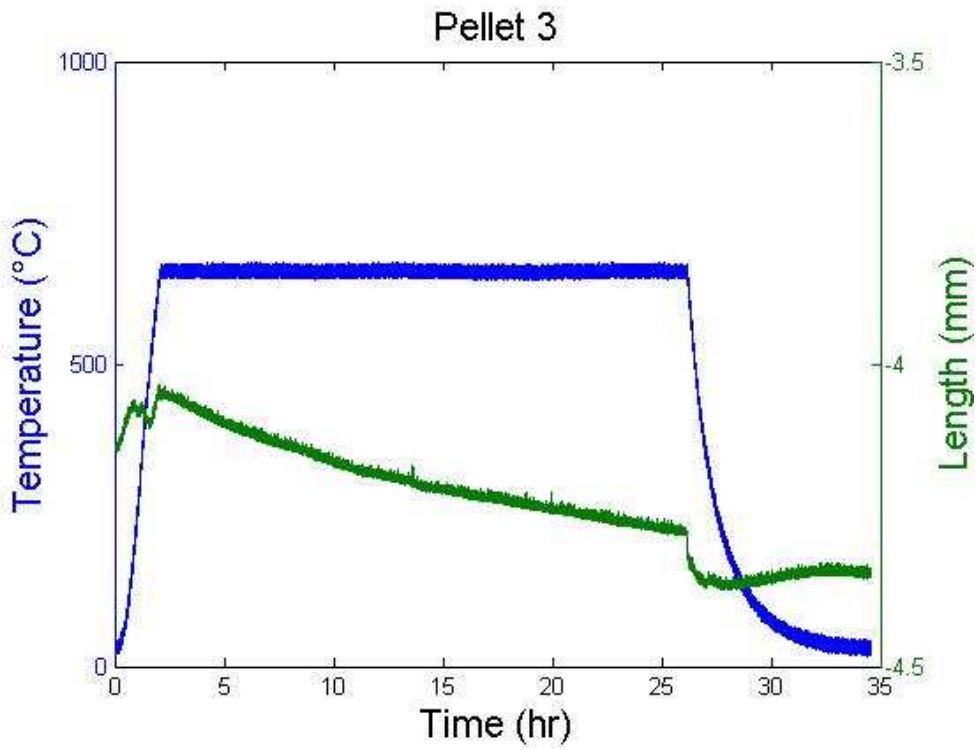

Fig. 4-25 Uncalibrated pellet 3 shrinkage data with temperature

Pellet 4 was press with a maximum load of 15,000 lbs. The initial height and diameter were 2.7864 mm and 9.6622 mm, respectively. The mass of the pellet was 2.2677 g, giving the pellet a green density of 71.3% theoretical density (11.19 g/cm$^{3)}$. The pellet was heated to 655˚C and allowed to dwell at this temperature for 30 minutes. Then the pellet was raised to 695°C, the beta phase, and allowed to dwell for 30 minutes before being cooled back to 655°C. This process was repeated once more, and then the pellet was allowed to dwell at 655°C for 5 hours. Post experiment, the pellet expanded both vertically and linearly. There was a gradient to the radial expansion of the pellet; the small expanded to 9.7409 mm, while the large end expanded to 9.8933 mm. The pellet expanded vertically to 2.8677 mm, however the LVDT data showed a continual decrease in length (see Figs. 4-

26 and 4-27). The phase transitions were too short in duration to be able to discern usable data from the system response to the temperature increase.

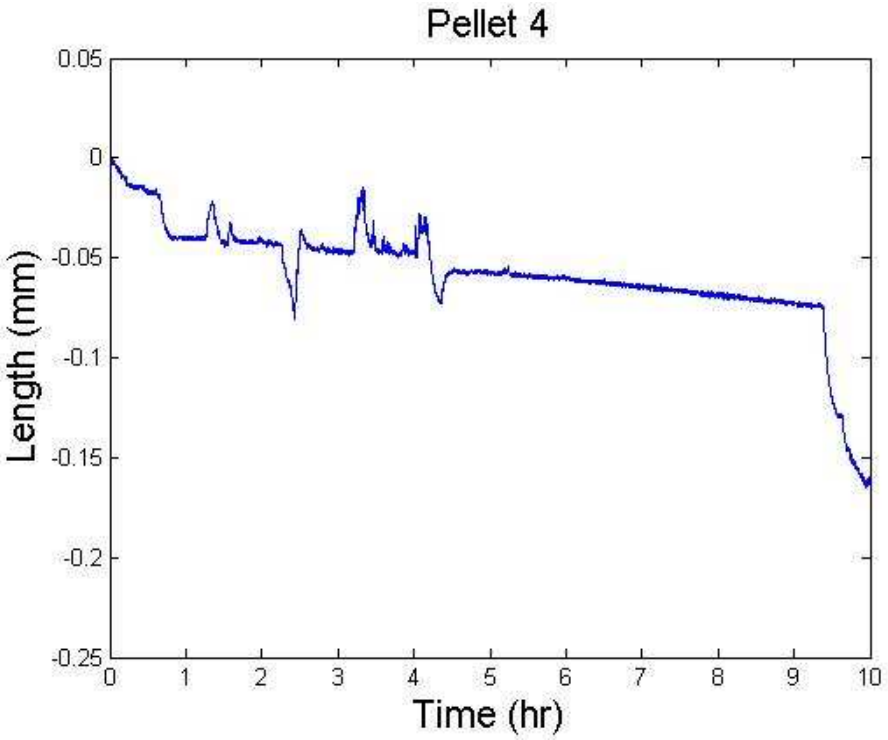

Fig. 4-26 The linear shrinkage of the Pellet 4, with time 0 beginning when the system reached an equilibrium at 650°C

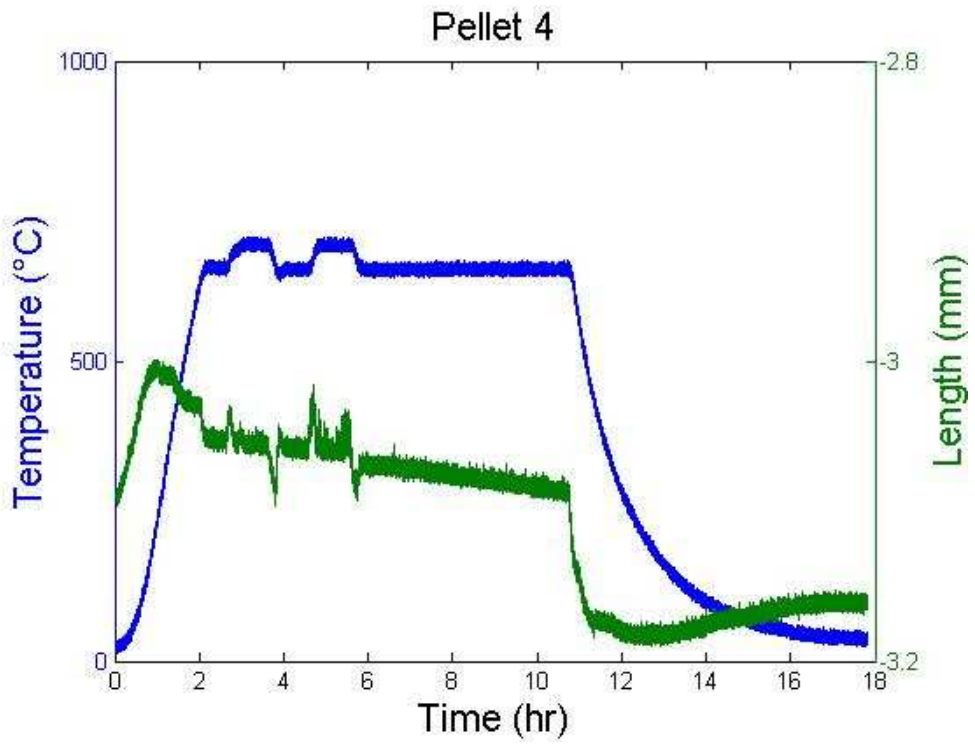

Fig. 4-27 Uncalibrated pellet 4 shrinkage data with temperature

Pellet 5 was fabricated as a DU-10Zr (Wt %) pellet. The masses of the powder used for this pellet were 2.7365 g of DU and 0.3055 g of Zr (the Zr powder was -325 mesh). The powder was placed in the Wig-L-Bug and mixed until homogenous. The final weight of the pressed pellet was 2.9438 g, a loss of 0.0982 g (3.2%) of material. The height and diameter of the pressed pellet was 3.5560 mm and 9.6673 mm respectively, which gives the pellet a green density of 63.47% theoretical (11.27 g/cm$^{3)}$. The pellet was held at 650°C for 12 hours, and then it was cycled three times from 650°C to 700°C with each cycle lasting between two and three hours. After the experiment, there was a visible second phase on the outside of the pellet (Fig. 4-28). The sintered pellet was conical in shape with one end having a diameter of 10.1219 mm and the other having a diameter of 9.8552 mm. The

thickness of the pellet was also slightly uneven with the shortest measurement being 3.6957 mm and the longest being 3.7592 mm. The LVDT data for the pellet is shown in Figs. 4-29 and 4-30.

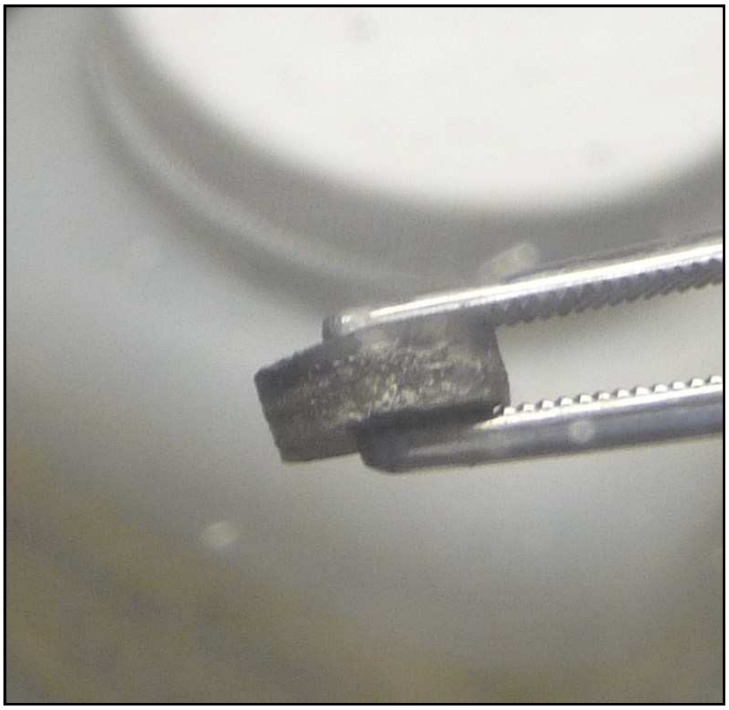

Fig. 4-28 Pellet 5 post experiment

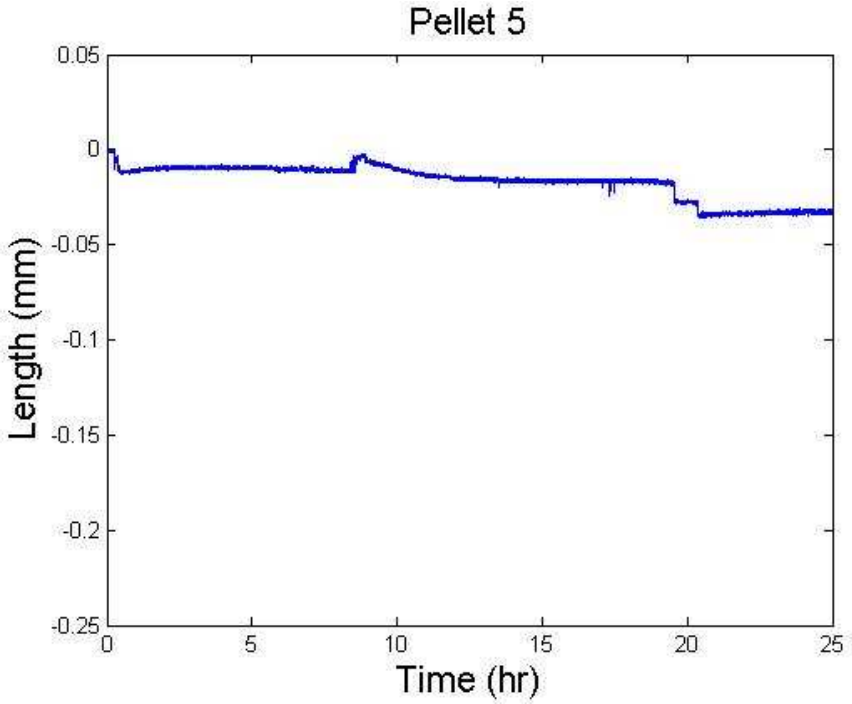

Fig. 4-29 The linear shrinkage of the Pellet 5, with time 0 beginning when the system reached an equilibrium at 650°C

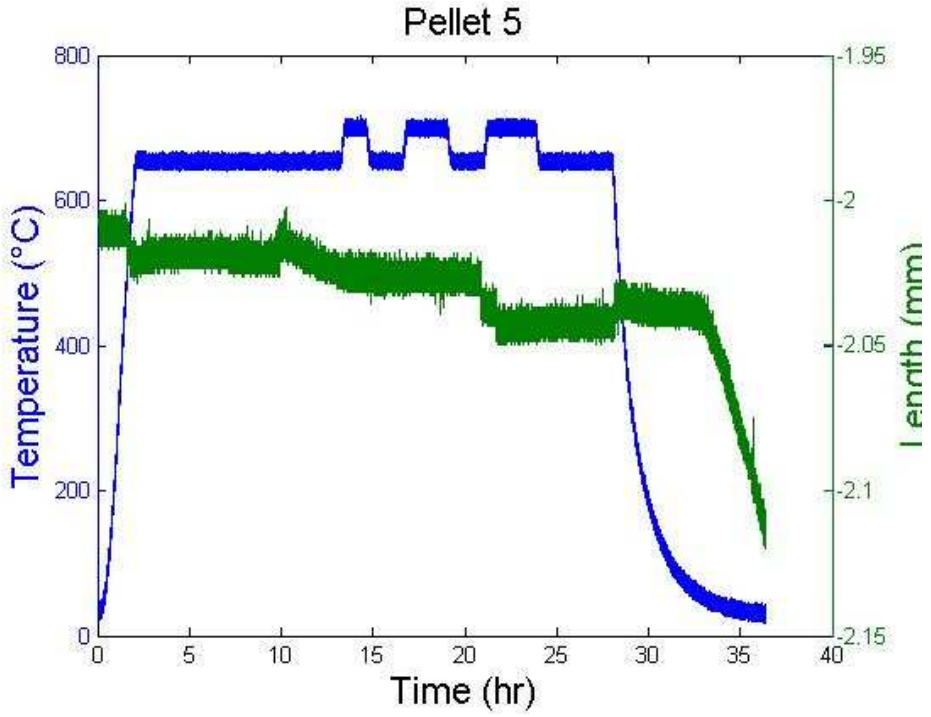

Fig. 4-30 Uncalibrated pellet 5 shrinkage data with temperature

Pellet 6 was a DU-Mg pellet. Mg was used as a surrogate for Pu in order to simulate the liquid phase sintering that would occur in a DU-Zr-Pu pellet. Mg was chosen because it has a similar melting point to Pu (640°C for Pu vs. 650°C for Mg). Because Pu has a much higher density than Mg, it was not prudent to use the same weight percent of Mg in the pellet to simulate plutonium. Instead, the atom % of Pu in a DU-10 wt. % Pu was calculated such that the Mg addition would be analogous to the Pu atom percent A 3 gram U-10 wt% Pu alloy pellet contains 0.00123 moles (0.3 g) of Pu. 0.00123 moles of Mg has a mass of 0.0290 g. Thus the pellet composition was DU-1Mg (wt%).

Pellet 6 was pressed using 2.7058 g of DU and 0.0290 g of Mg. The weight of the pellet after pressing was 2.641 g. The pressed dimensions of the pellet were a thickness of 2.9667 mm and a diameter of 9.6723 mm. This gave the pellet a green density of 64.02%

theoretical density, (12.11 g/cm$^{3)}$. The post experimental thickness of the pellet was 2.9845 mm. The pellet was conical shaped with one end having a diameter of 9.4488 mm and the other having a diameter of 9.3599 mm. During the sintering experiment there was a malfunction with LabView program which halted the data collection; therefore there is no real time sintering data was available.

Pellet 7 was a DU pellet that was pressed with a max load of 15,000 lbs. The pellet was not sintered and was fabricated to use as a structural comparison to the sintered pellets. Pellet 7 went through rapid oxidation while being prepared for analysis outside of the glovebox. Due to this event no useful data about the pellet structure could be obtained.

Pellet 8 was DU pellet that was press with a maximum load of 12,000 lbs. The pressed dimensions of the pellet were a thickness of 5.0495 mm and a diameter of 9.4234 mm. This gave Pellet 8 a green density of 59.60% theoretical density. The pellet was held 650°C for approximately 12 hours, then it was raised to 700°C for approximately 6 hours, then raised again to 796°C for approximately 4 hours, and finally the temperature was lowered back to 650°C for 6 hours. These temperature variations were used in order to observe changes in the linear shrinkage over the three phases, Figs. 4-31 and 4-32. Post experiment the thickness of the pellet was 5.2603 mm. The pellet was conical shaped with one end having a diameter of 9.3599 mm and the other having a diameter of 9.8171 mm, Fig. 4-33.

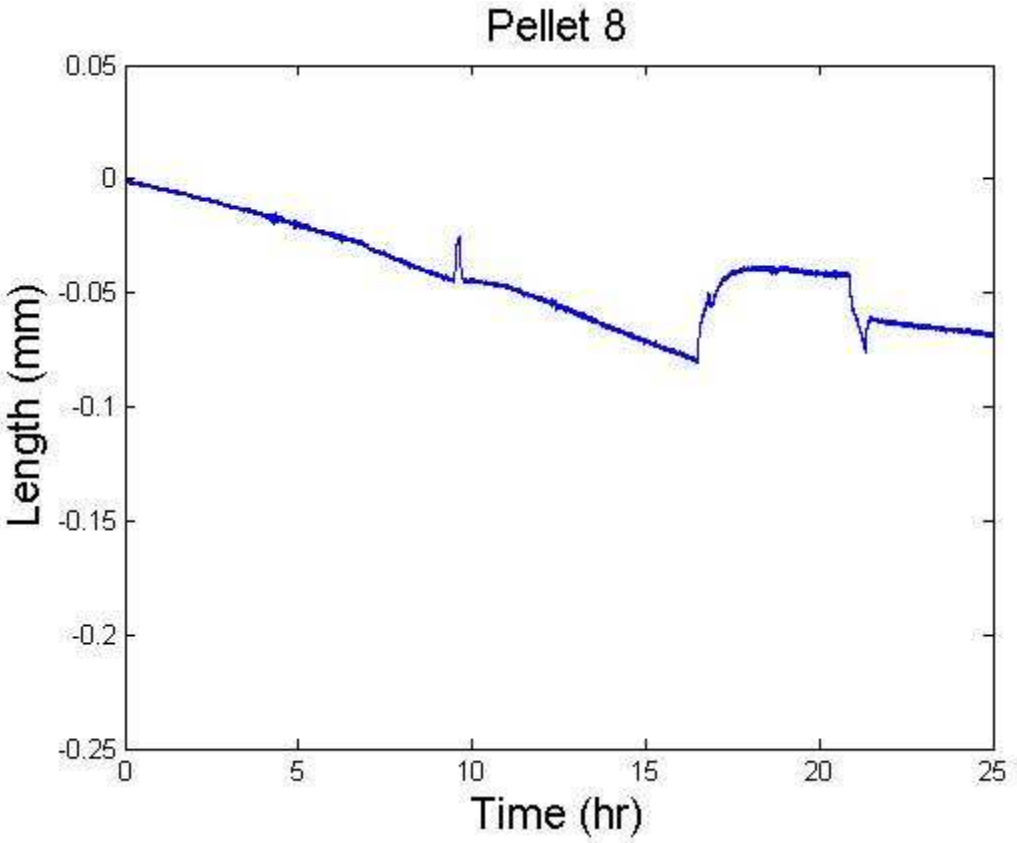

Fig. 4-31 The linear shrinkage of the Pellet 8, with time 0 beginning when the system reached an equilibrium at 650°C

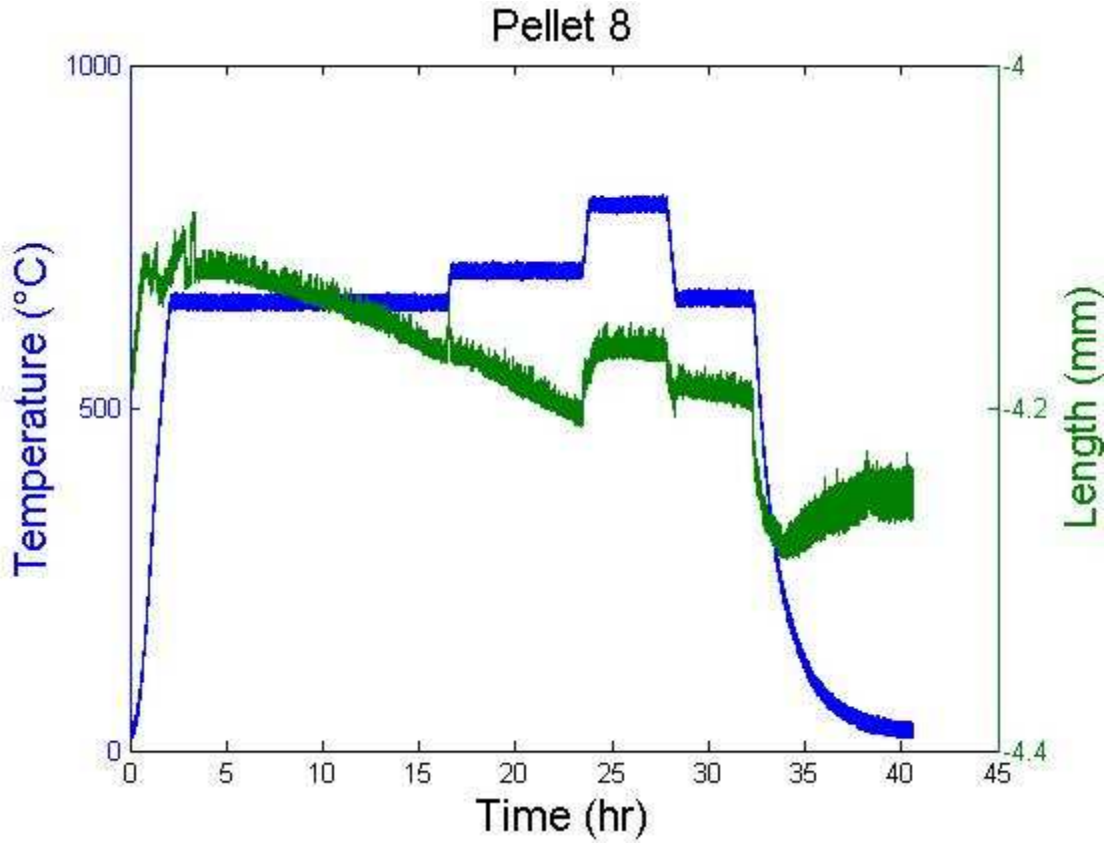

Fig. 4-32 Uncalibrated pellet 8 shrinkage data and temperature

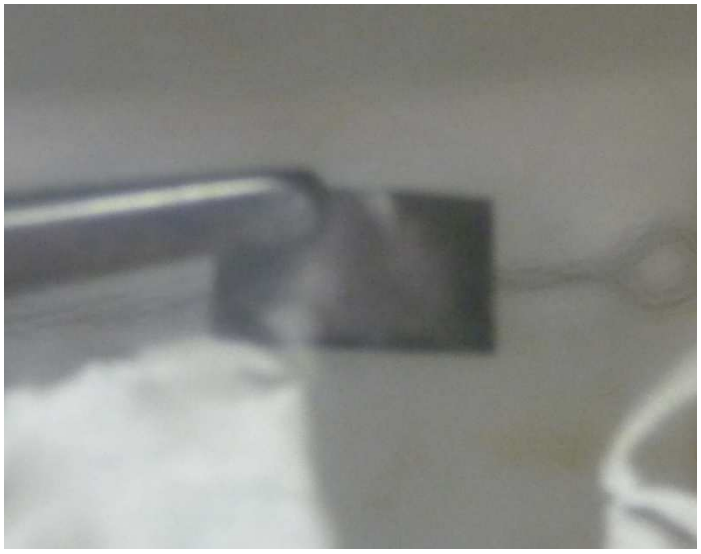

Fig. 4-33 Pellet 8 post experiment, pellet 8 is conical shaped

Pellet 9 was fabricated as a DU-10Zr pellet. The pellet was pressed with a maximum load of 14,000 lbs. The powder was fabricated from 2.6996 g of DU and 0.3004 g of Zr powder, Fig. 4-34. The final weight of the pressed pellet was 2.9188 g. The pressed thickness of the pellet was 3.9472 mm and the diameter was 9.4234 mm. This gave the pressed pellet a green density of 59.63% theoretical density (10.60 g/cm$^{3)}$. The pellet was heated to 650°C and held for approximately 12 hours. It was then raised to 695°C and held for approximately 4 hours. The pellet was then raised to 770°C and held for approximately 4 hours. When pellet 9 was removed from the reaction vessel, it was observed the bottom had been broken (Figs. 4-35 and 4-36). The bottom was rough and powder was continually falling off of the pellet at this point. As the pellet was being measured, the outside of the pellet began to breakaway. This made obtaining an accurate post experiment diameter or thickness impossible. The thickness measured was 4.0563 mm and the diameter was between 9.7790 mm and 9.5250 mm. During this experiment, there was a malfunction with the LVDT system which caused extreme swings in voltage thus making most the obtained data useless. However the initial data, at 650°C, did not suffer from these voltage swings. The data obtained was analogous to pellet 5, also a DU-10Zr pellet.

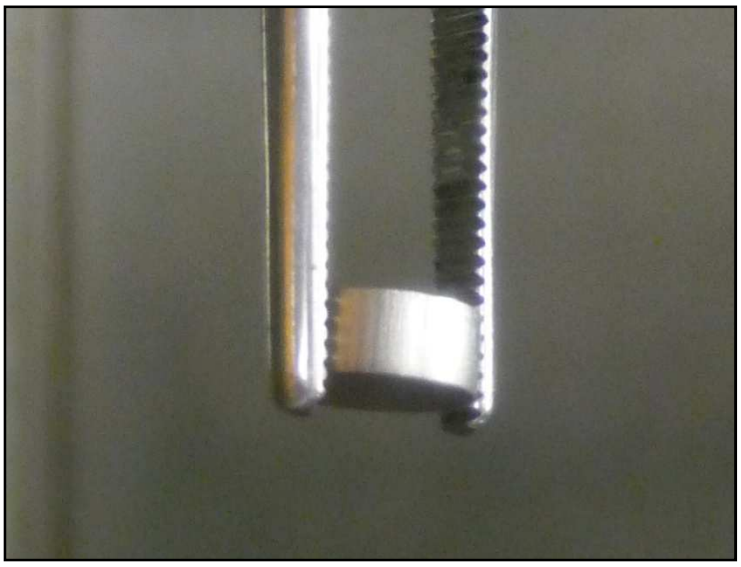

Fig. 4-34 Pellet 9 (DU-10Zr Wt %) pre experiment

Fig. 4-35 Pellet 9 (DU-10Zr Wt %) post experiment

Fig. 4-36 Pellet 9 (DU-10Zr Wt %) post experiment

Pellet 10 was fabricated as a DU-10Zr-2.4Mg pellet. The amount of Mg used was an equivalent At % as the amount of Pu in a 3g DU-10Zr-20Pu pellet. A 3 gram U-10Zr-20 wt% Pu alloy pellet contains 0.00246 moles (0.6 g) of Pu. 0.00246 moles of Mg has a mass of 0.0597 g. The mass of the components used to fabricate pellet 10 are as follows: DU 2.0998 g; Zr 0.3009; Mg 0.0595 g. The final mass of the pressed pellet was 2.3685 g. The powders were mixed together using the Wig-L-Bug until homogenous. The pressed thickness of the pellet was 3.5721 mm and the diameter was 9.6139 mm. This gave pellet 10 a green density of 53.49% theoretical density (9.13 g/cm$^{3)}$. The pellet was heated to 655°C and allowed to dwell at this temperature for 12 hours. Post experiment there was very little change in the dimensions of the pellet. The diameter was measured to be 9.6418 mm and the thickness was measured to be 3.5662 mm. The pellet was golden in color and

there was a dark mark on one side (Figs. 4-38 and 4-39). The portion with the dark mark was not as structurally stable as the rest of the pellet and was fragile when probed.

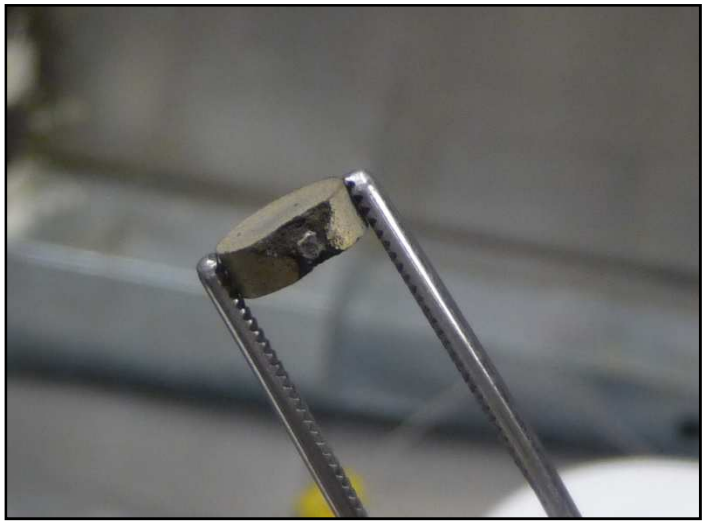

Fig. 4-37 Pellet 10 post experiment, pellet was gold and structurally damaged

Fig. 4-38 Pellet 10 post experiment, pellet was gold and structurally damaged33

4.2.3 Microscopy of the Pellets

The HIROX KH-1300 digital microscope and JOEL-6400 SEM were used to examine the pellets after sintering. The images were analyzed to characterize the the structure, porosity, and phase compositions. All pellets showed varying degrees of sintering and porosity. One constant was the presence of various sized cracks; the largest cracks were not captured during SEM imaging (in other words, the images were taken from regions between large cracks). The cracks appeared in greater frequency along the edges of the pellet. Porosity estimates were only able to be calculated for Pellets 2, 3, and 6, due to limitations of the SEM JOEL-6400. The pores in the SEM images of pellet 5 and 10 were obscured to the point at which an accurate porosity measure was not viable. The porosity was calculated using the image analysis software Image J. Using this software a number of pixels making up the pores were counted and the ratio of these pixels to the total pixels of the image was calculated. A detailed analysis of these images can be found in Section 5.2.2.

5. DISCUSSION OF RESULTS

5.1 Powder Production

5.1.1 Successful Development of a Powder Production System

A system to produce fine DU powder via the hydride/dehydride method was successfully designed and developed, but there were a number of key design changes along the way that highlight the need for gas purity, metal surface preparation, and well controlled vacuum conditions. In the final method, uranium slugs were hydrided at 225˚C to form UH_3 powder and dehydrided at 375˚C to form U metal powder. After the hydrogen disassociation step the powder was loosely sintered into fragile agglomerates. The agglomerates were broken apart using a stainless steel mortar and pestle and mechanical milling. These results agree with previous literature (Chiotti, Wilkinson). Using various starting DU masses (approximately 10-20 g), a single powder production run produces 6 to 12 g of fine DU powder in approximately 48 hours. The particle size of powder produced was on the order of 1 to 3 μm after mechanical milling. This system can be scaled up to produce a greater amount of powder.

5.1.2 Initial Failures and Contamination

The initial failures of the powder production experiment were indicative of contamination, most likely oxygen, in the process gas or hydriding environment. The contamination can cause a competing reaction with the hydrogen, in this case oxidation. This can inhibit or completely overtake the hydrogen reaction with the uranium. Even if hydriding and dehydring is successful in producing powder, oxygen contamination will also result in oxidation of the uranium powder. This was evident in the powder produced during

experiment 9 and the inability to dehydride to a pure DU powder. The leak that occurred during experiment 12 was obviously a major source of contamination, as well. This contamination led to the oxidation of the sample and all powder produced and also caused a "yellow" deposit to plate on the copper tubing in the reaction vessel. In an effort to rid the device of this deposit or at least limit its reactivity with any later experimental samples, the vessel was placed under an Ar-5%H_2 flow, heated to 500˚C for a short time and then the vessel was evacuated. The deposit appeared unchanged and showed no indication of reacting with the hydrogen flow. While the deposit was not effectively removed, it did not interact with process gas at operating temperature and therefore was not a concern of contamination during the subsequent experiments. The deposit remained on the reaction vessel hardware for the remainder of the powder production experiments with no visible impact on the sample or powder.

5.1.3 Powder Production Limitations

There were several factors which limited the production of UH_3 in the early development experiments. These factors include the ambient pressure of the hydrogen gas over the sample, temperature of sample, the percentage of hydrogen in the process gas, the surface area of the sample, and the previous mentioned oxygen contamination. In order maximize the effectiveness of the powder production the temperature and pressure parameters were adjusted throughout the experiments. The final settings had the pressure in the reaction vessel set to 2 psi, or 0.136 atm, over atmospheric pressure. This pressure was chosen due to its favorable hydrogen pressure, above atmosphere, for the UH_3 reaction. Due to the limitations of the powder production experimental set-up (glass overflow trap,

rubber stopper with weights, etc.), 2 psi was as high as the pressure of the reaction vessel could be safely raised without causing new complications.

The ideal temperature of the sample during hydration was found to be 235˚C, this is 10˚C above the consensus ideal hydration temperature. The temperature of the sample was increased because of the cooling effect the process gas had on the sample. Another factor which severely limited the rate and the quantity of DU powder producion was the composition of the process gas. The composition used throughout the experiments was Ar-5%H; this was chosen for safety reasons as H_2 is extremely flammable. The limited amount of H_2 in the reaction vessel, which limited the interaction between the hydrogen and DU sample. In an attempt to offset this limitation and increase the chances of a H_2 DU interaction, the process gas flowed directly over top of the sample at the relatively slow rate of approximately 2 SCFH. Another limitation of the powder production was the exposed surface area of the DU samples. This limitation was caused mainly by the size of the furnace well which directly led to the size of the reaction vessel. The samples were placed into a 10 mL cylindrical crucible. As the sample would hydride the bottom of the crucible would fill with powder, effectively limiting the ability of the process gas to reach the bottom portions of the sample until the original DU piece was surround of UH_3. This is evident by the non-hydrided portions of the samples being incased in the sintered DU powder post experiment.

5.1.4 Limitations on DU Powder Characterization

The powder production experiments successfully produced DU powder from experiment 13 onward; however the characterization of the powder was met with several limitations. From the physical observations the, process seemed to cause total or near total disassociation of the hydrogen from the DU. The powder was a dark gray in color, not black or dark brown. The powder sintered into loosely formed aggregates during the dehydriding phase of the process, and the resulting powder was very fine 1-3 microns. Due to the pyrophoric and radioactive nature of the material, characterization of the powder beyond physical observation proved to be difficult. A small sample of the power, < 0.1 mg, was placed in a Petri dish, removed from the glovebox and examined with KH-1300. The powder oxidized upon contact with air such that some of parts of the plastic Petri dish melted from the heat. Still the examination was successful in characterizing the size of the DU powder, albeit that the powder anylyzed was heavily oxidized.

It would be valuable to have the element composition characterized. This information would help determine if there are any contaminates in the powder, such as oxygen, or if the powder had fully dehydrided. Oxygen is a strong hindrance to the sintering of metal powders. UH_3 could also have notable effects on the sintering of DU pellets. Unfortunately no facility could be found on campus that was willing to characterize the powder due to the nature of DU. Characterization was performed on the sintered pellets using the EDS ability of the JOEL-6400; no significant contaminants were found in the pellets.

5.2 Alpha Phase Sintering Experiments

5.2.1 Proof of Concept of Alpha Phase Sintering and the System Design

SEM analysis showed various degrees of sintering in all the pellets examined. The pellets all showed visible signs of sintering via necking between particles grain growth, and pore morphology. The amount of sintering was not consistent throughout the pellets. There were areas with very low porosity and areas where no sintering appeared to occur (the initial powder particles were clearly visible). Despite these inconsistencies in porosity/sintering, the alpha phase sintering experiments were considered to successfully demonstrate that alpha phase sintering was achieved and that a reliable means of quantifying the sintering process has been established.. These experiments show that densification of powdered pressed DU/DU-Zr pellets will happen at temperatures below 660 ˚C. The lowest porosity samples contained Mg which caused liquid enhanced sintering to occur in the pellets; a similar phenomenon will occur if Pu metal is incorporated into this type of fuel form.. Using these experiments as a basis, a test matrix can be developed to calculate the activation energy of alpha sintering and the sintering rate for various pellet compositions.

5.2.2 SEM Image Analysis

The SEM image analysis performed provided the most robust evidence of sintering in the pellets. There are visible signs of sintering in all of the images. The pellets also are all consistently more porous near the radial edge. The reason for this is not clear, but uneven expansion/contraction during cool down maybe a contributing factor. Conglomeration of the powder is believed to be another contributing factor to the inconsistencies in porosity. This conglomeration is characteristic of a non-uniform powder particle size. The non-uniform powder particle size was most likely caused by insufficient milling of the powder.

As noted in Table 4.1, Pellet 2 was 100% DU sintered at 650°C, and it was found to have a porosity of 18 ± 3% using the pixel counting method in the Image J software.

Evidence of sintering can be seen in Fig. 5-1. Most of the original particles (1-3 μm) have sintered into large grains and are completely indistinguishable. In the areas of lower sintering there are visible signs of necking between separate powder particles. There are also areas of the pellet where very little sintering has taken place and the individual particles are intact. The various degrees of sintering can be attributed to variation in density in the green pressed pellet and conglomeration of particles, Section 5.2.3 contains a more detailed analysis of this phenomenon.

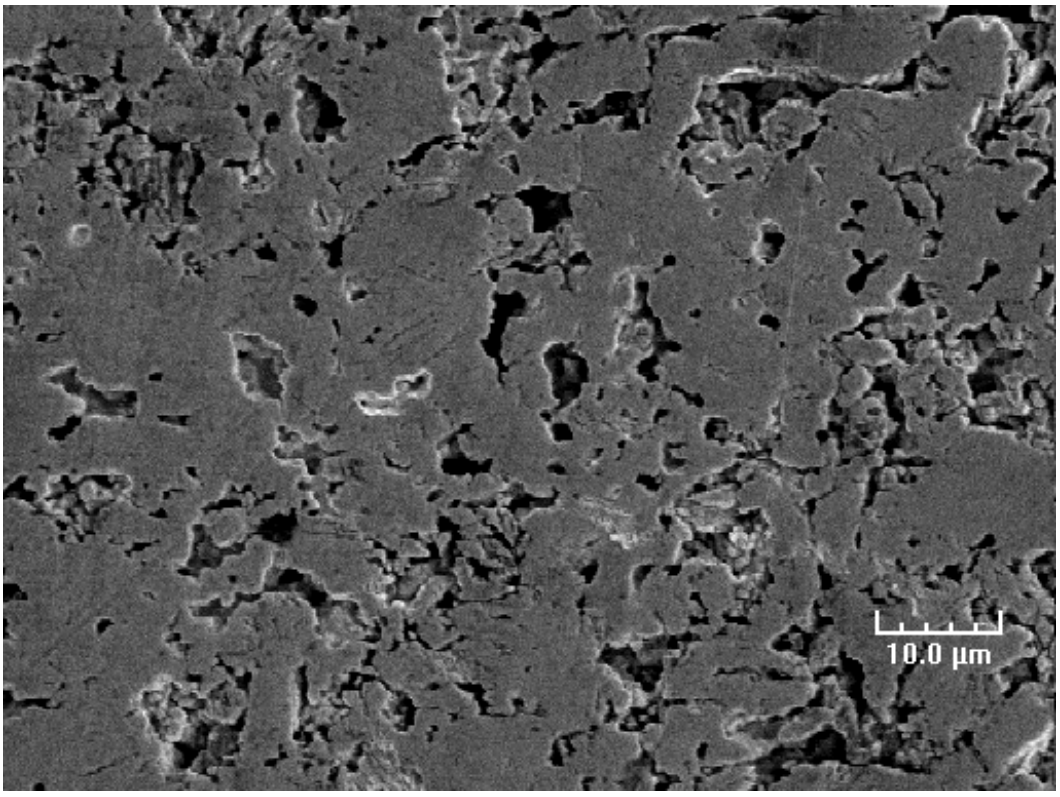

Fig. 5-1 1500X SEM image of pellet 2

Pellet 3, was 100% DU sintered at 650°C had a porosity 26 ± 2%. This porosity is significantly greater than the porosity of pellet 2. The difference in porosity is contributed to the amount of cracking in pellet 3, Fig. 5-2. The cracking was evident throughout the entirety of the pellet. The cracking is believed to be cause by the agglomeration of the particles and the non-uniform density of the pressed pellets (Section 5.2.3). There are large areas where individual particles are indistinguishable; however these areas are broken apart by large cracks and fissures. These fissures do not have the same appearance as the pores formed in other pellets. The cracks formed on different atomic planes as if a solid piece of DU was "shattered". This is indicative of the majority of the cracks forming after the pellet sintered, most likely during cool down.

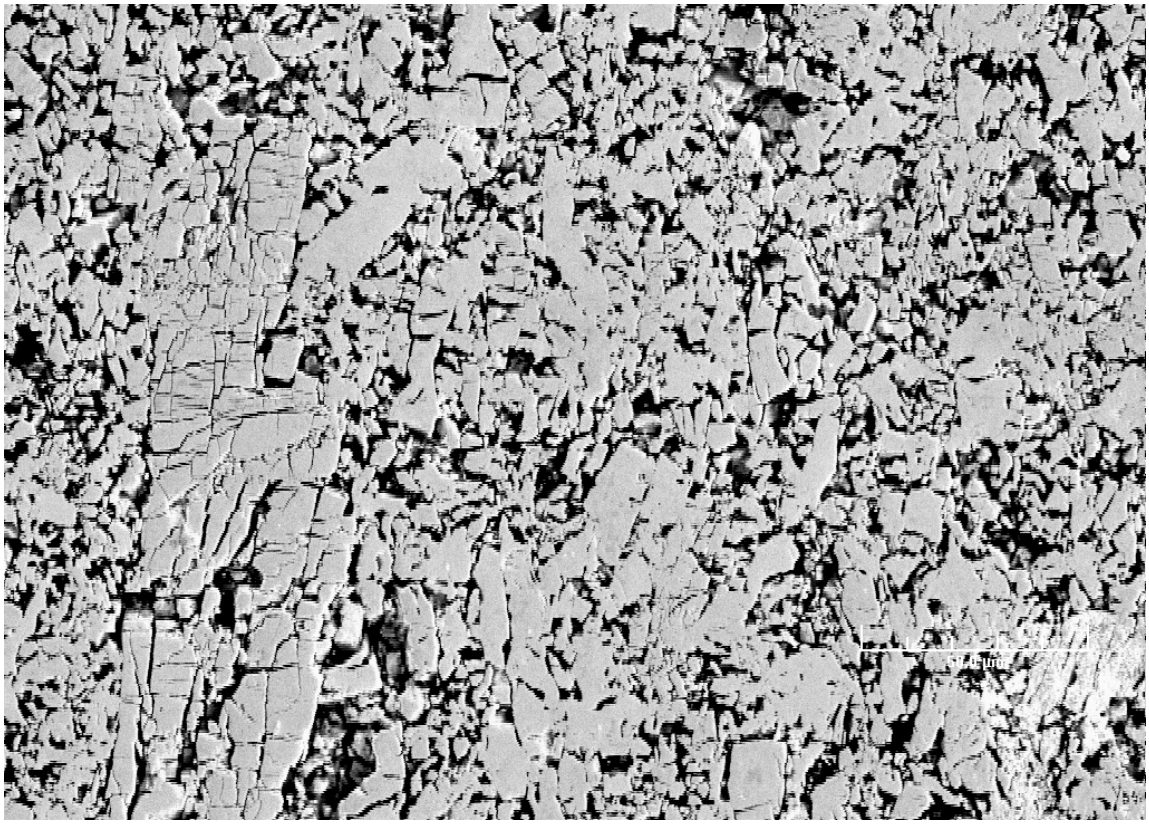

Fig. 5-2 500X SEM image of pellet 3

Pellet 5, DU-10Zr sintered at 650 and 700˚C (Table 4-1), showed visible signs of sintering. Pellet 5 had a similar porosity to that of the 100% DU Pellets 2 and 3. Once again most of the individual powder particles are no longer distinguishable. The particles have sintered and formed large grains.

There were two clear separate phases observed in Pellet 5, as seen in SEM and BSE images Figs. 5-3 and 5-4. The two phases were clearly defined in the BSE images: the light gray areas consist of DU while the dark grays consist of Zr. The Zr and DU stayed separated in the pellet and did not alloy; there was no apparent δ or γ phase. This was

confirmed through EDS of the image, Figs. 5-6 and 5-7. Six different points were chosen for EDS analysis; three points in the DU rich areas and three points in the Zr rich areas.

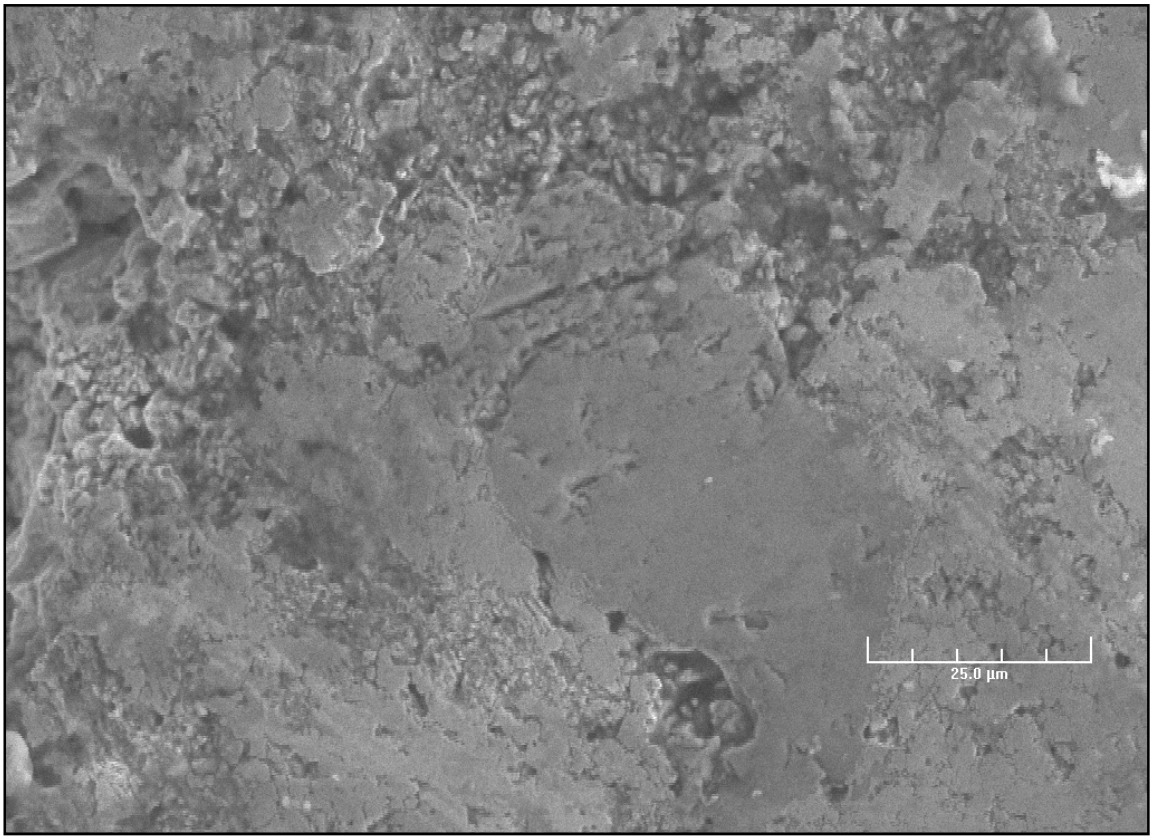

Fig. 5-3 1000X SEM image of pellet 5 (same area as Figure 5-4 and 5-5)

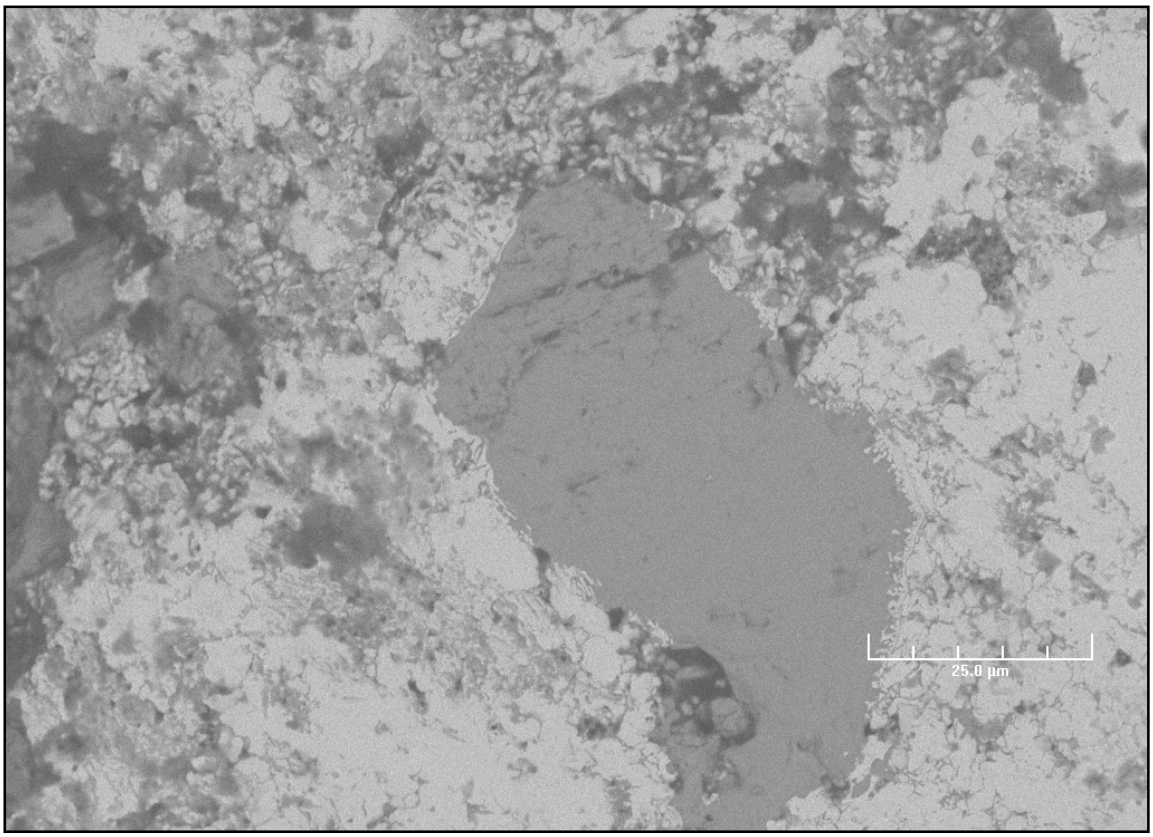

Fig. 5-4 1000X BSE image of pellet 5 (same area as Figure 5-3 and 5-5)

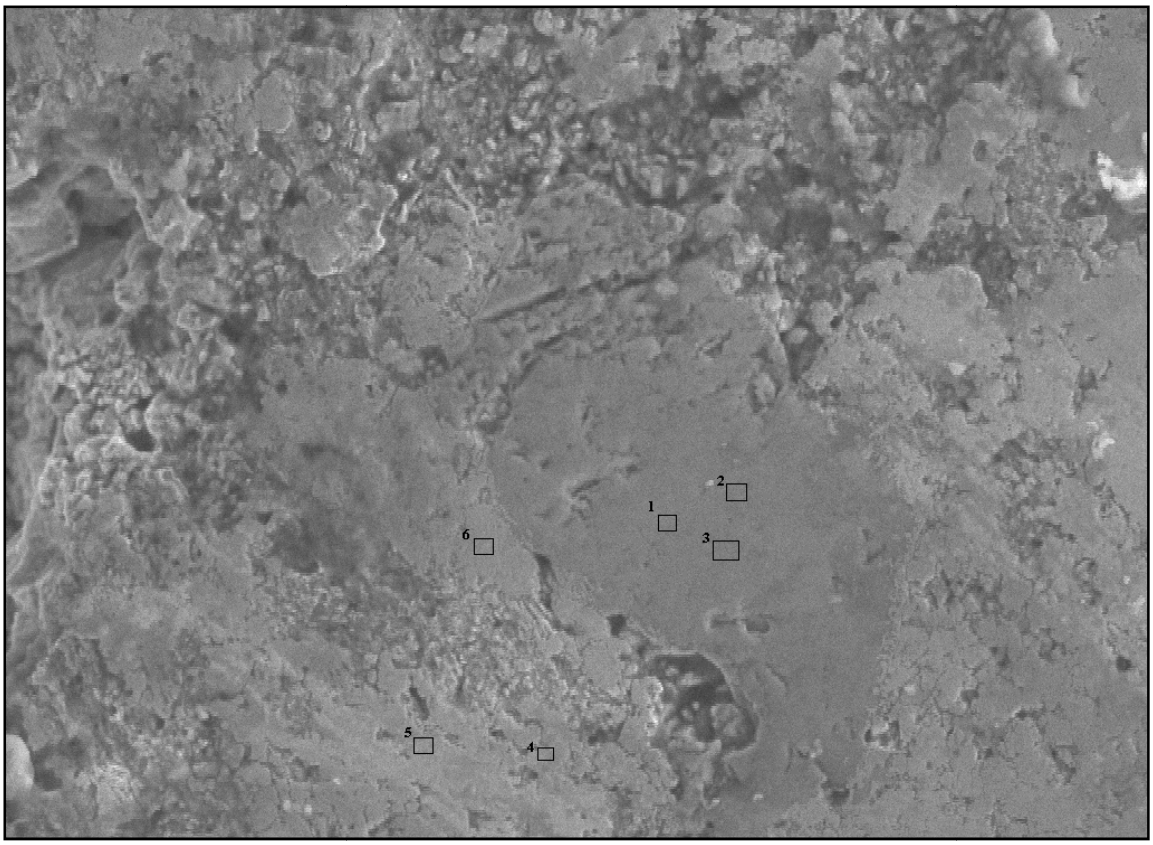

Fig. 5-5 1000X SEM image EDS map location map of pellet 5 (same area as Figure 5-3 and 5-4)

On the SEM image EDS map, Fig. 5-5, location 1 (Fig. 5-6), 2 and 3 consisted of 95.79%, 100%, and 100% Zr respectively with the remaining percentages being DU. Location 4 (Fig. 5-7), 5, and 6 consisted of 97.29%, 100%, and 99.54% DU respectively with the remaining percentages being Zr. These percentages show that a negligible amount of intermixing between the DU and Zr occurred during the sintering experiment. The separation of the U and Zr was not unexpected as most of the alloying between the two metals occurs above 865°C when both metals are in a BCC configuration.

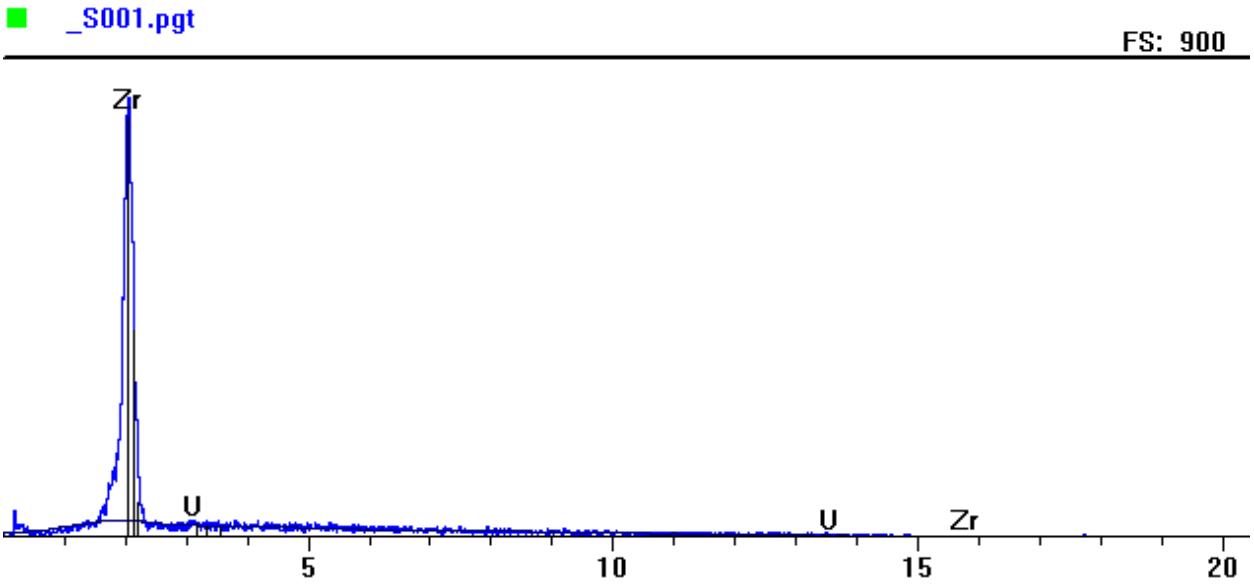

Element	Wt%	ChiSquared	Z Corr	A Corr	F Corr
Zr	95.79	7.54	0.989	1.016	1.000
U	4.21	0.50	1.307	1.264	1.000
Total	**100.00**	**0.58**			

Fig. 5-6 EDS spectrum of location 1

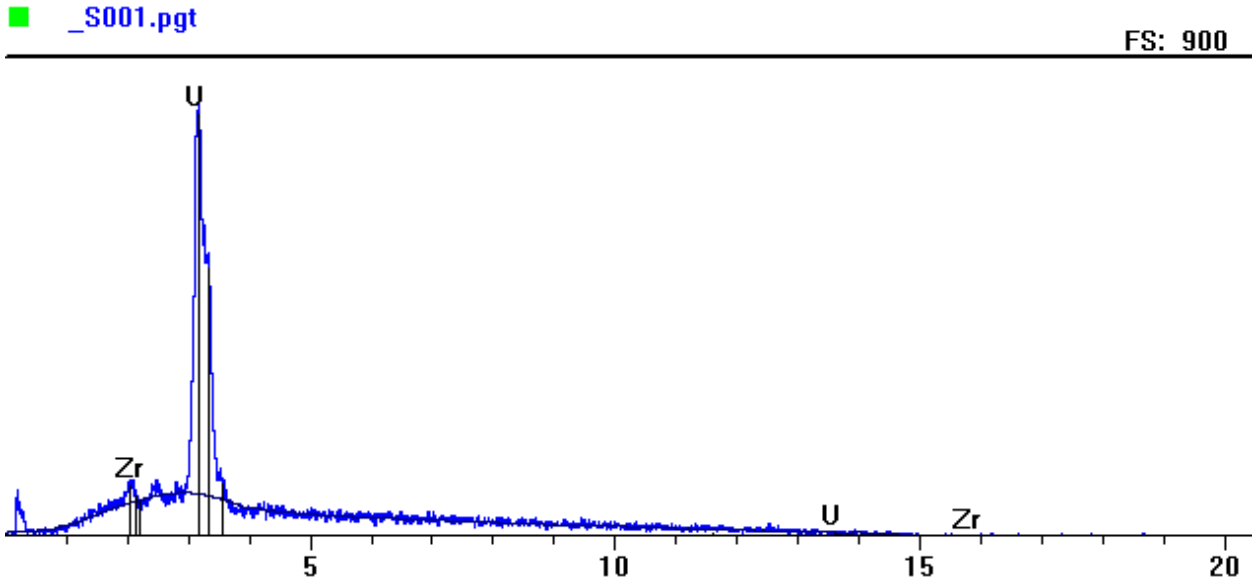

Element	Wt%	ChiSquared	Z Corr	A Corr	F Corr
Zr	2.71	0.29	0.758	1.361	1.000
U	97.29	3.12	1.009	1.007	1.000
Total	**100.00**	**0.95**			

Fig. 5-7 EDS spectrum of location 4

On lower magnification the Zr rich areas appeared to generally have less porosity than the pure DU phase of the pellet; however this is an artifact of the SEM. As the magnification was increased pores could be observed in the Zr rich areas. These pores were of a lighter color than the pores in the DU rich areas, making them more difficult to observe and account for on lower magnification settings, Fig. 5-8.

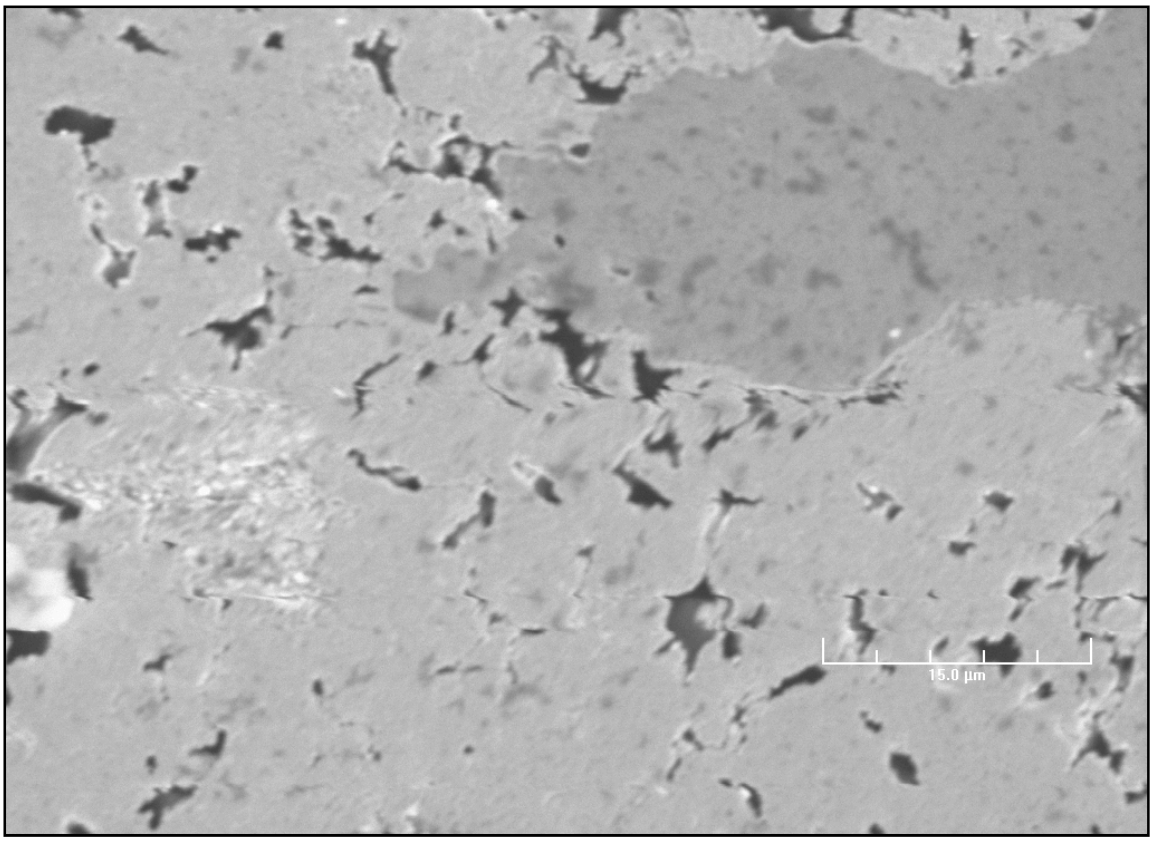

Fig. 5-8 2000X SEM image of pellet 5, the pores in the Zr rich areas are somewhat obscured

Pellet 6, DU-1Mg (wt %) sintered at 655˚C, had a porosity of 14 ± 2%. This porosity was lower than 100% DU Pellets 2 and 3 (Fig 5-9). Enhanced liquid phase sinter, due to the presence of Mg, led to the lower porosity. The images were characterized by areas with large amounts of sintering and low porosity, Fig. 5-10, and irregular shaped large pores scattered throughout the pellet, Fig. 5-11, (lengths could be greater than 25 microns).

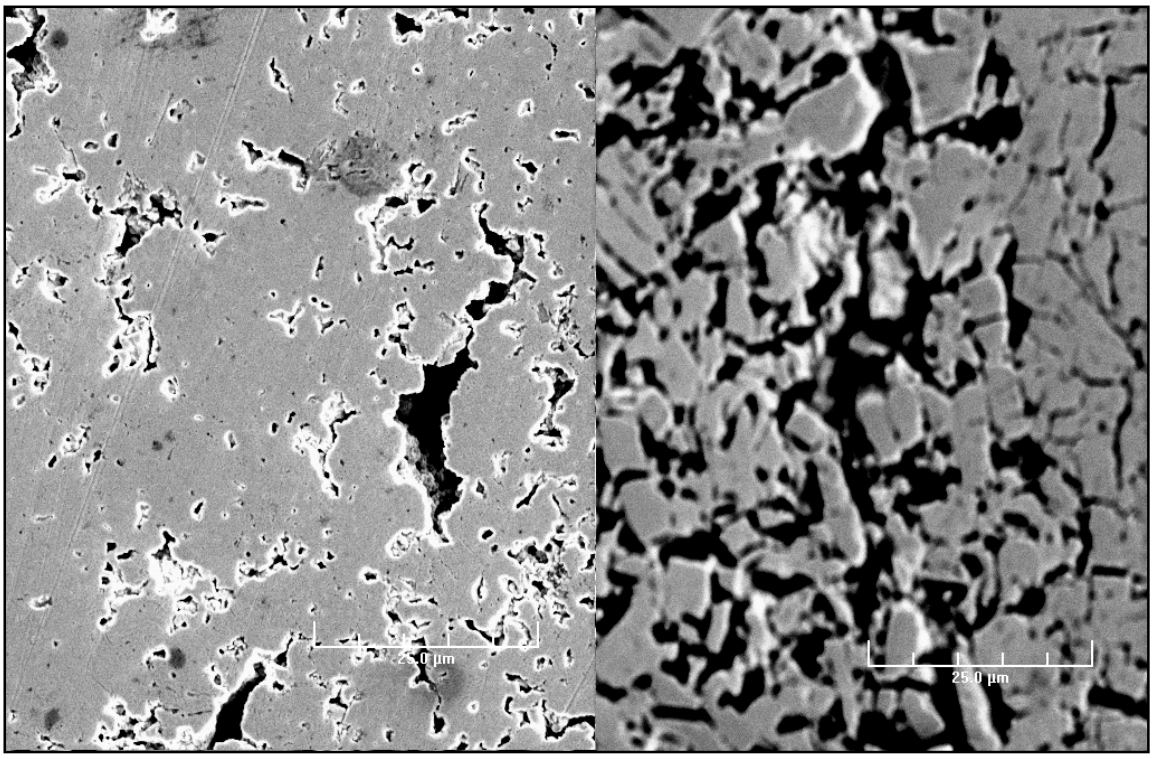

Fig. 5-9 Left 1000X SEM image Pellet 6, Right 1000X SEM image Pellet 3: Pellet 6 shows a greater amount of sintering than Pellet 3

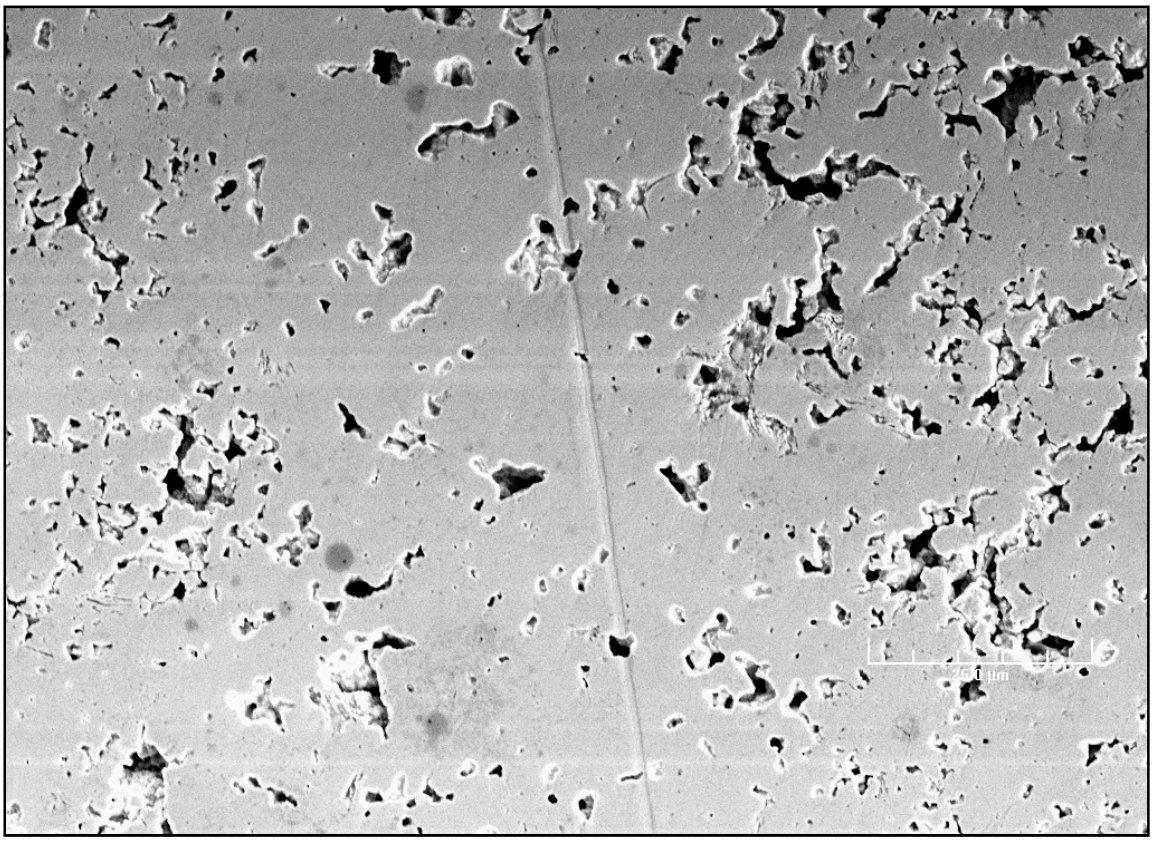

Fig. 5-10 1000X SEM image of pellet 6

Figure 5-10 shows a significant increase in sintering compared to the previous pellets. There are no grain boundaries visible and the original powder particles are not distinguishable. The increase in sintering was caused by the capillary action of the liquid Mg. There are several spherical shaped pores throughout the image along with some irregular shaped pores. There are also regions where no pores or cracking were present.

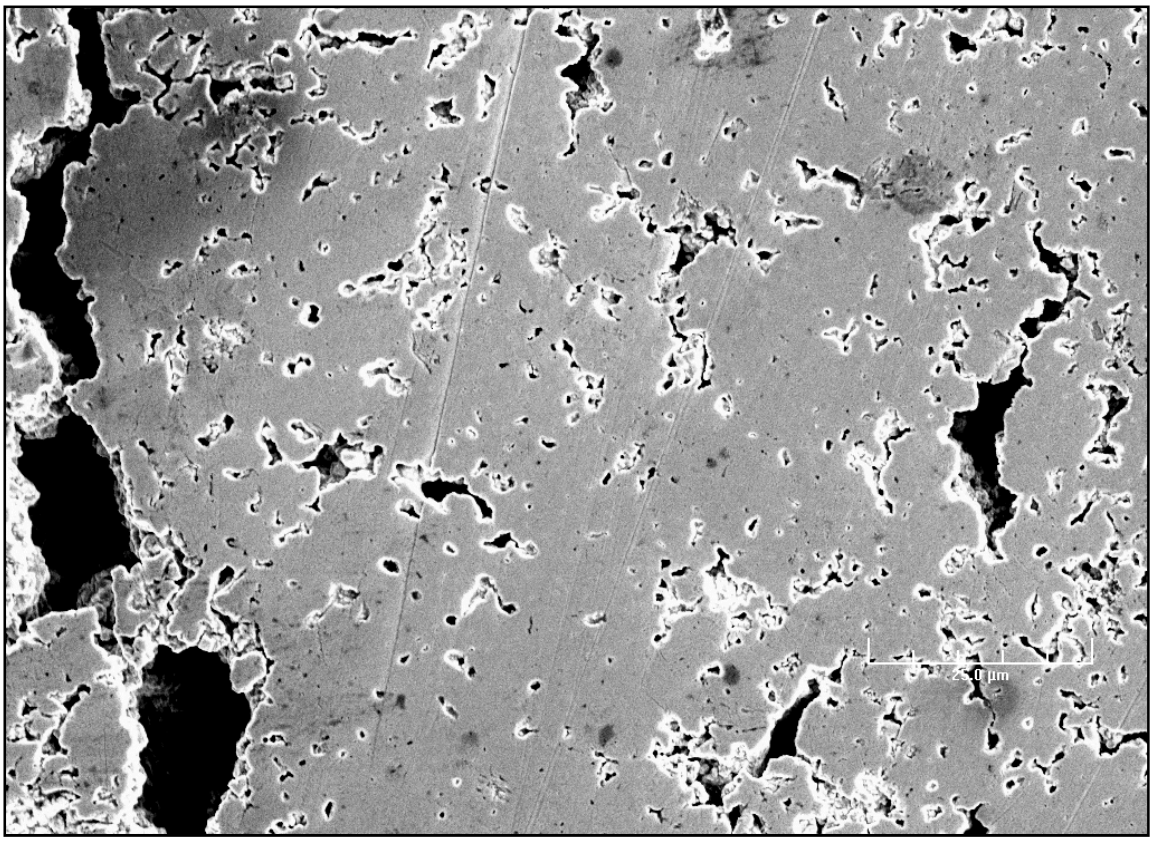

Fig. 5-11 1000X SEM image of pellet 6

Figure 5-11 contains areas of great sintering, small spherical pores, and irregular shaped pores similar in Fig. 5-10. Figure 5-11 also contains very large (greater than 25 µm) irregular pores. These large pores were consistent throughout Pellet 6 (DU-1Mg). This type of pore at this frequency was unique to Pellet 6 and not seen in the other pellets. The reason for the presence of this phenomenon in Pellet 6 is not clearly understood.

The SEM images of Pellet 10, DU-10Zr-2.4Mg sintered at 655 ˚C, show clear signs of sintering (Fig. 5-12). While there were no porosity measurements performed on Pellet 10, the porosity of the pellet was fairly low by observation. There were some small spherical

pores and some larger irregular pores. This porosity is analogous to Pellet 6, DU-1Mg, however the irregular pores in Pellet 10 were smaller and less frequent.

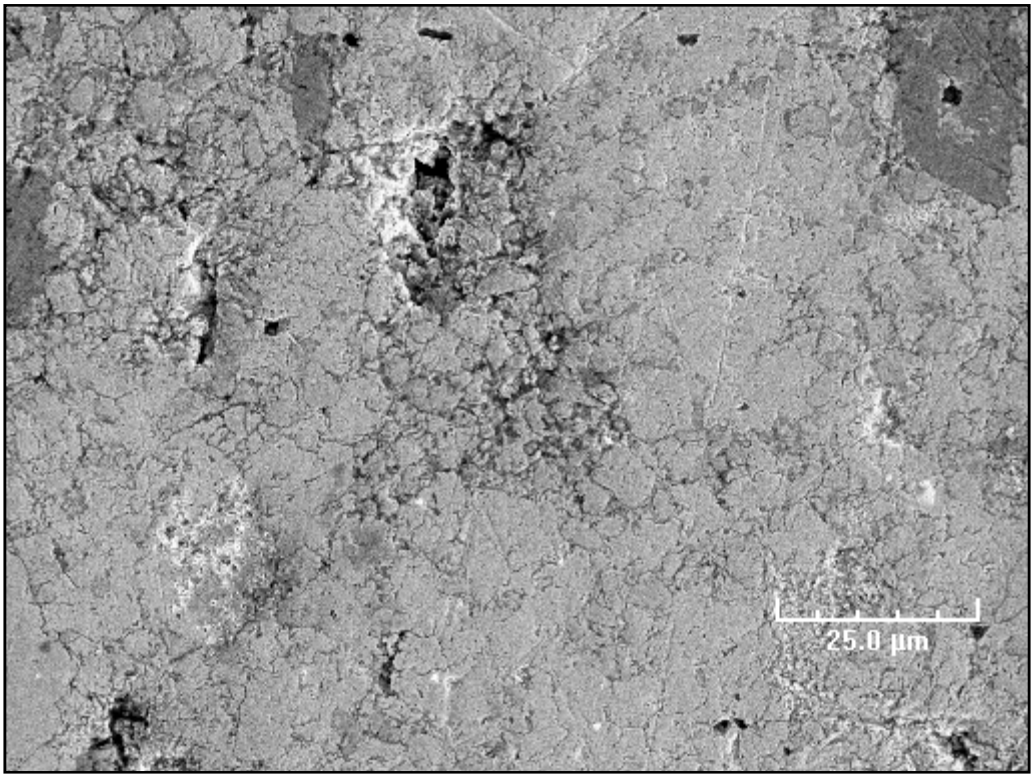

Fig. 5-12 1000X SEM image of pellet 10 (same area as figure 5-13)

There two distinct phases in the pellet. These phases can be seen in Fig. 5-13, a BSE image of the pellet, the light gray areas DU while the dark grays areas are Zr. In Pellet 10 a portion of the Zr phase gathered along the grain boundaries of the DU grains. This can be seen in Fig. 5-13 and 5-14; the dark lines between the DU grains are the Zr rich areas. The envelopment of the DU grains is attributed to the inclusion of Mg. Mg and Zr are completely soluble in each other at the sintering temperature. This solubility characteristic

combined with liquid enhanced sintering effect of the Mg caused the Zr to surround the DU grains.

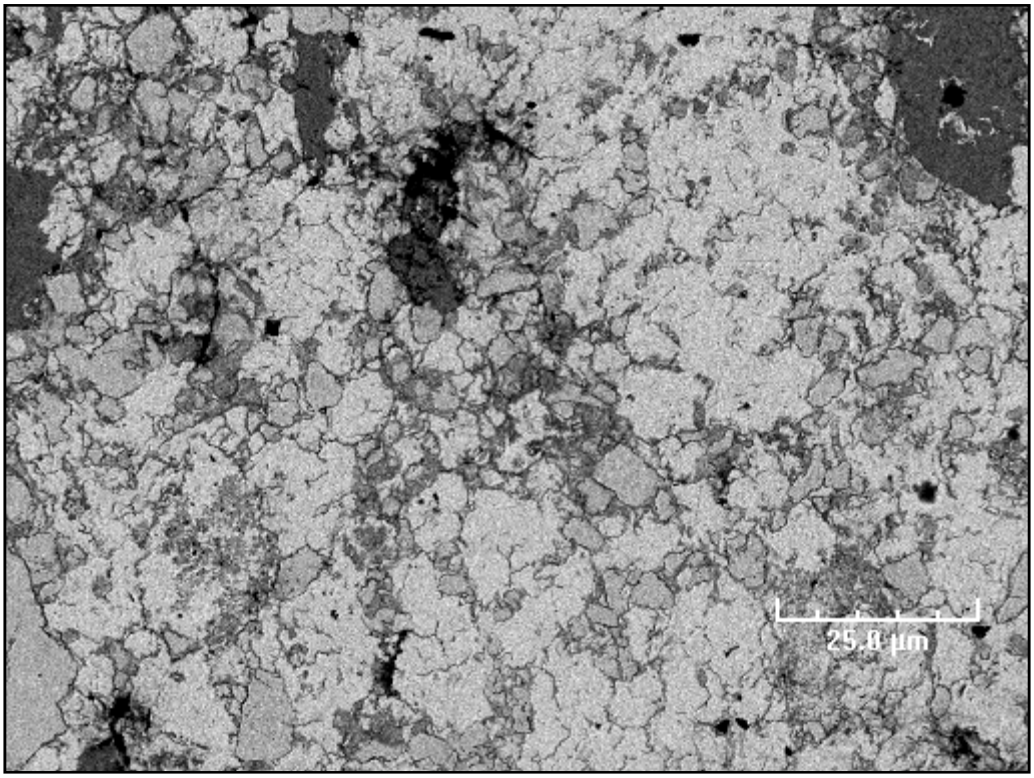

Fig. 5-13 1000X BSE of pellet 10 (same area as figure 5-12)

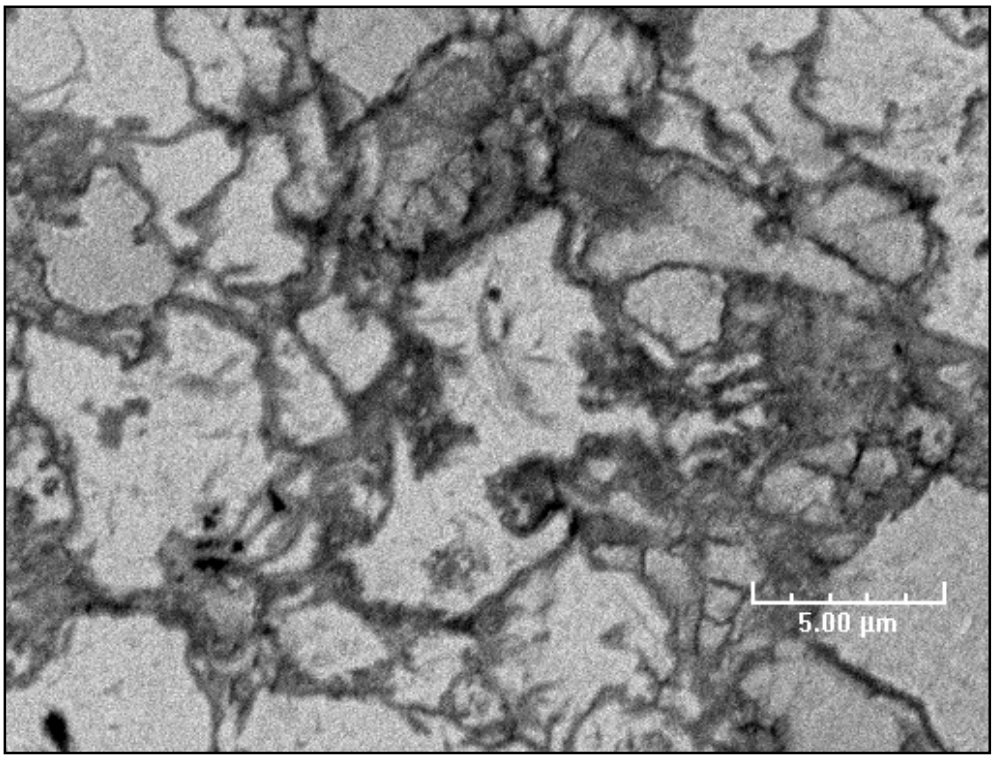

Fig. 5-14 5000X BSE image pellet 10 (close up of figure 5-15)

EDS analysis was performed on pellet 10, Figs. 5-15 through 5-17. The EDS analysis showed that the DU and Zr remained segregated. The EDS confirmed that the dark material along the grain boundaries of the DU was Zr. An EDS map is shown in Fig, 5-16. Locations 1 and 3 were in the Zr rich areas and contained 100% Zr. Figure 5-17 is a magnification of location 2 on the map. Location two consists of both the large DU grains and the surrounding Zr. This location contained 93.24 % DU, 6.76% Zr, and 0% Mg. The difficulty in detecting any significant amount of Mg in the EDS analysis can be attributed to the relative low weight percent of Mg in the pellet. There was no indication of Mg loss during the post experiment examination of the reaction vessel.

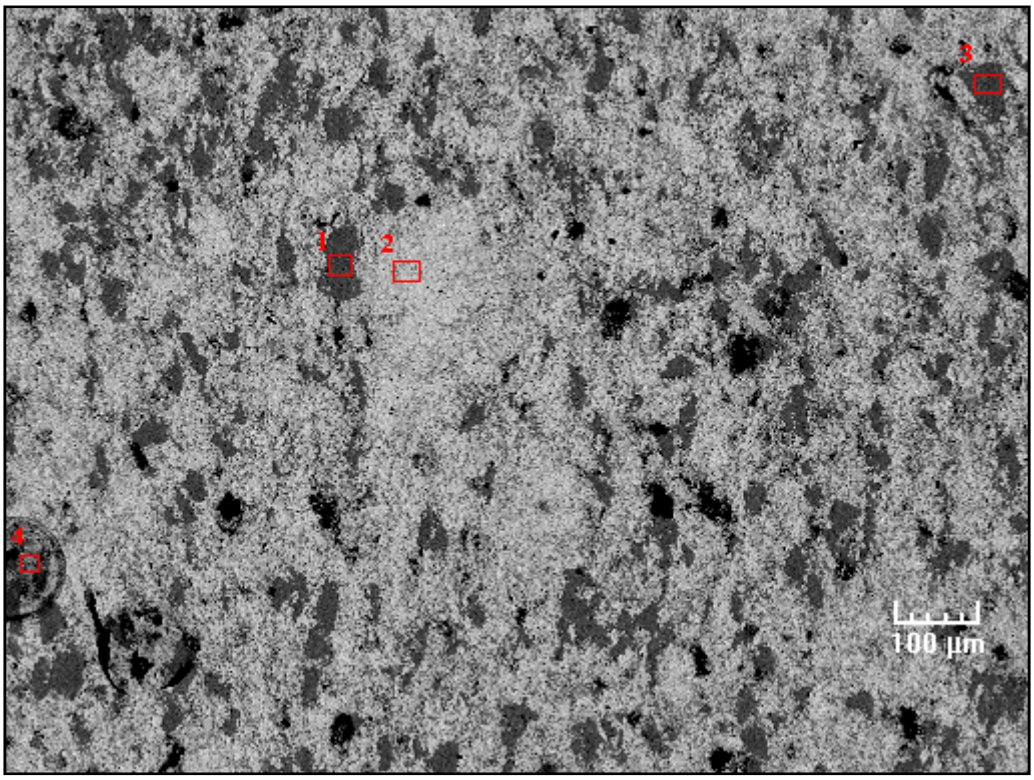

Fig. 5-15 100X BSE image EDS map

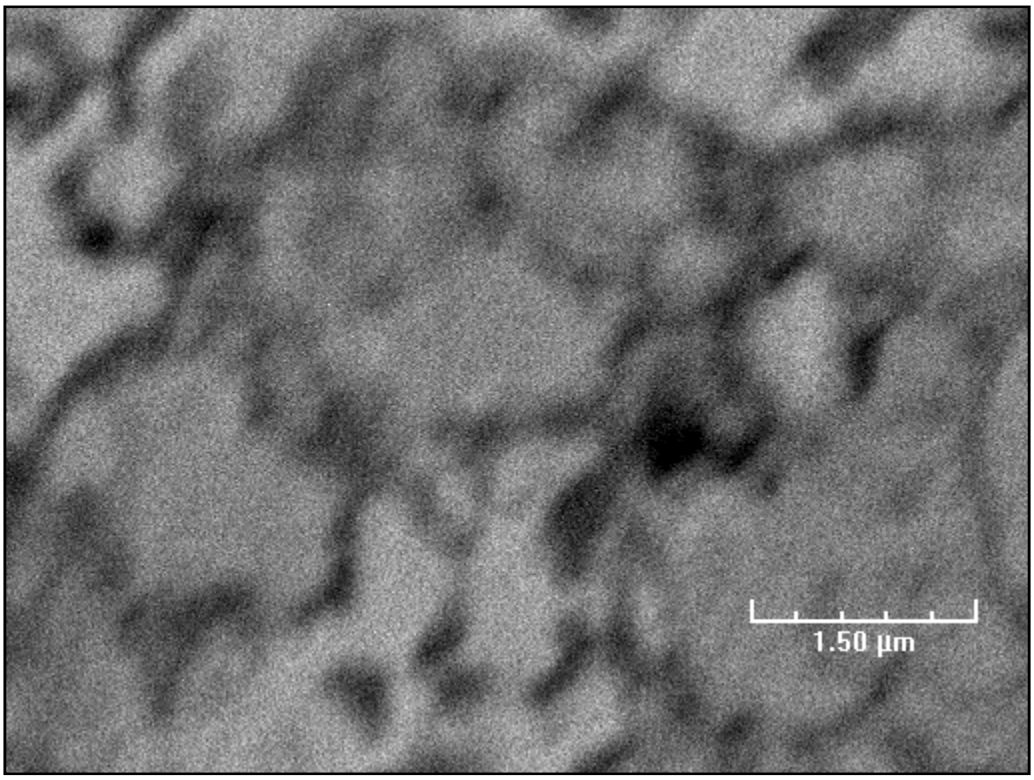

Fig. 5-16 BSE 18,000X of pellet 10 location 2

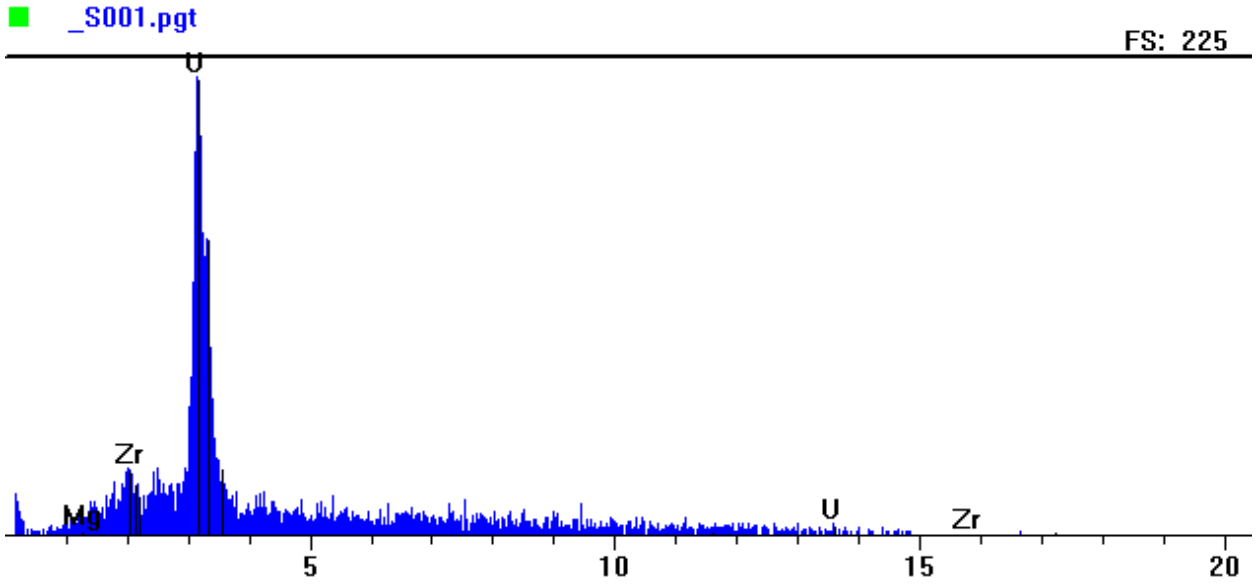

Element	Wt%	ChiSquared	Z Corr	A Corr	F Corr
U	93.24	0.67	1.022	1.018	1.000
Zr	6.76	0.90	0.769	1.347	1.000
Mg	0.00		0.578	2.502	1.000
Total	**100.00**	**0.21**			

Fig. 5-17 EDS of location 2 from Figure 5-16

5.2.3 Post Experiment Dimensional Measurements

There is a significant difference between the measured thickness of the pellet *in situ* via the LVDT and the post experiment measurements of the pellets. The LVDT data indicated a continuous shrinkage of the pellet during the sintering, while the post experiment measurements indicate an increase in the thickness of the pellet in all experiments expect experiment number 10, where there was a 0.0002 in decrease in thickness. Experiment 6 showed a slight increase in height of 0.6% and a decrease in the diameter of the pellet. While there are questions regarding the accuracy of the LVDT measurements (addressed

5.2.4), there is little doubt that the relative trends in the measurements taken by the LVDT are accurate (i.e. the pellet is shrinking along the vertical axis). The majority of the post experiment pellets, while conical shaped (addressed later in the section), do show an increase in the diameter.

The reason for the increase in thickness and diameter has not been conclusively determined, but it is believed that the cracking of the pellet during the cool down phase causes this phenomena, Fig. 5-18 and 5-19. The cracks appear mainly to be radial. The cracks were first noticed during the preparation of the pellets for SEM analysis. The cracks were initially contributed to the expansion of the pellet caused by the heat of cutting. It is appears that while the cutting of the sample exacerbated these cracks it did not cause them. The cracks appear to have formed during the cool down phase of the pellets. The effect of the cracks on the thickness of the pellets is masked during the LVDT measurements by the cool down and thermal contraction of the steel rod. It appears that the cracks could be caused by unevenly cooling of the samples or cooling the samples too quickly; the rate of cooling was approximately 5 ˚C a minute.

Agglomeration of the DU powder is another suspected cause of the cracking. Agglomeration will cause areas of varying densities throughout the pellet. These varying densities will cause differences in the rate and amount of sintering throughout the pellet. These differences can lead to the cracking of the pellet do to the internal stresses cause by this phenomenon. Another contributing factor to the cracking of the pellet could be the incomplete dehydriding of the DU powder. During the experiment, hydrogen could disassociate from any residual UH_3. The H_2 could then collect and eventually breach the pellet and be released, thus weakening the overall structure of the pellet and causing cracks.

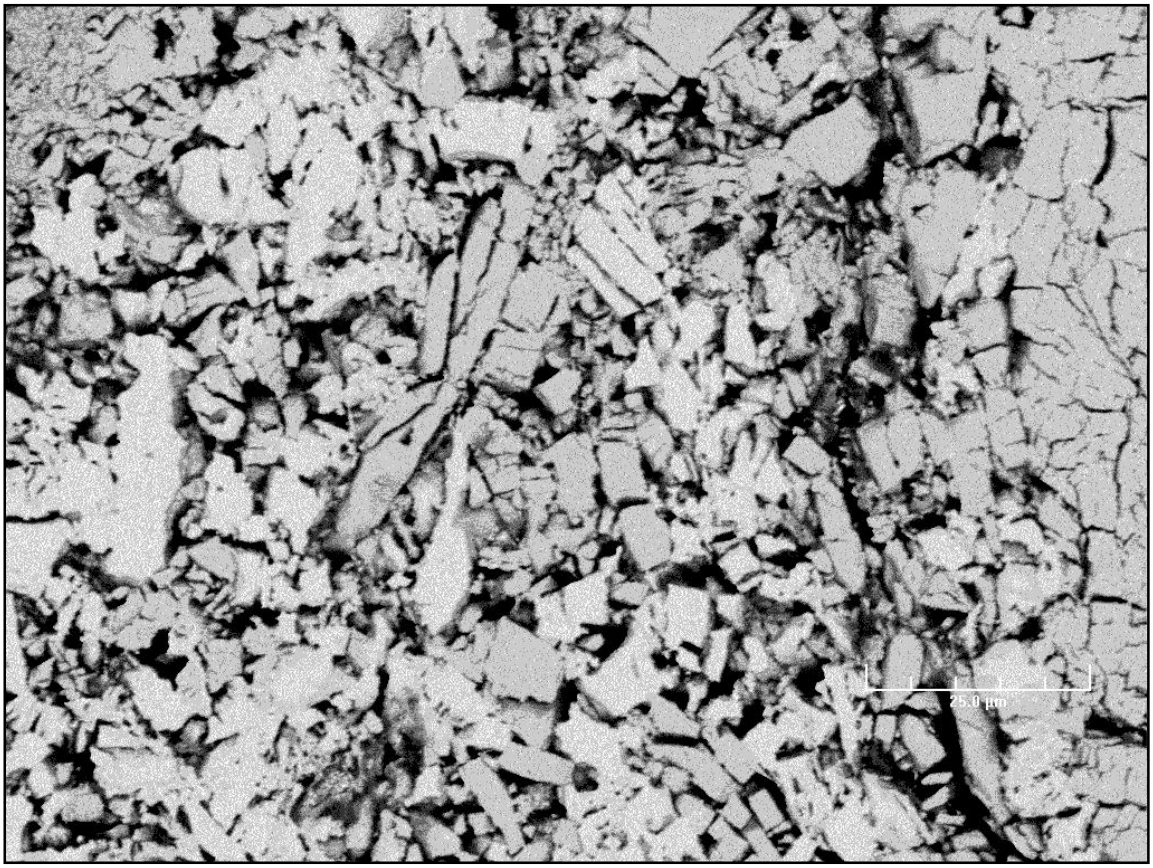

Fig. 5-18 Pellet 3 BSE 1000X visible cracks in structure

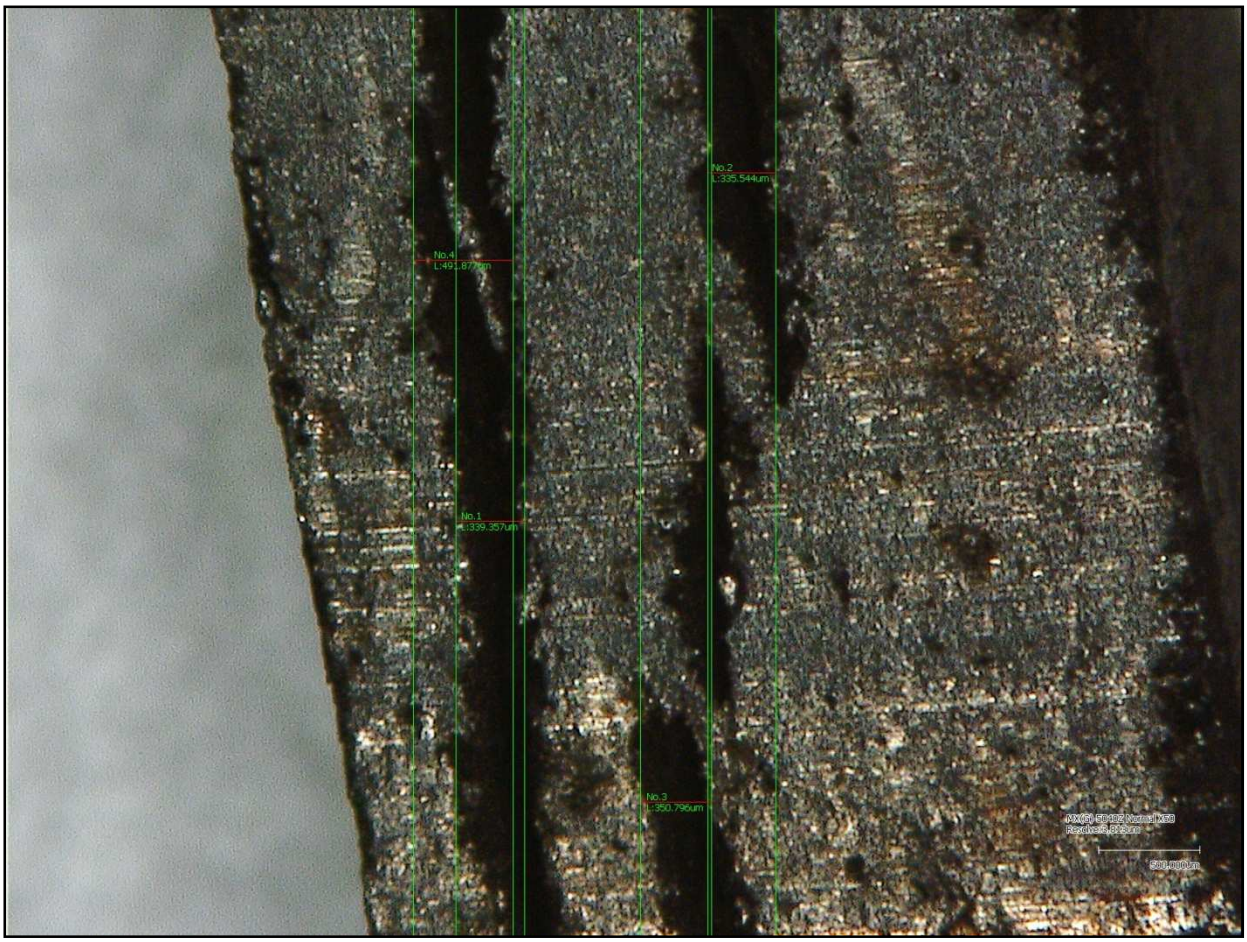

Figure 5-19 KH-1300 Image of Pellet 3

The pellets all have a slight conical post experiment shape (expect Pellet 10), with one end having a larger radius than the other. The change in shape attributed to the manner in which the pellets were pressed. When the pellets were pressed in the punch, there is a greater compaction of the powder in the lower region of the die. This leads to a higher density and lower porosity in the lower region of the pellet. With a lower porosity and higher density, there exists physical room for the pellet to compress during sintering in this region. This leads to the bottom end of the pressed pellet having a large diameter than the

top. This combined with the cracking of the pellet can give the pellet a measured increase in the post experiment diameter. Conversely, the greater porosity in the upper (pressed) region of the pellet could be a factor in the breakdown of Pellet 9. In this case the lower density portion of the pellet was placed faced down in the crucible. During the experiment the lower density region crumbled under the expansion of the pellet and weight of the LVDT measurement rod. This could also be a contributing factor to break down of the structure in Pellet 10.

5.2.4 LVDT Measurement Analysis

The LVDT provided a real time monitor of the change in pellet thickness. If one assumes the pellet shrank and swelled uniformly this can be translated into the total volume change during sintering. The LVDT was extremely sensitive to vibration or jarring of the reaction vessel during measurements. Any such action could cause a dramatic swing in voltage and skew any data taken after such a swing. Also during any ramp up or ramp down cycle the thickness change in the pellet would be loss in the expansion/contraction of the steel rod and cycling of the furnace. The data taken during a hold temperature is believed to be an accurate measurement of the thickness change of the pellet (with the possible exception of Pellet 5).

During the Pellet 4 and 8 experiment the furnace was raised to a temperature of approximately 700 ˚C, well into the temperature required for the beta phase of uranium. At this temperature the theoretical density of the uranium is 18.03 g/cm^3. and there should be a significant slowdown in the rate of sintering. The sintering rate of the pellet appeared unchanged during the hold time at the increased temperature, although most of the data at 700 ˚C is lost in the noise from the ramp up and ramp down. This would indicate that while

the thermocouple inside the crucible was at 700 ˚C the pellet did reach temperatures over 662 ˚C, the alpha beta phase transition line. During experiment 8 the furnace was raised to approximately 800˚C. At this temperature the pellet should be in the gamma phase which has a theoretical density of 18.11 g/cm^3. Also sintering of the pellet should continue in the gamma phase. However the LVDT data shows an insignificant increase in the volume of the pellet and flatting out of the shrinkage rate of the pellet. The increase could be caused by the thermal expansion of the pellet and the increased temperature or possible cracking of the pellet. The flatting of the shrinkage rate suggest that the pellet did not reach the temperature necessary to transition into the gamma phase but instead reached beta phase temperatures.

The LVDT data for pellet 4 exhibited some unexplained phenomena. After a temperature of 650 ˚C was reached there were two dramatic drops in the LVDT output voltage, Fig. 4-27. This phenomenon is believed to be caused by an error in the LVDT measurement system and not related to a change in the thickness of Pellet 4. For this reason the initial drops are not included in the $\Delta L/L$ calculation for Pellet 4.

The LVDT data for pellet 5 exhibited several rather peculiar phenomena that were not characteristic of the rest of the data obtained, Fig.4-29. There were several rapid changes in the measured pellet thickness both positive and negative. There also was a rapid increase in pellet thickness followed by a gradual decrease while the pellets temperature remained constant (650 ˚C). Also the data did not contain the immediate rapid decline followed by gradual increase in thickness during the ramp down that is characteristic of the other data collected, Fig 4-27. Instead LVDT recorded a constant thickness during the cool down period followed by a rapid decline with no gradual increase. For these reasons the

LVDT data collected for Pellet 5 is suspect however the slower rate of sintering recorded does corresponded with expected results of introducing Zr to the composition of the pellet.

6. SUMMARY AND RECOMMENDATIONS

A successful reusable system for powder production system was built. A methodology for producing fine DU powder from large chunks using the hydride/dehydride process was developed. The resulting powder from the system was pressed into a pellets of various compositions (DU, DU-10Zr, DU-Mg, DU-10Zr-Mg). These pellets were all heated to 650˚C. Some pellets were heated to 700˚C and 800˚C. The research above has laid the ground work for further experimentation and analysis of use of alpha sintering as a fuel fabrication technique.

The principle outcomes and observations from this work can be summarized as follows:

1. A successful reusable system, describe in section 3.1, was built to transform DU chunks in fine DU powder This system was used as the source of DU powder for the uranium alloy alpha phase sintering experiments.
2. The powder produced after mechanical milling was on the order of 1-3 microns in size.
3. Evidence of alpha phase sintering was observed in all of the pellets. The compositions of these pellets were: DU, DU-10Zr, DU-Mg, DU-10Zr-Mg.
4. Post experimental dimensional measurements of the pellets were found to be unreliable due to cracking during cool down.
5. The LVDT measurements were found to be extremely sensitive to outside vibrations. For this reason some the data collected was not considered to be accurate, Pellets 4 and 5.

6. The pellets of DU-10Zr showed no evidence of alloying between the Zr and DU.
7. The DU-10Zr-Mg contained large grains of DU with Zr collecting around the boundaries, Section 5.2.2.
8. The pellets had a slight conical shape post experiment. This was attributed to powder pressing procedures. During the powder pressing the density of the pressed pellet is greater on one end than the other. This leads to a gradient in the sinter rate and porosity of the green pellet and thus the conical shape post experiment.

The following observations and recommendations are presented to assist in further research in this area.

1. The rate at which the DU powder is hydrided can be increased by some or all of the following: a change to 100% H_2 process gas; an increase in the sample surface area exposed during the hydration; an increase in pressure of the process gas over the sample.
2. Oxidation of the DU powder is of the utmost concern. In order to help prevent oxidation the DU powder, the powder should be kept in an oxygen free environment and produced as needed.

REFERENCES

[1] D. E. Burkes, R.S. Fielding, and D.L. Porter, Metallic Fast Reactor Fuel Fabrication for the Global Nuclear Energy Partnership, Journal of Nuclear Materials 392 (2009), 158-163.

[2] C.E. Stevenson, The EBR-II Fuel Cycle Story, La Grange Park, Illinois: American Nuclear Society Inc. (1987).

[3] C.L. Trybus, J.E. Sanecki, S.P. Henslee, Casting of Metallic Fuel Containing Minor Actinide Additions, Journal of Nuclear Materials 204 (1993) 50-55.

[4] M.B. Waldron, B.L. Daniell, Sintering, Heyden & Son Ltd, London (1978).

[5] G.S. Udpahaya, Sintered Metallic, Ceramic Materials: Preparation, Properties and Applications, John-Wiley & Sons, Inc., Chichester (2000).

[6] R.M. German, Sintering Theory and Practice, John-Wiley & Sons, Inc., New York, (1996).

[7] J.J. Carroll, A.J. Melmed, Field Ion Microscopy of Alpha Uranium, Surface Science 116 (1982) 225-239.

[8] L. Grainger, Uranium and Thorium, George Newnes Limited, London (1958).

[9] S.F. Pugh, Swelling in Alpha Uranium due to Irradiation, Journal of Nuclear Materials 4 (2) (1961) 177-199.

[10] J.J. Burke, D.A. Colling, A.E. Gorum, J. Greenspan, Physical Metallurgy of Uranium Alloys, Brook Hill Publishing Company, Columbus (1976).

[11] W.D. Wilkinson, Uranium Metallurgy, John Wiley & Sons, Inc., New York (1962).

[12] S.M. McDeavitt (1992), Hot Isostatic Pressing of U-10Zr Alloy Nuclear Fuel by Coupled Grain boundary Diffusion and Power-Law Creep. Doctoral Thesis, Purdue University, West Lafayette, IN.

[13] S.M. McDeavitt, A.A. Solomon, Hot-Isostatic Pressing of U-10Zr by a Coupled Grain Boundary Diffusion and Creep Cavitation Mechanism, Journal of Nuclear Materials 228 (1996) 184-200.

[14] P. Chiotti, B.A. Rogers (1950), The Production of Uranium and Thorium in Powder Form, United States Atomic Energy Commission, AECD-2974.

[15] H.H. Chiswick, Advances in the Physical Metallurgy of Uranium and its Alloys, Geneva Conference Papers (1958), 713-735.

[16] C. B. Basak, R. Keswani, G.J. Prasad, H.S. Kamath, N. Prabhu, Phase Transformations in U–2 wt% Zr Alloy, Journal of Alloys and Compounds 471 (2009) 544–552.

[17] E. R. Boyko, The Structure 'of the δ Phase in the Uranium-Zirconium System, Acta Cryst. 10 (1957) 712-713.

[18] C.R. Clark, M.K. Meyer, Fuel Powder Production from Ductile Uranium Alloys, Presented at the 1998 International Meeting on Reduced Enrichment for Research and Test Reactors, Oct. 18 - 23, 1998, Sao Paulo, Brazil.

[19] T. Hashino, Y. Okijima, Mechanism of the Reaction of Hydrogen with Uranium, Journal of Physical Chemistry 77 (1973) 2236-2241.

[20] J. Bloch, The Hydriding Kinetics of Activated Uranium Powder Under Low (Near Equilibrium) Hydrogen Pressure, Journal of Alloys and Compounds 361 (2003) 130–137.

[21] A. J. Parkison (2008), Hydride Production in Zircaloy-4 as a Function of Time and Temperature, Master Thesis, Texas A&M University, College Station.

VITA

Name: David Joseph Garnetti

Address: Texas A&M University, 3133 TAMU, College Station, TX 77843-3133

Email Address: dgarnetti@tamu.edu

Education: M.S. Nuclear Engineering, Texas A&M University, 2009
B.S. Physics, Florida State University, 2005

URANIUM POWDER PRODUCTION VIA HYDRIDE FORMATION AND ALPHA PHASE SINTERING OF URANIUM AND URANIUM-ZIRCONIUM ALLOYS FOR ADVANCED NUCLEAR FUEL APPLICATIONS

9/18/09
M.S. Thesis
David Joseph Garnetti

Outline

- Introduction
- Background Research
- Experimental Setup and Procedures
- Results
- Discussion of Results
- Summary and Recommendations

Primary Sources

- D. E. Burkes, R.S. Fielding, and D.L. Porter, Metallic Fast Reactor Fuel Fabrication for the Global Nuclear Energy Partnership, Journal of Nuclear Materials, 392 (2009), p. 158-163
- W.D. Wilkinson, Uranium Metallurgy, John Wiley & Sons, Inc. (1962)
- S.M. McDeavitt (1992), Hot Isostatic Pressing of U-10Zr Alloy Nuclear Fuel by Coupled Grain boundary Diffusion and Power-Law Creep. Doctoral Thesis, Purdue University, West Lafayette, IN.
- P. Chiotti and B.A. Rogers (1950), The Production of Uranium and Thorium in Powder Form, United States Atomic Energy Commission, AECD-2974

Introduction

Introduction

- The research conducted for this thesis is part of the US Department of Energy's Nuclear Energy Research Initiative (NERI)
- Under the Advanced Fuel Cycle Initiative (AFCI) of NERI
- The main goal of the research project is to develop a method for U-Zr-Pu-TRU alloy fabrication that operates at temperatures below 660 °C

Work in Injection Casting

- Initial experiments showed a loss of 40% of the Am during injection casting
- Later experiments showed potential for much lower losses of Am and other TRUs with the use of a cover gas
  - 0.3 % Am loss with 670 Pa
  - 0.006 % Am loss with 30 Pa

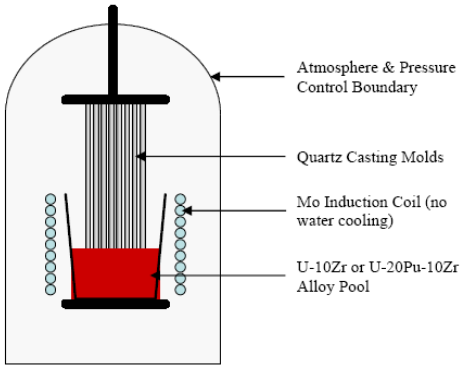

Drawing Courtesy of Dr. S. McDeavitt

Research Outline

- Development of a powder production system
- Initial demonstration of the alpha phase sintering fuel pellet fabrication
  - Pellets heated to approx 650 ˚C; Some also heated to 700 ˚C and 800 ˚C
  - Various pellet compositions: DU, DU-10Zr, DU-Mg, and DU-10Zr-Mg
  - Pellets measured pre and post experiment and in situ using a LVDT
  - Pellets analyzed using digital and SEM microscopy

Background Research

Background

- Sintering
- Alpha Phase Uranium
- The Uranium Hydride/Dehydride Process

Sintering

- The physical process where a form comprised of compacted particles is transformed into a dense structure at elevated temperatures through diffusion controlled mechanisms
- Main driving force of sintering is the reduction of surface area to minimize surface energy within the body

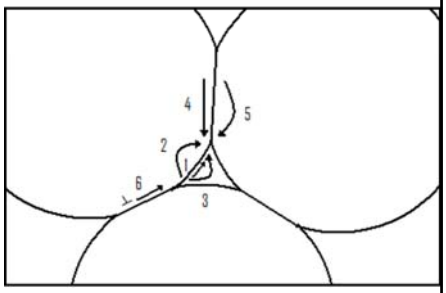

Porosity

- Particles come together by dominating mechanism
- The internal void space begins to close and internal porosity is formed
- Pores change from irregular shapes into spherical shapes to minimize surface energy effects
- The radius of the pores decreases until an equilibrium condition

$$p = \frac{2\gamma}{r}$$

Sintering Rate

- The rate at which the material densifies and is often modeled in terms of volumetric strain rate

$$\text{Sintering Rate} = \frac{d}{dt}\left(\frac{\Delta V}{V_o}\right)$$

Alpha Phase Uranium

- Uranium may exist in three allotropic phases named α, β, and γ
- α phase is stable from low temperatures up to 667°C and has a complex orthorhombic structure
- β phase is stable in the temperature range of 667 °C to 772 °C and has a complex tetragonal structure
- γ phase is stable from 772 °C up to1132°C and has a body centered cubic structure

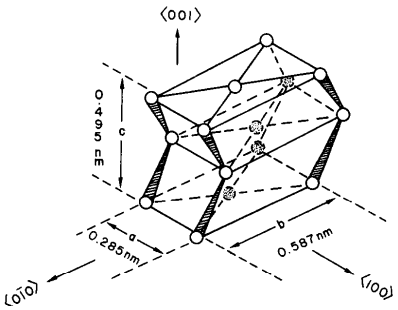

[7] Carroll

Initial Fuel Use

- At the advent of nuclear energy, pure uranium metal was one of the first fuel forms investigated
- Higher density and higher thermal conductivity than oxide fuel
- Irradiation induced swelling of pure uranium metal caused it to be an unusable fuel form

U-Zr Alloys

- Zirconium is a commonly-used alloying element with uranium in nuclear fuels for fast reactor systems
  - Zr alloying eliminated the α phase tearing
- Zirconium exists in two phases:
  - an hexagonal phase stable up to 862 ˚C (α)
  - a body center cubic phase stable from 826 ˚C to the melting point1852 ˚C (β)

U-Zr Phase Diagram

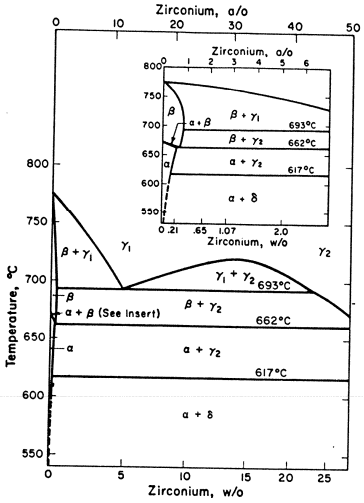

[15] Chiswick

Uranium Hydride

- Uranium Hydride (UH_3) is formed through the following reversible reaction

$$2U + 3H_2 \rightleftharpoons 2UH_3$$

- The reaction causes the complete destruction of the original structure of the metal
- Large difference in density of uranium metal (19.04 g/cm^3) and UH_3 (10.9 g/ cm^3)
- Fine powder black/dark brown color ranging from less than 1 μm up to ~10 μm, approximately -400 mesh (at 225 ˚C)

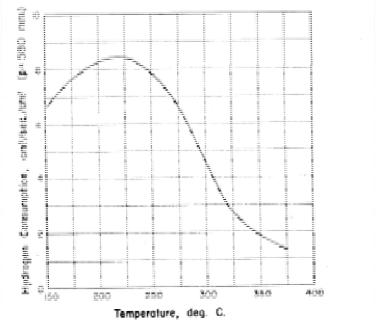

[14] Chiotti

Dehydriding Uranium

- UH_3 disassociates at atmospheric pressures at temperatures above 430 °C
- This process can be expedited by heating the UH_3 in a vacuum
- Uranium metal left behind is high purity powder with an average size of a less than 40 μm
- Powder sinters into aggregate particles at temperature over 300 °C

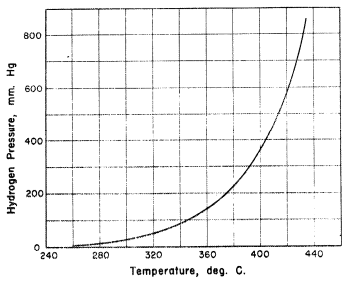

[14] Chiotti

Oxide Removal with Nitric Acid

- Oxide layer will create a barrier to the diffusion of hydrogen
- Oxide layer may also cause oxygen contamination in the powder produced
- 25% nitric acid by volume was sufficient for the removal of the oxide layer
- If the DU is left too long in the acid bath, the sample will reoxidize

Experimental Setup & Procedures

Experimental Setup & Procedures

- Powder Production Experimental Design & Procedures
- Pellet Pressing Design and Procedures
- Alpha Phase Sintering Experimental Design & Procedures

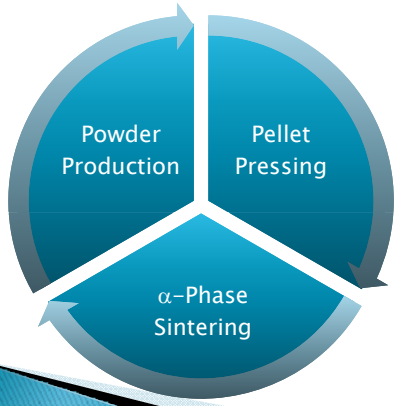

Each component of this research was designed and built specifically for the project.

A major portion of the work presented here involved equipment design and fabrication and process development.

Inert Atmosphere Glovebox

- In order to control oxygen contamination of the uranium metal all powder handling processes were performed in an inert atmosphere.

Powder Production

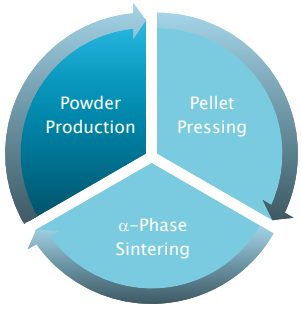

Powder Production Experiment

- High purity uranium metal powder is not readily available for purchase
- A reliable uranium powder production method was needed in the laboratory to create the powders required
- Hydride/De-hydride was the chosen process for producing uranium metal powder
- As-Received uranium was in the form of rectangular metal chunks weighing10-30 grams

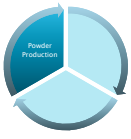

Powder Production System

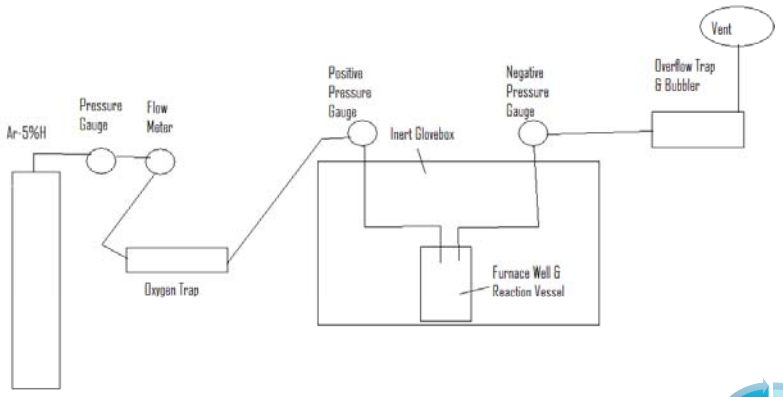

Process Gas Flow Chart

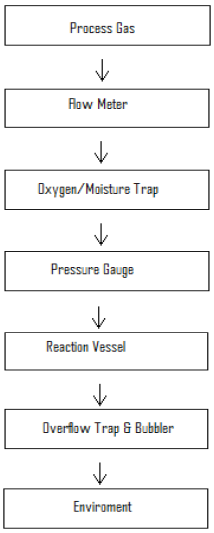

Initial Reaction Vessel

- Furnace system in the east airlock of the glovebox
- 350 W Watlow furnace was placed in the center of a stainless steel pot, diameter 20.32 cm (8 in)
  - Insulation between furnace and pot wall
- Samples placed Y_2O_3 crucible
- Top gasket of the airlock had a Conax Buffalo feed-through installed

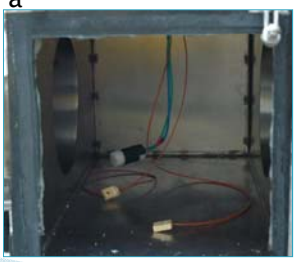

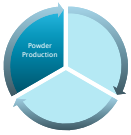

Reaction Vessel

- Fabricated out of 1.875 inch 304 SS plates connected by 24 inch long ¼ in diameter 316 SS thread rod
- A high temperature resilient rubber plug was located at the top of the vessel
- On the bottom plate a fabricated 304 SS cup affixed by a ¼ in screw
- The cup held a 10 mL alumina crucible
  - OD 22 mm, H 33 mm
- Copper tubing used for inflow/outflow of process gas

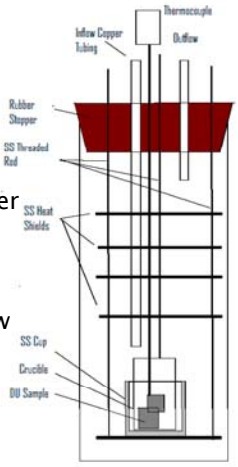

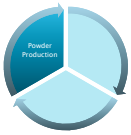

Sample Preparation

- Samples were weighed using AL-204 Balance (±0.0005 g)
- Cut down to a more manageable size and reweighed if necessary
- Washed in 35% Vol nitric acid bath, approx. 10-15 mins
- Washed samples were dull silver/gold
- Samples immediately taken back into the glovebox to limit oxygen exposure

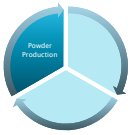

Hydride/Dehydride Procedures

- After connecting inflow and outflow lines the well was evacuated
- Flow rate ~ 2 SCFH; Vessel pressure ~ 2 psi
- Sample heated to 225 °C, allowed to sit for 24-48 hours (under Ar-5%H)
- Process gas shut off and the well is evacuated
- Well raised to 375 °C under vacuum
- Pressure gauge was observed for indication when H_2 has completely disassociated

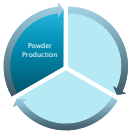

Pellet Pressing

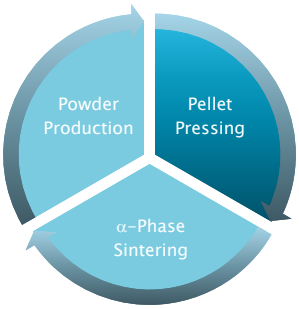

Powder Preparation Procedures

- After cooling the sample was removed from the vessel
- Loosely sintered pieces were broken apart by shaking and grinding with a mortar and pestle
- Powder placed in the Wig-L-Bug mixing device with or without the addition of a stainless steel bearing
- Non-hydrided pieces of DU saved for later use

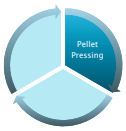

Powder Pressing Design

- Powder was pressed into a pellet using a double action punch and die
- Die fabricated from 303 SS; Punch fabricated from H-13 tool steel
- Pellets diameter approx. 9.5 mm (0.375 in)
- Punches incrementally turned down to ensure a tight fit
- Pressed with laboratory hydraulic press (Carver Model C)

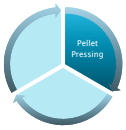

Powder Pressing Procedures

- Powders were mixed until homogenous via the Wig-L-Bug
- No lubrication used during pressing to limit contamination of samples
- Pressed with a maximum load 12,000-15,000 lbs(185-235 MPa)

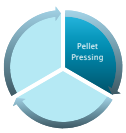

α-phase Sintering

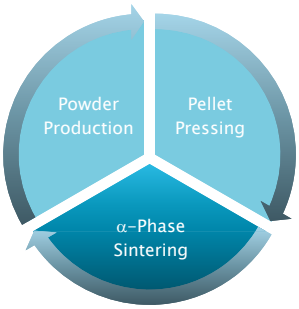

α-Sintering Experimental Design

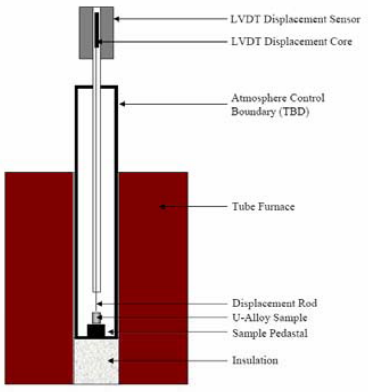

- Construction of reaction vessel similar to H/DH vessel
- Fabricated out of 304 SS plates connected by 316 SS thread rod
- Pellets held in 10 mL alumina, inside of 304 SS cup
- LVDT sits at the top of vessel; Magnet attached to threaded rod which rests on top of pellet (Y_2O_3 sheath surrounds end of rod)

α Sintering Experimental Procedure

- Pellets measured and weighed before being placed in crucible
- LVDT rod placed on pellet to measure shrinkage
- Pellet raised to desired temperature

Results

Results

- Powder Production Experiment
- Alpha Phase Sintering Experiment

Airlock Setup

- The airlock setup was never successful
- No apparent structural breakdown of samples
- DU appeared to have oxidized
- Failure of setup due to oxygen contamination

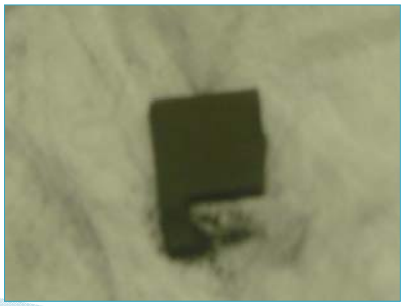

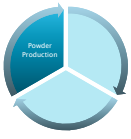

Initial Furnace Well Setup

- No oxygen trap
- No visible sign of structural breakdown
- Post H/DH the sample was dark brown
- When placed in an acid bath the DU turned silver with brown markings

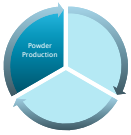

Ti Getter Addition

- Ti getter added to eliminate O_2, N_2, & moisture from the process gas
- Experiment 9 was successful but could not be repeated
- Ti getter was a constant suspect of contamination and time consuming to inspect and recharge
- Replaced by commercially bought oxygen and moisture trap

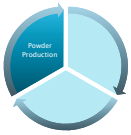

Experiment 9

- 6.2512 g sample of DU
- Sample was hydrided for 39 hours at 275 ˚C
- 3.1519 g of UH_3 was produced

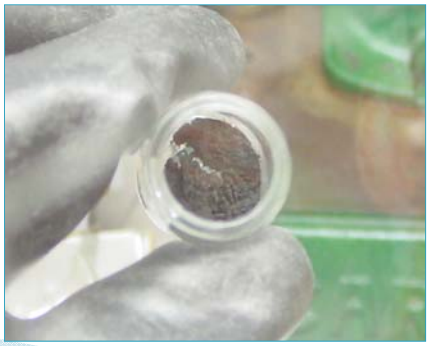

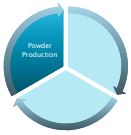

Experiment 12

- Ti getter leaked on 3rd day of experiment
- Post experiment a yellow plating was observed on the copper tubing
- Yellow plating proved not to be reactive during H/DH hold temperature
- The plating remained throughout the rest of the experiments
- Approx 1.5 g of UH3 produced

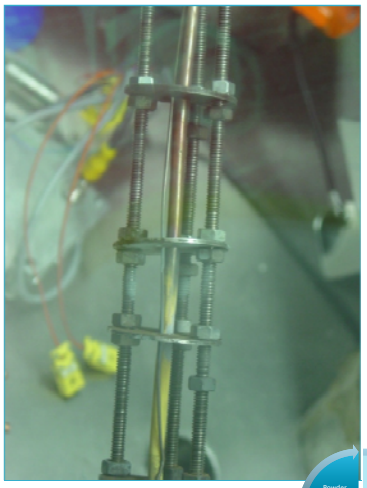

Experiment 13

- Oxygen and moisture trap added
- Hydrided for 24 hours at 265 ˚C
- Dehydrided at 450 ˚C
- Successfully produced DU metal powder
- All powder production experiments successful from here on

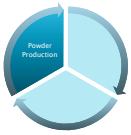

Experiment 13

- Powder sintered loosely
- Sintered chunk could not be broken apart with light pressure from tweezers
- But did break when more force was applied

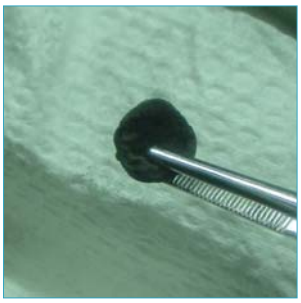

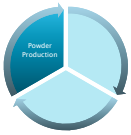

Non-Hydrided Uranium

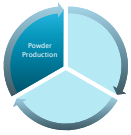

Powder Preparation

- 1. Sintered powder in the shape of the crucible
- 2. Sintered chunk broken apart from shaking
- 3. Grind with SS mortar and pestle
- 4. Fine powder after being milled with the Wig-L-Bug

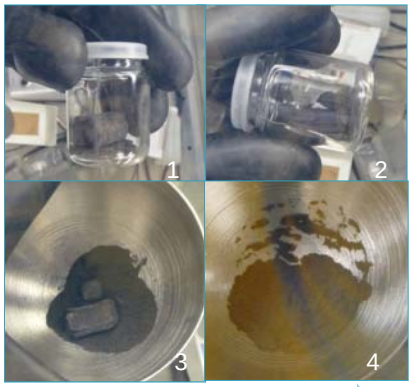

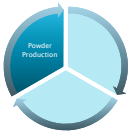

Powder Production After Experiment 13

- After experiment 13 powder production system and procedures established
- Powder hydrided at 225 ˚C
- Powder dehydride at 375 ˚C
- Able to produce ~6 to 12 g of uranium metal powder over a 48 hour period

Pellet Data Overview

Pellet #	Mass (g)	Pressed Thickness (mm)	Pressed Diameter (mm)	GD (% TD)	Post Thickness (mm)	Change (%)
Pellet 2	4.0368	4.3688	9.6215	66.78	4.4704	2.33
Pellet 3	3.3366	4.5288	9.6342	53.11	4.7117	4.04
Pellet 4	2.7656	2.7864	9.6622	71.13	2.8575	2.55
Pellet 5	2.9426	3.556	9.6647	63.47	3.6957	3.93
Pellet 6	2.6417	2.9667	9.6723	64.02	2.9845	0.6
Pellet 8	3.9946	5.0495	9.4234	59.6	5.2705	4.38
Pellet 9	2.9188	3.9472	9.4234	59.63	4.064	2.96
Pellet 10	2.3685	3.5712	9.6139	53.49	3.5687	-0.07

Pellet #	Post Diameter Max (mm)	Change (%)	Post Diameter Min (mm)	Change (%)	ΔL/L
Pellet 2	9.9568	3.37	9.8806	2.69	-
Pellet 3	9.8425	2.12	9.6901	0.58	0.0336
Pellet 4	9.8933	2.34	9.7409	0.81	0.0144
Pellet 5	10.1346	4.64	9.8552	1.97	-
Pellet 6	9.4488	-2.37	9.3599	-3.23	0.0506
Pellet 8	9.8171	4.01	9.3599	-0.67	0.0150, 0.0122*
Pellet 9	9.779	3.64	9.525	1.08	-
Pellet 10	9.652	0.39	9.6393	0.26	-

Pellet 1

- DU Pellet
- Pellet 1 was pressed to 40.7% TD
- Pellet was pressed using punches fabricated from 303 SS
  - Punches could not handle the force necessary to produce a high GD
- Pellet crumbled during experiment

Pellet 2

Composition	DU
Green Density (%TD)	66.6
Sintering (T,t)	650˚C, 24h
Final Porosity (%)	18.55 ± 3%

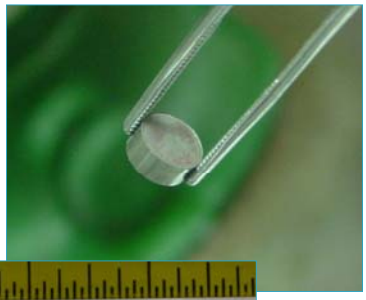

- No LVDT data taken during experiment
- Pellet had a mild conical shape post-sintering

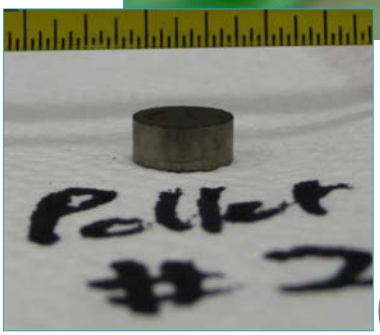

Pellet 2

Composition	DU
Green Density (%TD)	66.6
Sintering (T,t)	650˚C, 24h
Final Porosity (%)	18.55 ± 3%

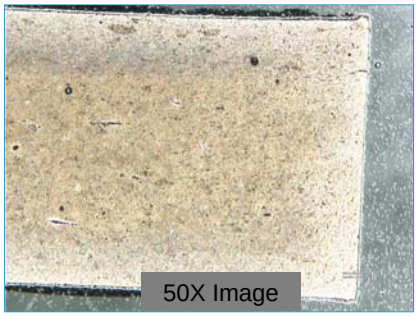

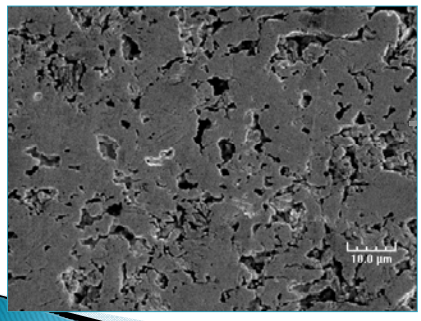

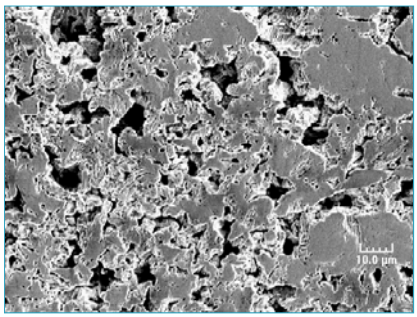

1000X SEM Images

Pellet 3

Composition	DU
Green Density (%TD)	53.3
Sintering (T,t)	650˚C, 24h
Final Porosity (%)	26.10 ± 2%

- LVDT data showed continuous shrinkage at hold temp.
- Post experiment analysis showed a mild conical shape and several cracks

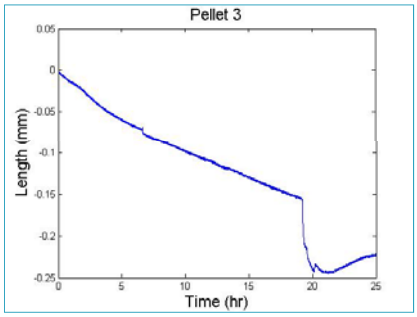

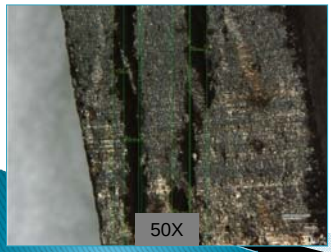

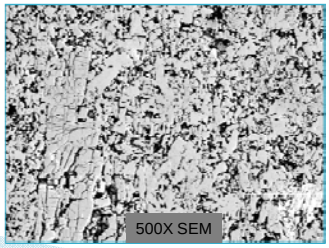

Pellet 4

Composition	DU
Green Density (%TD)	71.3
Sintering (T,t)	650˚C;695 ˚C (30min x2)

- LVDT data showed continuous shrinkage at hold temp.
- LVDT data during the 695 ˚C was unclear due to the system response to the temp. change

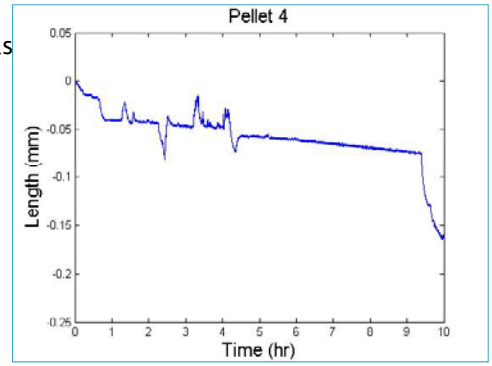

Pellet 5

Composition	DU-10Zr
Green Density (%TD)	63.47
Sintering (T,t)	650˚C; 700 ˚C (~3 hrs x3)

- LVDT data showed continuous shrinkage at hold temp.
- Analysis showed no alloying of the U and Zr
  - No evidence of a δ or γ phase during EDS measurements

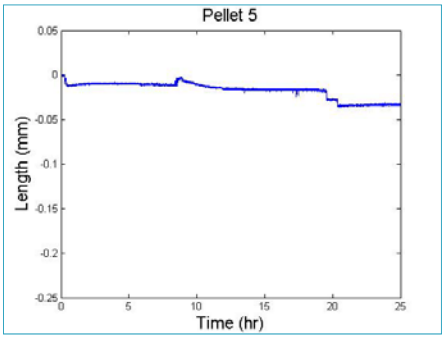

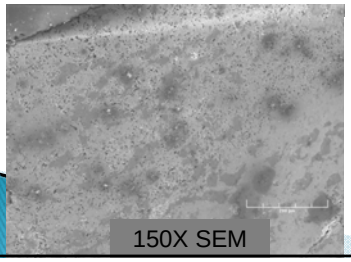

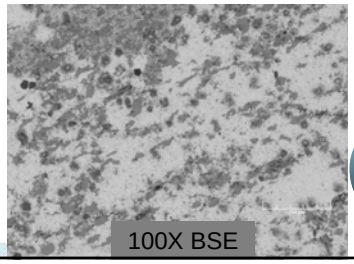

Pellet 5

Composition	DU-10Zr
Green Density (%TD)	63.47
Sintering (T,t)	650˚C; 700 ˚C (~3 hrs x3)

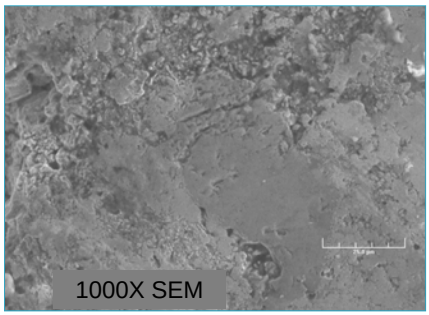

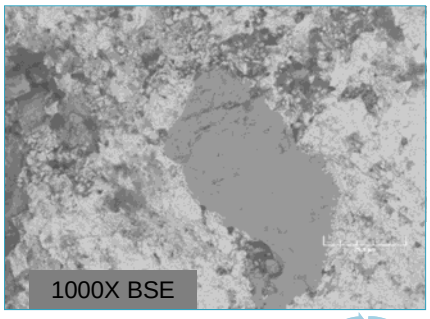

Pellet 5

Composition	DU-10Zr
Green Density (%TD)	63.47
Sintering (T,t)	650˚C; 700 ˚C (~3 hrs x3)

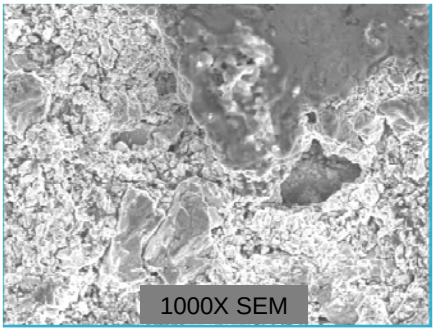

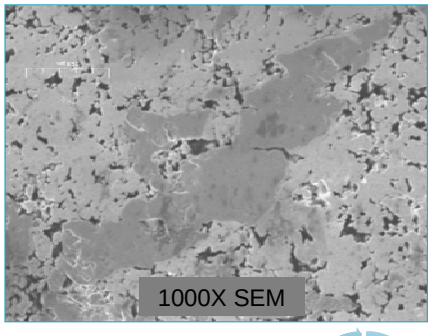

Pellet 6

Composition	DU-Mg
Green Density (%TD)	64.02
Sintering (T)	655˚C
Final Porosity (%)	14.17 ± 2 %.

- 0.0290 g of Mg and 2.7058 g of DU
  - Mg at% equal to the at% of Pu in a 3 g U-10Pu (wt%)
- Post experiment measurements showed a slight increase in thickness (0.06%) and a decrease in diameter (-2.37% and -3.23%)
- Areas very low porosity and large non-uniformed pores throughout
- No LVDT Data

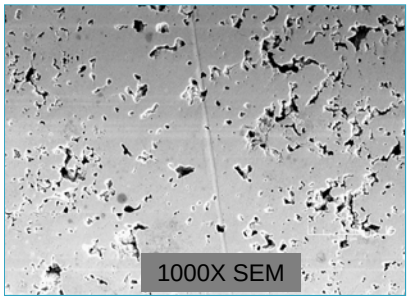

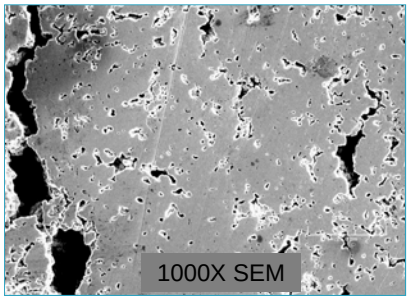

Pellet 8

Composition	DU
Green Density (%TD)	59.6
Sintering (T)	650˚C, 700˚C, 800˚C,

- LVDT showed continuous shrinkage when at 650 ˚C and 700 ˚C
- There was a stop in shrinkage at 800 ˚C
- SEM analysis showed areas of increased sintering

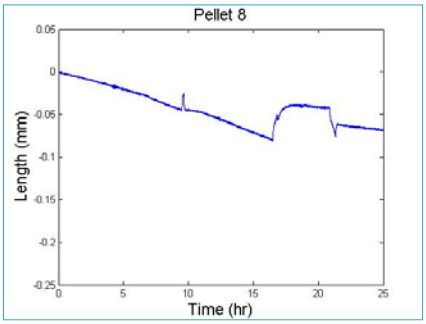

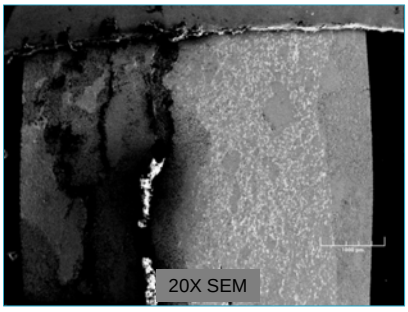

Pellet 8

Composition	DU
Green Density (%TD)	59.6
Sintering (T)	650˚C, 700˚C, 800˚C,

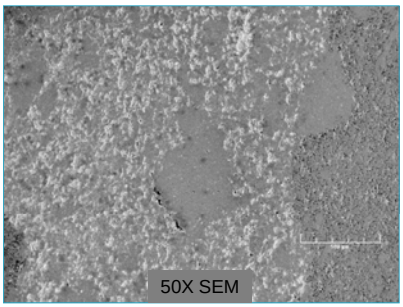

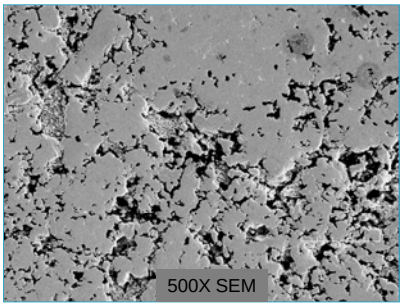

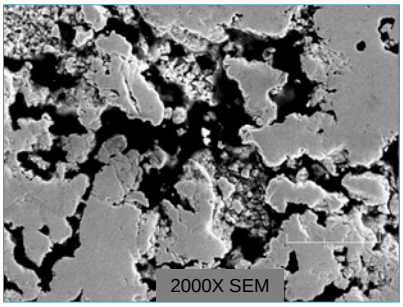

Pellet 9

Composition	DU-10Zr
Green Density (%TD)	59.63
Sintering (T)	650˚C, 700˚C, 770˚C,

- The LVDT system stop working during the beginning of the experiment
  - The LVDT data obtained was similar to the data from pellet 5
- The bottom of the pellet crumbled during the experiment

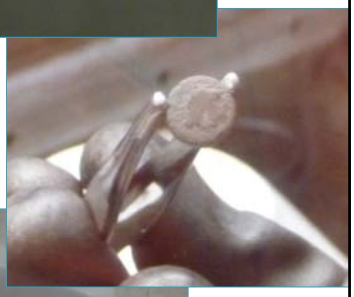

Pellet 10

Composition	DU-10Zr-Mg
Green Density (%TD)	53.49
Sintering (T)	655˚C

- 0.0595 g Mg; 0.3009 g Zr; 2.0998 g DU
  - Mg at% equal to at% of Pu in3g U-10Zr-20Pu (wt%)
- Post experiment measurements showed a slight decrease in thickness (-0.07%) and a slight increase in diameter (0.26% and 0.39%)
- The pellet showed structural damage on one side
- The pellet was golden post experiment
- DU and Zr stayed mostly segregated
- Very low porosity
  - Though no porosity measurements done
- Large grains of DU with the boundaries "filled" by the Zr rich phase

Pellet 10

Composition	DU-10Zr-Mg
Green Density (%TD)	53.49
Sintering (T)	655˚C

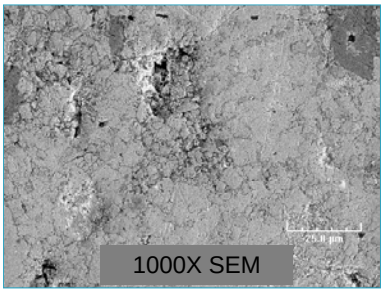

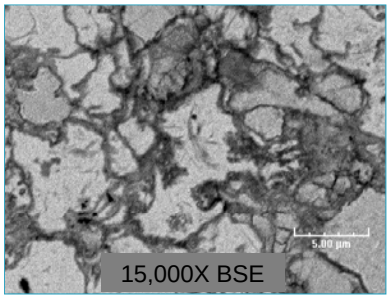

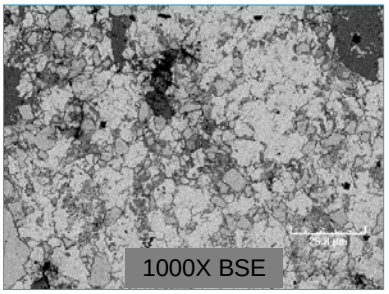

Discussion of Results

Powder Production System

- The powder production system was successfully developed, built, and installed
- The system produced between 6 and 12 g of DU metal powder over a 48 hr period
- The powder that was produced was on the order of 1-3 μm

α Phase Sintering

- All the pellets showed signs of sintering
- The porosity was not constant throughout the pellets
  - The most porous areas were consistently on the outer edges of the pellet
- The DU-Zr pellets did not show evidence of alloying
  - The DU-10Zr-Mg pellet had a greater dispersal of Zr throughout
- The pellets containing Mg had the lowest porosity and greatest degree of sintering

Post Experiment Shape

- Post experiment measurements did not agree with the LVDT measurement data
  - Measurements showed an increase in thickness while the LVDT data showed shrinkage
- The increase in thickness and diameter was attributed to the cracking of the pellet during the cool down
- The structural breakdown of pellets 9 & 10 was also attributed to cracking during the cool down

Post Experiment Shape

- Post Experiment the pellets were slightly conical in shape
- This has been attributed to powder pressing method
- The density of the pressed pellets was not constant, one end has a higher density than the other
- This gradient in density caused difference in the amount of sintering throughout the pellet, leading the conical shape

Summary & Recommendations

Summary

- A DU powder production system was built
- DU powder on the order of 1-3 μm was produced
- Sintering occurred in all test pellets
- Pellet cracking during cool down made the post experiment measurements unreliable
- Post experiment the pellets were conical shaped due to the differences in density throughout the pellet
- DU-Zr pellets showed no evidence of alloying
- The pellets containing Mg had the lowest porosity

Recommendations

- The rate of hydriding can be increased by the following changes
  - Switch a higher percentage H_2 process gas
  - Increase the surface area of sample exposed during hydration
  - Increase the pressure of the H_2 gas over the sample
- Oxygen contamination is of the utmost concern for the DU and DU powder
  - The DU should be kept in an oxygen free environment at all times
  - The powder should be produced as needed and not stored for long durations

Acknowledgements

- The Y-12 Plant at Oak Ridge and Dr. David Cecala for the help in obtaining the DU
- Dr. Kevin Hogan and Ryoji Oinuma for their help with the coding
- Grant Helmreich and Julie Borgmeyer for their help on this project and their microscopy work
- Zane Adams, Jeff Hausaman, and Michael Naramore for their work on the installation of the large glovebox system
- FCML Lab Group

References

- [1] D. E. Burkes, R.S. Fielding, and D.L. Porter, Metallic Fast Reactor Fuel Fabrication for the Global Nuclear Energy Partnership, Journal of Nuclear Materials, 392 (2009), p. 158-163
- [2] C.E. Stevenson, The EBR-II Fuel Cycle Story, La Grange Park, Illinois: American Nuclear Society Inc. (1987).
- [3] C.L. Trybus, J.E. Sanecki and S.P. Henslee, Casting of Metallic Fuel Containing Minor Actinide Additions, Journal of Nuclear Materials, 204 (1993), p. 50-55
- [4] M.B. Waldron and B.L. Daniell, Sintering, Heyden & Son Ltd (1978).
- [5] G.S. Udpahaya, Sintered Metallic and Ceramic Materials: Preparation, Properties and Applications, John-Wiley & Sons, Inc. (2000).
- [6] R.M. German, Sintering Theory and Practice, John-Wiley & Sons, Inc. (1996).
- [7] J.J. Carroll and A.J. Melmed, Field Ion Microscopy of Alpha Uranium, Surface Science, 116 (1982), p. 225-239
- [8] L. Grainger, Uranium and Thorium, London: George Newnes Limited (1958).
- [9] S.F. Pugh, Swelling in Alpha Uranium due to Irradiation, Journal of Nuclear Materials, Vol. 4 No. 2 (1961), p. 177-199
- [10] J.J. Burke, D.A. Colling, A.E. Gorum and J. Greenspan, Physical Metallurgy of Uranium Alloys, Brook Hill Publishing Company (1976).
- [11] W.D. Wilkinson, Uranium Metallurgy, John Wiley & Sons, Inc. (1962).
- [12] S.M. McDeavitt (1992), Hot Isostatic Pressing of U-10Zr Alloy Nuclear Fuel by Coupled Grain boundary Diffusion and Power-Law Creep. Doctoral Thesis, Purdue University, West Lafayette, IN.
- [13] S.M. McDeavitt and A.A. Solomon, Hot-Isostatic Pressing of U-10Zr by a Coupled Grain Boundary Diffusion and Creep Cavitation Mechanism, Journal of Nuclear Materials, 228 (1996), p. 184-200
- [14] P. Chiotti and B.A. Rogers (1950), The Production of Uranium and Thorium in Powder Form, United States Atomic Energy Commission, AECD-2974
- [15] H.H. Chiswick, Advances in the Physical Metallurgy of Uranium and its Alloys, Geneva Conference Papers (1958), p. 713
- [16] C. B. Basak, R. Keswani, G.J. Prasad, H.S. Kamath, and N. Prabhu, Phase Transformations in U-2 wt% Zr Alloy, Journal of Alloys and Compounds 471 (2009), p. 544-552
- [17] E. R. Boyko, The Structure 'of the δ Phase in the Uranium-Zirconium System, Acta Cryst. (1957). 10, p. 712-713
- [18] C.R. Clark and M.K. Meyer, Fuel Powder Production from Ductile Uranium Alloys, Presented at the 1998 International Meeting on Reduced Enrichment for Research and Test Reactors, Oct. 18 - 23, 1998, Sao Paulo, Brazil
- [19] T. Hashino and Y. Okijima, Mechanism of the Reaction of Hydrogen with Uranium, Journal of Physical Chemistry, 77 (1973), p. 2236-2241
- [20] J. Bloch, The Hydriding Kinetics of Activated Uranium Powder Under Low (Near Equilibrium) Hydrogen Pressure, Journal of Alloys and Compounds, 361 (2003), p. 130-137
- [21] A. J. Parkison (2008), Hydride Production in Zircaloy-4 as a Function of Time and Temperature, Master Thesis, Texas A&M University, College Station, Tx

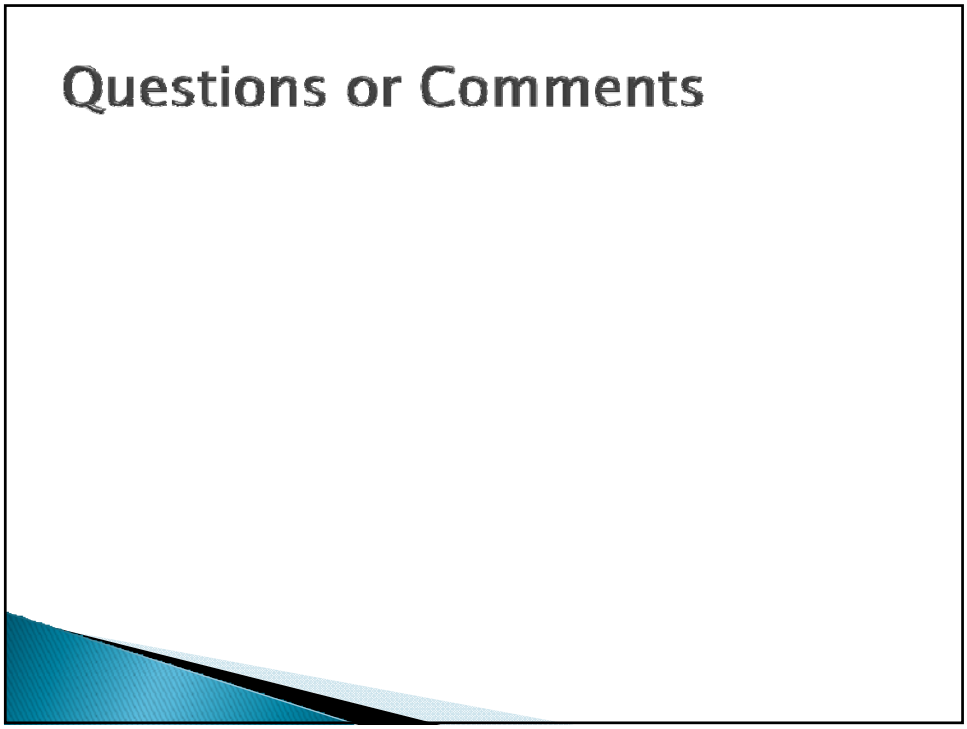
Questions or Comments

CHARACTERIZATION OF ALPHA-PHASE SINTERING OF URANIUM AND URANIUM-ZIRCONIUM ALLOYS FOR ADVANCED NUCLEAR FUEL APPLICATIONS

A Thesis

by

GRANT WILLIAM HELMREICH

Submitted to the Office of Graduate Studies of
Texas A&M University
in partial fulfillment of the requirements for the degree of

MASTER OF SCIENCE

December 2010

Major Subject: Nuclear Engineering

Characterization of Alpha-Phase Sintering of Uranium and Uranium-Zirconium Alloys for Advanced Nuclear Fuel Applications

CHARACTERIZATION OF ALPHA-PHASE SINTERING OF URANIUM AND URANIUM-ZIRCONIUM ALLOYS FOR ADVANCED NUCLEAR FUEL APPLICATIONS

A Thesis

by

GRANT WILLIAM HELMREICH

Submitted to the Office of Graduate Studies of
Texas A&M University
in partial fulfillment of the requirements for the degree of

MASTER OF SCIENCE

Approved by:

Co-Chairs of Committee,	Sean M. McDeavitt
	Lin Shao
Committee Member,	Miladin Radovic
Head of Department,	Raymond Juzaitis

.

December 2010

Major Subject: Nuclear Engineering

ABSTRACT

Characterization of Alpha-Phase Sintering of Uranium and Uranium-Zirconium Alloys for Advanced Nuclear Fuel Applications. (December 2010)

Grant William Helmreich, B.S. Nuclear Engineering; B.A. Chemistry, Texas A&M University

Chair of Advisory Committee: Dr. Sean M. McDeavitt

The sintering behavior of uranium and uranium-zirconium alloys in the alpha phase were characterized in this research. Metal uranium powder was produced from pieces of depleted uranium metal acquired from the Y-12 plant via hydriding/dehydriding process. The size distribution and morphology of the uranium powder produced by this method were determined by digital optical microscopy.

Once the characteristics of the source uranium powder were known, uranium and uranium-zirconium pellets were pressed using a dual-action punch and die. The majority of these pellets were sintered isothermally, first in the alpha phase near 650°C, then in the gamma phase near 800°C. In addition, a few pellets were sintered using more exotic temperature profiles. Pellet shrinkage was continuously measured in situ during sintering.

The isothermal shrinkage rates and sintering temperatures for each pellet were fit to a simple model for the initial phase of sintering of spherical powders. The material specific constants required by this model, including the activation energy of the process, were determined for both uranium and uranium-zirconium.

Following sintering, pellets were sectioned, mounted, and polished for imaging by electron microscopy. Based on these results, the porosity and microstructure of the sintered

pellets were analyzed. The porosity of the uranium-zirconium pellets was consistently lower than that of the pure uranium pellets. In addition, some formation of an alloyed phase of uranium and zirconium was observed.

The research presented within this thesis is a continuation of a previous project; however, this research has produced many new results not previously seen. In addition, a number of issues left unresolved by the previous project have been addressed and solved. Most notably, the low original output of the hydride/dehydride powder production system has been increased by an order of magnitude, the actual characteristics of the powder have been measured and determined, shrinkage data was successfully converted into a sintering model, an alloyed phase of uranium and zirconium was produced, and pellet cracking due to delamination has been eliminated.

DEDICATION

This thesis is dedicated to my grandmother, who first taught me to love learning.

ACKNOWLEDGEMENTS

I would like to thank Dr. McDeavitt for his continuing guidance, support, and encouragement throughout my research.

I would like to thank Dr. D. Cecala and the Y-12 plant in Oak Ridge, Tennessee for providing the depleted uranium used in this project.

I would like to thank Will Sames for his assistance in powder imaging.

I would like to thank Brandon Blamer for his assistance in sample preparation and polishing.

I would like to thank Dr. Guillemette for his expert assistance in SEM imaging.

NOMENCLATURE

TRU	Transuranics
DU	Depleted Uranium
EBR II	Experimental Breeder Reactor II
IFR	Integral Fast Reactor
LVDT	Linear Variable Differential Transformer
SEM	Scanning Electron Microscope
BSE	Backscatter Electron
WDS	Wavelength Dispersive Spectroscopy

TABLE OF CONTENTS

Page

LIST OF FIGURES

Page

Page

Page

LIST OF TABLES

1. INTRODUCTION

Advanced nuclear fuel cycles are currently under development around the world. In many cases, fuel cycle strategies call for the recycling of transuranic (TRU) isotopes for burning in advanced reactor systems. A reactor systems that is especially effective for TRU burning is the metal-fueled fast reactor [1]. Fast reactors driven by uranium alloy nuclear fuels have been operated for over 40 years with injection casting as the predominant fuel fabrication method. However, the low melting points and high vapor pressures of the TRU isotopes of neptunium, americium, and curium make fuel fabrication by melt casting a challenge [2]. Possible solutions to these issues have been proposed and tested [1]; however, alternative means of U-TRU-Zr fuel fabrication have been pursued as well.

Low temperature powder metallurgy methods for the fabrication of U-TRU-Zr alloys are under development at Texas A&M University's Fuel Cycle and Materials Laboratory as a part of the U.S. Department of Energy's Nuclear Energy Research Initiative (NERI). The focus of this particular NERI project is to develop two fabrication methods, alpha-phase sintering and hot extrusion, to produce U-Zr alloys that are either porous or dense at temperatures ranging from 600°C to 800°C. The focus of this thesis is on process development experiments relevant to the alpha phase sintering method. The initial establishment of the uranium powder preparation method and the processing and measurement equipment necessary to perform alpha phase sintering was reported in a previous thesis by D. Garnetti under the direction of S.M. McDeavitt [3]. The research presented in this thesis continues the development of the alpha phase sintering method.

This thesis follows the style of Journal of Nuclear Materials.

Uranium powder for use in sintering studies was generated using a hydride/dehydride process that was based on the method described in [3], but the process variables and methods were improved to increase powder production rates. Optical microscopy and image analysis of the powder produced by this method showed a rough, irregular morphology with a size distribution peak near 40 μm diameter particles.. Uranium alloy powder mixtures were pressed into pellets were with varying compositions, including pure DU, DU-10Zr, and DU-5Zr[1]. Sintering was performed under a variety of conditions, including isothermal alpha phase sintering between 625°C and 660°C, isothermal gamma phase sintering between 795°C and 820°C, and sintering with cyclic phase changes.

The shrinkage associated with sintering for each pellet was measured in situ in real time using a Linear Variable Differential Transformer (LVDT). This system allowed accurate determination of both time and temperature dependencies and calculation of thermodynamic sintering constants, leading to the development of basic sintering models. LVDT measurements were supported by direct physical measurements of pellet dimensions before and after sintering. Based on these measurements, it was found that DU-Zr mixtures sintered more rapidly and to a higher density then pure DU due to enhanced sintering by DU-Zr interdiffusion. In addition, the activation energy for sintering of DU and DU-10Zr were found to be 340 +/-41 kJ/mol and 272 +/-91 kJ/mol respectively.

Following sintering, pellets were sectioned axially, mounted in epoxy, polished, and imaged using SEM. These images were used to analyze the degree of sintering, determine porosity, and identify phases in pellets with alloying constituents. It was found that pellets with low compaction pressures sintered with an inner high density region and an outer low density region due to compaction density gradients; however, increased compaction pressure resulted in

[1] All compositions are presented as weight percent, unless otherwise noted.

uniform density. The sintered phases of DU-Zr pellets were identified to be a uranium rich phase containing small amounts of dispersed zirconium, a zirconium rich phase containing virtually no uranium, and a mixed phase containing both uranium and zirconium. The mixed phase consisted of lamellar $\alpha(DU)+\delta(DUZr_2)$ if the pellet was sintered in the γ-phase, and pure δ-phase if the pellet was sintered in the α-phase.

The following sections present detailed descriptions of the context, methods, results and interpretation of the results for the alpha phase sintering process development. Section 2 describes the scientific background for this thesis, including metal fuel background, sintering theory, and the hydride/dehydride method. Section 3 describes in detail the apparatus and procedures which were used in this research. Section 4 provides the results achieved. Section 5 discusses the significance and meaning of the results. Finally, Section 6 provides a brief summary of the primary results and suggestions for future research on this topic.

2. BACKGROUND

This section presents a summary of the prior experience and physical phenomena relevant to the alpha phase sintering method developed for this thesis. Section 2.1 describes the metal fuels used for fast reactor systems and the injection casting method which has predominantly been used in the past for their fabrication. Section 2.2 describes the basic theory behind sintering, along with a fundamental model for sintering rate. Section 2.3 describes the hydride-dehydride process which was used for the production of uranium powder.

2.1 Uranium Alloys as Nuclear Fuel

2.1.1 Uranium Metal

Uranium metal exists in three distinct phases depending on temperature. The alpha phase is stable at temperatures below 667°C and has a complex orthorhombic structure, as shown in Figure 2-1 [4]. The beta phase is stable between 667°C and 772°C and has a complex tetragonal structure. The gamma phase is stable from 772°C up to the melting point of 1132°C and has a body centered cubic structure [5]. The alpha phase of uranium, which is of primary interest in this work, has a density of 19.04 g/cm^3 at room temperature [6]. The lattice parameters of the alpha phase uranium unit cell, which are more accurate than those shown in Figure 2-1, are a=2.8541Å, b=5.8541Å, and c=4.9536Å [6].

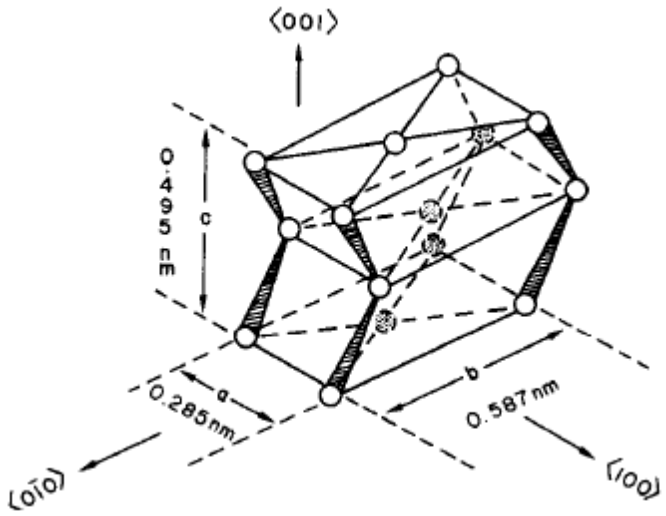

Figure 2-1: Complex orthorhombic structure of alpha phase uranium [4].

2.1.2 Uranium as a Nuclear Fuel

Metallic uranium was an early candidate for use as a fuel form for nuclear energy systems. This fuel form possesses two highly desirable qualities. First, the relatively high conductivity of uranium metal has the potential to minimize the temperature gradient within the fuel. Second, the higher density of uranium metal increases the potential power density available within the fuel. However, it was quickly noted that alpha phase uranium underwent severe swelling and tearing after brief levels of burnup within reactors; the orthorhombic alpha phase allotrope is the dominant microstructure at typical reactor operating temperatures [7]. This effect was caused by the coupling of expansion due to anisotropic fission product accumulation causing uniaxial growth and grain boundary tearing. Further research eventually determined that alloying uranium with small amount of zirconium, molybdenum, titanium and/or other noble metal elements eliminated the anisotropic swelling due to tearing. This enabled the use of uranium alloys as nuclear reactor fuel; however, fission gas bubble formation and gas release is still a performance limiting phenomenon [8]. Although the majority of nuclear reactors currently

utilize oxide fuels, metal fuels are especially viable in fast reactor systems designed to transmute and destroy transuranics (TRUs).

2.1.3 Fabrication of Metal Uranium Fuel

Injection casting is the method most commonly used for fabrication of uranium metal fuels for nuclear reactors, including the manufacture of U-Zr fuel for use at EBR II and in IFR demonstrations. A basic schematic of the injection casting system is given in Figure 2-2. The injection casting process begins by melting liquid U-Zr at approximately 1500°C in a coated graphite melt crucible. The inner crucible wall is typically coated with an oxide mixture consisting of yttria, zirconia, and thorium oxide to minimize interactions between the liquid fuel and the crucible. Quartz injection molds are inserted into the liquid, and pressure is applied to force the fuel into the molds. Once the liquid fuel is injected into the molds and solidified, the molds are destroyed and the cat fuel pins are removed and allowed to cool. The solid fuel is broken away from the molds and machined to the desired final fuel form [9].

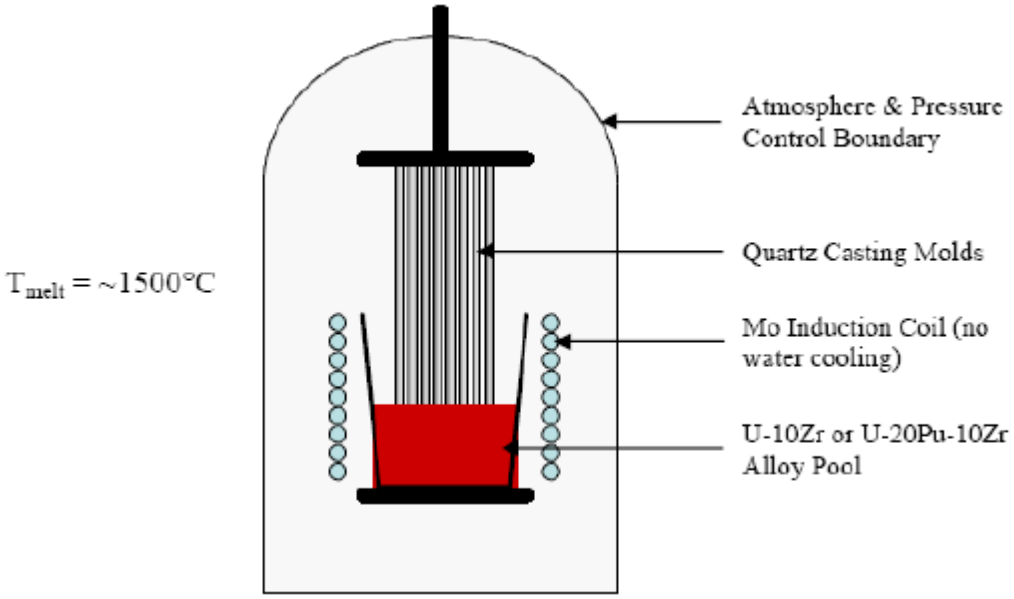

Figure 2-2: Schematic of injection casting system used for U-Zr fuel [3].

Although injection casting is highly effective for the manufacture of U-Zr fuel, it faces potential issues when applied to the fabrication of U-TRU-Zr fuel due to the volatility of some transuranics, most notably americium and neptunium. Figure 2-3 shows the vapor pressures of several transuranics in the temperature range of interest. Initial attempts to fabricate U-TRU-Zr fuel using unmodified U-Zr fabrication procedures resulted in a loss of 40% of the original 2.1wt% Am due to evaporation [2]. Some modifications to the standard U-Zr injection procedures have been shown to significantly reduce transuranic losses, most notably the use of a sealed vessel with a pressurized argon cover gas to reduce Am evaporation and a cold trap to collect the portion which still evaporates. Initial testing of this system with cover gas pressures of 670 Pa and 30 kPa resulted in Am losses of 0.3% and 0.006% respectively [1].

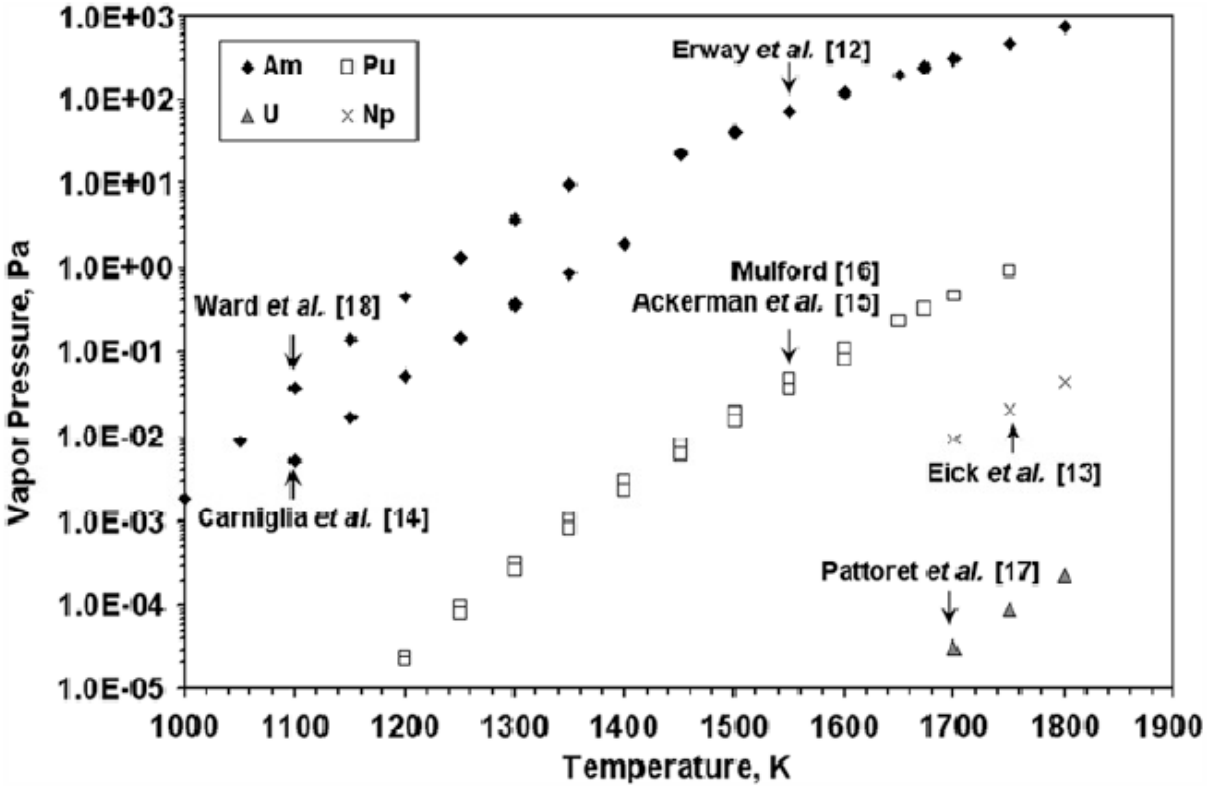

Figure 2-3: Vapor pressures of common transuranics at injection casting temperatures [1].

Previous research performed in the Texas A&M University Fuel Cycle and Materials Laboratory was focused on laying the foundation for an alternative U-TRU-Zr fabrication method based on a powder metallurgy approach with alpha phase uranium sintering [3]; the research described in this thesis continues this work. Sintering processes involving uranium metal are normally performed at temperatures in the gamma phase region, due to the high diffusivity of gamma phase uranium, the dependence of sintering rate on temperature, and for the prevention of oxidation during sintering [10]. However, evidence of low temperature sintering of alpha phase uranium was observed during uranium powder production [11], and during the initial heating regime of experiments focused on gamma phase sintering [10, 12]. The possibility of low temperature sintering is significant for fuel refabrication for TRU burning since the

temperatures used in gamma phase sintering would result in significant evaporative losses of some transuranics, reproducing the challenges encountered with melt-casting.

An initial investigation into the viability of uranium alpha phase sintering was performed as a part of the U.S. Department of Energy's Nuclear Energy Research Initiative (NERI), under the Advanced Fuel Cycle Initiative (AFCI) [3]. Using both live monitoring of pellet shrinkage and SEM imaging, alpha phase sintering was effectively demonstrated for pure uranium samples and for uranium with added zirconium and magnesium [3]. Basic studies of post-sintering porosity were performed; however, rate and thermodynamic analysis were left as potential future work [3].

2.2 Sintering

Sintering is a high temperature phenomenon in which compact powder performs may be densified to form solid materials via various mechanisms that are driven by forces which strive to minimize the overall surface energy within the material. On a practical level, sintering allows for the conversion of fine metallic, ceramic, and polymer powders into solid pieces of a desired shape. Prior to sintering, a typical fabrication process begins with the pressing of powder into a solid compact. This “green” form is then heated to allow bonding and atomic mobility. The typical process variables controlled during sintering include the compaction method, temperature, applied stress, and time. These process variables enable the precise control of the final microstructure and properties of the sintered material [13]. Sintering is commonly used for the fabrication of ceramic nuclear fuel pellets.

2.2.1 Sintering Theory

The microstructure of powder compacts before sintering may be envisioned as a 3-D collection of particles with only point contacts at each particle-particle interface. Due to the large open volume in this system, the overall density of a compact is much lower than the theoretical density of the true solid. In addition, due to the lack of bonding between particles, the strength of the unsintered powder compact is much lower than the strength of the bulk material [14]. As the compact is heated, typically to temperatures at least half of the absolute melting temperature, diffusion within and between particles leads to the formation of broad necks at the original contact points. The growth of necks between particles strengthens the material due to inter-particle bonding. As the sintering process continues, the open pores between particles gradually close, and may eventually be completely filled, resulting in a final strength and density approaching that of bulk material [13].

As studies of the theory behind sintering have progressed, a number of techniques have been developed to quantify the sintering process. The primary measure of sintering used in theoretical models is the neck size ratio, which is defined as the ratio of the neck diameter to the diameter of the particles themselves. Since direct measurement of neck size ratio, especially actively during sintering, is rather difficult, other methods to quantify sintering have been developed. Measurements of density, porosity, shrinkage, and surface area reduction are commonly used, along with measurements of electrical and mechanical properties in some cases. Shrinkage and surface area measurements are particularly useful, as they may be directly related to neck size ratio, and thus are the measurements most commonly used in sintering studies [13].

2.2.2 Sintering Mechanisms and Modeling

The driving factor behind sintering is the reduction of surface energy within the material. The large surface area present in the initial powder compact is gradually reduced as necks form and broaden between particles. Several distinct sintering mechanisms exist but the driving force is identical in each case. The sintering mechanisms may be broadly divided into two categories: surface transport mechanisms and bulk transport mechanisms. Both classes of mechanisms result in neck growth; however, surface transport mechanisms involve the movement of mass along particle surfaces without shrinkage while bulk transport mechanisms involve the movement of mass from within particles to the particle surface with shrinkage [13]. Figure 2-4 demonstrates the difference between surface transport and bulk transport, and shows the various individual mechanisms which contribute to each.

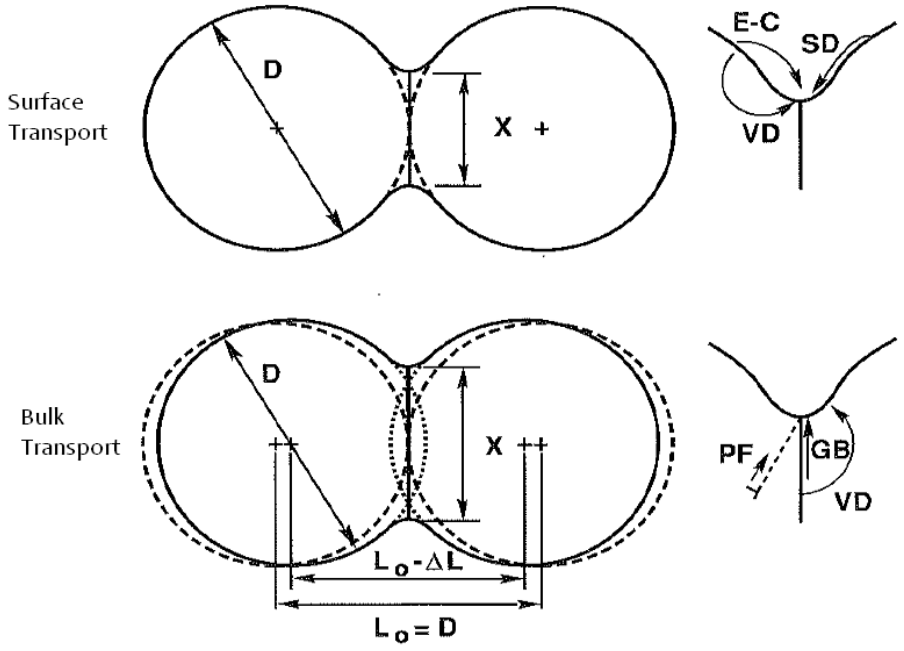

Figure 2-4: Visual representation of surface transport and bulk transport mechanisms, including evaporation-condensation (E-C), surface diffusion (SD), volume diffusion (VD), grain boundary diffusion (GB), and plastic flow (PF) [13].

Surface transport mechanisms include evaporation-condensation and surface diffusion. Evaporation-condensation occurs by the evaporation of surface atoms, transport across open pores, and finally condensation onto a surface. The overall effect of the evaporation-condensation process is the gradual transfer of mass from convex surfaces to concave surfaces, leading to increased necking without a corresponding increase in density. Evaporation-condensation is typically only important as a sintering mechanism at relatively high temperatures and for materials with high vapor pressure near their melting point [14]. Surface diffusion, the second surface transport mechanism, involves the transport of atoms across the free surfaces using surface defects such as kinks. Once again, although surface diffusion contributes to neck growth, it has no effect on density. The required temperature for significant surface diffusion is typically much lower than that of evaporation-condensation; thus, surface diffusion is a common contributor in many sintering processes [13].

Bulk transport mechanisms in sintering include volume diffusion, grain boundary diffusion, and plastic flow. Volume diffusion, which is also called lattice diffusion, is the motion of atoms within each particle by vacancy diffusion. Densification may occur during volume diffusion either by the annihilation of vacancies or by the motion of vacancies toward the boundaries between particles. As vacancies accumulate at particle intersections, layers of atoms between the particles are effectively removed, causing the particle centers to move closer together and broadening the neck between them [13]. Grain boundary diffusion occurs when mass is transported along grain boundaries to the growing bonds between particles. This process is coupled with surface diffusion, which serves to evenly distribute the material as it exits the grain boundary onto the open surface. Since grain boundary diffusion transfers mass from within the particles to the surface, it results in densification of the compact [4]. The final bulk transport

mechanism is plastic flow, in which densification occurs by the motion of dislocations. Plastic flow is inherently limited in its contribution to sintering, because it consumes dislocations as it progresses. Thus, the plastic flow mechanism is typically observed only during initial heating or under applied stress [13].

Theoretical models exist for the kinetics of sintering based on the various mechanisms for mass transport. These models relate the rate of sintering, as measured by neck diameter ratio, to the temperature, time, and particle size, as shown in Equation 2-1 [13].

$$\left(\frac{X}{D}\right)^n = \frac{B_0 \cdot t}{D^m} \cdot e^{\left(-Q/kT\right)} \qquad (2\text{-}1)$$

Where X is the average neck diameter, D is the average particle diameter, t is the isothermal sintering time, Q is the activation energy of the specific mechanism, k is Boltzmann's constant, T is the absolute temperature, B_0 is a constant dependent on mechanism and material properties, and n and m are integer constants dependent on the sintering mechanism. Since all sintering mechanisms result in neck growth, Equation 2-1 governs both surface and bulk transport mechanisms. Based on the assumption of isotropic sintering, shrinkage may be approximately related to average neck diameter as shown in Equation 2-2 [13].

$$\frac{\Delta L}{L} = \left(\frac{X}{2D}\right)^2 \qquad (2\text{-}2)$$

Where ΔL/L is the one-dimenstional sintering "strain" associated with isotropic shrinkage. If sintering is not isotropic, then this assumption will lead to a source of internal error as the

uniaxial shrinkage will no longer directly correspond to the degree of sintering. Based on this assumption, Equation 2-1 may be rewritten in terms of shrinkage as shown in Equation 2-3 [4].

$$\left(\frac{\Delta L}{L}\right)^{n/2} = \frac{B_0 \cdot t}{2^n \cdot D^m} \cdot e^{\left(-Q/kT\right)} \qquad (2\text{-}3)$$

Since Equation 2-3 uses shrinkage as its measure of sintering, it is only valid for modeling bulk transport mechanisms. The theoretical values of the integer constants *n* and *m* for each sintering mechanism are given in Table 2-1.

Table 2-1: Integer constants for various sintering mechanisms [13].

Mechanism	Form of Mass Transport	*n*	*m*
Plastic Flow	Bulk	2	1
Evaporation-condensation	Surface	3	2
Volume diffusion	Bulk	5	3
Grain boundary diffusion	Bulk	6	4
Surface diffusion	Surface	7	4

Although each mechanism has specific integer constants, actual experimental results typically show multiple sintering mechanisms over the course of the sintering process. As the relative effect of each mechanism varies, the actual observed values of *n* and *m* will shift gradually over time [13].

2.3 Hydride/Dehydride Processes

The study of uranium powder metallurgy in a laboratory setting necessitates a ready source of high purity, non-oxidized uranium powder. Due to the high susceptibility of uranium metal to oxidation, a hydride/dehydride process for uranium was previously established [3] and improved in this present work to effectively produce fine uranium powders in the quantities required for small scale laboratory research.

2.3.1 Uranium Hydride Formation

When heated to temperatures in excess of 150ºC uranium metal reacts reversibly with hydrogen gas to form UH_3 according to Equation 2-4 [5,15,16].

$$2\,U + 3\,H_2 \leftrightarrow 2\,UH_3 \qquad (2\text{-}4)$$

The density of UH_3 at 25°C is 10.9 g/cm^3, compared to a density of 19.04 g/cm^3 for uranium at 25°C [17]. The large decrease in density following conversion to UH_3 results in a correspondingly large increase in volume. As the reaction proceeds, hydrogen diffuses further into the uranium lattice, eventually causing small pieces of UH_3 powder to spall away from the remainder of the uranium. If the reaction is allowed to continue, it has to potential to fully convert bulk uranium samples into UH_3 powder [8].

The rate of formation of UH_3 depends predominantly on the temperature at which the reaction is performed, the partial pressure of hydrogen, and the presence of contaminants, such as oxygen, which may impede hydrogen diffusion. The temperature for which the hydriding reaction reaches a maximum rate depends somewhat on the partial pressure of hydrogen;

however, the maximum rate occurs at approximately 225°C [5,15]. The hydriding rate as a function of temperature under 580 mmHg of hydrogen is given in Figure 2-5, demonstrating a peak rate at ~225°C.

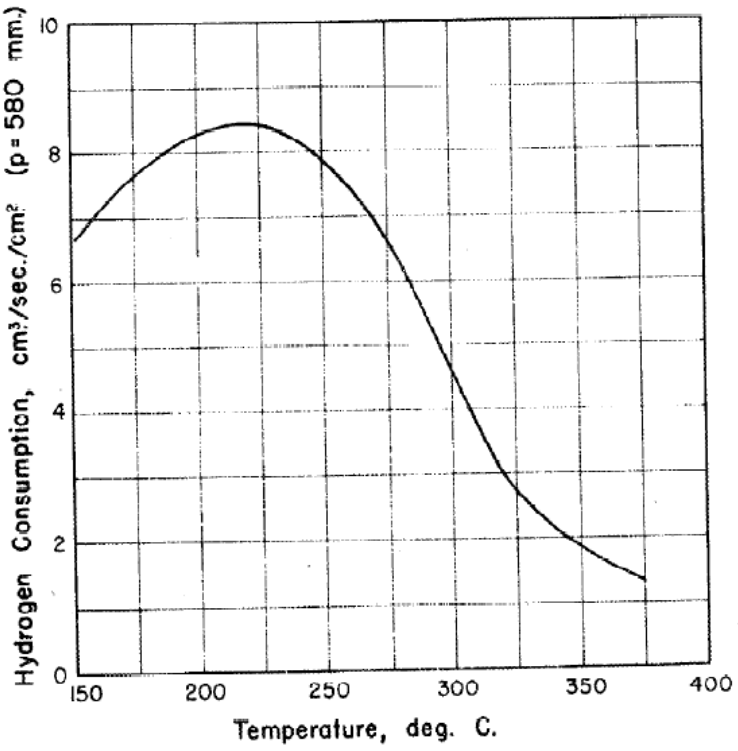

Figure 2-5: Uranium hydride rate of formation at constant pressure [11].

The third condition which strongly affects the rate of hydride formation is the presence of impediments to hydrogen diffusion, most commonly thin oxide films on the bulk uranium. At very low levels of oxygen contamination, a brief induction period may be observed before the hydride reaction commences. At higher levels of oxygen contamination, the oxide barrier to hydrogen diffusion may completely prevent the hydride formation reaction from proceeding [15].

2.3.2 Dehydriding of Uranium Hydride

Due to the reversible nature of the hydride forming reaction, the dehydride step may be performed by increasing temperature and lowering the partial pressure of hydrogen by establishing a rough vacuum [11]. The disassociation of hydrogen leaves behind a fine metal uranium powder, which may then be used for the desired application.

Compared to the hydride process, the dehydride process occurs relatively rapidly. The rate of hydrogen dissociation increases with increasing temperature and lowered hydrogen pressure, reaching a significant rate at temperatures above 300ºC when under vacuum [11]. Although the dehydriding rate may be increased by further increasing temperature, loose sintering of the uranium powder increases with temperature. Thus, if the dehydriding temperature is too high, significant undesired sintering may occur. The rate of hydrogen dissociation as a function of temperature and hydrogen pressure is shown in Figure 2-6.

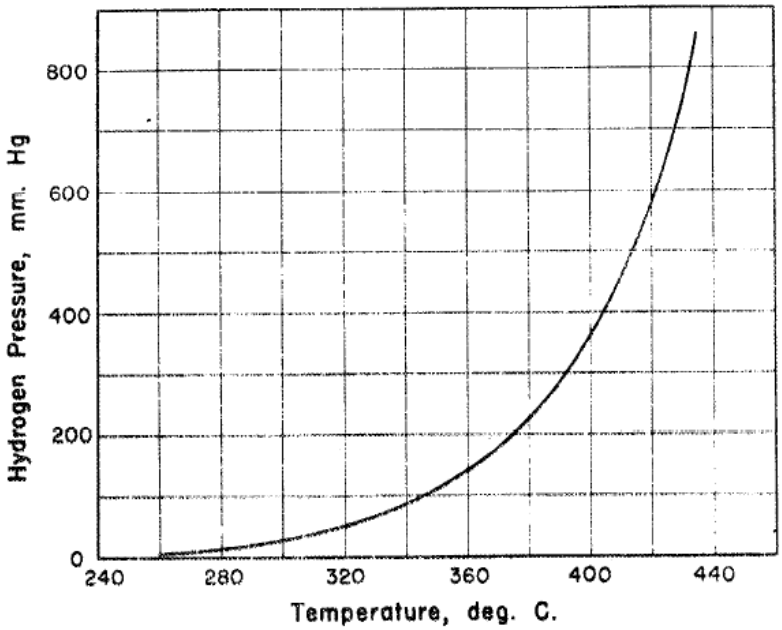

Figure 2-6: Dehydriding rate as a function of temperature and pressure [11].

3. EXPERIMENTAL DESIGN AND PROCEDURES

This section describes the equipment and experimental procedures used in the production of DU powder (3.1), the fabrication of pellets (3.2), the sintering of pellets (3.3), and pellet imaging (3.4). Due to extreme sensitivity to oxygen contamination, the majority procedures performed in this project took place within a large inert atmosphere glovebox with atmosphere recirculation and purification capabilities and a heated furnace well for controlled atmosphere thermal processing. The glovebox is shown in Figure 3-1.

Figure 3-1: Large inert atmosphere glovebox used for handling of pyrophoric uranium powder.

3.1 DU Powder Production

Due to the speed and ease with which uranium metal powder oxidizes, it was necessary to produce uranium metal powder for each test shortly before use within the glovebox shown in Fig. 3-1. Uranium metal coupons, supplied by the Y-12 plant at Oak Ridge National Laboratory, were converted to powder using a uranium hydride/dehydride process, as described in the background section. To increase the volume of powder produced by this process, a specialized set of equipment was designed and developed. The initial system was created by Garnetti [3]; however, modifications and improvements were made.

3.1.1 Acid Washing DU

The hydride formation reaction in Eq. 2-4 is completely inhibited by the presence of surface layers of oxidized uranium. The uranium coupons used for this research were received with oxidized surfaces. The acid washing procedure described here was implemented to remove the majority of this oxide layer, but a very thin oxide film was always present on the metal pieces.

It was determined that the acid wash station should be operated under an inert argon gas atmosphere to minimize re-oxidation of the uranium coupons during and after acid washing. However, it is not possible to perform this water-based operation inside of the inert atmosphere glovebox since the acidic aqueous solution would evaporate rapidly, contaminate the dry atmosphere and degrade the performance of the glovebox purification system. Therefore, the wet chemistry operations were established inside of an the argon-filled glovebag system, as shown in Figure 3-2.

Figure 3-2: Glovebag acid wash station.

The acid washing procedure began with immersion of DU coupons in a beaker containing 25% by volume nitric acid. Light bubbling from the DU was immediately apparent and as the reaction progressed the solution turned light yellow. Visual inspection was used to determine when the oxide layer had been removed, as the coupon changed from dark black when oxidized to a dull gray when clean. Typically the oxide layer would be entirely removed within 5-10 minutes.

Following acid washing, the DU coupons were rinsed with deionized water and then ethanol to clean the surface. The ethanol was allowed to evaporate from the surface before returning the washed DU coupons to the large argon glovebox for hydriding. Due to the potentially volatile result of mixing nitric acid with ethanol, the acid washing station was divided into an aqueous section and an organic section. Strict separation was maintained between the sections to preclude the possibility of an acid-ethanol reaction.

3.1.2 Hydride/Dehydride Process

The hydride/dehydride processing system was designed to be inserted into a 5.08cm (2in) diameter furnace well (Fig. 3-3) located below the large argon atmosphere glovebox and to provide a sealed controllable atmosphere during operation.

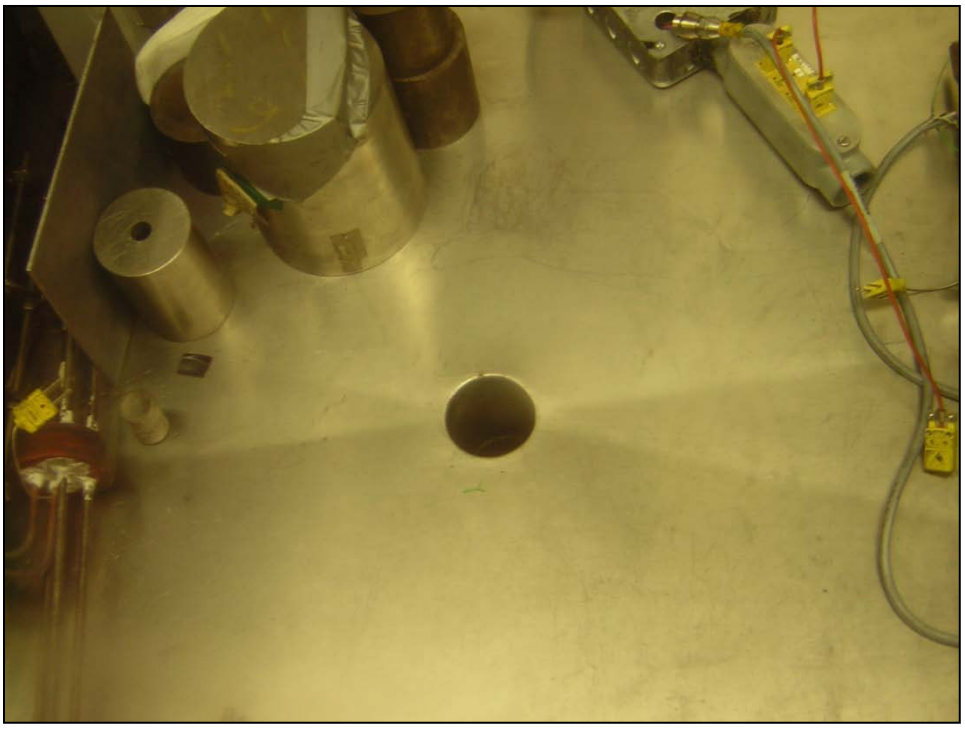

Figure 3-3: Inert atmosphere glovebox furnace well used for powder production and sintering.

The hydride/dehydride well insert (Fig. 3-4) was constructed from three 0.635cm (0.25-in) diameter 316 stainless steel rods with five 304 stainless steel heat shields along their length. A rubber plug was fitted to the top of the steel rods to provide a seal at the top of the furnace. Copper tubing inlet and outlet gas lines (0.635cm dia.) were inserted through the plug, with the inlet line continuing down the full length of the system and the outlet extending only a small amount through the plug. This design produced steady process gas flow through the entire

system. A large yttria crucible was suspended from the bottom of the well insert as the reaction vessel. A fitted piece of coarse stainless steel mesh separated the top and bottom halves of the crucible, allowing solid DU to be positioned in the upper half of the crucible while DU powder fell through to the bottom half as it was produced. Figure 3-5 shows the crucible loaded with several DU coupons before the hydride/dehydride process.

Figure 3-4: Hydride/dehydride well insert used for uranium powder production.

Figure 3-5: DU coupons loaded into yttria crucible for hydriding.

The inlet line of the hydride/dehydride well insert was connected to an Ar-5%H_2 tank with moisture and oxygen traps in line to reduce oxygen contamination. This system delivered the process gas with less than 1 ppm oxygen. The outlet line of the hyrdride/dehydride well insert was connected to an oil bubbler to prevent backflow into the system from the outside atmosphere. The valve system on the outlet line allowed connection to a vacuum pump for evacuation of the furnace well.

The hydride formation reaction was initiated by positioning the loaded hydride/dehydride rig into the glovebox furnace well such that the chamber is sealed from the glovebox atmosphere. The seal formed by the rubber plug at the top of the hydride/dehydride rig was established by a static load distributed on the plug using steel plate with several heavy weights. The furnace well was brought to rough vacuum using the outlet line, then backfilled with Ar-5%H_2 to a gauge pressure of 30 to 50 kpa and a controlled flow rate of 1.4 to 2.4 L/min was established. Once the

system atmosphere was established, the well was heated to 235°C, using a Barnstead 21100 Tube Furnace with attached Eurotherm 211 controller (Fig. 3-6). The temperature and gas flow conditions were maintained for approximately 24 hours to complete the hydriding formation process.

Figure 3-6: Furnace used for hydride/dehydride process.

The dehydride step was initiated immediately following the hydride step. Gas flow through the inlet line was shutoff and the outlet line was used to bring the furnace well to a rough vacuum. The temperature of the furnace was then increased to 325°C. The dehydriding process was observed by monitoring the increase in pressure caused by hydrogen release from the UH_3.

Dehydriding was continued until the pressure reading indicated all hydrogen had been removed from the sample; this was typically accomplished in approximately 30 minutes.

The system was allowed to cool to room temperature following dehydriding before the hydride/dehydride rig was removed. After removal, the DU within the yttria crucible was divided into two portions: 1) solid DU chunks coated with a layer of DU powder resting on the wire mesh and 2) fine DU powder that had fallen through the wire mesh. The powders above and below were normally partially sintered and loose agglomerates of powder were observed. Images of the loosely sintered coupons from atop the wire mesh and the loose powder from below are shown in Figure 3-7 and Figure 3-8 respectively. The large remnant chunks were gently shaken to remove any remaining loose powder and set aside for use in the next powder production run. A typical uranium slug would be fully consumed after three runs. The DU powder which had fallen through the wire mesh was collected and any agglomerates were broken up by light grinding with a steel mortar and pestle. The yttria crucible could be loaded with approximately 80 grams of DU coupons and approximately half of the loaded DU was typically converted into powder each run, resulting in an output of approximately 40 grams of powder per hydride/dehydride run.

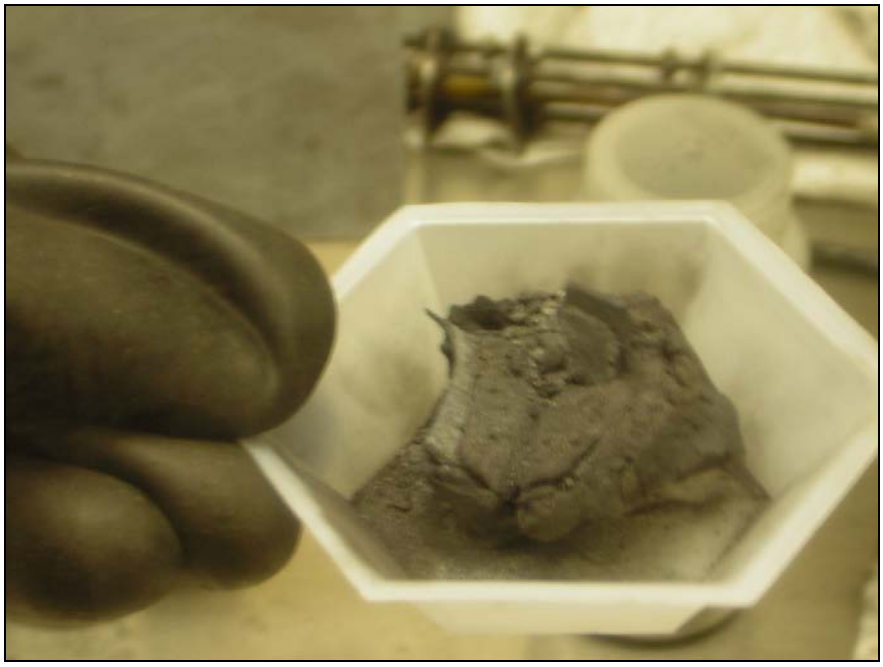

Figure 3-7: Loosely sintering DU coupons coated in powder following dehydriding.

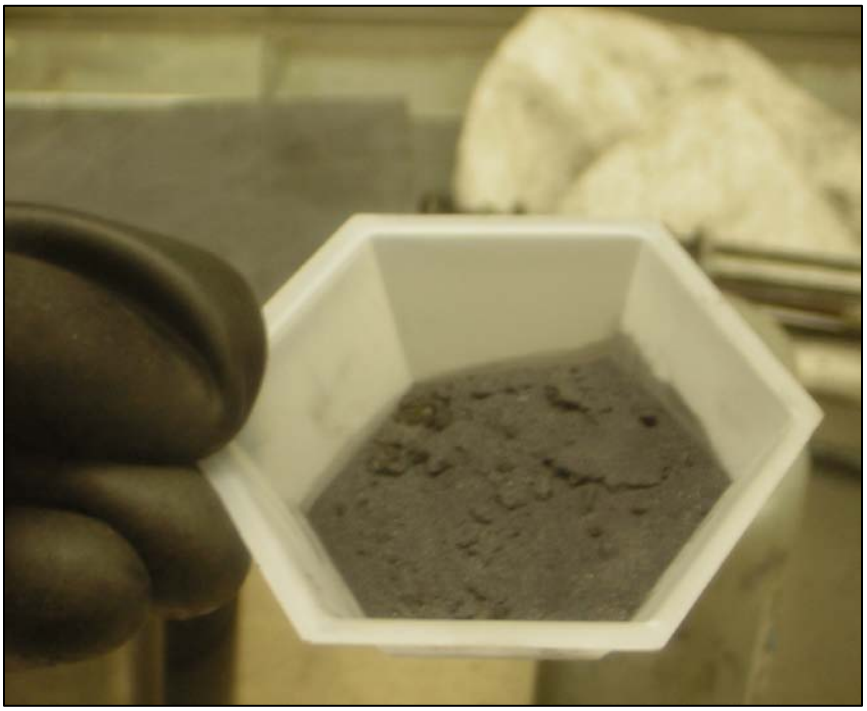

Figure 3-8: DU powder produced by the hydride/dehydride process.

3.1.3 Powder Characterization

The powder produced by the hydride/dehydride process was characterized using optical microscopy. To allow transport of pyrophoric DU powder outside the inert atmosphere glovebox, and Atmospheric Containment Vessel (ACV) was constructed. The ACV, shown in Figure 3-9, consisted of a 1.8 (0.75 in) cm tall, 6.35 cm (2.5 in) diameter nipple with a flange on either side. The top flange had a quartz viewing crystal built in to allow for imaging of powder within the ACV.

Figure 3-9: Atmospheric Containment Vessel (ACV) used for powder transfer.

The ACV was loaded with DU powder within the large inert atmosphere glovebox. The amount of powder used was very small, as it was desired that each particle be isolated from the others. Once loaded, the ACV was sealed and removed from the glovebox for imaging with a Hirox KH-1300 Digital Microscope, shown in Figure 3-10. Images from multiple powder

production runs at 800x magnification were used with ImageJ grayscale analysis to determine the size distribution of particles.

Figure 3-10: Hirox KH-1300 Digital Microscope used for powder imaging.

3.2 Pellet Fabrication

This section reviews the essential steps in converting DU powder into complete sample pellets, including mixing in additive powders (3.2.1), pressing powders into compacts (3.2.2), and sintering green compacts into solid pellets (3.2.3). All processes described in this section were performed in the large inert atmosphere glovebox.

3.2.1 Mixing Powders

For pellets containing zirconium in addition to DU, mixing of the powders was the first step in pellet formation. The DU powder used was produced by a hydride/dehydride process as

described in Section 3.1. The zirconium powder used was 99.7% pure and 325 mesh, supplied by Cerac Inc. Specialty Inorganics.

The mixing procedure started by weighing the DU powder in a small glass jar on a Mettler Toledo AL204 scale, accurate to +/- 0.0005g. A calculation was then performed to determine the total weight which was required to obtain a given weight percent of additives. The additive powders were slowly added to the glass jar while still on the scale, until the appropriate total weight was achieved.

Once all desired powders had been combined, the lid was securely fastened to the glass jar. The jar was shaken with irregular motions for at least ten minutes to ensure thorough homogenization of all constituents.

3.2.2 Compact Pressing

A dual-action punch and die was used to convert loose powder into compacts. The die was fabricated from 303 stainless steel and had a diameter of 0.95 cm (0.375 in). The punches were fabricated from H13 tool steel and were incrementally turned down until they just fit through the die. The punches were heat treated to increase their hardness and prevent bending under pressure.

Powder was loaded into the die by pouring through a funnel while the bottom punch was in place, as shown in Figure 3-11. Once the powder had been loaded, the top punch was inserted. The punch and die were then inserted into a hydraulic Carver Laboratory Press Model C, as shown in Figure 3-12. The compacts were pressed with a load of 44.5 kN (10,000 lbf) for a period of 15 seconds, equating to a pressure of 624,000 MPa.

Figure 3-11: Loading powder into dual-action punch and die for compaction.

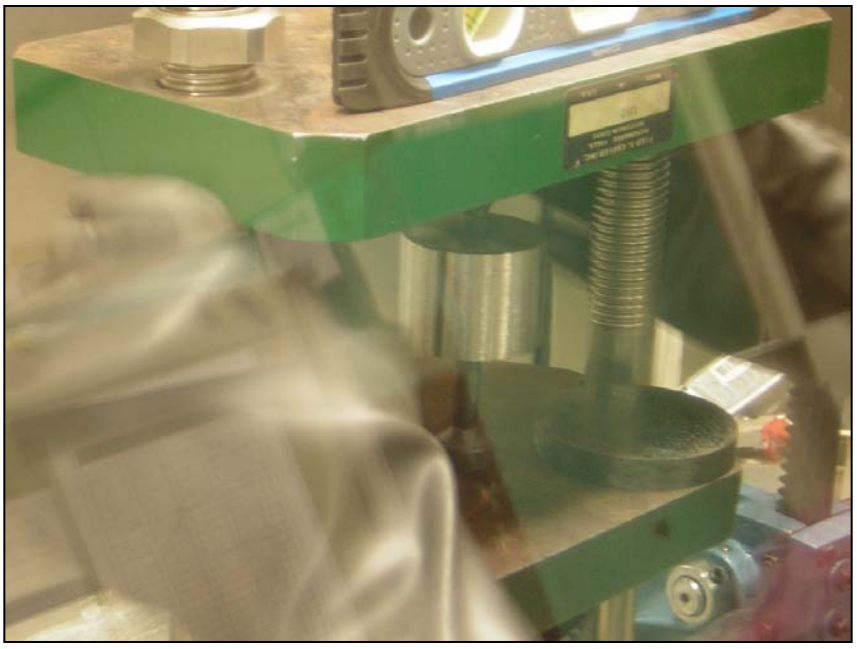

Figure 3-12: Pressing powder compact using hydraulic press.

Following pressing, compacts were removed and pre-sintering measurements of weight, height, and diameter were taken. Five measurements of each value were taken to provide an accurate average result.

3.2.3 Pellet Sintering

The sintering apparatus used in this research was similar to the hydride/dehydride rig described in Section 3.1. The body of the sintering apparatus consisted of three 316 stainless steel rods held together by a series of 304 stainless steel heat shields. The top of the sintering apparatus was a large disk, broad enough to overlap the furnace well opening and suspend the entire apparatus. Powder compacts to be sintered were loaded into a small yttria crucible, which fit into a small cup at the bottom of the sintering apparatus. Figure 3-13 provides an image of the sintering apparatus.

.

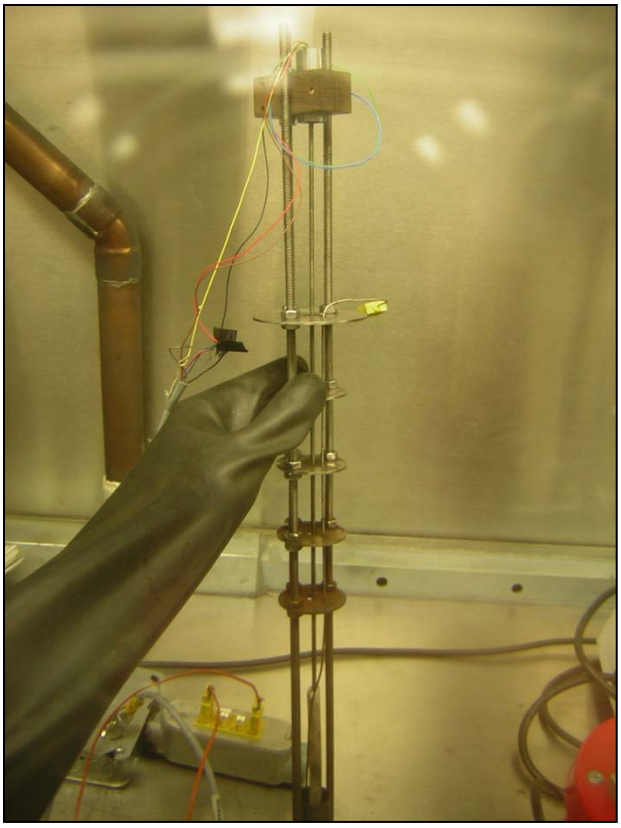

Figure 3-13: Photograph of the sintering apparatus showing LVDT at top and sample holder at bottom.

In situ measurements of the sintering process were provided by a thermocouple inserted into the yttria crucible and a Linear Variable Differential Transformer (LVDT). The magnet within the LVDT was coupled to the sintering pellet by means of a long steel rod which sat on the top of the pellet. As shrinkage occurred in the pellet due to sintering, the rod and magnet shifted in the LVDT sleeve, providing an electrical output. A yttria sleeve was added to the bottom end of the rod to prevent contact, and possible interactions, between the pellet and the steel rod. Both the LVDT and the thermocouple outputs were processed using a National Instruments USB-6210 system, which in turn output to Labview SignalExpress.

Once compacts were loaded into the sintering apparatus, they were heated to temperature in the same furnace well used for the hydride/dehydride process in Section 3.1. Several forms of temperature profiles were used to provide multiple perspectives on the sintering process. Some pellets were sintered isothermally at temperatures in the α-phase of uranium, then sintered isothermally at temperatures in the γ-phase of uranium. Some pellets were sintered exclusively in the α-phase of uranium. Finally, some pellets were sintering with cyclic temperature changes to induce internal stresses, promoting plastic deformation.

After sintering was complete, the measurements performed before sintering to determine height, diameter, and mass of the pellet were repeated. Once again, each measurement was made five times to provide an accurate average.

3.3 Pellet Imaging

After sintering, pellets were sectioned, polished, and SEM imaged. Pellets were sectioned axially using a LECO VC-50 Diamond saw. The pellet samples were then mounted in epoxy with the freshly sectioned face exposed. A Buehler Minimet-1000 was used to polish the exposed face of each pellet, starting with coarse 400 grit abrasive paper and finishing with 1 micron diamond paste.

After polishing was complete, pellets were imaged using a Cameca SX50 Electron Microprobe equipped with a PGT Energy Dispersive X-ray (EDS) system. In addition to traditional SEM images, the EDS system was used to identify the elemental compositions of various phases which were observed.

3.4 Sintering Calculations

The ultimate goal of the experiments performed was to quantify the sintering rates and mechanism by identifying the constants associate with the German model presented in Eq. 2-3 . To accomplish this goal, basic calculations and analyses of the raw data were required. The equations used to model sintering rates are described in Section 2.1.3. During isothermal sintering, the exponential term becomes constant, simplifying Equation 2-3 to Equation 3-1.

$$\frac{\Delta L}{L} = C \cdot t^{2/n} \tag{3-1}$$

Equation 3-1 may be further simplified for modeling by taking the logarithm of each side, producing Equation 3-2.

$$Ln\left(\frac{\Delta L}{L}\right) = Ln(C) + \frac{2}{n} Ln(t) \tag{3-2}$$

In this form, *n* may be easily calculated by finding the slope of a log-log plot of shrinkage versus time. This method was applied to each pellet which was isothermally sintered. An initial guess for the isothermal sintering starting time was determined by the approximate point at which temperature stabilized for each pellet. This starting time was then modified slightly in each direction to determine the point at which the greatest degree of linearity occurred in the log-log plot of shrinkage vs. time. The validity of this technique is demonstrated by the divergence from linearity to a curve if the starting time of the model is shifted forward or backward.

Once *n* was determined for several pellets of the same composition at different isothermal sintering temperatures, the data from the pellets was combined to form an Arrhenius plot. Once

again starting from Equation 2-3, if time is set to be constant across multiple temperatures, Equation 3-3 results.

$$\frac{\Delta L}{L} = C \cdot \left[\exp\left(-{}^{Q}/_{kT}\right)\right]^{2/n} \tag{3-3}$$

In a similar fashion to Equation 3-1, taking the logarithm of both sides of Equation 3-3 results in a form which is much simpler to analyze, as shown in Equation 3-4.

$$Ln\left(\frac{\Delta L}{L}\right) = Ln(C) - \frac{2 \cdot Q}{n \cdot k} \cdot \frac{1}{T} \tag{3-4}$$

Based on Equation 3-4, *Q* for the process may be determined from the slope of a plot of the logarithm of shrinkage at a specific time versus inverse temperature, if *n* is already known. The key to this analysis was the selection of the specific sintering time to use. Since the greatest variation typically occurred during the initial and final stages of sintering, the times selected were from the middle stage.

4. RESULTS

This section describes the characterization of uranium powder produced by the hydride/dehydride process (4.1) and the sintering of uranium and uranium alloys under various conditions (4.2).

4.1 Uranium Powder Characterization

Images of uranium powder generated by the hydride/dehydride process were taken using a Hirox KH-1300 Digital Microscope and analyzed using ImageJ software. The images used were taken at 800x magnification. Images containing a total of nearly 6000 particles were used, taken from powder samples from three separate hydride/dehydride runs. These images consistently showed that the powder consisted of many small particles with some larger particles and aggregates. The individual particles were irregularly shaped with rough surfaces. An example image showing these characteristics is given in Figure 4-1.

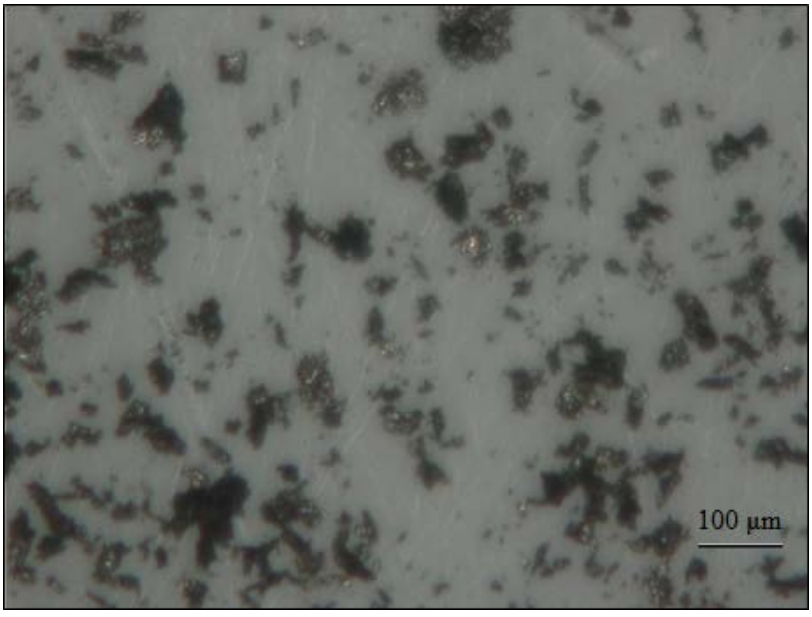

Figure 4-1: Image of uranium powder produced by hydride/dehydride process.

The particle size distribution, as shown in Figure 4-2, was determined in terms of both number density and volume density, based on a simplifying assumption of approximately spherical particles.

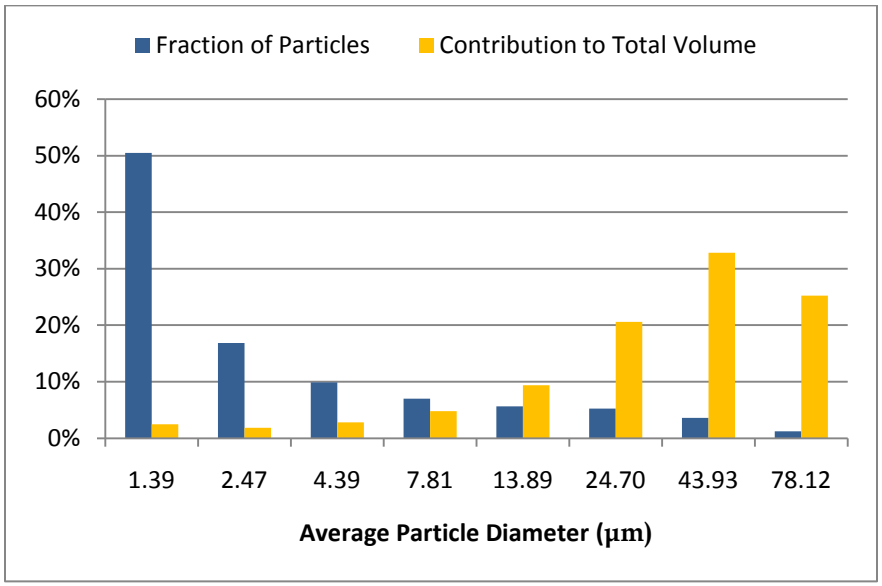

Figure 4-2: Size distribution of uranium powder produced via hydride/dehydride process.

4.2 Uranium and Uranium Alloy Sintering

The pressed uranium pellets were sintered under a wide variety of conditions. Variations in zirconium content, sintering temperature, and temperature profile were used to analyze the sintering process.

4.2.1 Isothermal Sintering of Uranium

The first set of sintering experiments performed used pure uranium pellets with isothermal sintering temperatures. Each pellet was sintered for several hours in the alpha phase, then for several hours in the gamma phase. A total of eight pellets were manufactured, with five

successful sintering runs. A description of each pellet and its sintering conditions is given in Table 4-1.

Table 4-1: Summary of isothermally sintered uranium pellets.

Pellet #	Powder Source	Contents	α-Temperature	γ-Temperature	Green Density	Sintered Density
1	H/dH Run 1	DU	630 °C	N/A	N/A	N/A
2	H/dH Run 1	DU	N/A	N/A	N/A	N/A
3	H/dH Run 2	DU	655 °C	N/A	N/A	N/A
4	H/dH Run 2	DU	655 °C	831 °C	53.95%	57.87%
5	H/dH Run 3	DU	643 °C	820 °C	47.21%	49.88%
6	H/dH Run 3	DU	634 °C	809 °C	46.68%	50.46%
7	H/dH Run 3	DU	659 °C	834 °C	47.17%	51.22%
8	H/dH Run 3	DU	651 °C	826 °C	48.20%	51.97%

Pellet 1 was pressed with a force of 66.8 kN (15,000 lbs), corresponding to 936,000 MPa. The press was raised to this force a total of eight times, and each time the pressure was allowed to bleed naturally. Upon removal from the die, several small pieces of the pellet chipped off one of the faces, indicating excessive stresses within the pellet and possible binding to the inner walls of the die. In spite of this, the pellet was sintered at 630ºC for 24 hours. The LVDT output showed no signs of sintering.

Pellet 2 was pressed with a sustained force of 44.5 kN (10,000 lbs), corresponding to 624,000 MPa, for 30 minutes. Significant portions of the pellet crumbled upon removal from the die, even more so than Pellet 1. Due to the lack of success in sintering Pellet 1, no attempt was made to sinter Pellet 2.

Pellet 3 was pressed with a force of 44.5 kN (10,000 lbs), corresponding to 624,000 MPa, for 15 seconds, after which the pressure was allowed to bleed off naturally. The pellet did not

crumble upon removal from the die; therefore, this pressing regime was used for all future pellets. An image of Pellet 3 as pressed is shown in Figure 4-3. Pellet 3 was sintered at 655ºC for 24 hours; however, shrinkage was only observed during temperature ramping from 300ºC up to the isothermal hold temperature. The lack of isothermal sintering in Pellet 3 was attributed to the source powder used. Pellet 3 was comprised entirely of powder which had loosely sintered during the dehydride process. These chunks were broken and ground with a steel mortar and pestle, then mechanically agitated in a small steel vial with a steel ball bearing; however, the resulting particle size was still likely larger than that of the loose powder. Due to this, all future pellets were fabricated using only the loose powder.

A red powder was observed on the top of the pellet after sintering, as shown in Figure 4-4. This powder was likely an iron-bearing reaction product generated by hot contact between the steel LVDT rod and the sample. All subsequent sintering experiments were performed with a ceramic sleeve over the LVDT rod to prevent this.

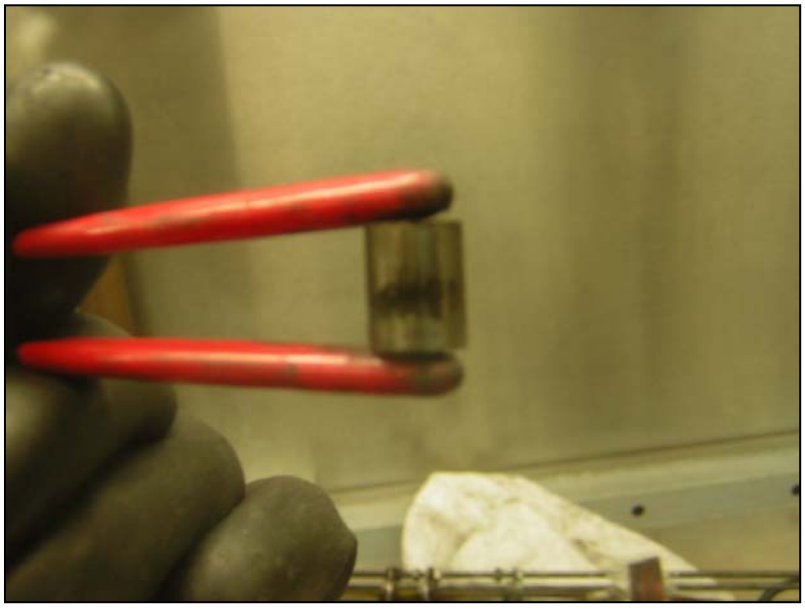

Figure 4-3: Pellet 3 as pressed, before sintering.

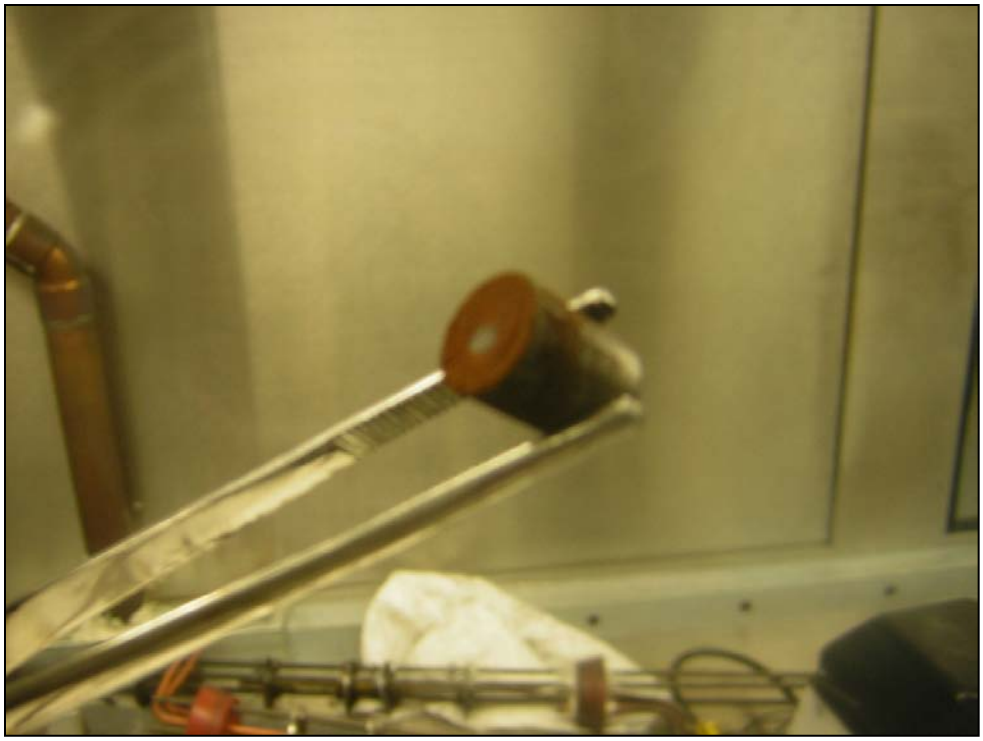

Figure 4-4: Pellet 3 after sintering, with red U-Fe powder formation.

Pellet 4 was the first fully successful isothermal sintering experiment performed. Like Pellet 3 and all following pellets, Pellet 4 was pressed with a force of 44.5 kN (10,000 lbs), corresponding to 624,000 MPa, for 15 seconds, after which the pressure was allowed to bleed off naturally. Pellet 4 was sintered for 4 hours at 655ºC (α-phase), then for 11 hours at 831ºC (γ-phase). A ramp rate of 5ºC/min was used during heating, and a rate of 2ºC/min was used during cooling. An Image of Pellet 4 after sintering is given in Figure 4-5. The light blue coating on the side of the pellet after sintering was likely due to the presence of trace contaminants in the system.

Figure 4-5: Pellet 4 after sintering.

The LVDT data for Pellet 4 exhibited an initial shrinkage during heating similar to that observed for Pellet 3. However, sustained shrinkage was observed at the each of the isothermal holding temperatures. The measured shrinkage (based on LVDT data) for Pellet 4 and the associated temperature profile of the experiment are given in Figure 4-6. The density of Pellet 4 increased during sintering from a green density of 54.0% T.D. to a final density of 58% T.D. This is a relatively small increase, but it should be noted that sintering metals at relatively low temperatures will typically produce low density products. It was noted that densities of 90% T.D. are not normally realized when sintering metal powders below ~90% of the absolute meting temperature [14].

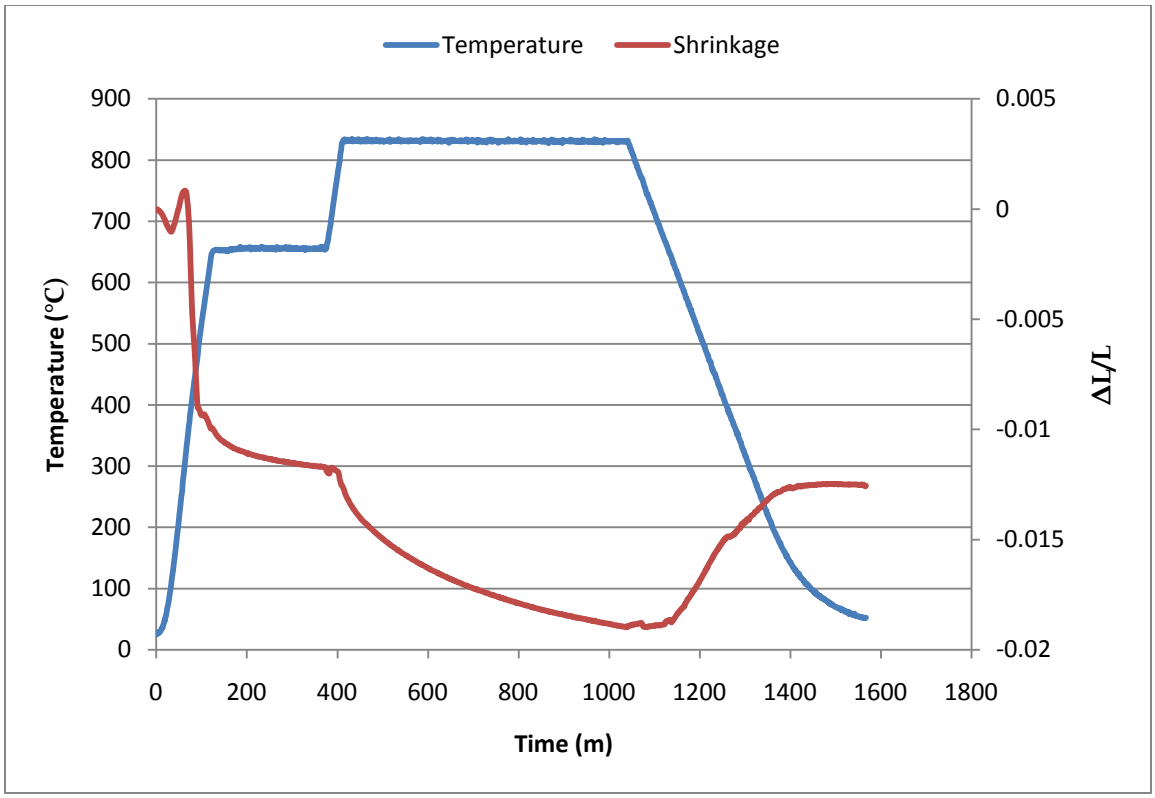

Figure 4-6: Shrinkage and temperature profile for Pellet 4.

Pellet 5 was pressed, using the method described for Pellets 4 and 5, to 47%TD, and was sintered for 6 hours at 643ºC(-phase), then for 8 hours at 820ºC(-phase). A ramp rate of 5ºC/min was used during heating, and a rate of 1ºC/min was used during cooling. An image of Pellet 5 after sintering is given in Figure 4-8. As can be seen in Figure 4-7, a crumbling black layer ~1mm thick formed on the top of Pellet 5 during sintering, and a black powder formed on the sides. This powder was most likely oxidized uranium, formed by leeching oxygen from the ceramic sleeve which held the LVDT rod on top of the pellet.

Figure 4-7: Pellet 5 after sintering.

Due to a technical malfunction, LVDT data for a portion of the heating period for Pellet 5 was not recorded; however, the increase in shrinkage before and after heating was consistent with what had previously been observed in Pellets 3 and 4. Sustained shrinkage was observed at both isothermal holding temperatures. The slight expansion observed near the end of the second sintering step was likely due to expansion by oxide formation on the top of the pellet. The measured shrinkage and temperature profile for Pellet 5 are given in Figure 4-8. The density of Pellet 5 increased during sintering from 47%TD to 50%TD.

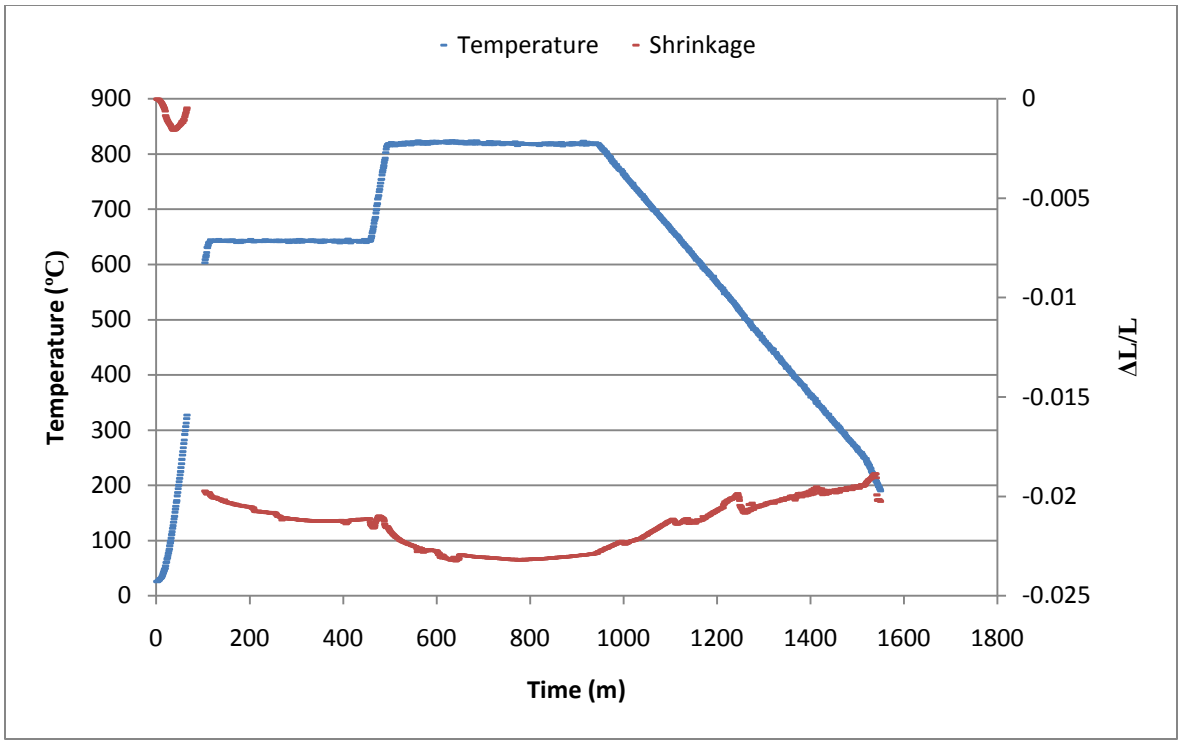

Figure 4-8: Shrinkage and temperature profile for Pellet 5.

Pellet 6 was pressed to 47%TD, and sintered for 8 hours at 634ºC(-phase), then 8 hours at 809ºC (γ-phase). A ramp rate of 5ºC/min was used during heating, and a rate of 1.5ºC/min was used during cooling. Images of Pellet 6 before and after sintering are given in Figure 4-9 and Figure 4-10 respectively. As can be seen in Figure 4-10, a black oxide layer was once again formed on the top of the pellet. In addition, a portion of this layer was orange tinted, indicated possible contamination with iron.

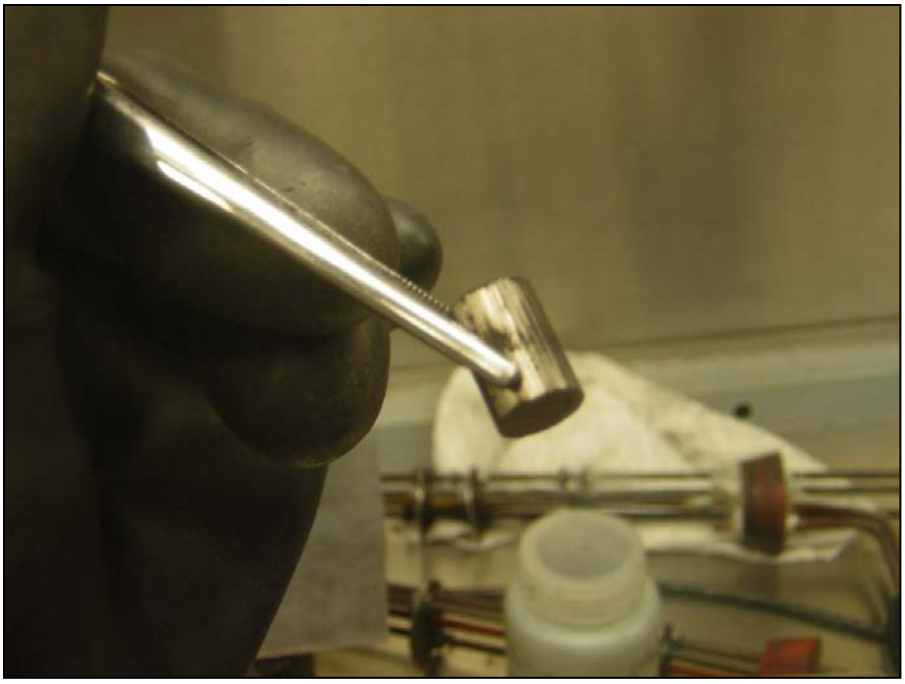

Figure 4-9: Pellet 6 as pressed, before sintering.

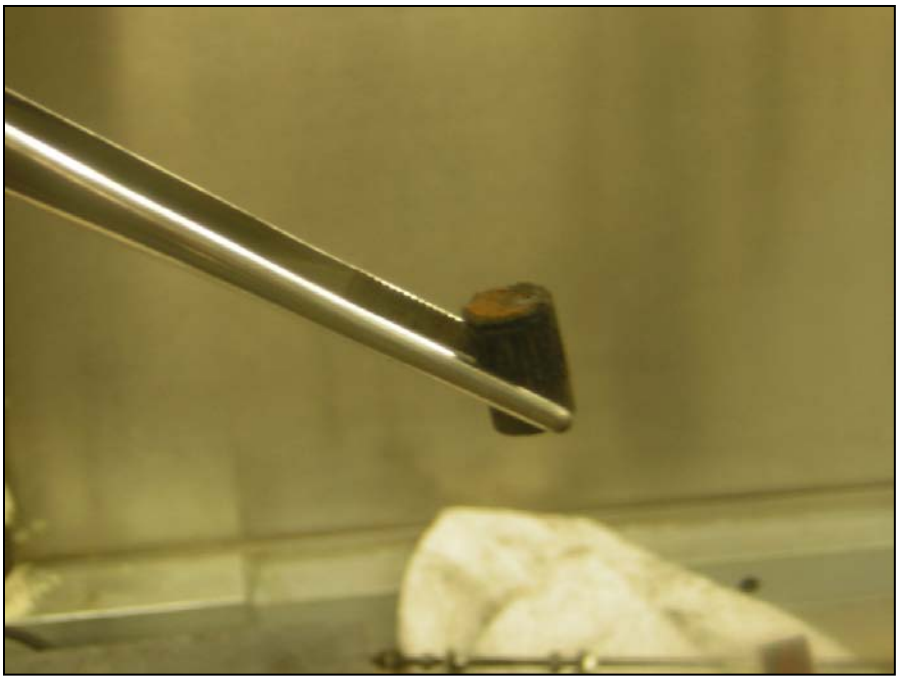

Figure 4-10: Pellet 6 after sintering.

The LVDT data for Pellet 6 showed familiar features from previous pellets. Strong initial shrinkage during heating, gradual shrinkage during isothermal sintering, and eventual expansion due to oxide formation. The measured shrinkage and temperature profile for Pellet 6 are given in Figure 4-11. The density of Pellet 6 increased during sintering from 47%TD to 50%TD.

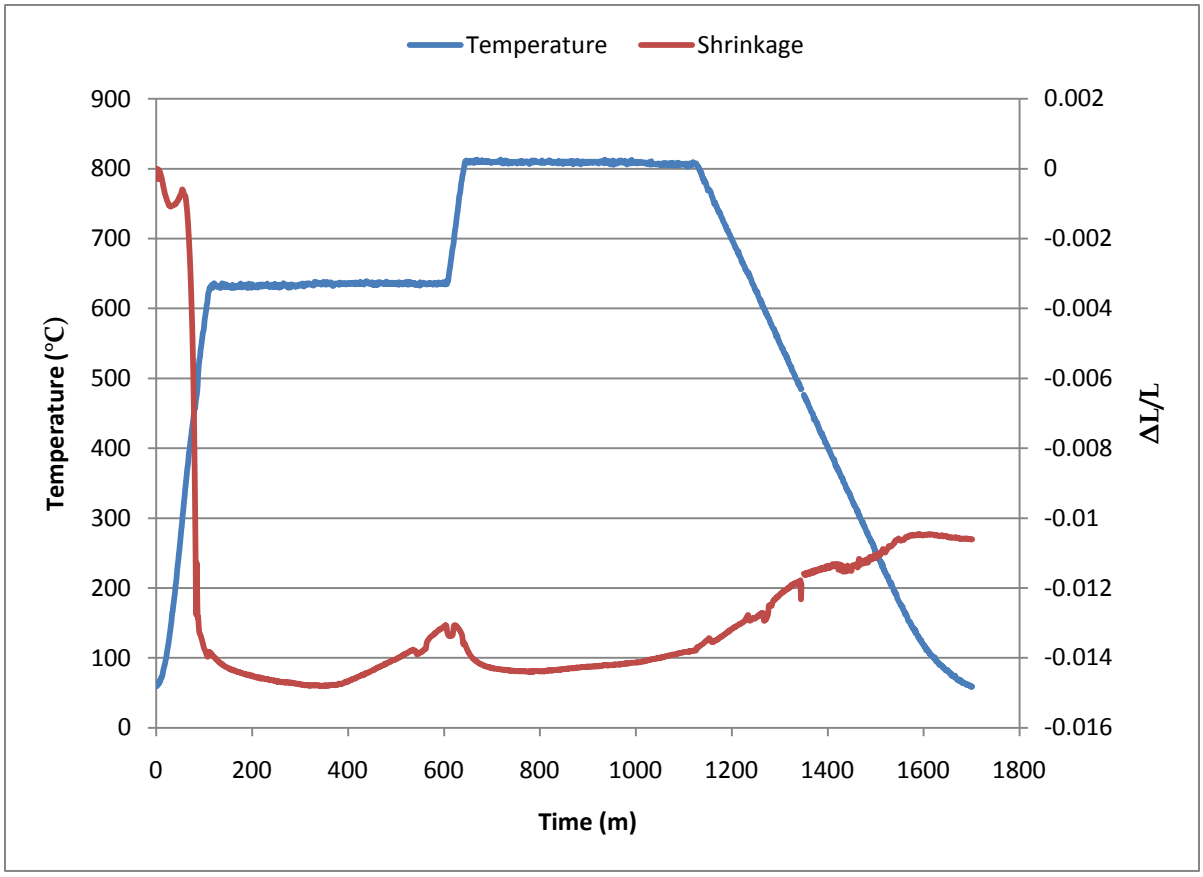

Figure 4-11: Shrinkage and temperature profile for Pellet 6.

Pellet 7 was pressed to 47%TD, and sintered for 9 hours at 659ºC(-phase), then 8 hours at 834ºC (γ-phase). A ramp rate of 5ºC/min was used during heating, and a rate of 1.5ºC/min was used during cooling. An image of Pellet 7 after sintering are given in Figure 4-12. As can be

seen in Figure 4-12, an oxide coating formed once again on the top and sides of the pellet; however, the thickness of the coating was much less severe.

Figure 4-12: Pellet 7 after sintering.

LVDT data for Pellet 7 showed initial shrinkage during heating and gradual shrinkage during isothermal sintering; however, expansion due to oxide formation was not observed. This was reasonable, given the limited degree of oxide formation seen in Figure 4-12. The measured shrinkage and temperature profile for Pellet 7 are given in Figure 4-13. The density of Pellet 7 increased during sintering from 47%TD to 51%TD.

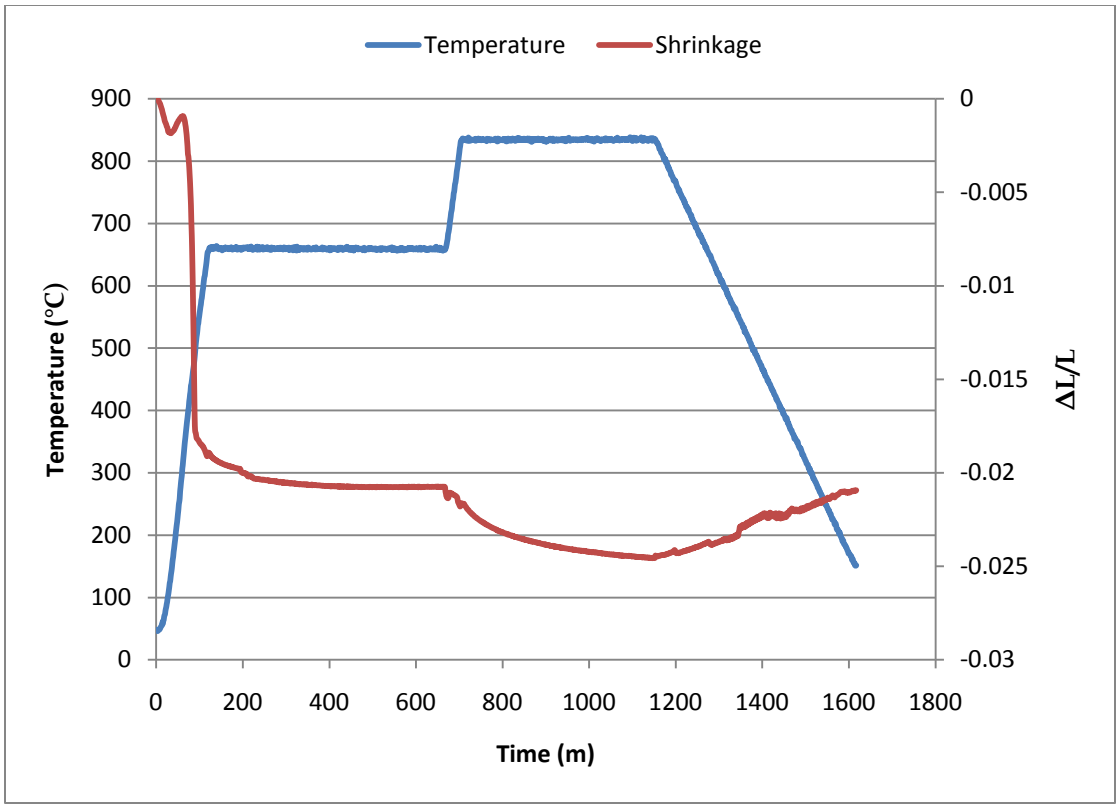

Figure 4-13: Shrinkage and temperature profile for Pellet 7.

Pellet 8 was pressed to 48%TD, and sintered for 8 hours at 651ºC (α -phase), then 7 hours at 826ºC (γ-phase). A ramp rate of 5ºC/min was used during heating, and a rate of 1.5ºC/min was used during cooling. An image of Pellet 8 after sintering is given in Figure 4-14. Similar to Pellet 7, Pellet 8 formed a light oxide powder coating on the top and sides of the pellet during sintering, as can be seen in Figure 4-14.

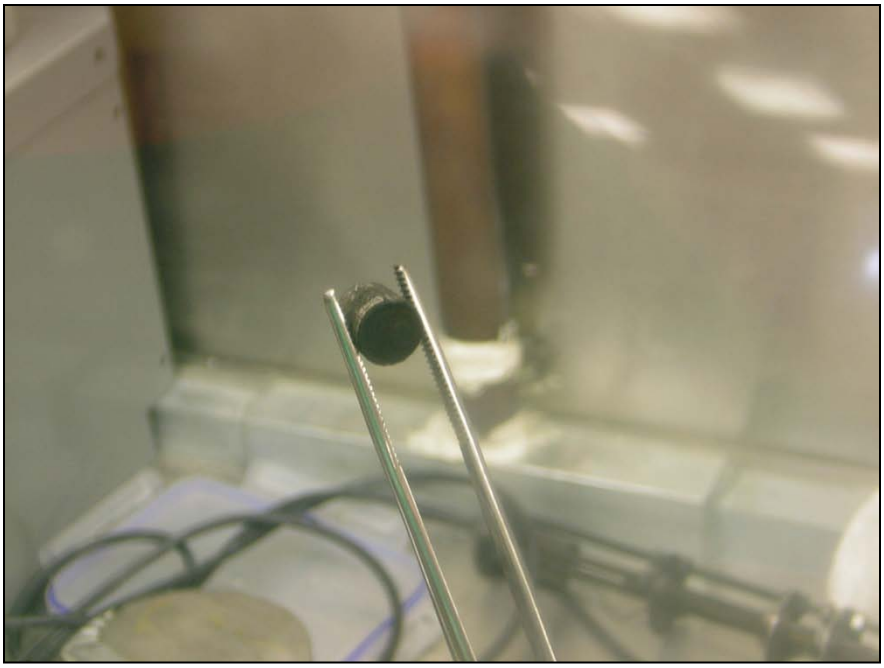

Figure 4-14: Pellet 8 after sintering.

LVDT data for Pellet 8 showed initial shrinkage during heating and gradual shrinkage during isothermal sintering. The measured shrinkage and temperature profile for Pellet 8 are given in Figure 4-15. The density of Pellet 8 increased during sintering from 48%TD to 52%TD.

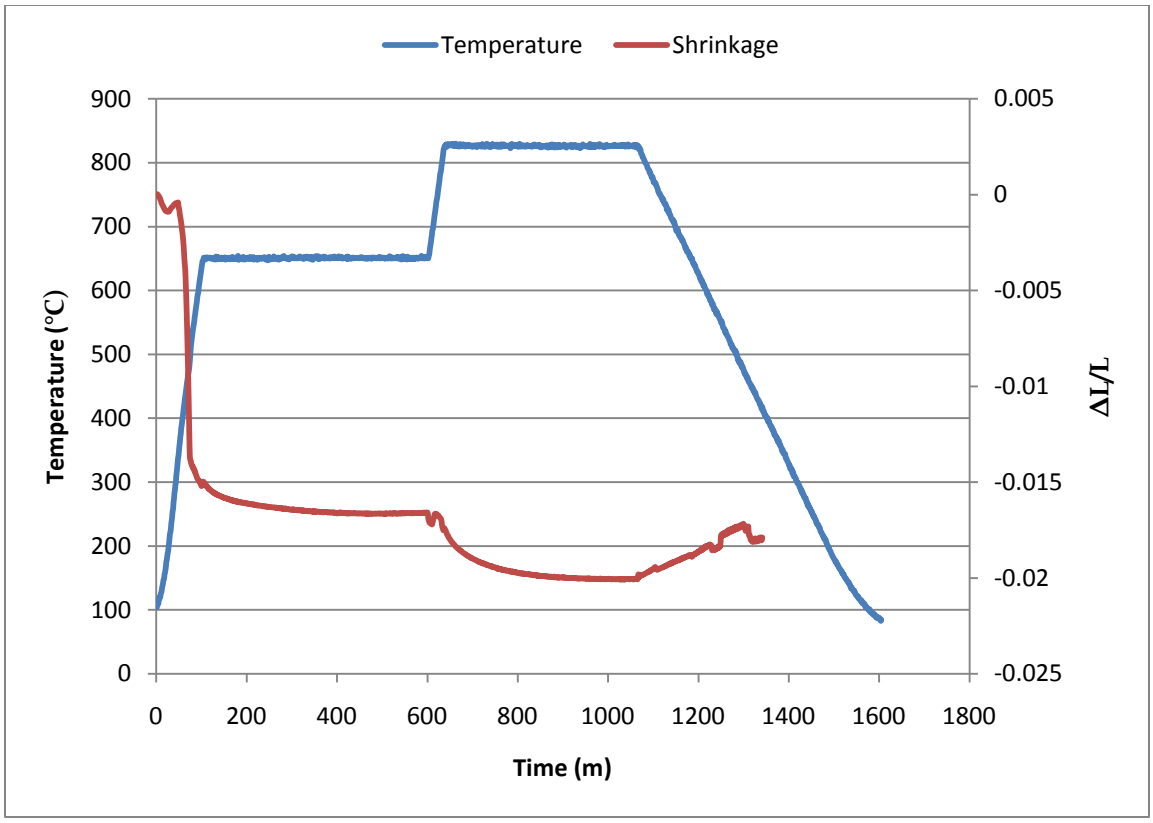

Figure 4-15: Shrinkage and temperature profile for Pellet 8.

The α-phase isothermal region of each pellet which demonstrated sintering was analyzed using Equation 3-2 to determine the value of *n*, as described in the models given in Section 2.1.3. The resulting plot is shown in Figure 4-16. Linear trendlines were fitted to the results for each pellet, producing the effective value of *n* for each pellet. These values are reported in Table 4-2. The data used to determine *n* contains some natural variations, observable as slight deviations from linearity in Figure 4-16; however, these minor variations did not appear to significantly affect the results.

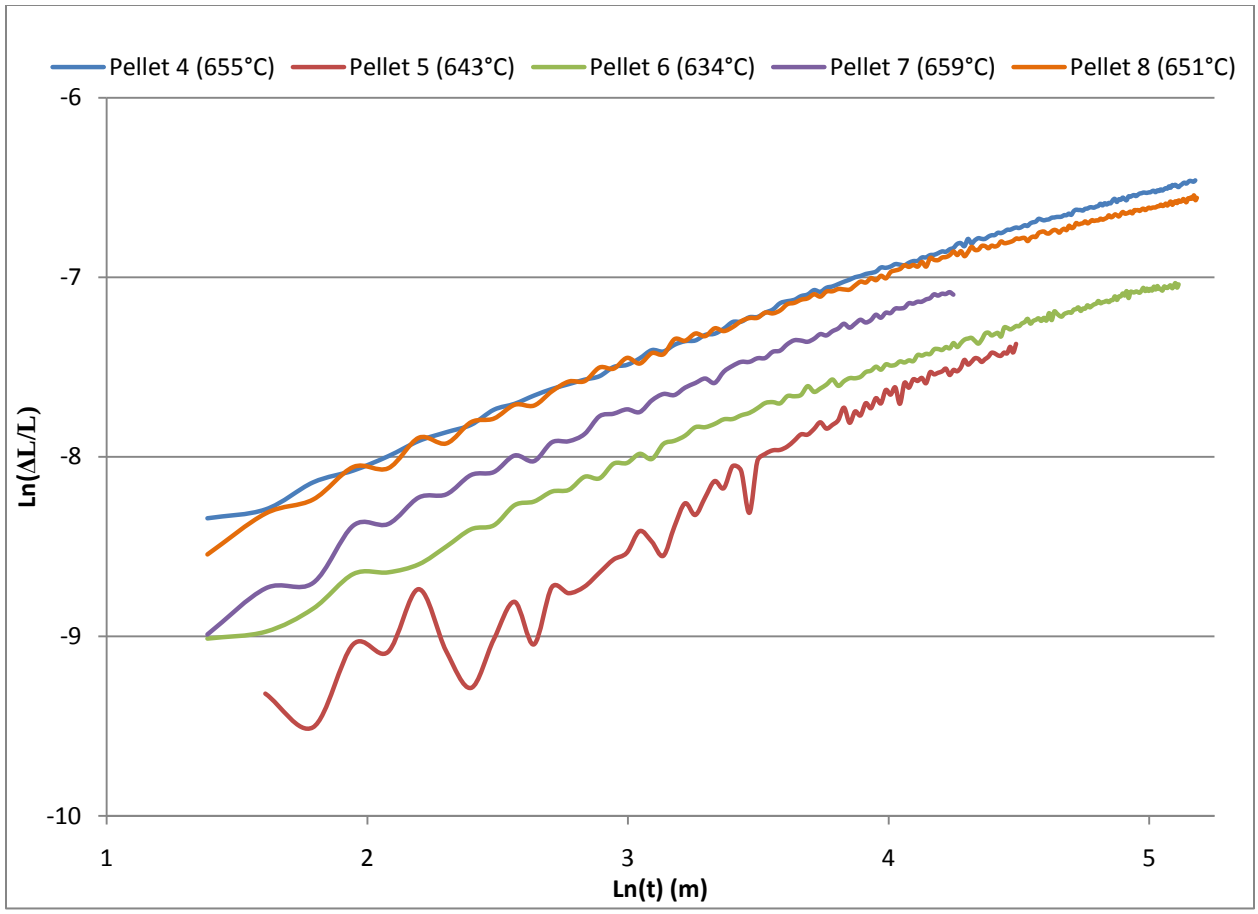

Figure 4-16: Log-log plot of shrinkage vs. time for determination of DU sintering constants.

Table 4-2: Calculated values of *n* for isothermal α-phase sintering of pure DU.

	Contents	α-Phase Temperature	Calculated *n*	R^2
Pellet 4	DU	655°C	4.11	0.9933
Pellet 5	DU	643°C	2.60	0.9693
Pellet 6	DU	634°C	3.93	0.9860
Pellet 7	DU	659°C	3.26	0.9870
Pellet 8	DU	651°C	4.36	0.9812

The activation energy, *Q*, for α-phase sintering of uranium was determined by using Equation 3-4 to construct an Arrhenius plot of the shrinkage after three hours for Pellet 4, Pellet 6, Pellet

7, and Pellet 8. Pellet 5 was excluded as an outlier, for reasons discussed later in Section 5.2.1. The resulting Arrhenius plot is given in Figure 4-17. Based on this plot and the previously determined value of *n*, the activation energy for α-phase uranium sintering was 340 +/-41 kJ/mol.

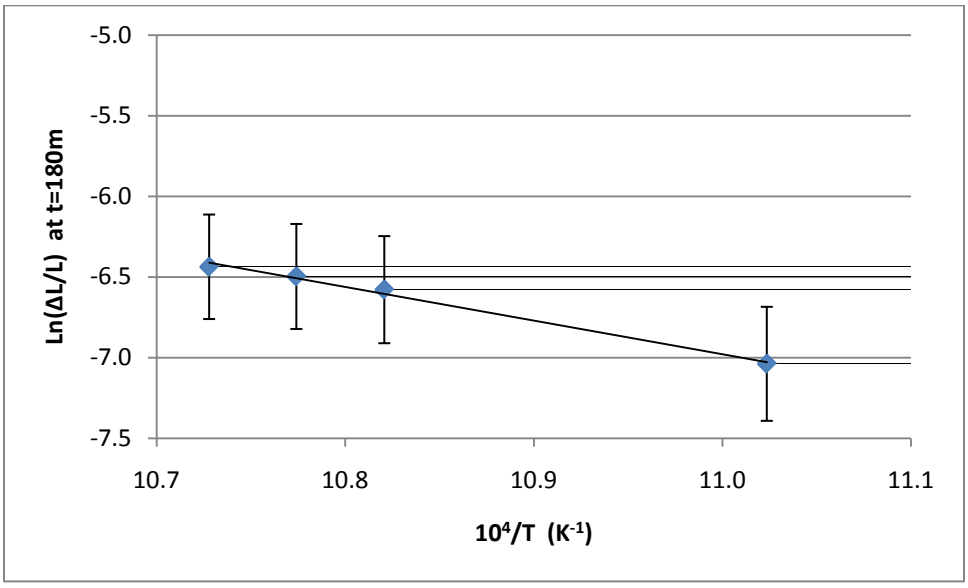

Figure 4-17: Arrhenius plot for α-phase sintering of uranium.

4.2.2 BSE Imaging of Sintered Uranium

Backscatter Electron (BSE) imaging was performed on a cross section of each of the successfully sintered uranium pellets. The cross section of each pellet demonstrated a pronounced dog-bone shaped region of higher sintered density in the center of the pellet, and an outer region of lower density. This effect can clearly be seen in the optical image of Pellet 4, shown in Figure 4-18.

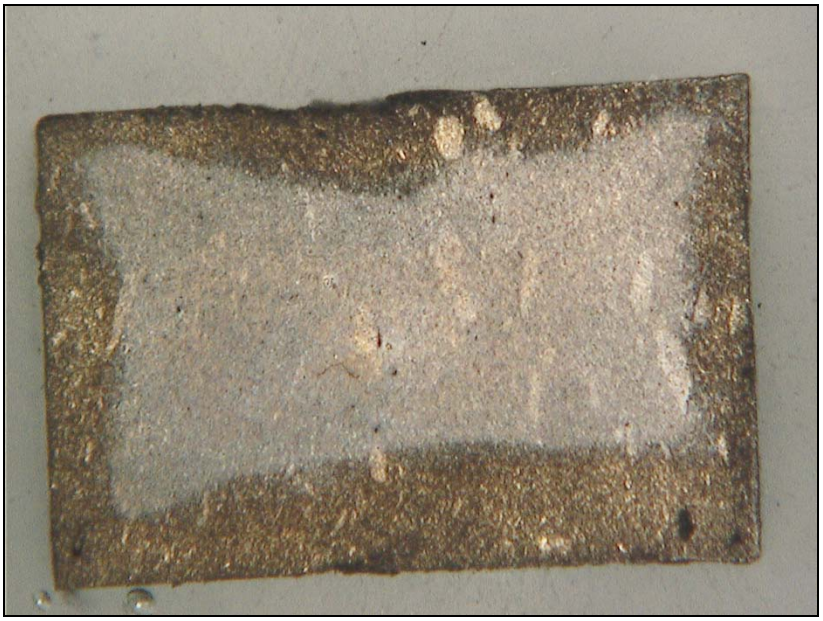

Figure 4-18: Polished cross section of Pellet 4 at 25x magnification demonstrating inner and outer regions.

The difference in microstructure between the inner and outer sintered regions is shown in Figure 4-19. In this BSE image of Pellet 4, the upper section shows the relatively high porosity region near the edge of the pellet, while the lower section shows the relatively low porosity region near the center of the pellet. Even in the more porous section of the pellet, the size of the pores was fairly uniform, with very few large pores. This result was typical for each of the sintered pellets. One of the few larger pores observed in the samples is shown in Figure 4-20.

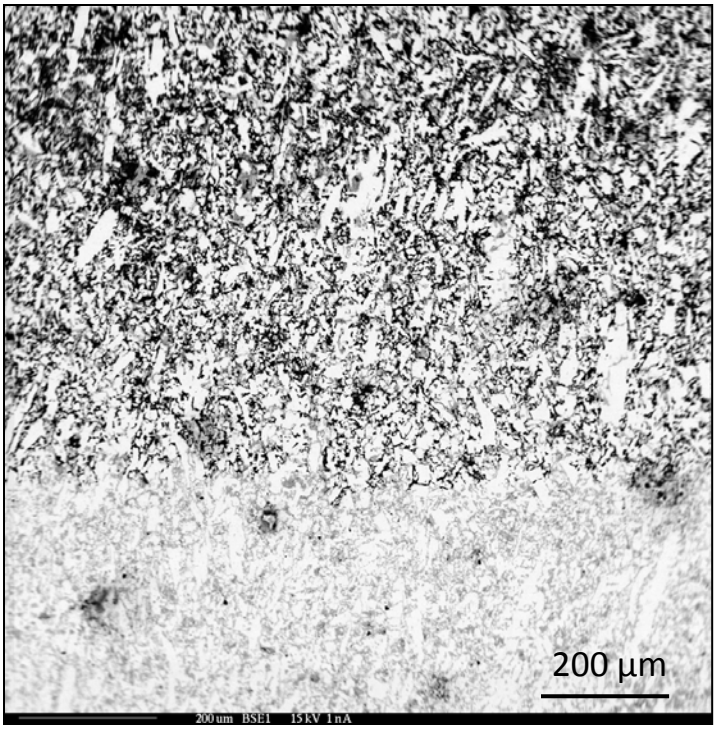

Figure 4-19: BSE image of boundary between low and high porosity regions of Pellet 4.

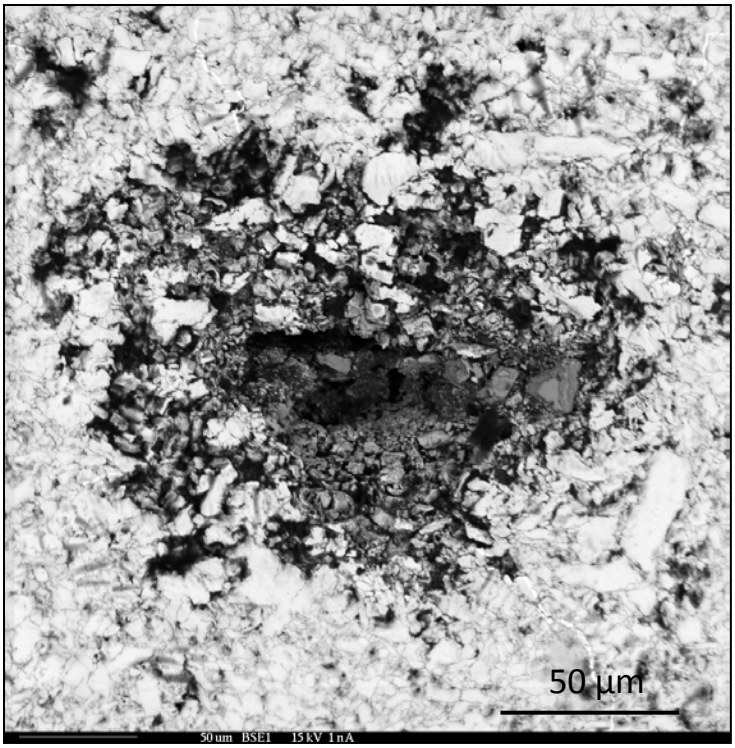

Figure 4-20: BSE image of rare, larger pore in Pellet 8.

For the most part, the sintered pellets did not show signs of cracking due to delamination during cooling. There were only two cases in which cracks greater than several microns long were formed, and in each case these cracks occurred near the edge of the pellets in the high porosity region. Images of these cracks are shown in Figures 4-21, 4-22, and 4-23.

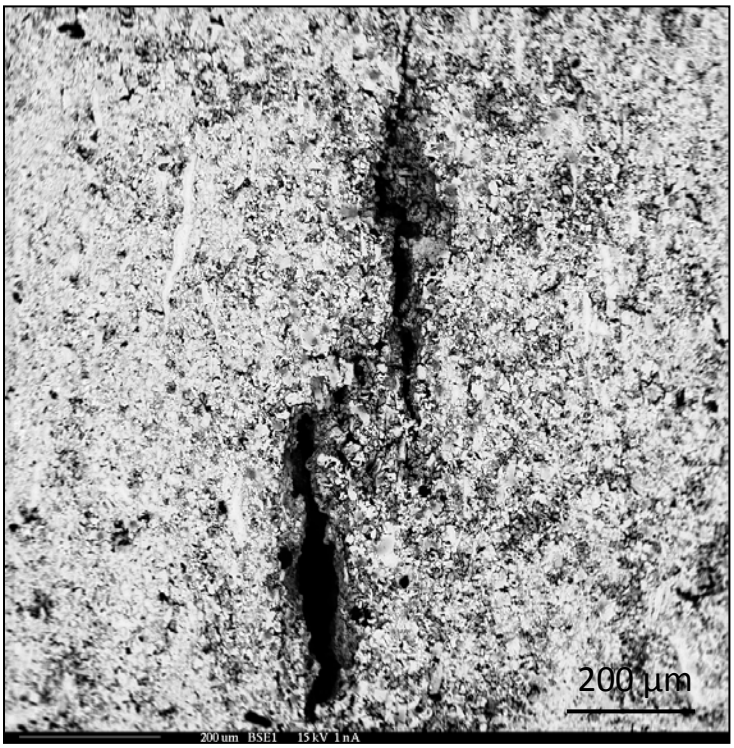

Figure 4-21: BSE image of cracking in Pellet 6.

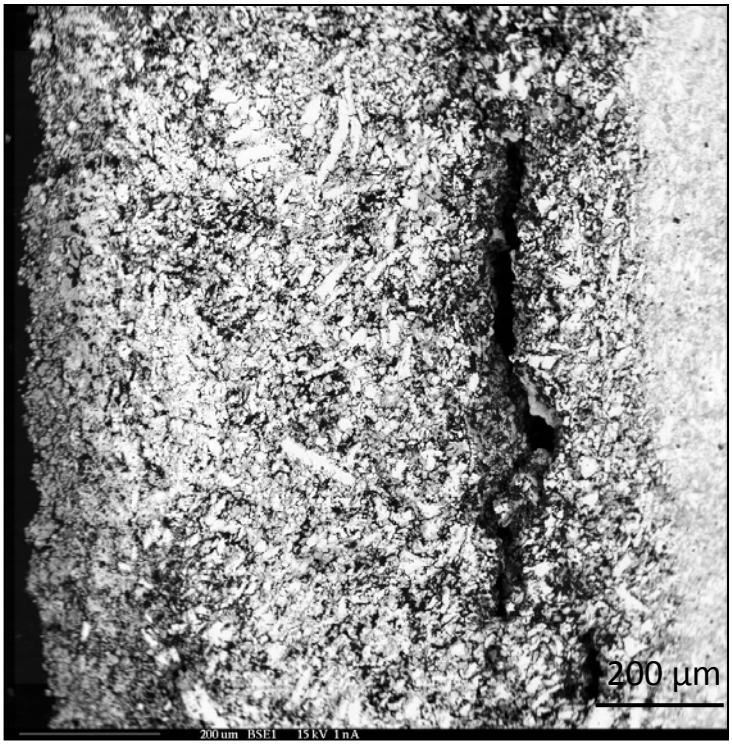

Figure 4-22: BSE image of cracking in Pellet 7.

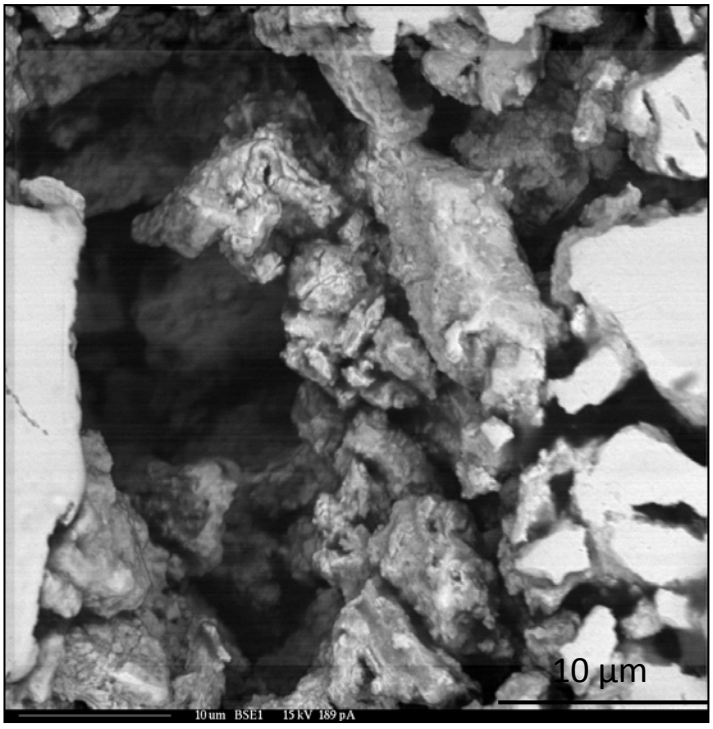

Figure 4-23: BSE image within large crack in Pellet 6.

Although large cracks showing delamination were rare, series of small cracks potentially demonstrating delamination were observed in some pellets. The length of these cracks were typically on the order of 10 microns. An examples of these micro-cracks is shown in Figure 4-24.

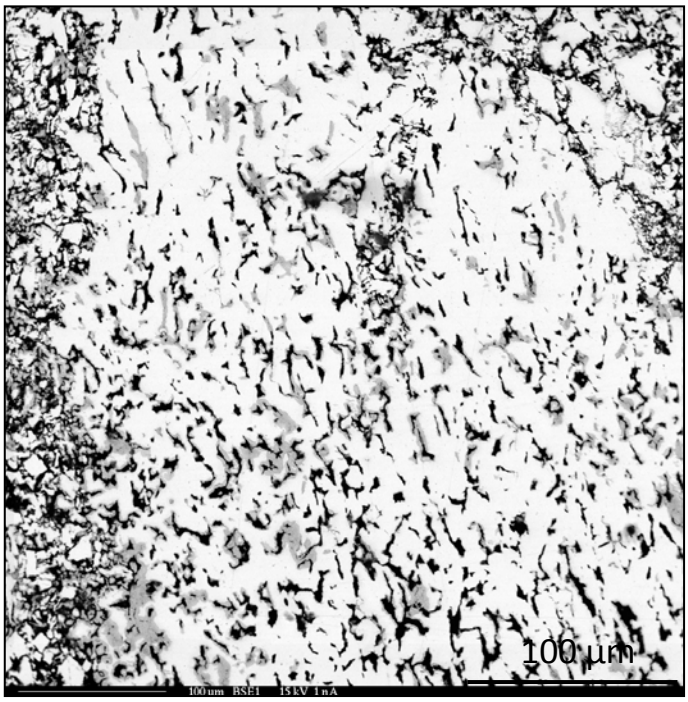

Figure 4-24: BSE image of small cracks in Pellet 5.

A series of images of each pellet were analyzed to determine the porosity of each pellet within the low porosity inner region and the high porosity outer region. The results of this analysis are given in Table 4-3.

Table 4-3: Porosity of sintered uranium pellets as determined from SEM images.

	Porosity of Outer Region	Porosity of Inner Region
Pellet 4	32.3%	11.5%
Pellet 5	36.2%	13.2%
Pellet 6	40.0%	9.7%
Pellet 7	30.9%	3.2%
Pellet 8	23.0%	1.1%

4.2.3 Isothermal Sintering of DU-10Zr

The second set of experiments performed sintered DU-10Zr pellets isothermally at several temperatures in the α and γ phases. A total of three DU-10Zr pellets were fabricated, and each pellet was successfully sintered. A summary of the conditions and properties of each pellet is given in Table 4-4. Based on experiences with fabrication of uranium pellets described in Section 4.2.1, each U-10Zr pellet was pressed with a force of 44.5 kN (10,000 lbf) for 15 seconds.

Table 4-4: Summary of isothermally sintered DU-10Zr pellets.

Pellet #	Powder Source	Contents	α-Temperature	γ-Temperature	Green Density	Sintered Density
9	H/dH Run 4	DU-10Zr	635 °C	817 °C	51.27%	55.74%
10	H/dH Run 4	DU-10Zr	642 °C	819 °C	50.67%	55.80%
11	H/dH Run 4	DU-10Zr	652 °C	829 °C	51.28%	56.47%

Pellet 9 was pressed to 51%TD, and sintered for 7 hours at 635ºC (α -phase), then 6 hours at 817ºC (γ-phase). A ramp rate of 5ºC/min was used during heating, and a rate of 1.5ºC/min was used during cooling. Images of Pellet 9 before and after sintering are given in Figure 4-25 and

Figure 4-26 respectively. As can be seen in Figure 4-26, some black powder formation still occurred on the top of the pellet during sintering; however, the severity of the phenomena continued to decrease relative to previous pellets.

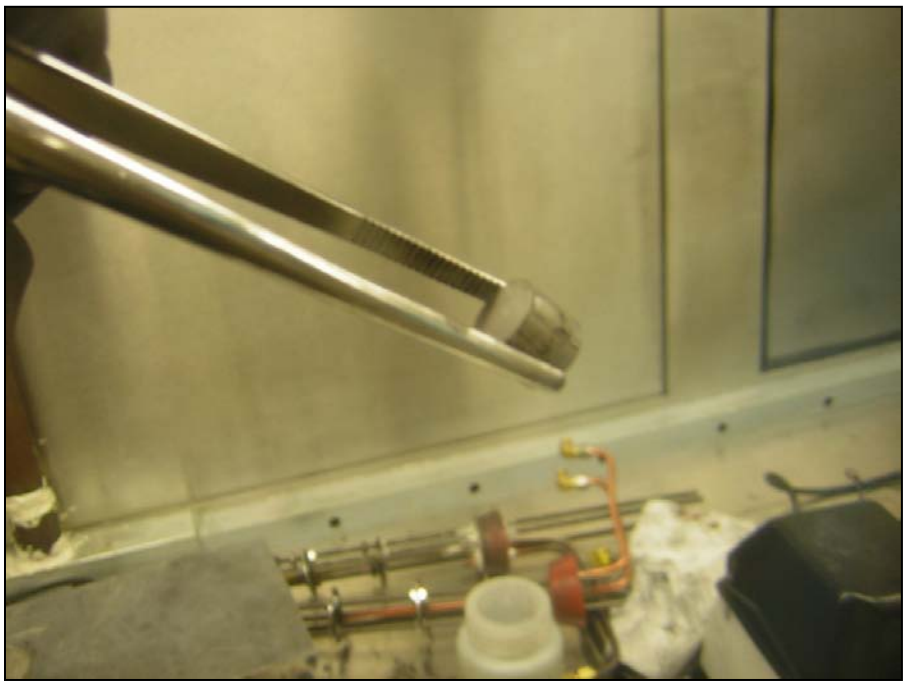

Figure 4-25: Pellet 9 as pressed, before sintering.

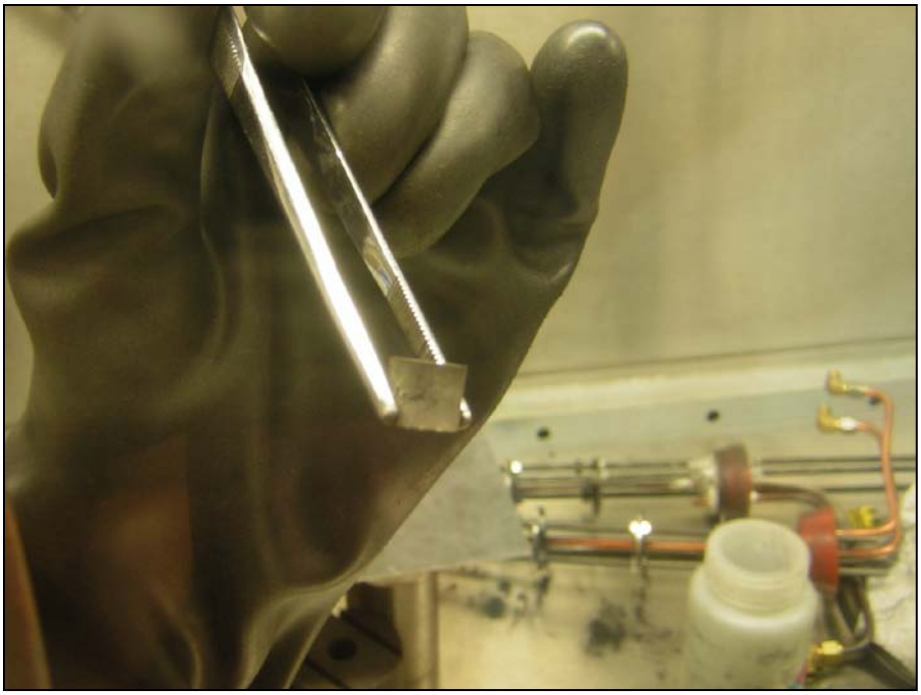

Figure 4-26: Pellet 9 after sintering.

The LVDT data for Pellet 9 showed a couple of distinct differences from the DU samples in the previous section. First, a smaller degree of shrinkage was observed during heating and second, the shrinkage in both the α and γ phase were much more pronounced than for pure uranium pellets. Further, there was a slight deflection in the shrinkage vs. time curve for the γ-phase sintering portion of the experiment. The measured shrinkage and temperature profile for Pellet 9 are given in Figure 4-27. The density of Pellet 9 increased during sintering from 51%TD to 56%TD.

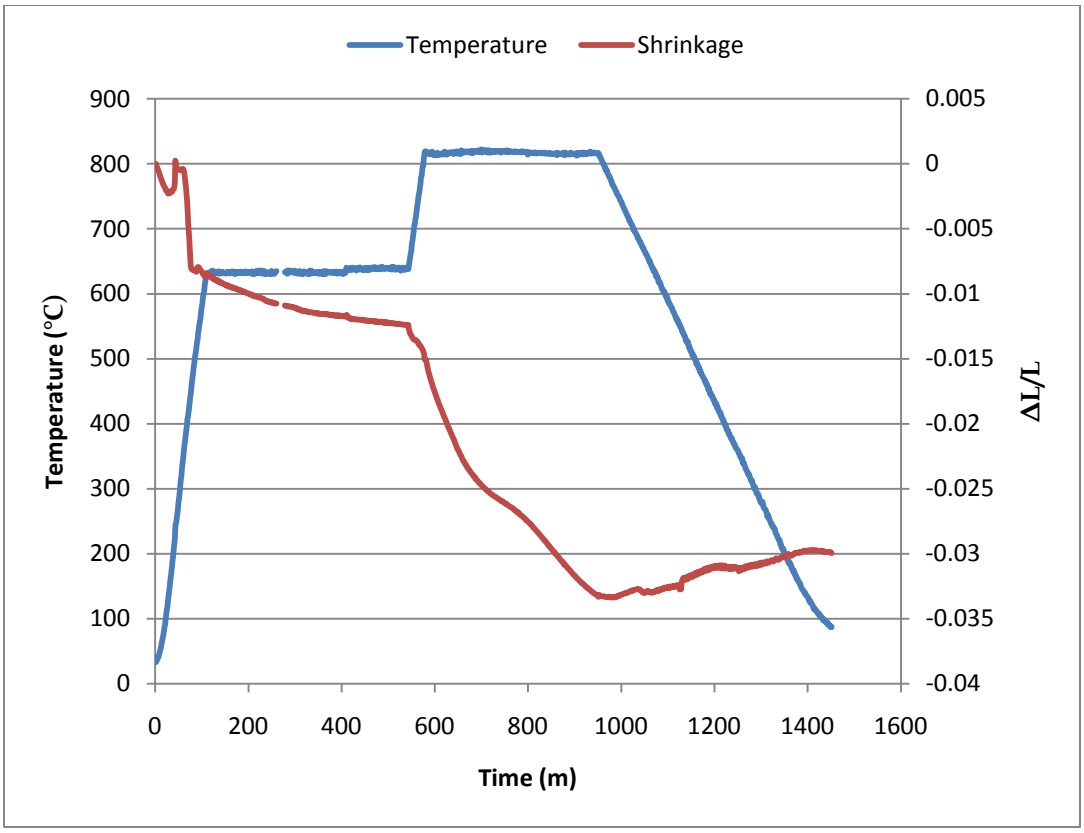

Figure 4-27: Shrinkage and temperature profile for Pellet 9.

Pellet 10 was pressed to 51%TD, and sintered for 7 hours at 642ºC (α-phase), then 7 hours at 819ºC (γ-phase). A ramp rate of 5ºC/min was used during heating, and a rate of 1.5ºC/min was used during cooling. Images of Pellet 10 before and after sintering are given in Figure 4-28 and Figure 4-29 respectively. The appearance of Pellet 10 after sintering was very similar to Pellet 9; a light formation of black powder was formed on the top of pellet.

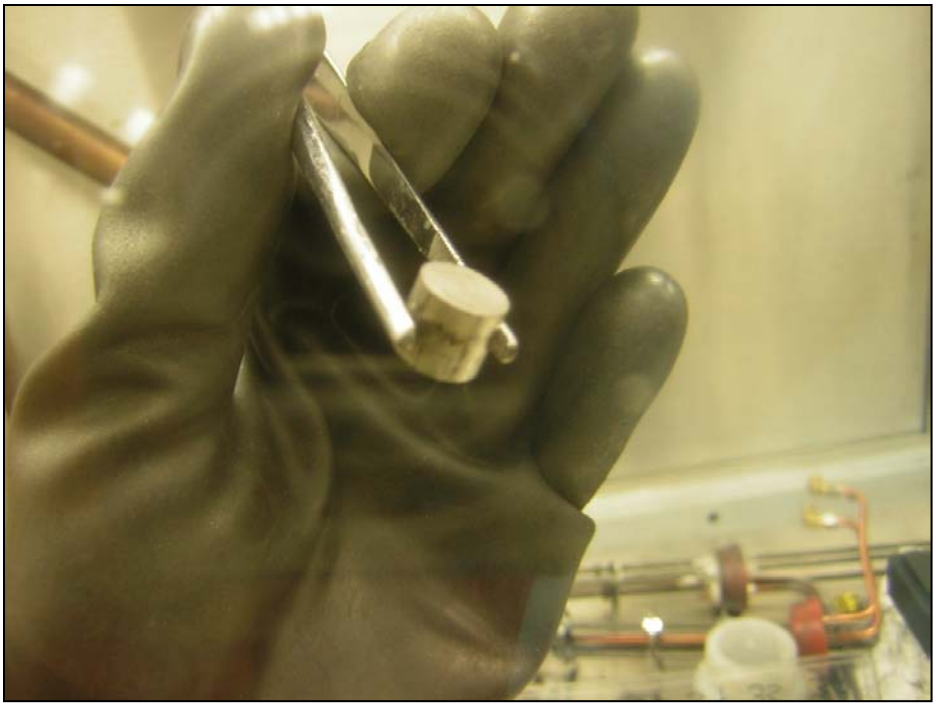

Figure 4-28: Pellet 10 as pressed, before sintering.

Figure 4-29: Pellet 10 after sintering.

The LVDT data for Pellet 10 was very similar to Pellet 9, demonstrating reduced shrinkage during heating and enhanced shrinkage during isothermal sintering relative to pure uranium pellets. In addition, the hump in shrinkage was once again observed during isothermal γ-phase sintering. The measured shrinkage and temperature profile for Pellet 10 are given in Figure 4-30. The density of Pellet 10 increased during sintering from 51%TD to 56%TD.

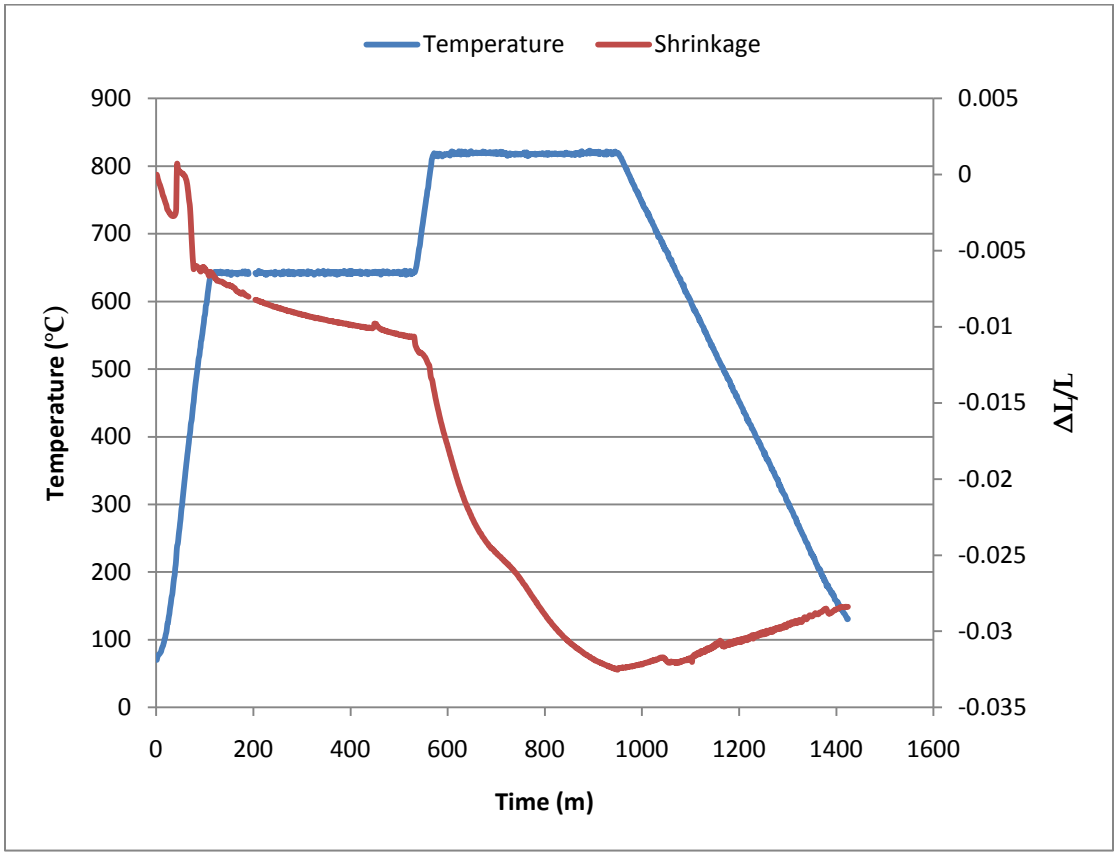

Figure 4-30: Shrinkage and temperature profile for Pellet 10.

Pellet 11 was pressed to 51%TD, and sintered for 7 hours at 652ºC, then 3 hours at 829ºC. The relatively short sintering time in the gamma phase was due to operator error, which also resulted in uncontrolled cooling following sintering. In spite of this deviation, the sintering

behavior of Pellet 11 was still very similar to that of Pellet 9 and Pellet 10. Images of Pellet 11 before and after sintering are given in Figure 4-31 and Figure 4-32 respectively.

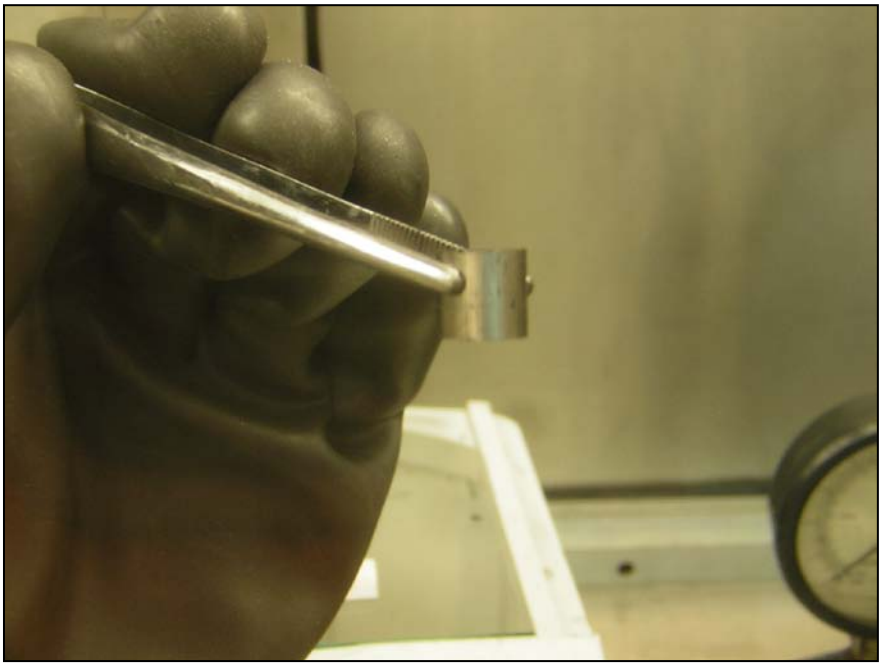

Figure 4-31: Pellet 11 as pressed, before sintering.

Figure 4-32: Pellet 11 after sintering.

The LVDT data for Pellet 11 showed some initial shrinkage during heating and steady shrinkage during isothermal sintering. The hump in shrinkage previously observed in γ-phase sintering DU-10Zr pellets was once more evident, although it was terminated prematurely by the shortened γ-phase sintering time. The measured shrinkage and temperature profile for Pellet 11 are given in Figure 4-33. The density of Pellet 11 increased during sintering from 51%TD to 56%TD.

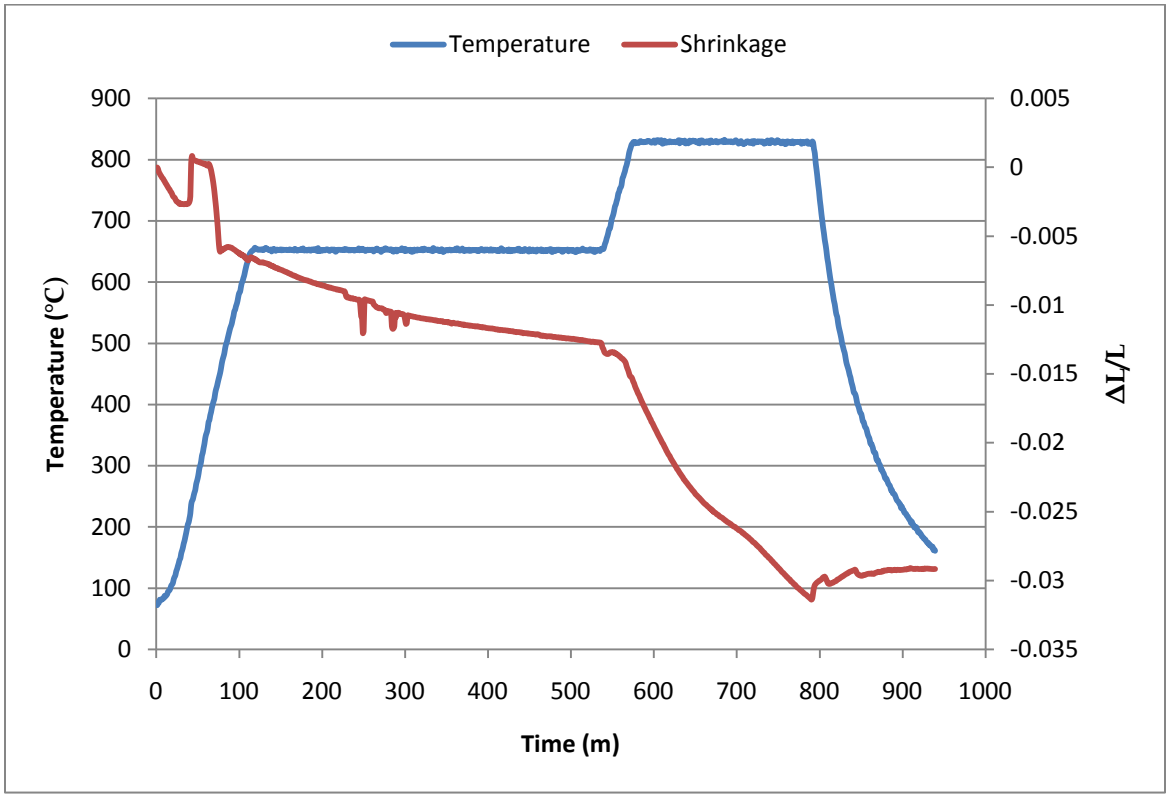

Figure 4-33: Shrinkage and temperature profile for Pellet 11.

As was done for isothermally sintered pellets of pure DU, the α-phase sintering of U-10Zr pellets was analyzed to determine the value of *n*. The plot used in these calculations is shown in Figure 4-33. The resulting values of *n* for each U-10Zr pellet are given in Table 4-5. As was observed previously in Figure 4-16, some oscillation in occurs in Figure 4-34, particularly in the

early stages of sintering. The appearance of these oscillations are exaggerated in the early stages due to the logarithmic nature of the graph. The calculated values of *n* for DU-10Zr were significantly lower than those calculated for DU, indicating a more rapid rate of sintering.

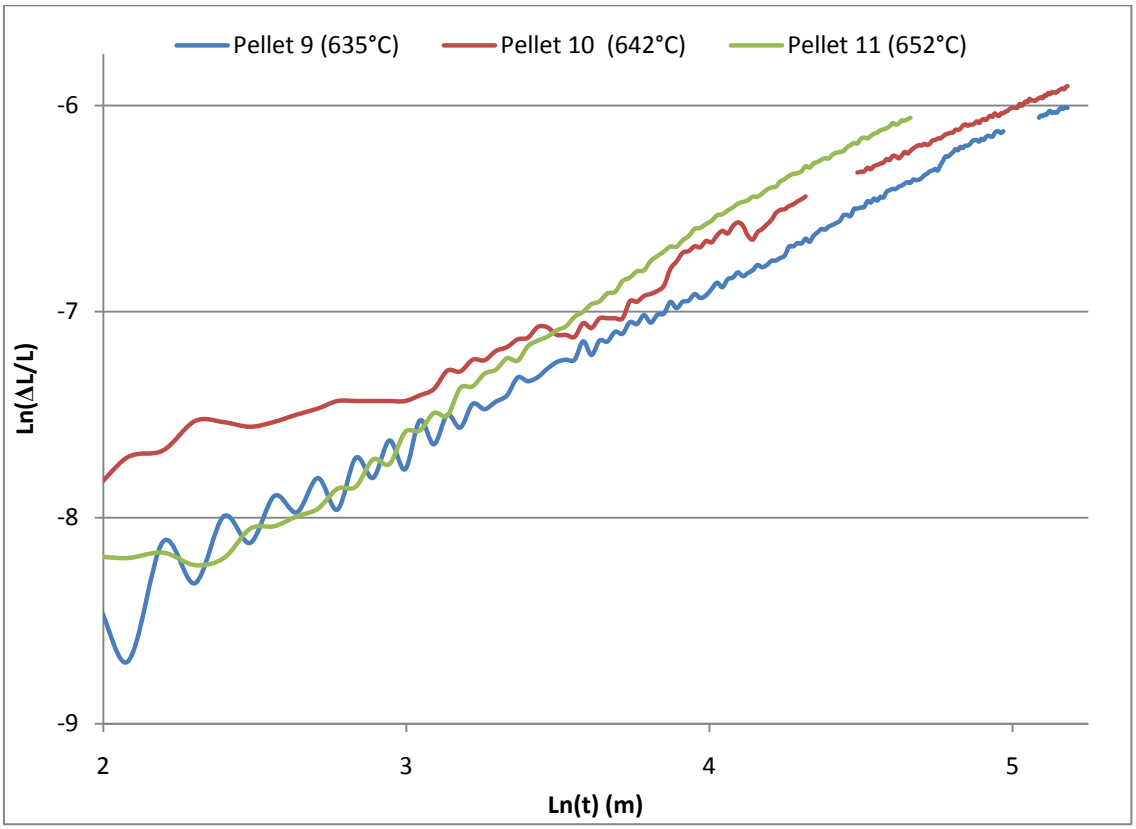

Figure 4-34: Log-log plot of shrinkage vs. time for determination of DU-10Zr sintering constants.

Table 4-5: Calculated values of *n* for isothermal α-phase sintering of DU-10Zr.

	Contents	α-Phase Temperature	Calculated *n*	R^2
Pellet 9	DU-10Zr	635°C	2.55	0.9871
Pellet 10	DU-10Zr	642°C	2.29	0.9855
Pellet 11	DU-10Zr	652°C	3.11	0.9876

The activation energy, *Q*, for α-phase sintering of U-10Zr was determined based on an Arrhenius plot of the shrinkage after three hours for Pellet 9, Pellet 10, and Pellet 11. The resulting Arrhenius plot is given in Figure 4-34. Based on this plot and the previously determined value of *n*, the activation energy for α-phase U-10Zr sintering was 272 +/-91 kJ/mol

.

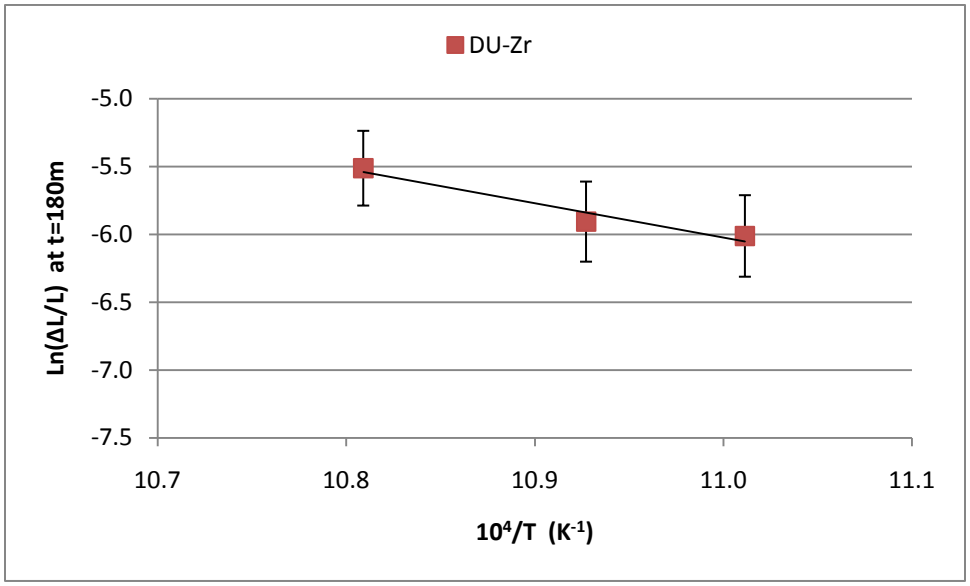

Figure 4-35: Arrhenius plot for α-phase sintering of DU-10Zr.

4.2.4 BSE Imaging of Sintered DU-10Zr

As was observed in sintered uranium pellets, pellets of DU-10Zr included a dog-bone shaped inner region of lower porosity and an outer region of higher porosity. The difference between these two regions is shown in Figures 4-36 and 4-37. In these images, white regions represent uranium, gray regions represent zirconium, and black regions represent pores. In addition to showing the pore microstructure, Figures 4-36 and 4-37 also show the distribution of zirconium in the DU-10Zr pellets. Although large particles of zirconium remain, they are distributed

throughout the material, and a portion of the zirconium has diffused into the surrounding uranium.

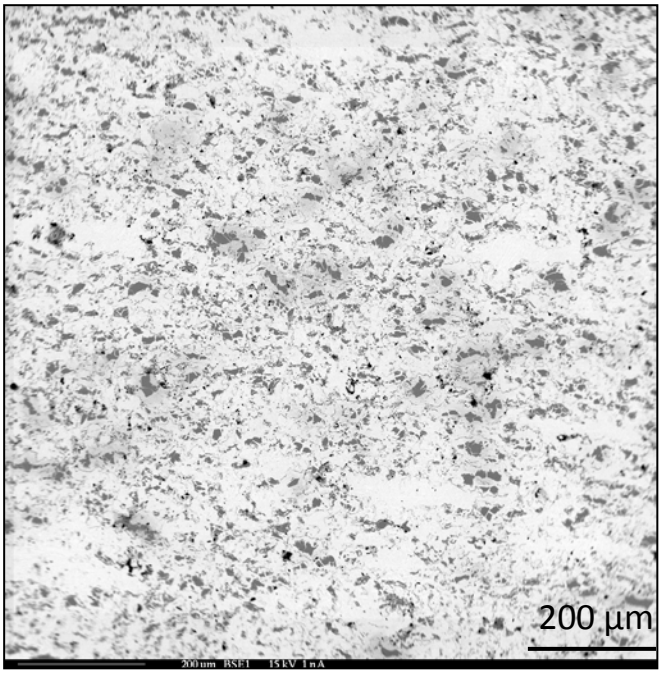

Figure 4-36: BSE image of inner, low porosity region of Pellet 9.

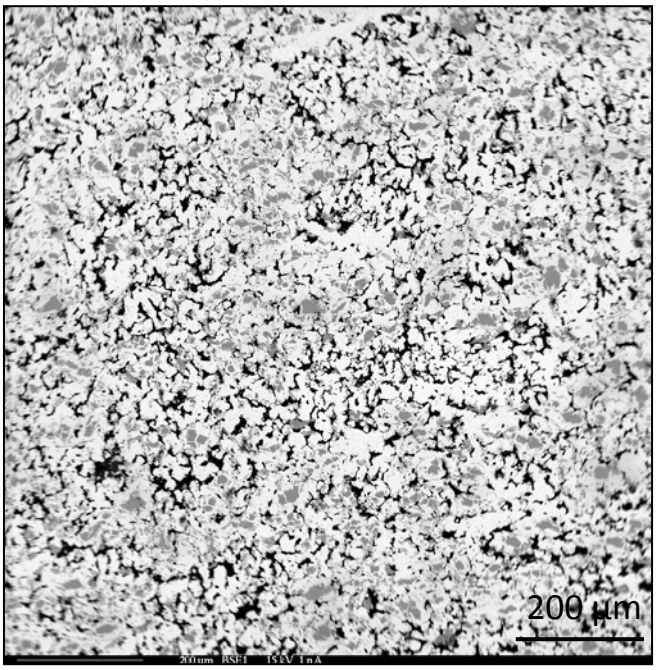

Figure 4-37: BSE image of outer, high porosity region of Pellet 10.

Images taken at higher magnifications of the DU-10Zr pellets showed the formation of mixed uranium-zirconium microstructure in regions surrounding zirconium particles, as shown in Figures 4-38 and 4-39. In addition, small amounts of zirconium were observed within the uranium, even in areas further away from zirconium particles. Quantitative analysis by Wavelength Dispersive Spectrometer (WDS) provided average elemental compositions in each region of the DU-10Zr pellets as described in Table 4-6.

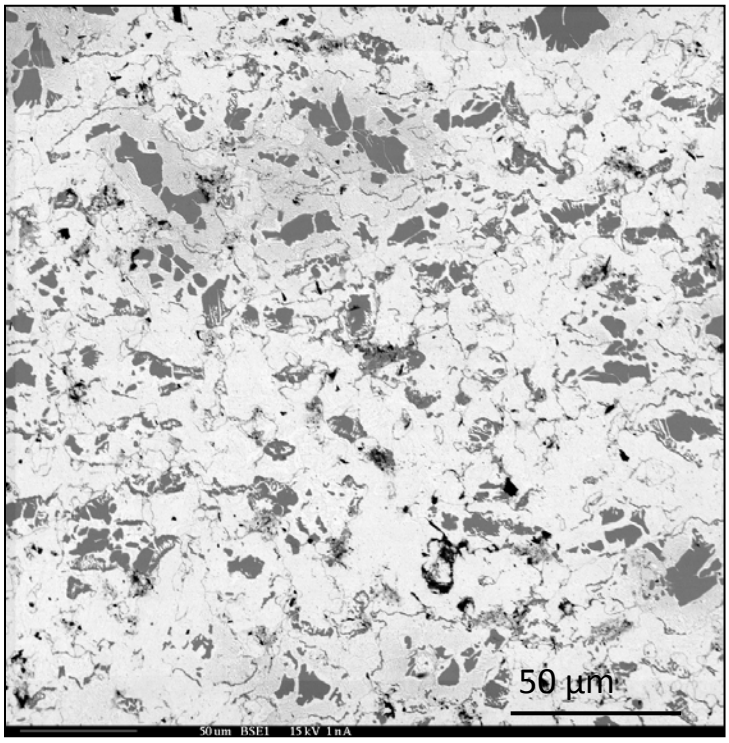

Figure 4-38: BSE image of Pellet 9 showing U-Zr microstructure.

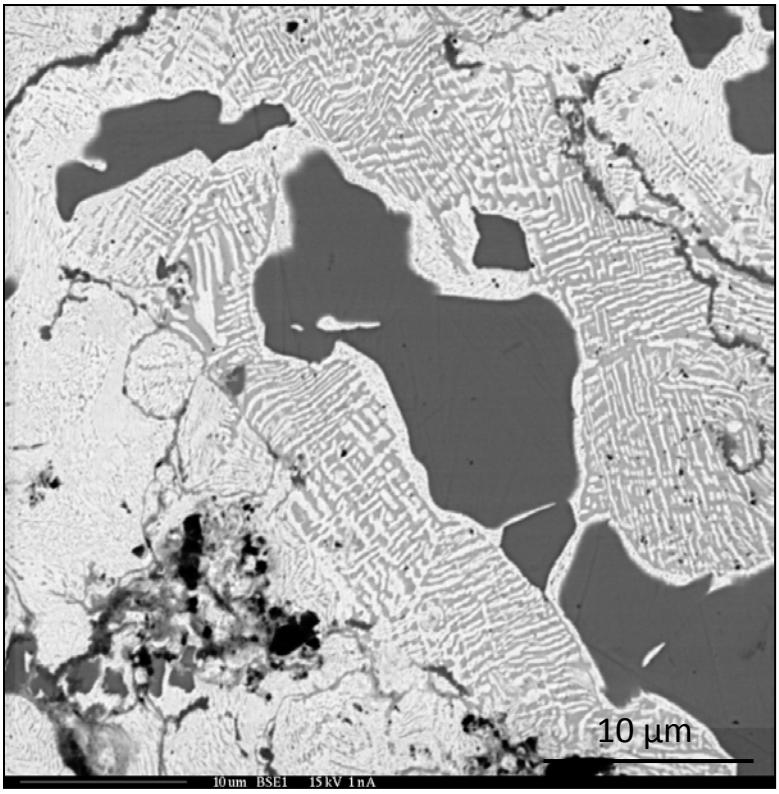

Figure 4-39: BSE image of Pellet 9 showing further U-Zr microstructure.

Table 4-6: Average elemental composition of various regions in DU-10Zr pellets.

	Zr Atom%	U Atom%
Zirconium Particles	99.998	0.002
Lamellar Structure	41.251	58.749
Bulk Uranium	13.628	86.372

As was done previously with uranium pellets, a series of images of each DU-10Zr pellet were analyzed to determine the porosity of each pellet within the low porosity inner region and the high porosity outer region. The results of this analysis are given in Table 4-7.

Table 4-7: Porosity of sintered DU-10Zr pellets as determined from SEM images.

	Porosity of Outer Region	Porosity of Inner Region
Pellet 9	12.0%	1.0%
Pellet 10	14.2%	1.5%
Pellet 11	8.7%	5.8%

4.2.5 Sintering of DU-5Zr

After completion of isothermal sintering studies on DU and DU-10Zr pellets, a final series of sintering experiments were performed using DU-5Zr pellets. These experiments focused on complementing the results previously obtained and filling in any gaps in knowledge. The two basic sintering experiments performed with DU-5Zr were extended alpha-phase sintering and sintering with cyclical alpha/beta phase transitions.

Imaging of previously sintered pellets indicated the consistent presence of inner regions with low porosity and outer regions with higher porosity. In an effort to reduce this effect, Pellet 14 was compacted with increased force and sintered in the alpha phase for a significantly longer period. The compaction force was doubled, to 89 kN (20,000 lbf). This resulted in a green density of 48.8%TD.

Pellet 14 was sintered in the alpha phase for 48 hours at a temperature of 650°C. Shrinkage data for this run is unavailable, due to a technical malfunction; however, the sintered density was measured to be 52.5%.

BSE images of a cross-section of Pellet 14, shown in Figures 4-40 and 4-41, show that it sintered to a very low porosity solid. Image analysis calculated 0.5% porosity, which was consistent across the entire cross-section. Quantitative analysis of Pellet 14 showed three primary regions. First, areas of pure zirconium were spread throughout the pellet. Second,

bands of UZr_2 on the order of 10 microns thick surrounded each of the pure zirconium areas. Finally, the remainder of the material consisted of uranium containing small amounts of zirconium. The grain boundaries in this region were typically filled in with zirconium.

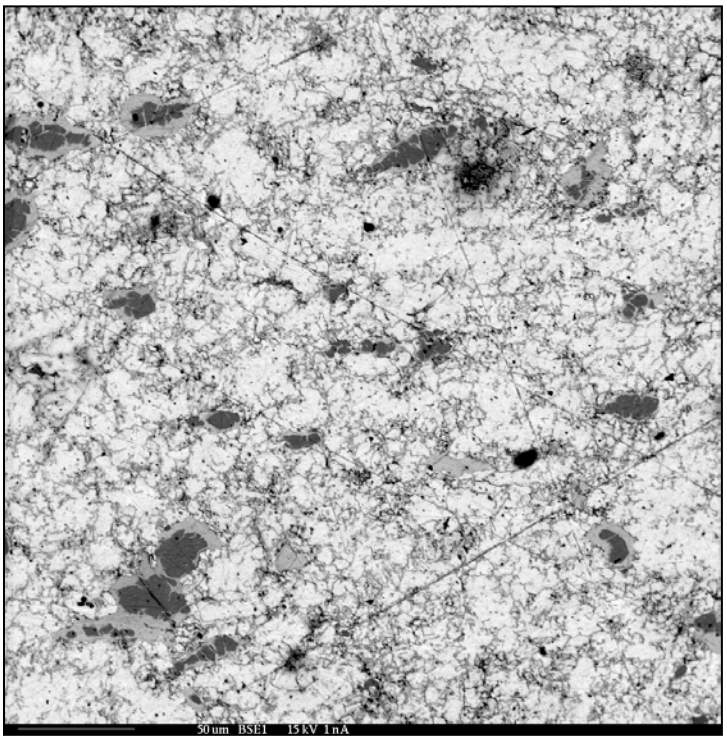

Figure 4-40: BSE image of Pellet 14 demonstrating low porosity.

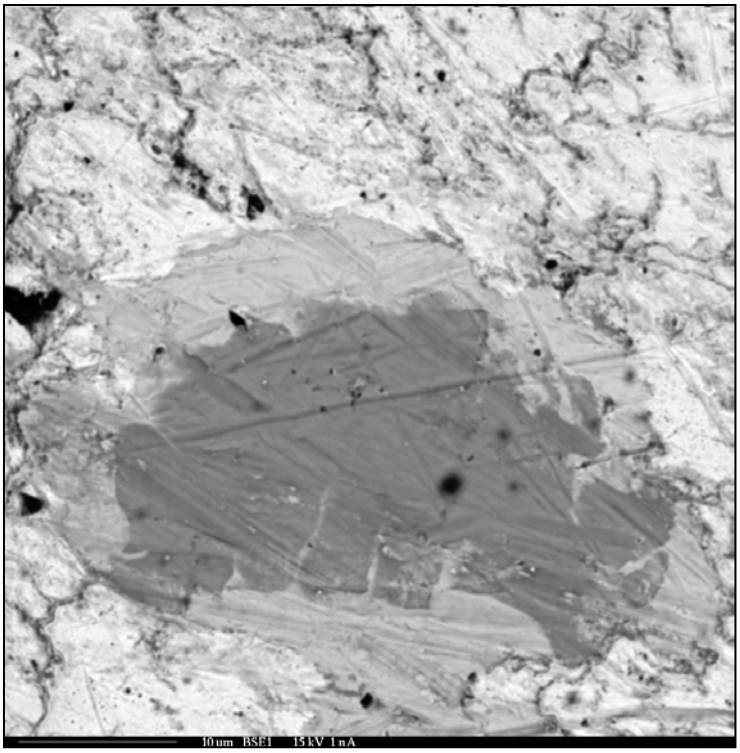

Figure 4-41 BSE image of Pellet 14 showing three region microstructure.

The final two DU-5Zr pellets were sintered using a novel technique involving cyclical transitions between the alpha and beta phases during sintering. The purpose of this method was to enhance sintering rate through the increase in atomic motion generated by phase changes. Pellet 15 was compacted with a pressure of 936 GPa. Pellet 15 was then sintered through ten alpha/beta phase transition cycles. In each cycle, the pellet was heated to the beta phase for approximately ten minutes, then cooled to the alpha phase for approximately twenty minutes. The shrinkage data acquired by LVDT is given in Figure 4-42.

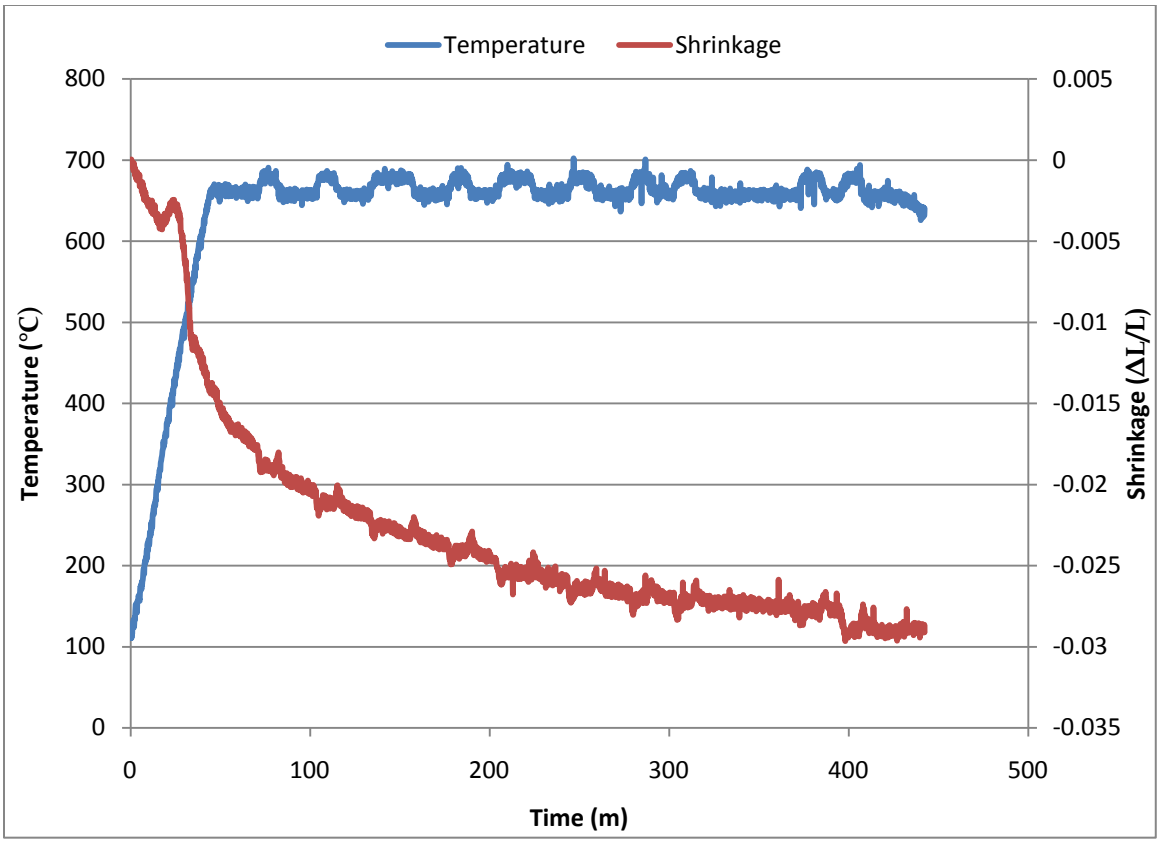

Figure 4-42: Shrinkage and temperature profile for Pellet 15.

As was done with other pellets, an attempt was made to section, polish, and image Pellet 15; however, Pellet 15 began to oxidize rapidly shortly following removal from the inert atmosphere of the glovebox. This oxidation was likely due to increased surface area from micro-cracks generated by density changes during phase transitions.

Pellet 16 was fabricated and sintered in a manner similar to Pellet 15, with the addition of a several hour period of isothermal alpha phase sintering following cyclical phase transition sintering. The purpose of this additional step was to reduce the micro-crack based surface area which was presumed to cause rapid oxidation in Pellet 15. The shrinkage and temperature data for Pellet 16 is given in Figure 4-43.

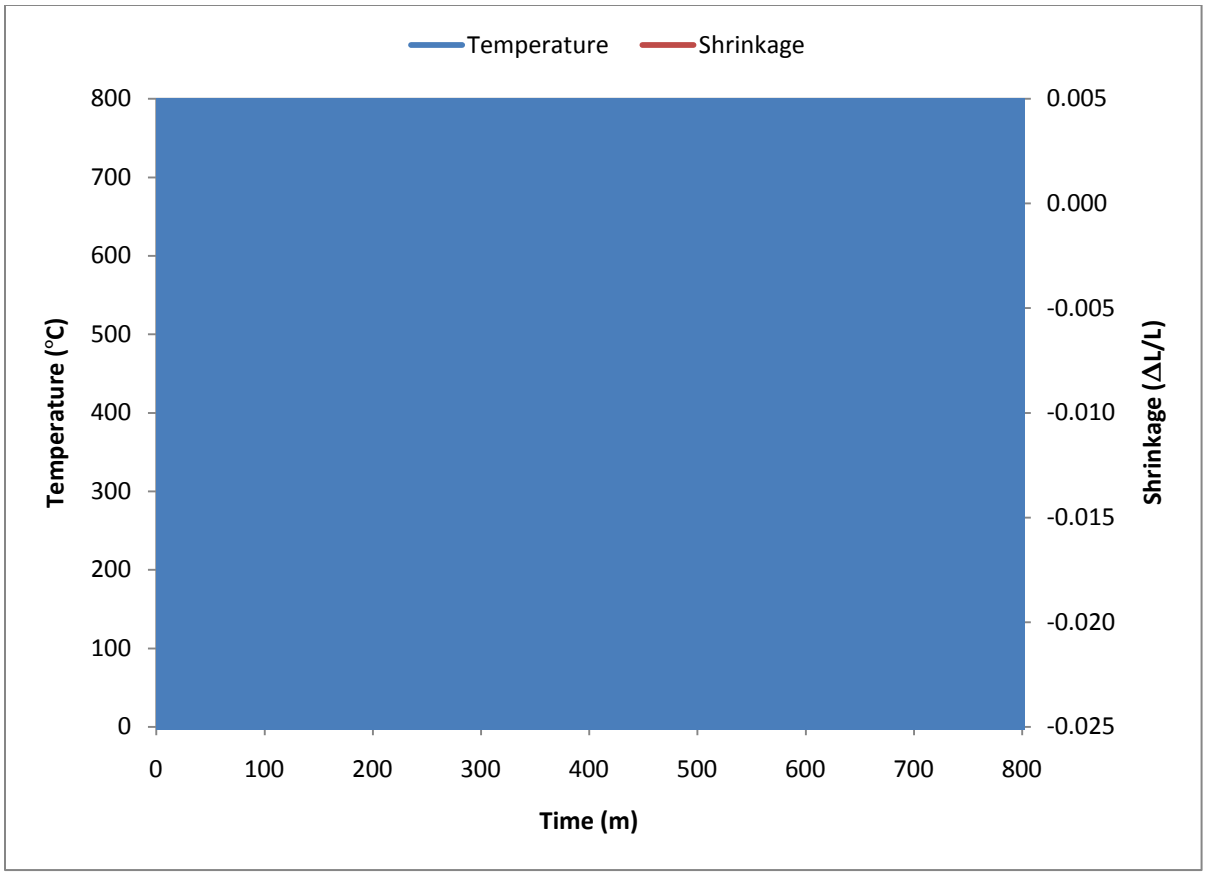

Figure 4-43: Shrinkage and temperature profile for Pellet 16.

Unlike Pellet 15, Pellet 16 did not rapidly oxidize following removal from an inert atmosphere, and thus it was sectioned, polished and imaged by SEM. Once again, porosity was consistent throughout the cross-section, with a calculated porosity from image analysis of 4.5%. The microstructure of Pellet 16 was similar to that of Pellet 14. The primary difference was in the composition of the boundary layer between the zirconium and uranium regions. The thickness of the boundary layer in Pellet 16 was smaller, on the order of only a few microns. In addition, the composition of the boundary region was higher in zirconium, with approximately 80a% Zr and 20a% U. Representative images of Pellet 16 showing these features are given in Figures 4-44 and 4-45.

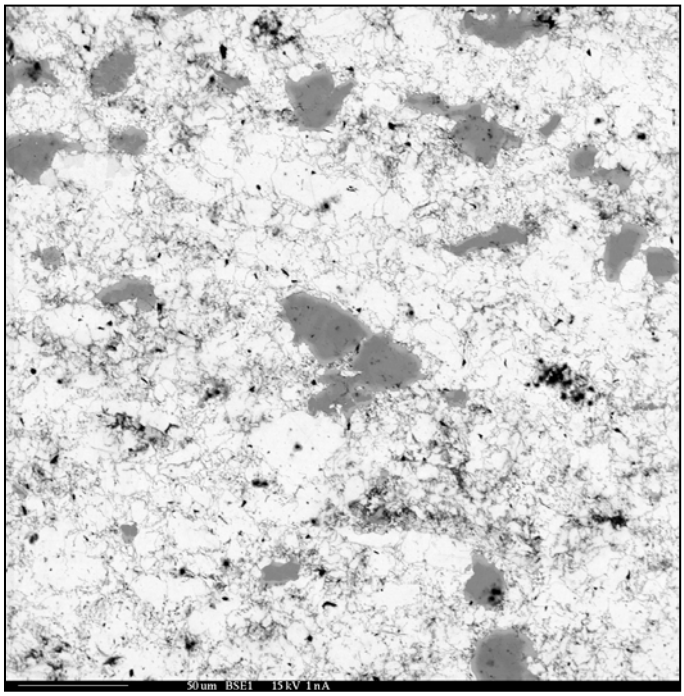

Figure 4-44: BSE image of Pellet 16.

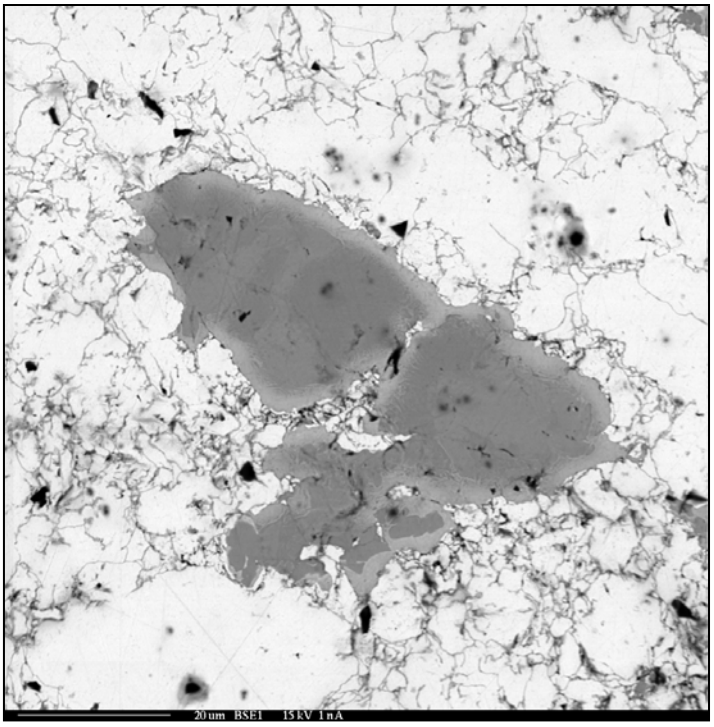

Figure 4-45: BSE image of Pellet 16 at higher magnification.

5. DISCUSSION

5.1 Uranium Powder Characterization

The size distribution (Fig. 4-2) and morphology (Fig. 4-1) of the uranium powder produced using the hydride/dehydride method were both consistent with expectations based on prior work and literature. The spalling process by which uranium hydride powder separates from bulk uranium produces fine powder with rough irregular shapes [16].

The average uranium particle size produced by the hydride/dehydride process is commonly noted in literature to be 40μm diameter [12,16]. This agrees well with the experimentally determined particle distribution in Fig. 4-2, which shows that the nominal particle size is very near to a particle diameter of 40μm. The shape of the distribution also corresponded well with expectations. The number distribution of particles peaked for very small diameter, then dropped with increasing size, while the volume distribution of particles follows a normal distribution with a long tail extending into the smaller particle region.

5.2 Uranium Sintering

An effect common to all sintered pellets, regardless of contents or processing conditions, was a dog-bone shaped region of increased density in the axial cross section of the pellet. This effect was a result of the pressing method used for pellet compaction. All pellets were fabricated using a dual-action punch and die. This method produces density gradients within the pellet, as shown in Figure 5-1. These gradients lead to slightly anisotropic sintering, making the sides of the pellet convex. This effect was also observable in post-sintering measurements of pellet diameter, as the top and bottom of each pellet were always slightly wider than the middle.

Electron microscope images, as shown in Figures 4-19 and 4-22 revealed a strong difference between the microstructures of the interior low porosity regions in the center of the pellets and the exterior high porosity regions of the pellets. In the high porosity region, necking and interparticle bonding is observed, but limited, and the original particles are still distinguishable. In the low porosity region, on the other hand, individual particles are no longer distinguishable, having sintered into a solid material with some remaining pores. This result indicates that the extra stress applied during compaction to the inner region directly resulted in better sintering, suggesting increased compaction pressure as a potential means to improve the quality of sintered pellets.

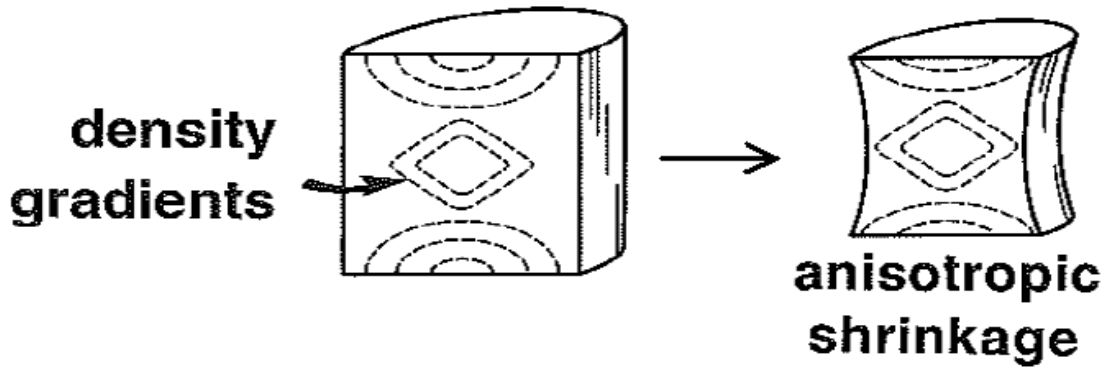

Figure 5-1: Density gradients and anisotropic sintering due to compaction method [4].

Another effect observed in many pellets was strong initial shrinkage during heating. The shrinkage typically began around 300ºC, lasting until the isothermal sintering temperature was reached. The two mechanisms which were initially thought to be responsible for this effect were sintering by plastic flow of dislocations, as described in Section 2.1.2 and removal of residual hydrogen gas from the hydride/dehydride process. It was found that increasing the duration of

the dehydriding step significantly reduced the degree of initial shrinkage, indicating that residual hydride decomposition was the most probable source of the majority of shrinkage during heating. The onset temperature for initial shrinkage of ~300°C agrees with this as well, since this is the temperature at which dehydriding become significant, and very little sintering would be expected at such a low temperature.

One of the issues encountered during previous work in alpha phase sintering of uranium and its alloys was widespread cracking due to delamination during the cooling phase following sintering. The severity of cracking ranged from moderate cracks a few millimeters in length to extended cracks across the full width of the pellets [3]. Analysis of previous results indicated that the probable causes of delamination were rapid cooling of the sample and poor control over the quality of the source powder used to fabricate the uranium pellets. Rapid cooling could potentially result in excess stress due to temperature gradients across the pellet, while the presence of large particles within the powder could result in localized areas with poor sintering which would be more susceptible to cracking. The lack of widespread delamination cracking in the sintered pellets from this research is attributed to 1) a uniform pressure distribution to minimize differentials in compaction stress across the pellet, 2) the sieving method used to remove large particles from the source uranium powder, and 3) the low controlled cooling rates used after sintering to minimize thermal stress. As shown in Figures 4-21, 4-22, and 4-23, the largest cracks were only a few hundred microns long, and most were only several microns in length.

5.2.1 Sintering of Uranium

Both the α-phase and γ-phase isothermal sintering curves were of the expected form, with initially rapid sintering gradually slowing as time passes. For each pellet, sintering in the γ-phase was significantly faster, as was expected due to the higher temperature and the higher diffusivity of uranium in the γ-phase [14].

Based on the sintering models described in Section 2.1.3, it was expected that log-log plots of sintering rate vs. time would be linear. Increases in isothermal sintering temperature were expected to shift the rate upwards (increase the y-intercept), while leaving the slope constant. These effects were generally observed, although Pellet 5 diverged from these expectations. In this case, the position of the log-log plot of sintering rate vs. time was lower than would be expected, based on the sintering temperature. In addition, the resulting slope varied slightly relative to the other experiments. The source of error for Pellet 5 may be related to the missing section of data from the experiment. Without this data, the true starting point for isothermal sintering may be slightly off.

The expected isothermal sintering mechanisms, as described in Section 2.1.2, were grain boundary diffusion and volume diffusion. Isothermal sintering by plastic flow occurs only in the presence of outside stress to generate dislocations, and surface transport mechanisms, such as evaporation-condensation and surface diffusion do not result in shrinkage, and would therefore not be measurable by the LVDT apparatus used in these experiments. Given the expectation of grain boundary diffusion and volume diffusion, the expected value of n was between five (volume diffusion) and six (grain boundary diffusion). The actual value of n would vary between these two values, depending on the relative contribution of each mechanism. However,

in the isothermal sintering experiments for pure DU, the average measured value of *n* was 3.92, excluding Pellet 5 and Pellet 7 for reasons discussed previously.

The discrepancy between the predicted and measured values of *n* is probably due to a combination of the morphology of the uranium powder and initial sintering contributions from plastic flow. The grain boundary diffusion and volume diffusion sintering models were based on the assumption of spherical particles; however, the uranium powder produced by the hydride/dehydride process was irregularly shaped. This deviation from the assumptions used by the sintering model may have resulted in a lower value of *n.*

The experimentally determined activation energy for alpha phase uranium sintering was 340 +/-41 kJ/mol. This value is significantly higher than the activation energy for gamma phase uranium sintering, which is 186.6 kJ/mol for the grain boundary diffusion mechanism [13]. This difference is consistent with previously made comparisons of diffusion in the alpha and gamma phases of uranium, which have concluded that diffusion in the alpha phase is far slower, requiring a greater activation energy.

5.2.2 Sintering of DU-10Zr

The isothermal sintering of U-10Zr was similar in several respects to the isothermal sintering of pure DU; however, some notable differences were observed. The most evident difference was the increased rate of isothermal sintering observed for U-10Zr, both for the α-phase and the γ-phase. Since the sintering process is driven by diffusion, the higher diffusivity of zirconium relative to uranium may be accredited for at least a portion of this increase in sintering rate. The mechanisms of two-component sintering may also contribute to the increased sintering rate of U-10Zr, due to activated sintering as zirconium accelerates the diffusion of uranium [4].

Interdiffuison between uranium and zirconium would be particularly active in the γ-phase, due to the high solubility of zirconium in γ-phase uranium.

In addition to increased sintering rate, the γ-phase sintering of U-10Zr demonstrated a a hump in shrinkage after several hours. It is likely that this shift was due to a transfer from the initial stage of sintering, which assumes point-contacts between particles, to the secondary stage of sintering, in which particles have densified to form an interconnected network. Once the initial phase of sintering formed sufficient connections between particles, interdiffusion and alloying of uranium and zirconium would become much more significant.

In similar fashion to pure DU sintering, the expected isothermal sintering mechanisms for U-10Zr were grain boundary diffusion and volume diffusion; however, the calculated values for *n* once again did not match with the predictions based on models of these mechanisms. This discrepancy was, as for pure DU, attributed to a combination of contributions from plastic flow and differences between the dendritic morphology of the uranium powder and the spherical particle assumptions employed by the sintering models. The average calculated value for *n* for α-phase sintering of U-10Zr was 2.65, compared to 3.92 for pure DU sintering. The lower value of *n* for U-10Zr may indicate a shift from grain boundary diffusion to volume diffusion, as sintering models predict a lower *n* for volume diffusion [4]. The lower value for *n* may also be an effect of sintering a mixture of powders, rather than a single powder, as the model used was developed for use with single powders.

In addition to the lower value of *n* observed for sintering of U-10Zr relative to DU, there was a difference in the calculated activation energy. The calculated activation energy for U-10Zr was 272 +/-91 kJ/mol, compared to a calculated value of 340 +/-41 kJ/mol for DU. When combined with the lower value of *n* observed for U-10Zr, this results in both faster sintering at a given

temperature and a higher sustained sintering rate over time relative to DU. The lower activation observed for U-10Zr is consistent with a shift from grain boundary diffusion to volume diffusion, based on activation energies for volume diffusion and grain boundary diffusion in gamma phase uranium. In the gamma phase, the activation energy of volume diffusion is lower than that of grain boundary diffusion. If the alpha phase of uranium behaves in a similar fashion, the lower activation energy for U-10Zr relative to DU may be caused by a zirconium driven shift to the volume diffusion mechanism. This would also be consistent with the lower value of *n* found for U-10Zr as previously discussed.

The uranium-zirconium microstructure as shown in Figures 4-37 and 4-38 contained three distinct regions. First, there were areas of pure zirconium within the sintered material. These regions were likely created by zirconium particles which did not fully diffuse into the uranium. Some of the pure zirconium regions included comb-like fingers extending into the uranium, indicating a partially completed diffusion process.

The second area observed is the lamellar structure containing significant amounts of both uranium and zirconium. The lamellar structure was found around the previously described pure zirconium regions. Quantitative analyses of the lamellar structure indicated an average smear composition of 41.3a% zirconium and 58.7a% uranium; however, the structure was too fine to allow quantitative analysis of the individual lamella. In spite of this, it may be reasonably surmised that the light gray portion of the lamellar structure is delta phase UZr_2, based on the much lighter shade of gray in this region relative to the regions of pure zirconium. Since the brightness of BSE images increases with atomic number, the lighter shade indicates the presence of a heavier material, such as uranium. This assumption is additionally validated by the smear

composition of the lamellar structure, which is approximately what would be expected if the light gray region were UZr_2 and there were equal amounts of both regions.

The final region of uranium-zirconium microstructure observed was the most prevalent, and consisted of sintered uranium with small spots of zirconium mixed throughout. This region had an average smear composition of 13.6a% zirconium and 86.4a% uranium. The amount of zirconium varied slightly throughout these regions; however, there were no areas of pure uranium found in the sintered samples.

5.2.3 Sintering of DU-5Zr

The primary goal for Pellet 14 was to demonstrate the feasibility of an exclusively alpha-phase sintering process for pellet fabrication. The compaction pressure was doubled from that used previously in an effort to remove the outer low-porosity region observed previously. Based on SEM imaging of Pellet 14, this increase was effective, as consistently low porosity was observed throughout the full cross-section of Pellet 14. This consistency would be ideal for fabrication of nuclear fuel.

The cyclical phase transition sintering technique used for Pellets 15 and 16 was designed to increase the rate of sintering by increasing atomic motion and diffusion. This method produced mixed results, as greatly enhanced sintering was observed in Pellet 15, but not in Pellet 16. It is unknown why this difference occurred, as very similar processing techniques were used for both pellets. Further studies of cyclical sintering for DU-Zr should be performed to determine if the increased sintering rate observed in Pellet 15 may be consistently reproduced.

One of the expected side effects of cyclical phase transition sintering was an increase in porosity due to repeated density changes during phase transitions. The porosity observed for

Pellet 16 was slightly higher than the porosity previously observed for isothermally sintered DU-Zr pellets, indicating that a degree increased porosity may have occurred due to repeated phase changes. However, the sintering time for Pellet 16 was significantly lower than that of isothermally sintered DU-Zr pellets, which may have contributed to the slightly increased porosity.

Pellets 14 and 16 were both sintered without reaching the gamma phase, which resulted in a slightly different final microstructure. Previous DU-Zr pellets which had been sintered partially in the gamma phase produced a lamellar $\alpha+\delta$ microstructure in some regions as shown in Figure 4-39. In Pellets 14 and 16, on the other hand, no lamellar region was observed. In Pellet 14, an equilibrium UZr_2 phase was observed, as shown in Figure 4-41. The presence of this phase indicates inter-diffusion of uranium and zirconium during sintering. Further studies varying the sintering time may be useful in determining the rate of diffusion based on the thickness of the UZr_2 region.

The uranium-zirconium phase in Pellet 16, shown in Figure 4-45, was slightly different, as quantitative analysis showed greater zirconium concentration than would be expected for UZr_2. This result may be explained by the fact that the sintering time for Pellet 16 was approximately one fourth of the sintering time for Pellet 14. The shorter time period for diffusion likely resulted in the formation of a non-equilibrium UZr_2+Zr phase. Since this phase contained excess zirconium, it may be concluded that inter-diffusion occurs by diffusion of uranium into zirconium. As the diffusion time increases, the uranium content would increase, eventually resulting in the formation of the equilibrium UZr_2 phase observed in Pellet 14.

6. SUMMARY

The alpha phase sintering of uranium and uranium-zirconium were successfully characterized in this research. These results provide the scientific background necessary to demonstrate the feasibility of a low temperature powder metallurgy process for the fabrication of metal uranium fuel. A summary of the primary conclusions are as follows:

1. A model for the initial phase of sintering for uranium and uranium-zirconium was evaluated based on isothermal shrinkage rates during sintering. Based on the model the activation energy for sintering DU and DU-10Zr in the alpha phase were found to be 340 +/-41 kJ/mol and 272 +/-91 kJ/mol respectively.
2. The effects of zirconium addition to uranium during sintering were analyzed and the resulting pellets were compared to those composed exclusively of uranium. It was found that the addition of zirconium accelerated sintering due to uranium-zirconium inderdiffusion.
3. The microstructure of sintered uranium-zirconium pellets was analyzed, indicating the presence of the alloyed alpha+delta phase when sintered in the gamma phase, and the presence of the alloyed delta phase when sintered in the alpha phase. This result was attributed to the relative solubility of zirconium in the uranium gamma and alpha phases.
4. The previously developed hydride/dehydride process for powder production was vastly improved to increase the volume of powder produced, and the uranium powder produced by this method was characterized to determine size distribution and morphology.

5. Previous issues with pellet cracking during cooling due to delamination were resolved by the use of controlled cooling and finer control over the quality of the uranium powder used.

If further research is undertaken in this area, the following recommendations are made:

1. The sintering models produced should be expanded by the use of further uranium-zirconium compositions and small amounts of secondary elements to represent transuranics.
2. The effects of pressure-assisted sintering should be analyzed to increase the rate and quality of sintering.
3. Possible applications for the fabrication of metal fuel with low smear density utilizing the low temperature sintering techniques developed in this thesis should be investigated.

REFERENCES

1. D. E. Burkes, R.S. Fielding, and D.L. Porter, Metallic Fast Reactor Fuel Fabrication for the Global Nuclear Energy Partnership, Journal of Nuclear Materials 392 (2009), 158-163.
2. C.L. Trybus, J.E. Sanecki, S.P. Henslee, Casting of Metallic Fuel Containing Minor Actinide Additions, Journal of Nuclear Materials 204 (1993) 50-55.
3. D. Garnetti, S.M. McDeavitt, Uranium Powder Production via Hydride Formation and Alpha Phase Sintering of Uranium and Uranium-Zirconium Alloys for Advanced Nuclear Fuel Applications. Masters Thesis, Texas A&M University, College Station, TX.
4. J.J. Carroll, A.J. Melmed, Field Ion Microscopy of Alpha Uranium, Surface Science 116 (1982) 225-239.
5. W.D. Wilkinson, Uranium Metallurgy, John Wiley & Sons, Inc., New York (1962).
6. L. Grainger, Uranium and Thorium, George Newnes Limited, London (1958).
7. S.F. Pugh, Swelling in Alpha Uranium due to Irradiation, Journal of Nuclear Materials 4 (2) (1961) 177-199.
8. J.J. Burke, D.A. Colling, A.E. Gorum, J. Greenspan, Physical Metallurgy of Uranium Alloys, Brook Hill Publishing Company, Columbus, Ohio(1976).
9. C.E. Stevenson, The EBR-II Fuel Cycle Story, American Nuclear Society Inc. La Grange Park, Illinois (1987).
10. S.M. McDeavitt, A.A. Solomon, Hot-Isostatic Pressing of DU-10Zr by a Coupled Grain Boundary Diffusion and Creep Cavitation Mechanism, Journal of Nuclear Materials 228 (1996) 184-200.
11. P. Chiotti, B.A. Rogers (1950), The Production of Uranium and Thorium in Powder Form, United States Atomic Energy Commission, AECD-2974.

12. S.M. McDeavitt (1992), Hot Isostatic Pressing of DU-10Zr Alloy Nuclear Fuel by Coupled Grain boundary Diffusion and Power-Law Creep. Ph.D Thesis, Purdue University, West Lafayette, IN.

13. R.M. German, Sintering Theory and Practice, John-Wiley & Sons, Inc., New York, (1996).

14. F.V. Lenel, Powder Metallurgy, Metal Powder Industry, (1980).

15. T. Hashino, Y. Okijima, Mechanism of the Reaction of Hydrogen with Uranium, Journal of Physical Chemistry 77 (1973) 2236-2241.

16. C.R. Clark, M.K. Meyer, Fuel Powder Production from Ductile Uranium Alloys, Presented at the 1998 International Meeting on Reduced Enrichment for Research and Test Reactors, Oct. 18 - 23, 1998, Sao Paulo, Brazil.

17. J. Bloch, The Hydriding Kinetics of Activated Uranium Powder Under Low (Near Equilibrium) Hydrogen Pressure, Journal of Alloys and Compounds 361 (2003) 130–137.

VITA

Grant William Helmreich received his Bachelor of Science degree in Nuclear Engineering and his Bachelor of Arts degree in Chemistry from Texas A&M University in 2009. He then received a Masters of Science in Nuclear Engineering at Texas A&M University in December 2010. His research interests include the fabrication and testing of advanced nuclear fuels, particularly metal fuels.

Grant William Helmreich may be reached at Dept of Nuclear Engineering, Texas A&M University, College Station, TX 77843-3133. His email is granthelmreich@gmail.com.

CHARACTERIZATION STUDY OF ALPHA PHASE URANIUM SINTERING FOR ADVANCED NUCLEAR FUEL APPLICATIONS

10/11/2010

M.S. Thesis

Grant W. Helmreich

Outline

- Introduction
- Background
- Experimental Design and Procedures
- Results
- Discussion and Summary

Introduction

Introduction – Basis for Research

- This research was conducted as a part of the DOE Nuclear Energy Research Initiative (NERI), under the Advanced Fuel Cycle Initiative (AFCI)
- The primary goal of this research was to characterize the α-phase sintering of uranium and uranium-zirconium
  - Providing a scientific basis to understand industrial techniques for powder metallurgy fabrication
- This thesis forms a portion of a larger research initiative into low temperature fabrication of U-Pu-TRU-Zr alloy fuel

Introduction – Research Overview

- Uranium powder was produced using a hydride/dehydride process
- Depleted Uranium (DU) and DU-Zr pellets were fabricated and sintered
- Rate of sintering was monitored by Linear Variable Differential Transformer (LVDT)
- Sintering rates under varying temperature profiles were analyzed based on a theoretical model
- Sintered microstructures were analyzed by SEM

Background

Uranium Fuel Fabrication

- Previous metal fuel fabrication predominantly used injection casting
  - Uranium and alloying constituents melted at ~1500°C
  - Liquid fuel is forced into quartz mold by pressure differential
  - Fuel is broken away from molds once cool

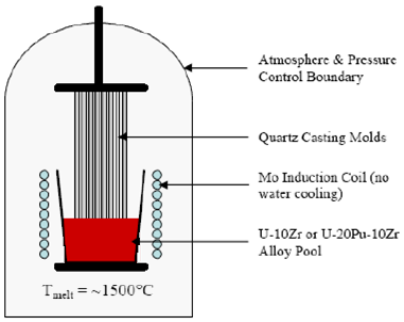

Injection Casting Issues

- Some transuranics (americium, curium, neptunium) have high vapor pressures at injection casting temperatures
- Initial efforts at U-TRU-Zr fabrication resulted in 40% americium losses
- Process modification with cover gas and cold trap reduced losses to under 1%, potentially resolving this issue
- A powder metallurgy approach based on extrusion may provide a viable, low temperature alternative

Prior Work in α-Phase Uranium Sintering

- Low temperature sintering of U-TRU-Zr in the uranium α-phase was investigated at Texas A&M in the FCML by D. Garnetti
- Sintering was observed at temperatures below 660°C for DU and DU-Zr samples
- Rate studies and modeling were not performed
- No alloying was observed
- Delamination cracking was an issue

Basics of Sintering

- Conversion of compacted particles into interconnected solids by heating
- Driving force is reduction of surface energy
- Surface transport and bulk transport are two primary categories of sintering mechanisms
  - Surface transport mechanisms include surface diffusion, evaporation/condensation, and volume diffusion
  - Bulk transport mechanisms include grain boundary diffusion, volume diffusion, and plastic flow

Modeling Sintering

- German sintering rate model based on shinkage

$$\left(\frac{\Delta L}{L}\right)^{n/2} = \frac{B_0 \cdot t}{2^n \cdot D^m} \cdot e^{-Q/kT}$$

$$Ln\left(\frac{\Delta L}{L}\right) = Ln(C_1) + \frac{2}{n} Ln(t)$$

$$Ln\left(\frac{\Delta L}{L}\right) = Ln(C_2) - \frac{2 \cdot Q}{n \cdot k} \cdot \frac{1}{T}$$

R.L. German, Sintering Theory and Practice

Uranium Hydride

$$2U + 3H_2 \leftrightarrow 2UH_3$$

- Uranium reacts reversibly with hydrogen to form UH_3
- Volume increase causes spalling, producing fine UH_3 powder
- Temperature increase and vacuum reverses reaction, leaving fine uranium powder
- Thin oxide layer sufficient to prevent hydriding

Experimental Design and Procedures

Large Inert Atmosphere Glovebox

Hydride Dehydride Apparatus

- Uranium coupons loaded into yttria crucible with stainless steel mesh
- Hydride/dehydride apparatus inserted and sealed within glovebox furnace well
- Tubing with purification system allowed controlled gas flow or vacuum

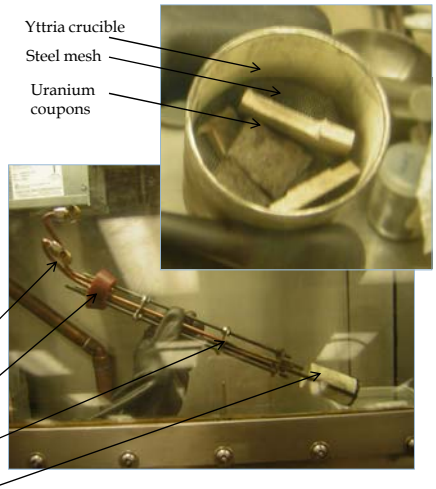

Processing Conditions

- Hydriding: 235°C, ~24 hours, 3-5 psi Ar-5%H_2, 2-4 SCFH
- Dehydriding: 330°C, 30-60 minutes, 10^{-3} torr
- Dehydriding step could result in light sintering of uranium powder

Lightly sintered powder following dehydriding

Unsintered loose powder following dehydriding

Powder Characterization

- Atmospheric Containment Vessel (ACV) used to transfer pyrophoric uranium powder outside glovebox
- Quartz viewing lens allowed imaging with Hirox KH-1300 Optical Microscope
- Particle size distribution based on ImageJ analysis

Powder Compaction

- Powder loaded into SS 303 die with dual action, heat treated H13 steel punches
- Carver Mini-C pressed pellets with 10,000 lbs (90,500 psi) for 15 seconds

Sintering Apparatus

- Pellets sintered in yttria crucible suspended in glovebox furnace well
- Steel rod resting on pellet connected to magnet within Linear Variable Differential Transformer (LVDT)
- Thermocouple provided accurate measure of sintering temperature

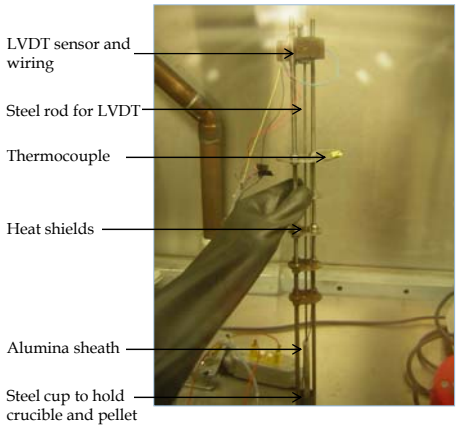

Data Collection and Analysis

- Labview SignalExpress converted output into temperature and relative LVDT position
  - LVDT output converted to pellet shrinkage
  - Shrinkage data used with German model
- Pellet cross-sections polished and imaged
  - Optical imaging with Hirox KH-1300
  - SEM imaging with Cameca SX50 Electron Microprobe

Results

Results – Powder Analysis

Sample Powder Image

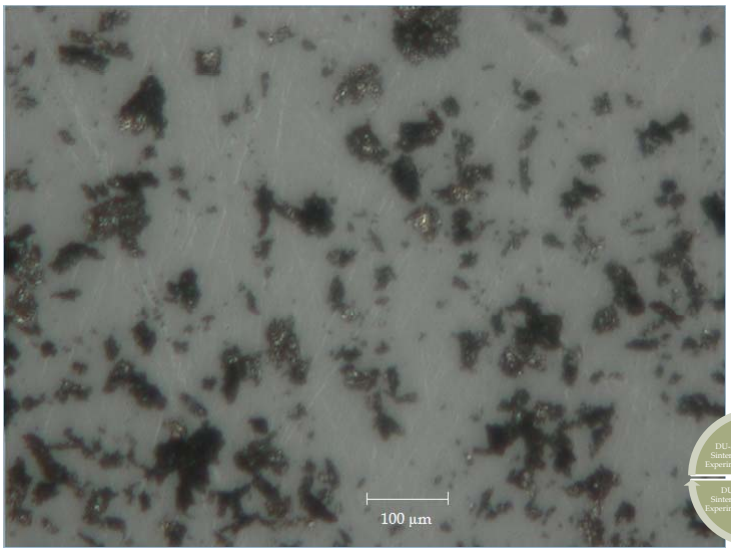

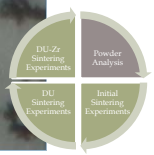

Particle Size Distribution

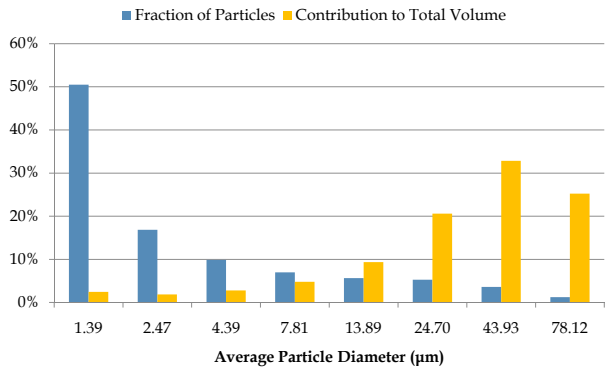

- Size distribution calculated assuming approximately spherical particles
- Volume distribution peaks at ~40µm diameter particles
- Number distribution weighted to smallest particles

Results – Initial Sintering Experiments

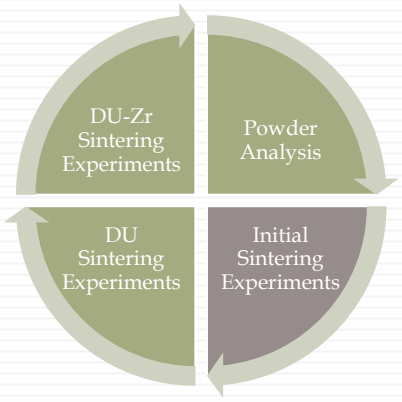

Pellet 1

- Pressed to 15,000 lbs (135.8 ksi) then allowed to rest a total of eight times
- Small chips broke from pellet upon removal from die
- LVDT showed no signs of sintering after 24 hours at 630°C

Pellet 2

- Pressed to 10,000 lbs (90.5 ksi) for 30 minutes
- Significant crumbling occurred upon removal from the die
- Due to similarity to Pellet 1, no attempt was made to sinter Pellet 2
  - In both cases, crumbling was likely due to powder binding to sides of die

Pellet 3 – Sintering

- Pressed to 10,000 lbs (90.5 ksi) for 15 seconds
- No chipping or crumbling upon die removal
- Isothermal sintering was not observed
  - Probably due to partial sintering during dehydride process
- Red powder observed at contact between pellet and steel LVDT rod

Results –DU Sintering Experiments

Sintered DU Pellet Summary

	α-Phase Temperature	γ-Phase Temperature	Green Density	Sintered Density
Pellet 4	655°C	831 °C	53.95%	57.87%
Pellet 5	643°C	820 °C	47.21%	49.88%
Pellet 6	634°C	809 °C	46.68%	50.46%
Pellet 7	659°C	834 °C	47.17%	51.22%
Pellet 8	651°C	826 °C	48.20%	51.97%

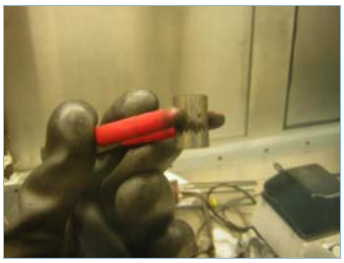

Pellet 4 – Sintering

- Initial shrinkage observed during heating
- Steady isothermal shrinkage observed during both α-phase and γ-phase

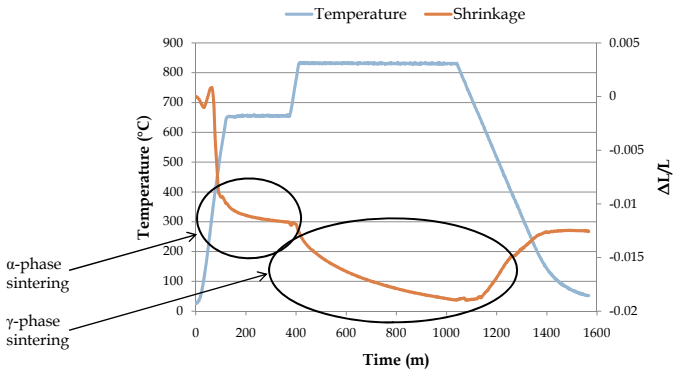

Pellet 4 – Imaging

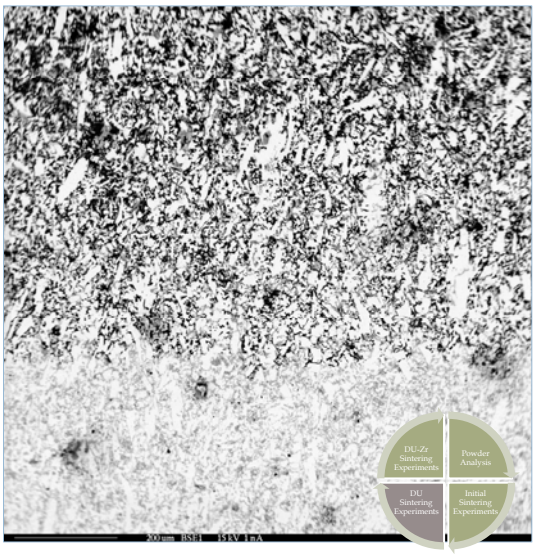

Pellet 5 – Sintering

- Black oxide layer formed at contact between pellet and alumina sleeve holding LVDT rod

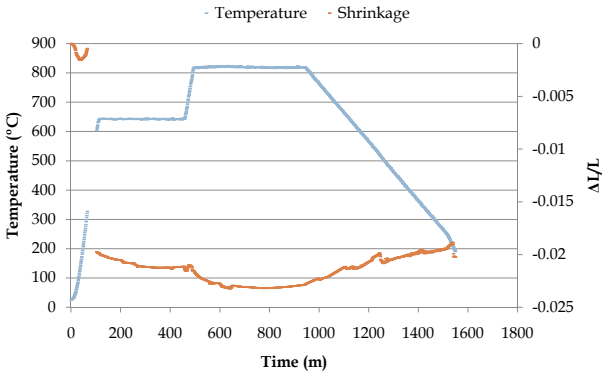

Pellet 5 – Imaging

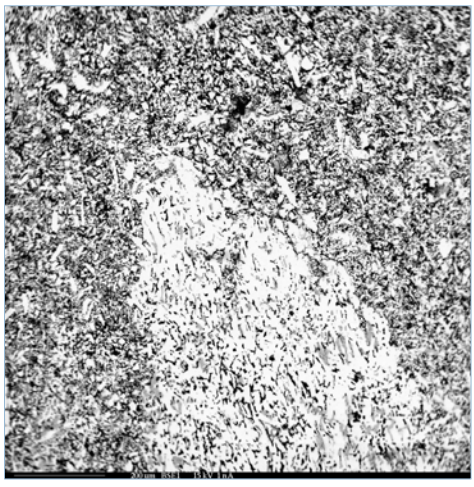

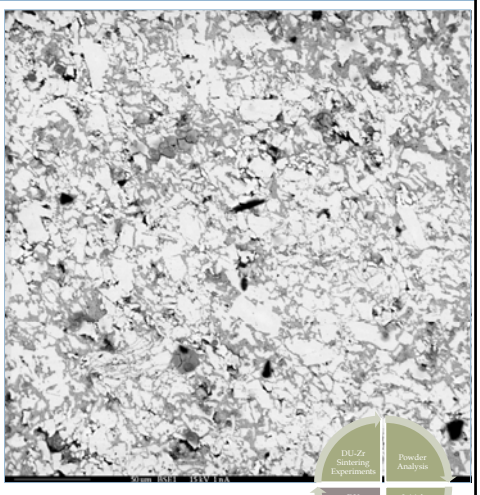

Pellet 6 – Sintering

- Slow shrinkage followed by expansion
- Black oxide formation was once again present

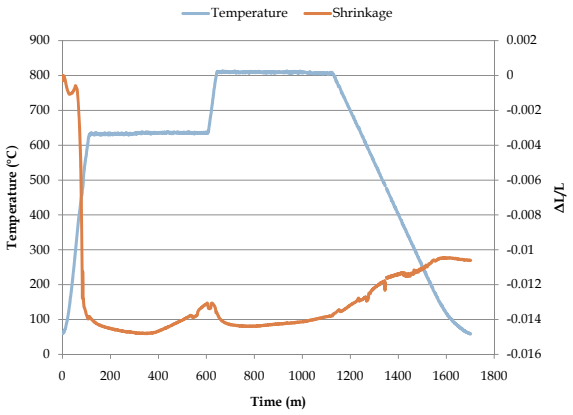

Pellet 6 – Imaging

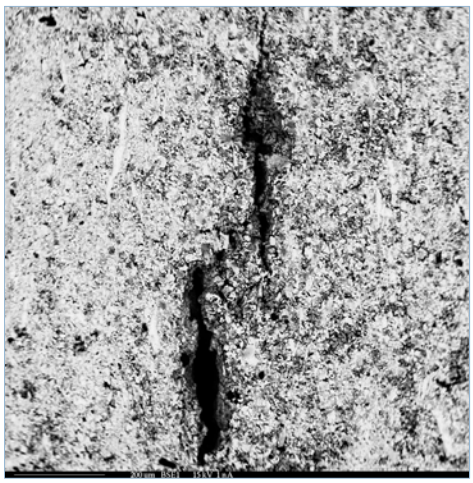

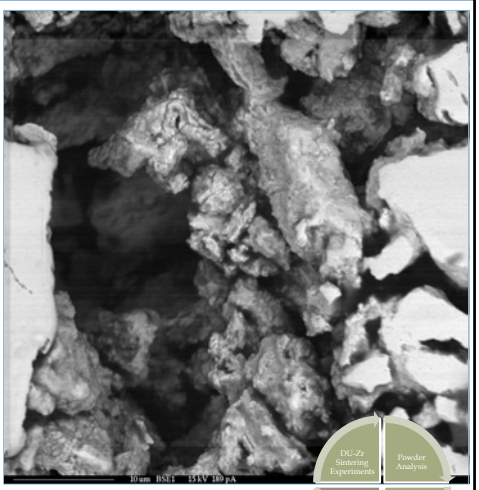

Pellet 7 – Sintering

- Oxide formation was limited

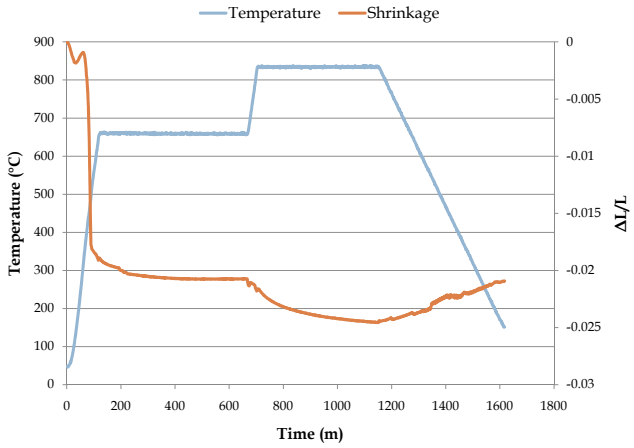

Pellet 7 – Imaging

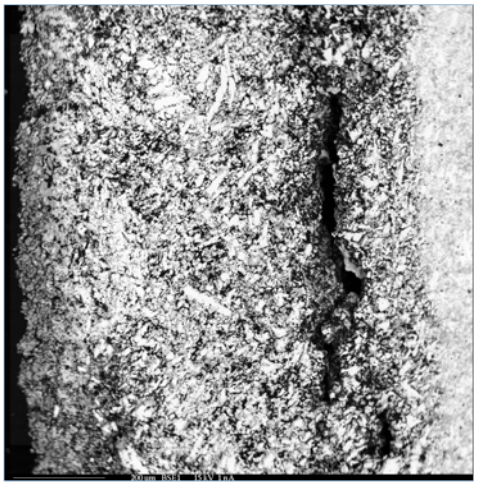

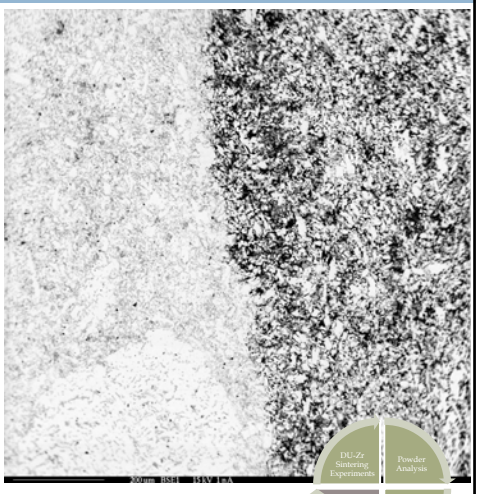

Pellet 8 – Sintering

- Steady sintering observed in both phases
- Oxide formed only light powder

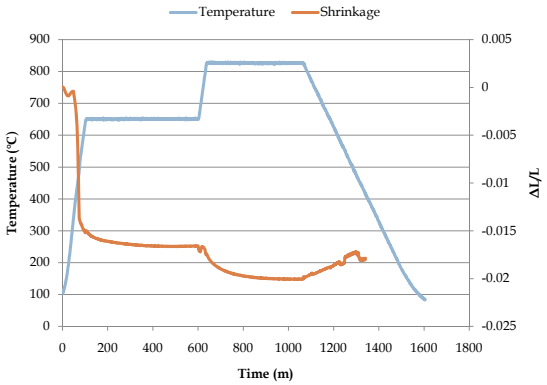

Porosity of Sintered DU Pellets

- All DU pellets had inner low porosity region and outer high porosity region

	α-Phase Temperature	γ-Phase Temperature	Porosity of Outer Region	Porosity of Inner Region
Pellet 4	655°C	831 °C	32.3%	11.5%
Pellet 5	643°C	820 °C	36.2%	13.2%
Pellet 6	634°C	809 °C	40.0%	9.7%
Pellet 7	659°C	834 °C	30.9%	3.2%
Pellet 8	651°C	826 °C	23.0%	1.1%

Determination of *n* for Isothermal DU

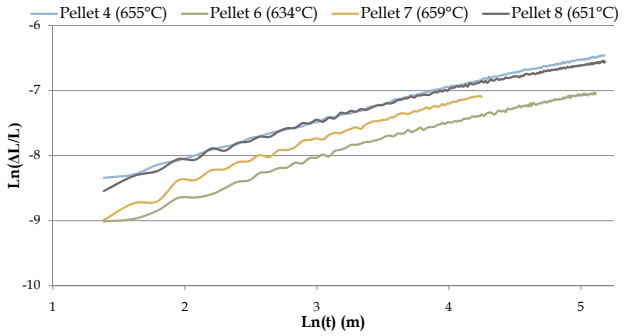

	α-Phase Temperature	Calculated n	R^2
Pellet 4	655°C	4.11	0.9933
Pellet 6	634°C	3.93	0.9860
Pellet 7	659°C	3.26	0.9870
Pellet 8	651°C	4.36	0.9812

Determination of *Q* for Isothermal DU

- Activation energy of 340 kJ/mol

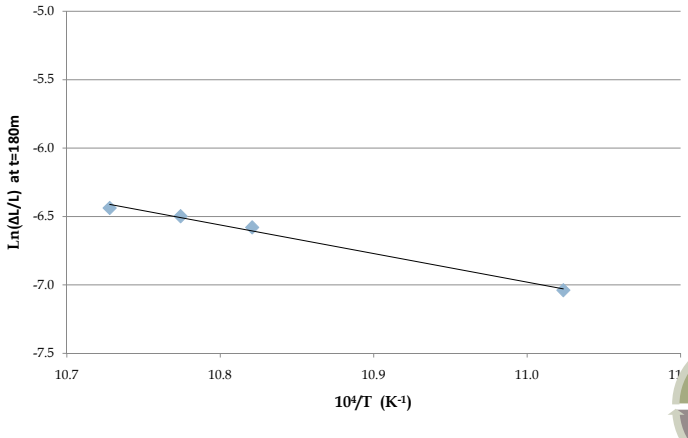

Results – Isothermal DU-Zr Sintering

Isothermal DU-Zr Pellet Summary

	Contents (wt%)	Compaction Pressure	α-Phase Temperature	γ-Phase Temperature	Green Density	Sintered Density
Pellet 9	DU-10Zr	90.5 ksi	635 °C	817 °C	51.3%	55.7%
Pellet 10	DU-10Zr	90.5 ksi	642 °C	819 °C	50.7%	55.8%
Pellet 11	DU-10Zr	90.5 ksi	652 °C	829 °C	51.3%	56.5%
Pellet 14	DU-5Zr	181 ksi	650°C	N/A	52.4%	58.7%

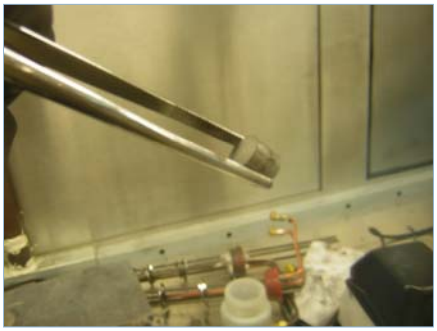

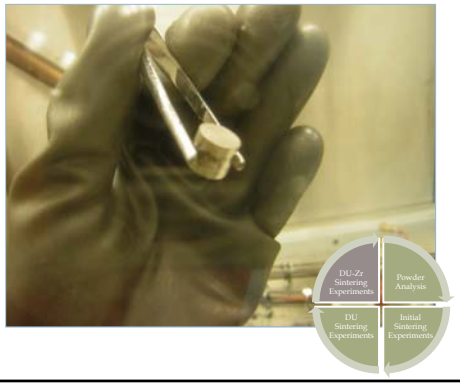

Pellet 9 – Sintering

- Sintering in both phases much more rapid than for DU

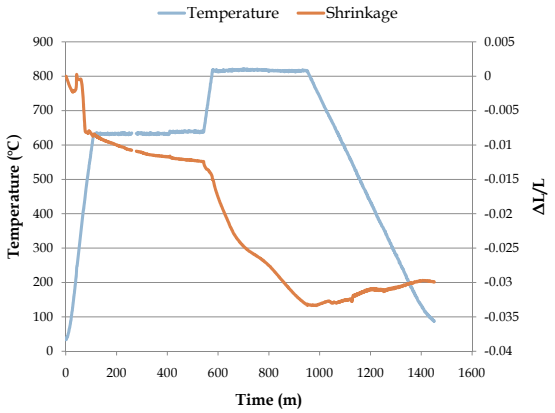

Pellet 9 – Imaging

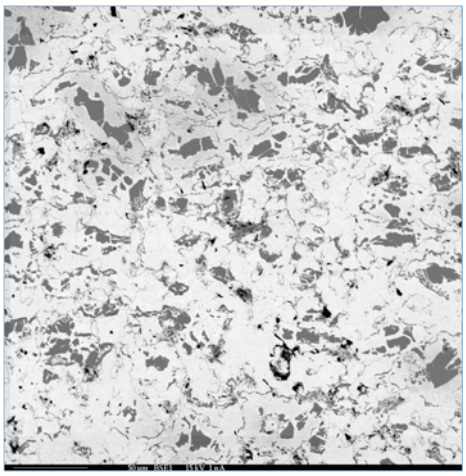

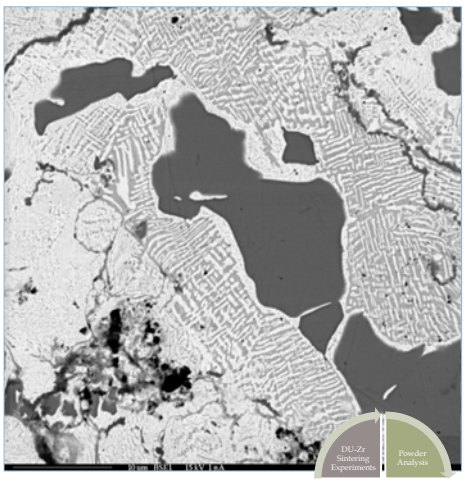

Pellet 9 – Imaging

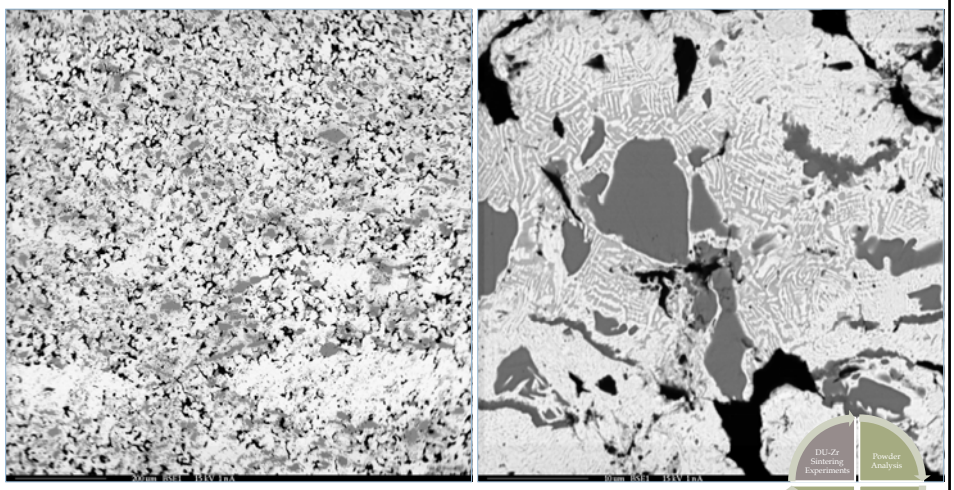

Pellet 10 – Sintering

- Repeated 'hump' in γ-phase

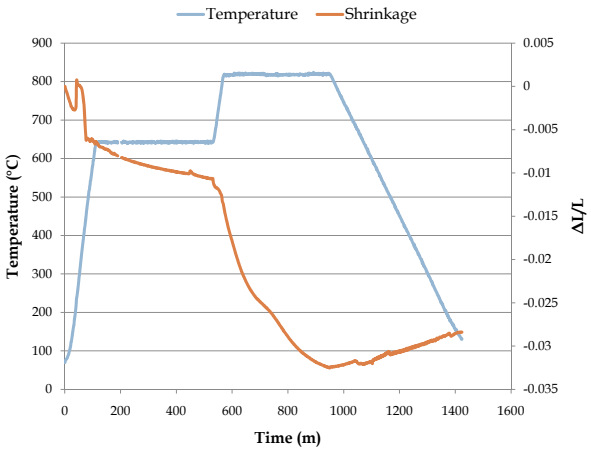

Pellet 10 – Imaging

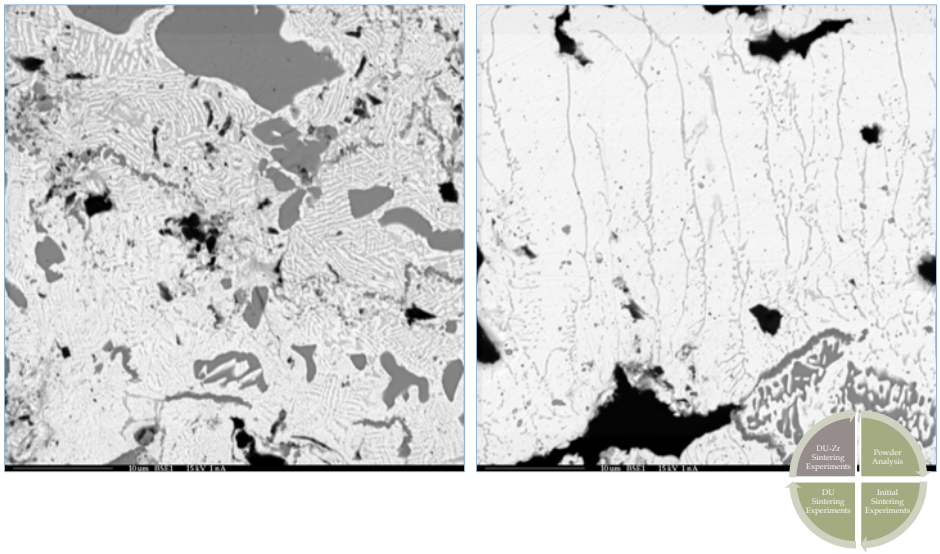

Pellet 11 – Sintering

- Furnace malfunction cut γ-phase sintering short and resulted in natural cooling

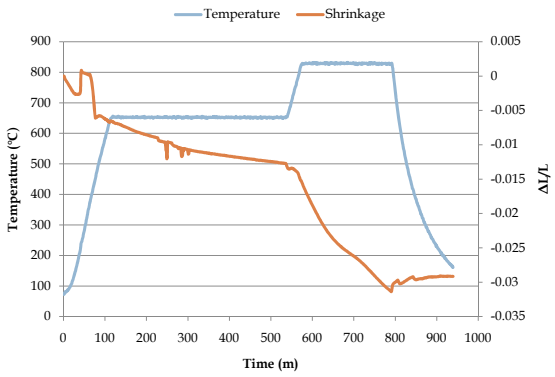

Pellet 14 – Sintering

- Double compaction force of prior pellets
  - Porosity was low, and constant across full cross section (0.5%)
- Sintered for 48 hours at 650°C
  - Only pellet sintered exclusively in α-phase
- SignalExpress crashed mid-run
  - Densification still indicates that significant sintering took place

Pellet 14– Imaging

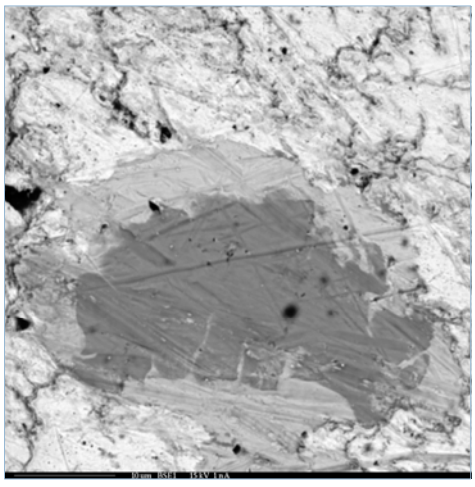

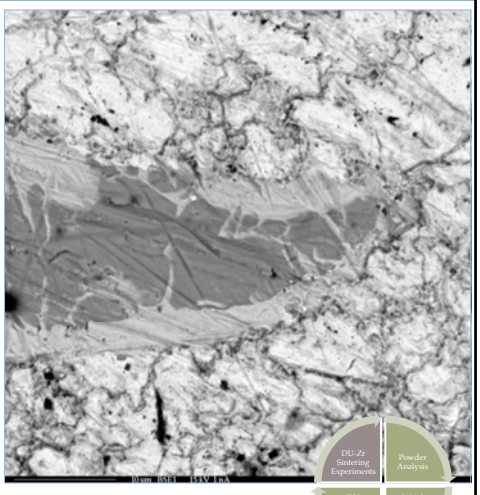

Porosity of DU-Zr Pellets

- The porosity of DU-Zr pellets was consistently lower than DU pellets

	Porosity of Outer Region	Porosity of Inner Region
Pellet 9	12.0%	1.0%
Pellet 10	14.2%	1.5%
Pellet 11	8.7%	5.8%
Pellet 14	0.5%	0.5%

Determination of *n* for DU-10Zr

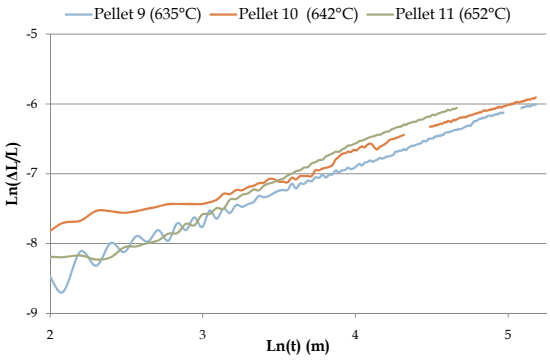

	α-Phase Temperature	Calculated n	R^2
Pellet 9	635°C	2.55	0.9871
Pellet 10	642°C	2.29	0.9855
Pellet 11	652°C	3.11	0.9876

Determination of *Q* for DU-10Zr

- Activation energy of 278 kJ/mol

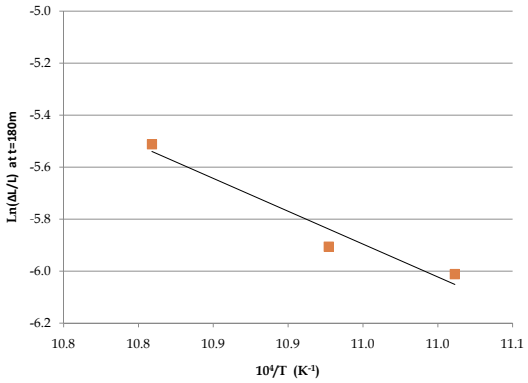

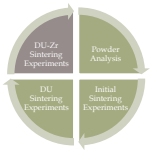

Discussion and Summary

DU Versus DU-Zr

- Both DU and DU-Zr pellets sintered in the α and γ phases
- In both phases, the sintering of DU-Zr was significantly faster
- The sintered porosity of DU-Zr was lower than that of DU, even for shorter durations

Sintering Models

- The German model worked with sintering data from both DU and DU-10Zr
  - n and Q values for both have been determined
- The calculated values of Q were lower than the known values for γ-phase uranium, which is reasonable given slower diffusion in α-phase

Sintered Phases in DU-Zr

- Pure zirconium and uranium with some dispersed zirconium were consistently observed
- Sintering in the γ-phase produced a lamellar α+δ phase
- Sintering for exclusively in the α-phase produced a homogeneous δ-phase

Heterogeneous Porosity

- Pellets pressed to 90.5 ksi had inner low porosity region and outer high porosity region
- Likely the result of density gradients during compaction
- Increasing compaction pressure to 181 ksi resulted in consistently low, even porosity

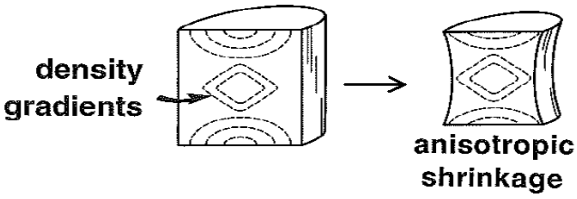

Reduction of Delamination Cracking

- Previous α-phase sintering experiments resulted in widespread cracking due to delamination during cooling
- This issue was addressed by sieving to remove large particles and slow controlled cooling
- Using these protocols, cracking was rare, and cracks were much smaller

Summary of Results

- A model for the initial phase of sintering for DU and DU-10Zr was developed based on isothermal shrinkage rates during sintering
- The effects of zirconium addition to uranium during sintering were measured
- The microstructure of sintered uranium-zirconium pellets was analyzed, indicating the presence of the alloyed α+δ phase when sintered in the γ-phase and the presence of δ phase when sintered in the α-phase
- The uranium powder produced by the hydride/dehydride method was characterized to determine size distribution and morphology
- Previous issues with pellet cracking during cooling due to delamination were resolved by the use of controlled cooling and finer control over the quality of the uranium powder

Acknowledgements

- Dr. McDeavitt for his guidance and counsel throughout this project
- Dr. David Cecala and the Y-12 Plant at ORNL for supplying the DU used in this project
- Will Sames for designing apparatus and assisting in powder characterization
- Brandon Blamer for his assistance in sectioning and polishing samples
- David Garnetti for prior research in the FCML which formed the starting point of this project

References

1 - D. E. Burkes, R.S. Fielding, and D.L. Porter, Metallic Fast Reactor Fuel Fabrication for the Global Nuclear Energy Partnership, Journal of Nuclear Materials 392 (2009), 158-163.

2 - C.L. Trybus, J.E. Sanecki, S.P. Henslee, Casting of Metallic Fuel Containing Minor Actinide Additions, Journal of Nuclear Materials 204 (1993) 50-55.

3 – D. Garnetti, S.M. McDeavitt, Uranium Powder Production via Hydride Formation and Alpha Phase Sintering of Uranium and Uranium-Zirconium Alloys for Advanced Nuclear Fuel Applications. Masters Thesis, Texas A&M University, College Station, TX.

4 - R.M. German, Sintering Theory and Practice, John-Wiley & Sons, Inc., New York, (1996).

5 - Powder Metallurgy by Fritz V. Lenel, pg 211-268

6 – J.J. Carroll, A.J. Melmed, Field Ion Microscopy of Alpha Uranium, Surface Science 116 (1982) 225-239.

7 - W.D. Wilkinson, Uranium Metallurgy, John Wiley & Sons, Inc., New York (1962).

8 – L. Grainger, Uranium and Thorium, George Newnes Limited, London (1958).

9 – S.F. Pugh, Swelling in Alpha Uranium due to Irradiation, Journal of Nuclear Materials 4 (2) (1961) 177-199.

10 – J.J. Burke, D.A. Colling, A.E. Gorum, J. Greenspan, Physical Metallurgy of Uranium Alloys, Brook Hill Publishing Company, Columbus (1976).

11 - C.E. Stevenson, The EBR-II Fuel Cycle Story, La Grange Park, Illinois: American Nuclear Society Inc. (1987).

12 - P. Chiotti, B.A. Rogers (1950), The Production of Uranium and Thorium in Powder Form, United States Atomic Energy Commission, AECD-2974.

13 - S.M. McDeavitt (1992), Hot Isostatic Pressing of DU-10Zr Alloy Nuclear Fuel by Coupled Grain boundary Diffusion and Power-Law Creep. Doctoral Thesis, Purdue University, West Lafayette, IN.

14 - S.M. McDeavitt, A.A. Solomon, Hot-Isostatic Pressing of DU-10Zr by a Coupled Grain Boundary Diffusion and Creep Cavitation Mechanism, Journal of Nuclear Materials 228 (1996) 184-200.

15 - T. Hashino, Y. Okijima, Mechanism of the Reaction of Hydrogen with Uranium, Journal of Physical Chemistry 77 (1973) 2236-2241.

16 - C.R. Clark, M.K. Meyer, Fuel Powder Production from Ductile Uranium Alloys, Presented at the 1998 International Meeting on Reduced Enrichment for Research and Test Reactors, Oct. 18 - 23, 1998, Sao Paulo, Brazil.

17 - J. Bloch, The Hydriding Kinetics of Activated Uranium Powder Under Low (Near Equilibrium) Hydrogen Pressure, Journal of Alloys and Compounds 361 (2003) 130–137.

Appendices

Sintering Mechanisms

- Surface Transport
  - Evaporation Condensation
  - Surface Diffusion
  - Volume Diffusion
- Bulk Transport
  - Grain Boundary Diffusion
  - Volume Diffusion
  - Plastic Flow

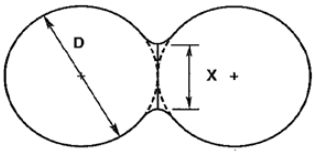

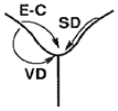

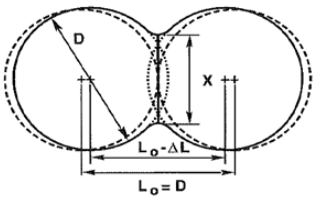

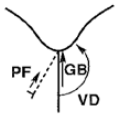

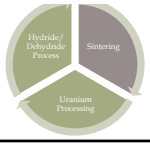

Uranium Metallurgy

- Three allotropes of uranium: α (T<667°C), β (667°C<T<772°C), and γ (772°C<T)
- α uranium possesses complex orthorhombic lattice structure
- Orthorhombic structure undergoes anisotropic expansion during cyclic heating and irradiation
- Addition of zirconium reduces anisotropic swelling issues

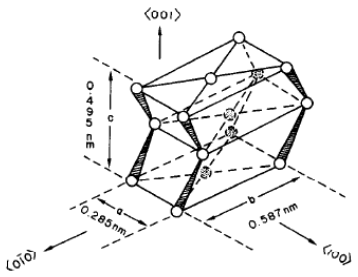

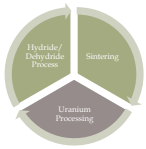

Hot Extrusion of Alpha Phase Uranium-Zirconium Alloys for TRU burning Fast Reactors

Jeffrey S. Hausaman, Sean M. McDeavitt

Texas A&M University, 3133 TAMU, College Station, Texas 77843-313, jeffrey.hausaman@gmail.com

OBJECTIVES

Conventional nuclear reactors generate transuranic (TRU) isotopes from normal operation. These isotopes have high radiotoxicity, high heat load and relatively long half lives which complicate the disposition of them in a geologic repository. By utilizing these TRU isotopes as fuel for fast reactors, they may be consumed to produce an additional energy yield. In support of this goal, the fabrication of metal fuel elements for fast reactors which contain TRU isotopes is being explored.

This project utilizes powder metallurgy to fabricate U-Zr-TRU alloys using hot extrusion at relatively low temperatures (600-650°C) with magnesium and manganese used as surrogates for TRU elements. Magnesium and manganese were chosen as surrogates for this project due to americium and curium being highly radioactive elements. Magnesium and manganese both have vapor pressures on the order of or higher than americium and curium, thus it can be expected that if the hot extrusion process results in full retention of the surrogate material it will be a good indication that americium and curium would also be retained. The alpha phase sintering and hot extrusion properties of these powdered materials are the processes which are being quantified.

CURRENT RESEARCH STATUS

The preferred method of fabricating metal fuel elements has historically been a casting method, where a molten uranium alloy mix was drawn up into an evacuated quartz mold, allowed to cool and broken open to produce a pin. Introducing the transuranic elements americium and curium into the casting caused evaporative losses due to the high vapor pressure they possess at the temperature that uranium and zirconium melt.

In order to be able to incorporate these elements without suffering evaporative losses, alternative methods of fabrication are being explored. This project is part of an investigation into the application of powder metallurgy through sintering and hot extrusion for fabricating these volatile alloy components into a usable fuel form.

Previous research in this area of uranium powder metallurgy involved a series of alpha phase sintering experiments performed by David Garnetti and Grant Helmreich[1]. These experiments quantified the rate at which alpha phase uranium would sinter at temperatures below 650°C. Sintering is a process where heat is applied to a powdered material and diffusion drives the particles to combine and form a uniform matrix.

The process of hot extrusion of metal powders is in fairly common use for fabricating a large variety of materials. An advantage to the hot extrusion process is the favorable economics of fabrication when working with pieces smaller than a ton in weight, as compared to other fabrication methods[2]. Previous work has studied hot extrusion of uranium alloys, however they were not performed with uranium powders[3].

WORK TO BE COMPLETED

The majority of the work completed thus far has centered around developing a suitable method for producing powdered uranium that could then be used to perform the sintering and extrusion studies. The method that was chosen for generating uranium powder was a hydride-dehydride process. Pieces of depleted uranium metal, supplied by the Y-12 National Security Complex, are washed in nitric acid to clean any oxidation off of them and moved into an argon atmosphere glovebox. Within the glovebox, they are placed into a furnace well and exposed to hydrogen at 225°C. The resulting density change from the hydride process results in a uranium hydride powder. This powder is then placed under vacuum and heated to 430°C, which disassociates the hydrogen from the uranium[4].

After this uranium powder has been generated it can then be used either in the sintering studies or to make hot extruded samples. The uranium, zirconium and TRU surrogate powders are thoroughly mixed to ensure uniformity. This powder mixture is then loaded into a copper extrusion canister and sealed with a crimped lid for hot extrusion, or pressed into pellets for studying sintering. The canister is then moved outside the glovebox to the extrusion apparatus, which consists of a 100 ton hydraulic press, a die apparatus constructed from H-13 tool steel (shown in Fig 1.) and a Watlow tube furnace.

Fig 1. The hot extrusion tooling assembly. From left to right: The top piece which holds the sample canister, the base, the extrusion ram, and the reduction die.

The canister is then placed inside the die apparatus with a copper plug on top of the canister. The assembly is pressed such that the copper plug and canister deform and form an airtight seal in the extrusion apparatus. The apparatus is heated to between 600°C and 650°C and upon reaching the desired temperature, the press activates and extrudes the sample into a U-Zr-Mg/Mn alloy with a copper jacket. This sample is then analyzed via optical and electron microscopy to evaluate the degree of densification and phase morphology. Other methods of analysis will include differential scanning calorimetry, which will be used to observe phase transformations in the extruded alloys as well as quantify the heat capacity of the alloy. To quantitatively analyze the samples based off of the electron microscopy images and wavelength dispersive x-ray spectroscopy will be used to evaluate if the concentration of magnesium or manganese was maintained during the extrusion process to demonstrate if there was any loss of material.

REFERENCES

1. D. J. GARNETTI, “Uranium Powder Production Via Hydride and Alpha Phase Sintering of Uranium-Zirconium Alloys for Advanced Nuclear Fuels Applications,” M.S. Thesis, Texas A&M University (2009).

2. Drozda, Tom; Wick, Charles; Bakerjian, Ramon; Veilleux, Raymond F.; Petro, Louis (1984), *Tool and manufacturing engineers handbook: Forming*, **2**, SME, ISBN 0872631354.

3. C. S. CHOI, "Texture of Extruded Uranium Alloy by Neutron Diffraction", Journal of Applied Crystallography (1985). **18,** 413-418.

4. G. HELMREICH, W. SAMES, et al "Uranium Powder Production and Characterization from a Hydride-Dehydride Process," Poster, ANS Student Conference (2010)

APPENDIX B

External presentations at the 2010 American Nuclear Society Winter Meeting

Powder Metallurgy of Alpha Phase Uranium Alloys for TRU burning Fast Reactors

Jeffrey S. Hausaman, David J. Garnetti and Sean M. McDeavitt

Texas A&M University, 3133 TAMU, College Station, Texas 77843-313, jeffrey.hausaman@gmail.com

INTRODUCTION

Conventional nuclear reactors generate transuranic (TRU) isotopes from normal operation. These isotopes have high radiotoxicity, high heat load and relatively long half lives which complicates their disposition in a geologic repository. By utilizing these TRU isotopes as fuel for fast reactors, they may be consumed to produce an additional energy yield. In support of this goal, the fabrication of metal fuel elements for fast reactors which contain TRU isotopes is being explored.

This project utilizes powder metallurgy to fabricate U-Zr-M alloys at relatively low temperatures (600-650°C), where M stands for magnesium and manganese which are used as surrogates for TRU elements. More specifically, a hot extrusion method has been developed to fabricate surrogate fuel alloys within a thin metal sheath. (A second component of this project is focused on alpha phase sintering; that work is outside the scope of this paper.)

WORK COMPLETED

The initial accomplishment of this project was the establishment of a suitable method for producing powdered uranium metal. Uranium powder slugs are converted to fine powder using a hydride-dehydride process. The depleted uranium metal was obtained from the Y-12 National Security Complex. The U slugs are washed in nitric acid to to remove surface oxidation and moved into an argon atmosphere glovebox. Within the glovebox, they are placed into a furnace well and exposed to hydrogen at 225°C. The resulting density change from U (~19.0 g.cm^3) to UH_3 (~10.9 g/cm^3) causes the solid chunk to disassemble into a fine hydride powder. The process vessel is then evacuated and heated to 430°C, which disassociates the UH_3 powder to form uranium metal powder [1]. The uranium powder is generated on an as-needed basis due to the rapid oxidation of the metal, even in a glovebox with ~5 ppm oxygen present.

The desired powder composition is prepared, thoroughly mixed to ensure uniformity, and then loaded into a copper extrusion canister and sealed with a crimped lid for hot extrusion. The canister is then moved outside the glovebox to the extrusion apparatus, which consists of a 100 ton hydraulic press, a die apparatus constructed from H-13 tool steel (shown in Fig 1.) and a Watlow tube furnace (T_{max} = ~1000°C).

The canister is placed inside the die apparatus with a copper plug on top of the canister. The assembly is pressed such that the copper plug and canister deform and form an airtight seal in the extrusion apparatus. The apparatus is heated to between 600°C and 650°C and upon reaching the desired temperature; the press activates and extrudes the sample into a U-Zr-M alloy with a copper jacket. This sample is then analysed via microscopy to evaluate the degree of densification and phase morphology.

Fig 1. Extrusion tooling assembly. From left to right: The top piece which holds the sample canister, the base, the extrusion ram, and the reduction die.

RESULTS

The uranium composition process currently converts an average of 30% of the solid uranium input into a free powder form suitable for experiments. The powder produced ranged from 1-100 μm, with a volumetric mode of 44 μm[2].The extrusion die was stress tested through extrusion of surrogate materials in order to verify the integrity of the apparatus. Extrusion and analysis of uranium alloy samples is currently underway.

ACKNOWLEDGEMENTS

David Garnetti, Grant Helreich and Will Sames, who each made significant contribution which enabled this work to be performed.

This research was performed in the Fuel Cycle Materials Laboratory at Texas A&M University as part of a project funded by the U.S. Department of Energy's Nuclear Energy Research Initiative (Project No. 07-060). Additionally, Dr. D. Cecala from Y-12 is acknowledged for providing depleted uranium.

REFERENCES

1. D. J. GARNETTI, "Uranium Powder Production Via Hydride and Alpha Phase Sintering of Uranium-Zirconium Alloys for Advanced Nuclear Fuels Applications," M.S. Thesis, Texas A&M University (2009).

2. G. HELMREICH, W. SAMES, et al "Uranium Powder Production and Characterization from a Hydride-Dehydride Process," Poster, ANS Student Conference (2010)

Powder Metallurgy of Alpha Phase Uranium Alloys for TRU Burning Fast Reactors

J. Hausaman, D. Garnetti, S. McDeavitt

FCML Fuel Cycle & Materials Laboratory

NERI Nuclear Energy Research Initiative

Advanced Fuel Cycle Initiative

Outline

- Introduction
- Powder Extrusion Method
- Description of Experimental Setup
- Analysis of Results

Introduction

- Motivation for incorporating other TRU in fuel
  - Waste Management
  - Fissile Nuclide Utilization
- Past Experience:
  - Up to 40% of the Americium content vaporizes out of the Injection Casting process.
  - Injection Casting challenges and impurities in fuel.

Powder Extrusion Process

- Convert U, Zr, TRU into powder.
- Mix powdered metals to designed composition.
- Load and seal metal powder mixture into extrusion canister.
- Heat extrusion canister and assembly to process temperature.
- Extrude through die to produce jacketed metal pin.

Experiment Flow

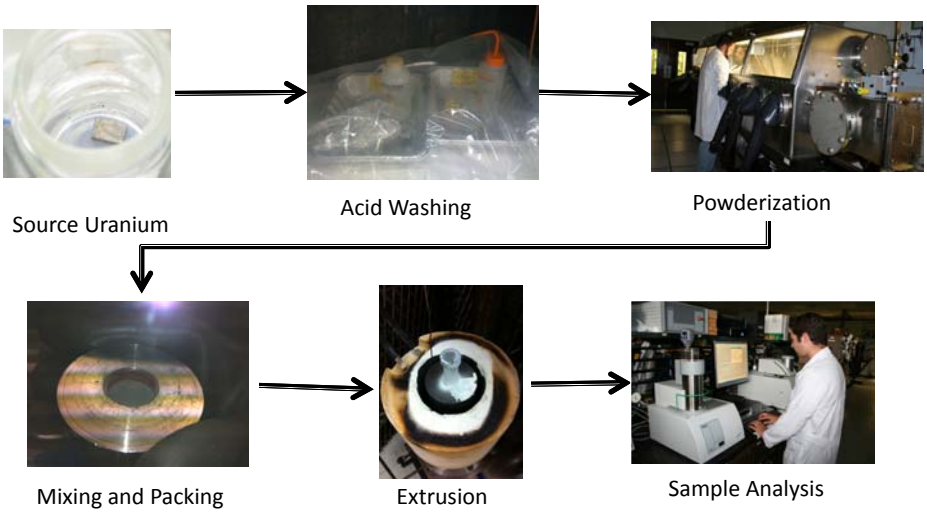

Experimental Procedure

- Acid Wash Uranium
  - Oxide layer is removed using nitric acid.
  - Uranium is transported from glovebag to glovebox.
- Generate Uranium Powder
  - Hydrided in Ar-5%H atmosphere at 225°C for 24 hours
  - UH_3 powder dehydrided in vacuum at 325°C for 35 minutes

Uranium-Zirconium Phases

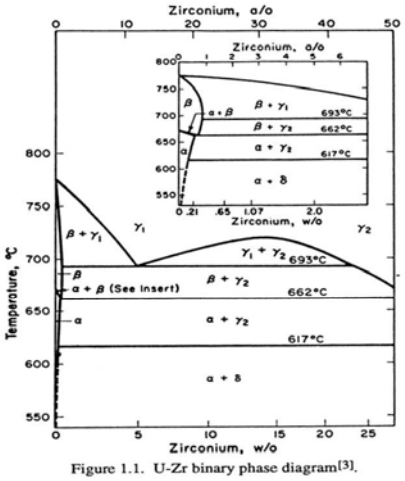

Figure 1.1. U-Zr binary phase diagram[3].

Experimental Procedure

- Mix together powdered U, Zr, Mg.
  - Mg used as a substitute for TRU
  - Similar melting point to Pu (650°C vs. 640°C)
  - More prone to vaporization than Am
- Load and seal metal powder into extrusion canister
  - Initial canisters: Copper
  - Final canister: Vanadium

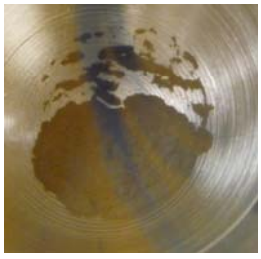

Experimental Procedure

- Heat extrusion canister and assembly to 600-650°C
  - Keeps uranium in alpha and gamma phase while avoiding beta phase.
  - Explores effects of liquid Mg phase sintering effects
- Extrude jacketed metal pin

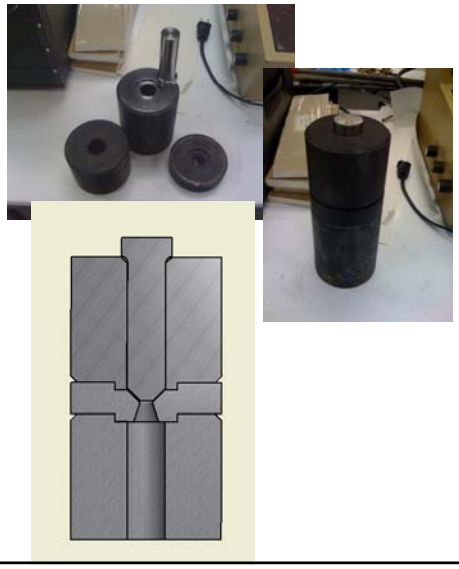

Extruded Sample

- Extrusion canister reduced from 1.905 cm (0.75 in) to 0.635 cm (0.25 in) diameter
- Extruded sample length 3.81-5.08 cm (1.5-2 in)

U-10Zr As Fabricated

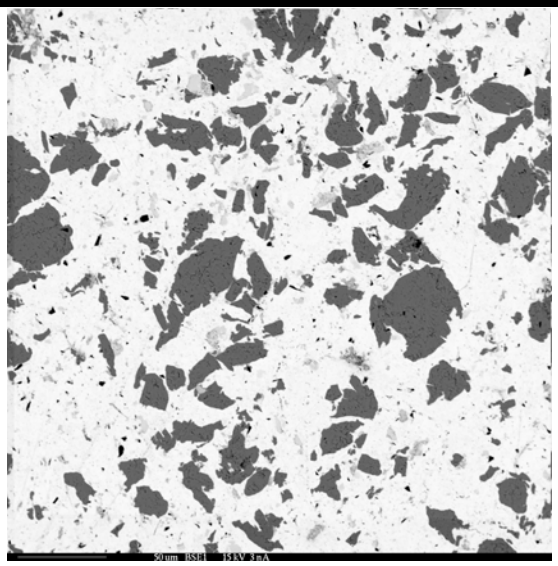

U-10Zr Heat Treated 800°C – 1hr

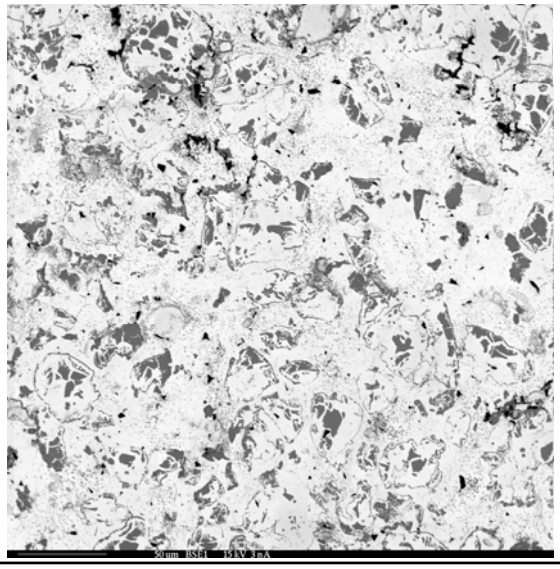

U-10Zr Heat Treated 800°C – 6hrs

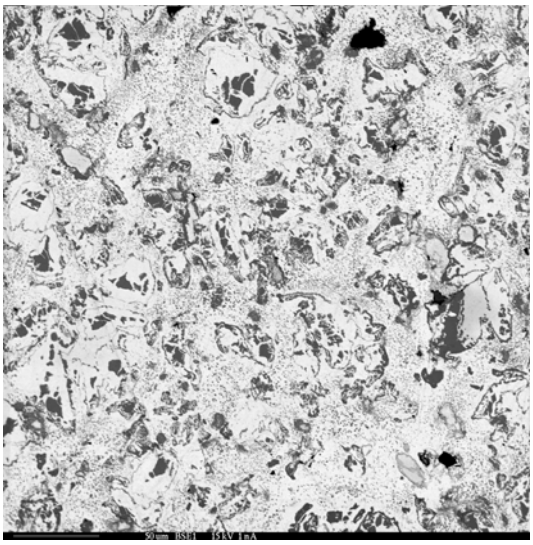

U-10Zr Heat Treated 800°C – 6hrs

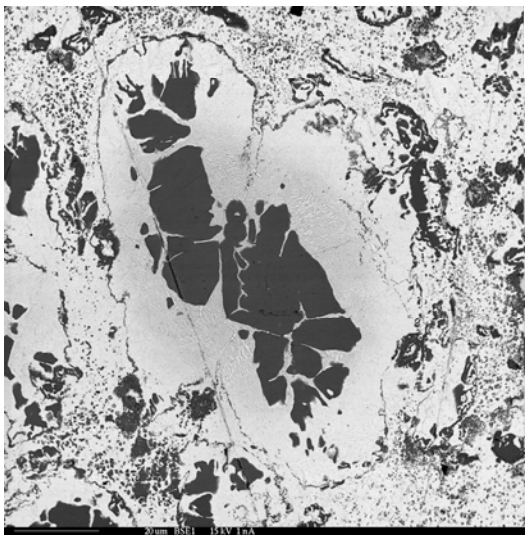

U-10Zr DSC Analysis

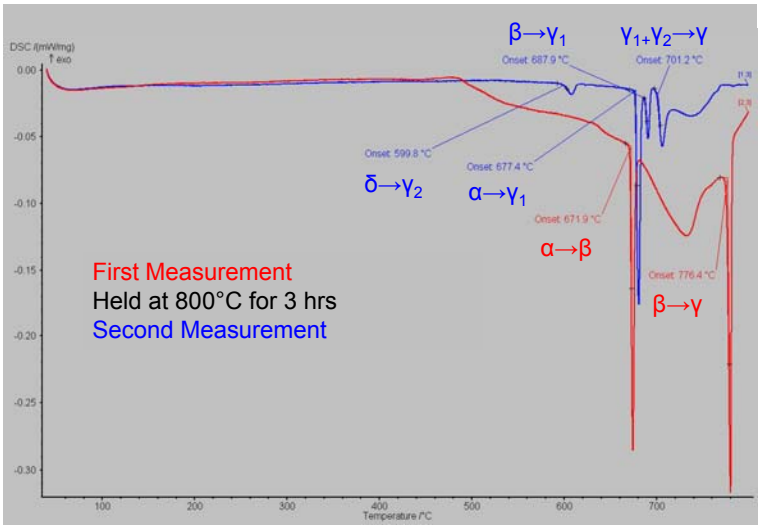

U-11Zr-4Mg As Fabricated (1000X)

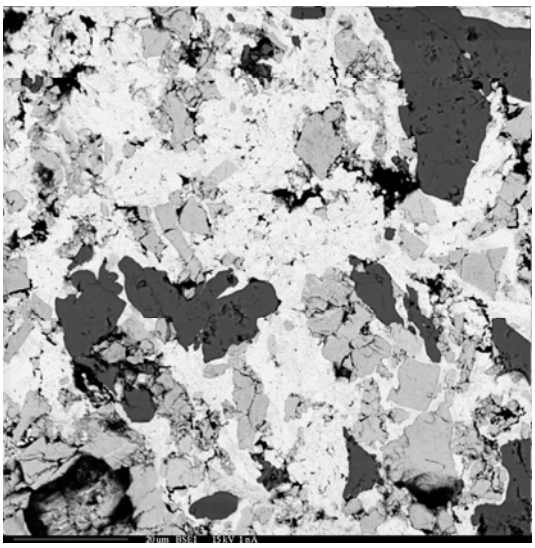

20 µm

U-11Zr-4Mg As Fabricated

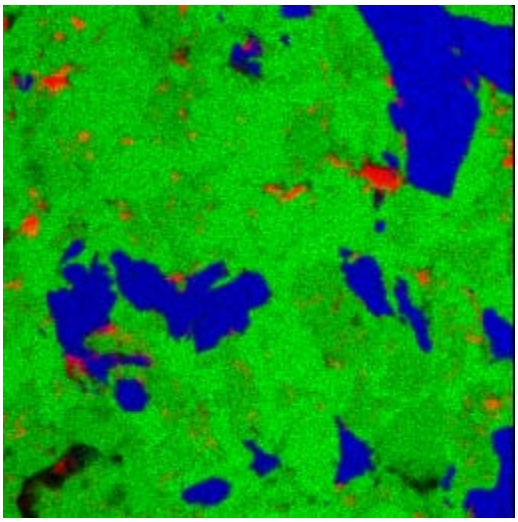

- Uranium
- Zirconium
- Magnesium

Summary

- Hot extrusion produces a very dense, highly segregated internal structure.
- Heat treatment will allow constituents to diffuse and form structures dependent on time and temprature.
- Magnesium appears to be retained during the process.

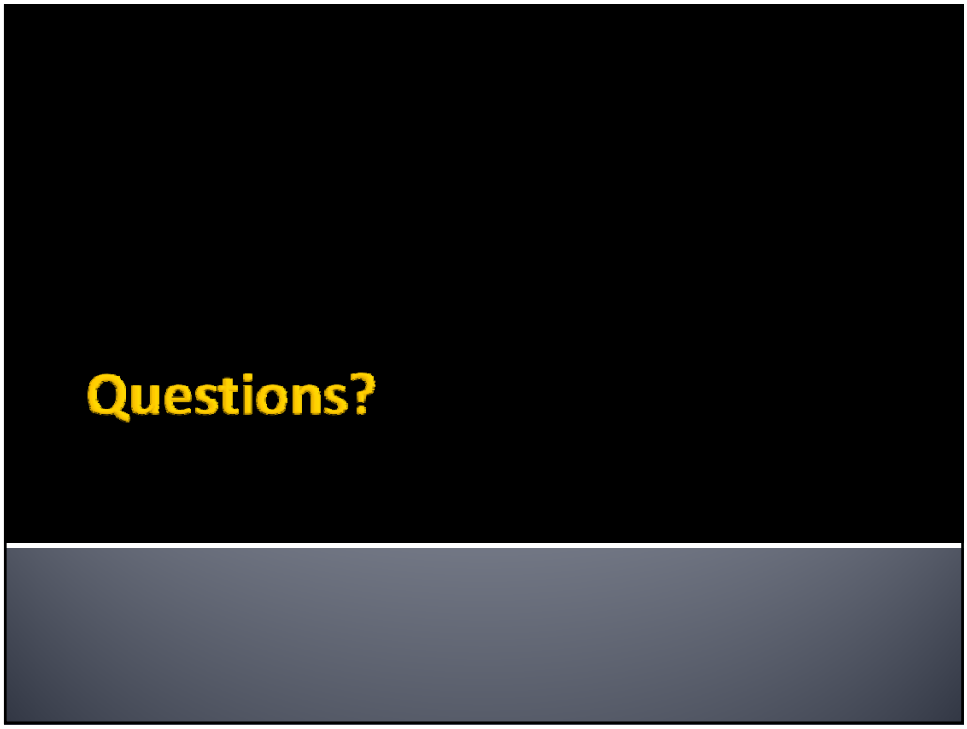
Questions?

Uranium Powder Production Using a Hydride-Dehydride Process

Grant W. Helmreich, William J. Sames, David J. Garnetti, and Sean M. McDeavitt

Department of Nuclear Engineering, Texas A&M University

I. INTRODUCTION

A hydride-dehydride process has been developed and successfully demonstrated in the Fuel Cycle and Materials Laboratory (FCML) at Texas A&M University. The particle size distribution for uranium metal powders produced by this process has been characterized.

This uranium powder production method was developed as part of a Department of Energy project for the Nuclear Energy Research Initiative (NERI). The motivation for this research was to develop an in-house powder production method to enable the development of powder metallurgical fabrication methods for uranium alloy nuclear fuels. The initial results were reported by D. Garnetti[1] and the continued investigation is reported below.

II. PROCESS

Powder Production

Solid depleted uranium slugs from the Y-12 plant were converted to powder using a hydride-dehydride process. The outer oxide layer on each sample was removed before hydriding by washing in a 35% by volume solution of nitric acid. Samples were then transferred to an argon glovebox equipped with a furnace well. Samples were sealed within the well under vacuum.

The hydriding process was accomplished by heating the well to 235°C while flowing argon-5%-hydrogen over the sample at 34.5 kPa (5 psig) and 1.2 L/min (2.5 SCFH) for twelve hours in each run.

Following the hydriding step, the dehydride process was initiated by ceasing gas flow to the well, drawing a vacuum of 0.1 Pa (1E-3 Torr), and increasing the well temperature to 400°C. The dehydride step was continued for two hours, after which the sample was cooled and the fresh uranium powder was removed.

The primary challenge encountered in this process was oxygen contamination. The presence of even 2-3 ppm of oxygen in the process gas was found to severely hinder hydriding of the uranium. This was addressed by the addition of oxygen and moisture traps to supply lines, which reduced oxygen levels to ~200 ppb.

Powder Characterization

Special capabilities were developed to prevent oxidation of uranium powder during imaging. An Atmosphere Containment Vessel (ACV) was created using simple KF vacuum fittings to enable the removal of uranium powder from the argon glovebox under a hermetic argon atmosphere. A fused silica view port with high optical resolution allowed capture of digital images using a Hirox MX-5040SZ Microscope.

Image analysis was performed using ImageJ software (version 1.38x 2007). Grayscale threshold image analysis was used to identify the number of pixels in each particle, then the pixel length of the image scale was used to determine the physical area each pixel represented. The area of each particle was converted into particle diameter and volume by assuming roughly spherical particles.

III. RESULTS

An example of a larger, 70 μm diameter uranium metal particle is shown in Figure 1. This particle demonstrates both shiny metallic regions and dull dark areas indicating oxidation. This image was taken using the ACV and Hirox MX-5040SZ.

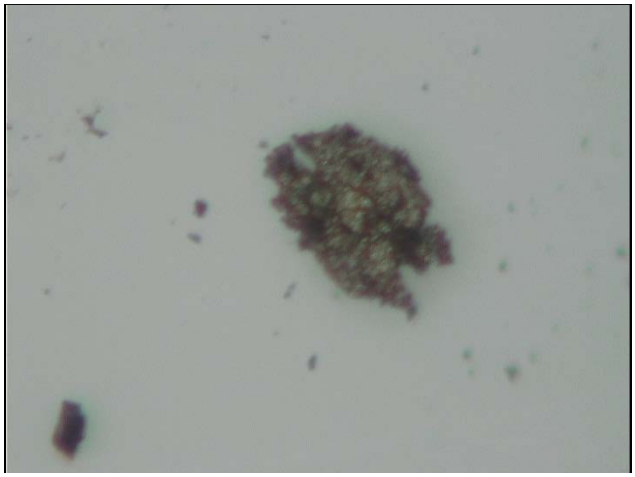

Fig. 1. Image of Uranium Powder at 800x.

The particle size distribution of uranium metal powder produced by the hydride-dehydride process is shown in Figure 2 (5895 particle sample set). The majority of particles were relatively small, with diameters of ~2 μm;

however, the majority of uranium by volume existed in larger particles with average diameter of ~40 μm. These results agreed with prior research which indicated the dominant particle diameter produced by the hydride-dehydride process to be 40 μm.[2,3]

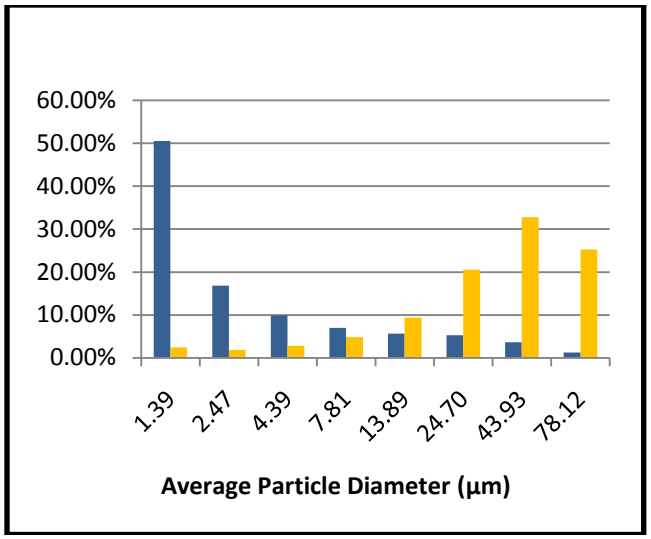

Fig. 2. Particle Size Distribution of Uranium Powder.

IV. FUTURE WORK

Future work will include characterization of hydriding rates with respect to temperature, time, and gas pressure. Further powder characterization work will be performed using SEM and XRD.

ACKNOWLEDGEMENTS

The authors would like to acknowledge the U.S. Department of Energy support under the Nuclear Energy Research Initiative (Project No. 07-060). Additionally, Dr. D. Cecala from Y-12 is acknowledged for providing the depleted uranium used in this project. This research was supported by TEES, the research arm of Texas A&M.

REFERENCES

1. D. J. GARNETTI, Uranium Powder Production Via Hydride and Alpha Phase Sintering of Uranium-Zirconium Alloys for Advanced Nuclear Fuel Applications, M.S. Thesis, Texas A&M University (2009).
2. J. BLOCH, "The Hydriding Kinetics of Activated Uranium Powder Under Low (Near Equilibrium) Hydrogen Pressure," *Journal of Alloys and Compounds*, 361 (2003), p. 130–137.
3. J.B. CONDON, E.A. LARSON, "Kinetics of the uranium-hydrogen system," Journal of Chemical Physics, Vol. 59, Number 2 (1973), p. 855-865.

CHARACTERIZATION STUDY OF ALPHA PHASE URANIUM SINTERING FOR ADVANCED NUCLEAR FUEL APPLICATIONS

Outline

- Introduction
- Background
- Experimental Design and Procedures
- Results
- Discussion and Summary

Introduction

Introduction – Basis for Research

- This research was conducted as a part of the DOE Nuclear Energy Research Initiative (NERI), under the Advanced Fuel Cycle Initiative (AFCI)
- The primary goal of this research was to characterize the α-phase sintering of uranium and uranium-zirconium
  - Providing a scientific basis to understand industrial techniques for powder metallurgy fabrication
- This thesis forms a portion of a larger research initiative into low temperature fabrication of U-Pu-TRU-Zr alloy fuel

Introduction – Research Overview

- Uranium powder was produced using a hydride/dehydride process
- Depleted Uranium (DU) and DU-Zr pellets were fabricated and sintered
- Rate of sintering was monitored by Linear Variable Differential Transformer (LVDT)
- Sintering rates under varying temperature profiles were analyzed based on a theoretical model
- Sintered microstructures were analyzed by SEM

Background

Uranium Fuel Fabrication

- Previous metal fuel fabrication predominantly used injection casting
  - Uranium and alloying constituents melted at ~1500°C
  - Liquid fuel is forced into quartz mold by pressure differential
  - Fuel is broken away from molds once cool
- Some transuranics (americium, curium, neptunium) have high vapor pressures at injection casting temperatures
- A powder metallurgy approach based on extrusion may provide a viable, low temperature alternative

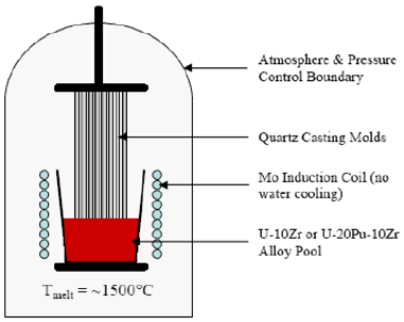

Basics of Sintering

- Conversion of compacted particles into interconnected solids by heating
- Driving force is reduction of surface energy
- German sintering rate model based on shinkage

$$\left(\frac{\Delta L}{L}\right)^{n/2} = \frac{B_0 \cdot t}{2^n \cdot D^m} \cdot e^{-Q/kT}$$

$$Ln\left(\frac{\Delta L}{L}\right) = Ln(C_1) + \frac{2}{n} Ln(t)$$

$$Ln\left(\frac{\Delta L}{L}\right) = Ln(C_2) - \frac{2 \cdot Q}{n \cdot k} \cdot \frac{1}{T}$$

R.M. German, Sintering Theory and Practice, John-Wiley & Sons, Inc., New York, (1996).

Uranium Hydride

$$2U + 3H_2 \leftrightarrow 2UH_3$$

- Uranium reacts reversibly with hydrogen to form UH_3
- Volume increase causes spalling, producing fine UH_3 powder
- Temperature increase and vacuum reverses reaction, leaving fine uranium powder

Experimental Design and Procedures

Large Inert Atmosphere Glovebox

Hydride Dehydride Apparatus

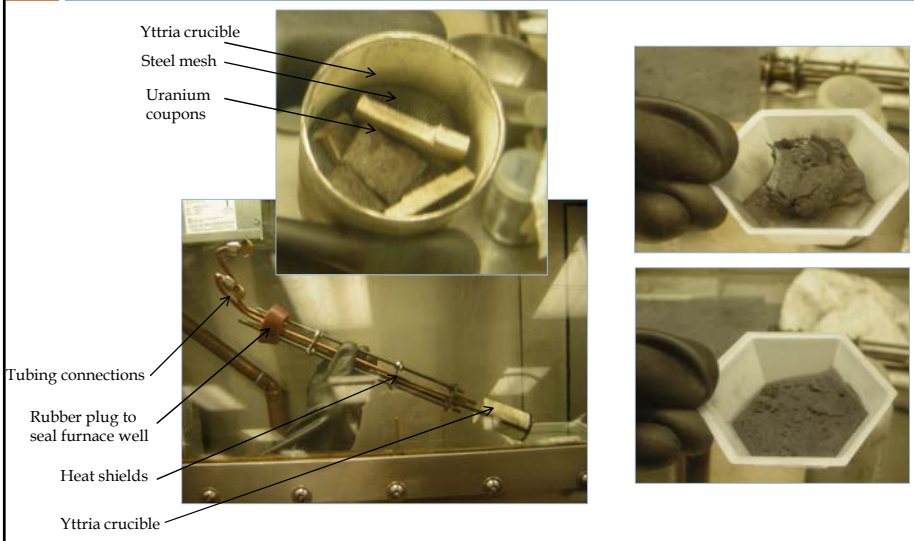

Powder Compaction

Results – DU Sintering Experiments

Sintered DU Pellet Summary

	α-Phase Temperature	γ-Phase Temperature	Green Density	Sintered Density
Pellet 4	655°C	831 °C	53.95%	57.87%
Pellet 5	643°C	820 °C	47.21%	49.88%
Pellet 6	634°C	809 °C	46.68%	50.46%
Pellet 7	659°C	834 °C	47.17%	51.22%
Pellet 8	651°C	826 °C	48.20%	51.97%

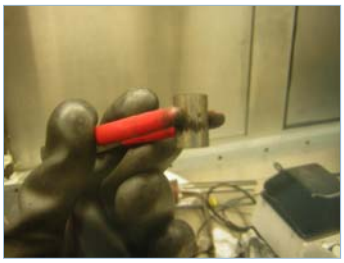

Representative DU Sintering

- Initial shrinkage observed during heating
- Steady isothermal shrinkage observed during both α-phase and γ-phase

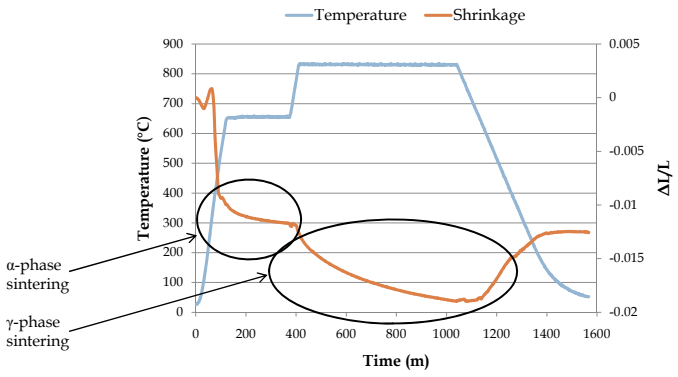

DU Imaging

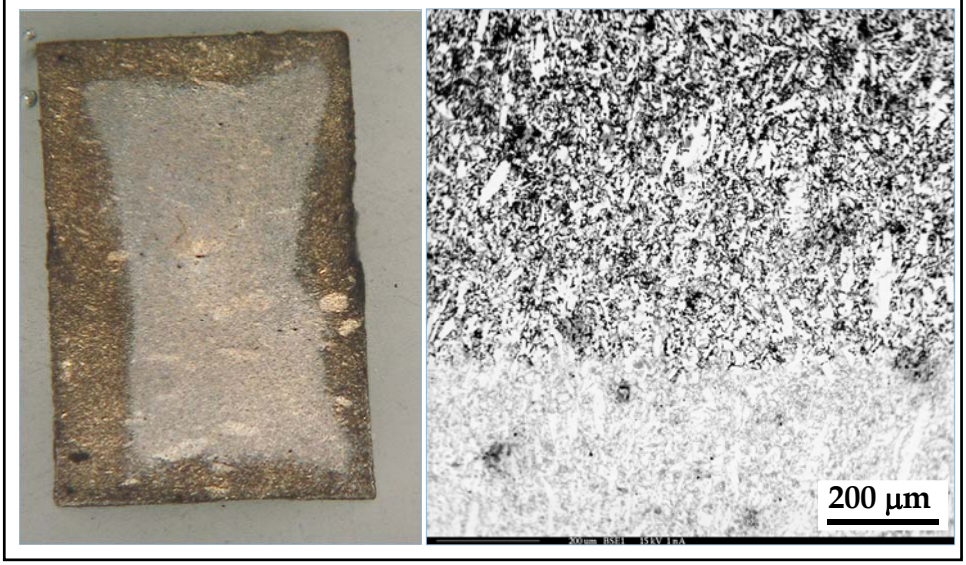

DU Imaging

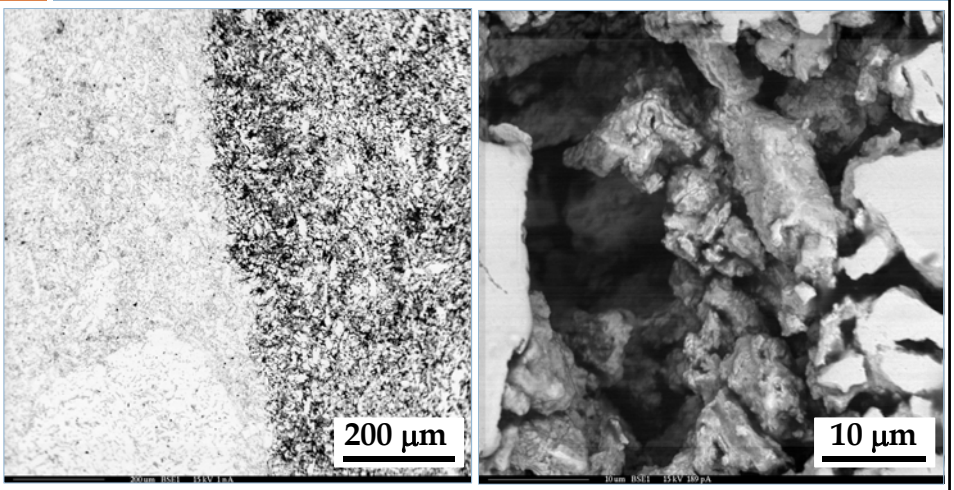

Porosity of Sintered DU Pellets

- All DU pellets had inner low porosity region and outer high porosity region

	α-Phase Temperature	γ-Phase Temperature	Porosity of Outer Region	Porosity of Inner Region
Pellet 4	655°C	831 °C	32.3%	11.5%
Pellet 5	643°C	820 °C	36.2%	13.2%
Pellet 6	634°C	809 °C	40.0%	9.7%
Pellet 7	659°C	834 °C	30.9%	3.2%
Pellet 8	651°C	826 °C	23.0%	1.1%

Determination of *n* for Isothermal DU

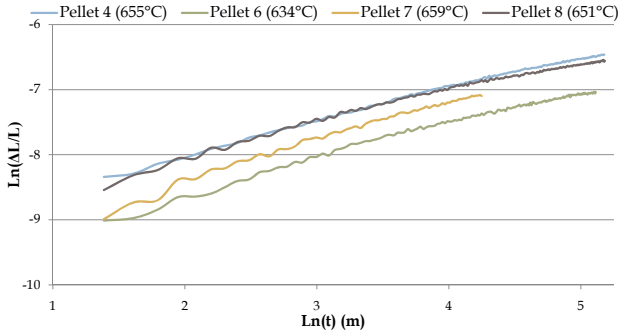

	α-Phase Temperature	Calculated n	R^2
Pellet 4	655°C	4.11	0.9933
Pellet 6	634°C	3.93	0.9860
Pellet 7	659°C	3.26	0.9870
Pellet 8	651°C	4.36	0.9812

Determination of *Q* for Isothermal DU

- Activation energy of 340 +/- 41 kJ/mol

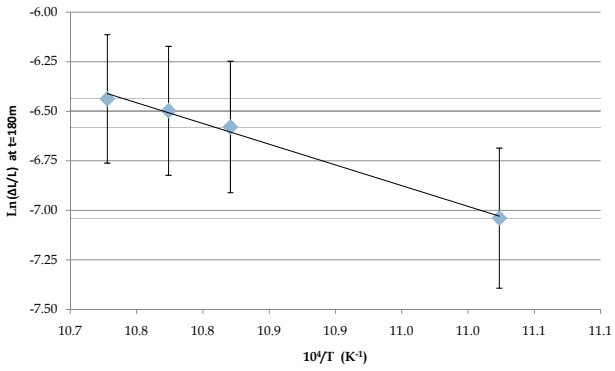

Results – DU-Zr Sintering Experiments

Isothermal DU-Zr Pellet Summary

	Contents (wt%)	Compaction Pressure	α-Phase Temperature	γ-Phase Temperature	Green Density	Sintered Density
Pellet 9	DU-10Zr	90.5 ksi	635 °C	817 °C	51.3%	55.7%
Pellet 10	DU-10Zr	90.5 ksi	642 °C	819 °C	50.7%	55.8%
Pellet 11	DU-10Zr	90.5 ksi	652 °C	829 °C	51.3%	56.5%
Pellet 14	DU-5Zr	181 ksi	650°C	N/A	52.4%	58.7%

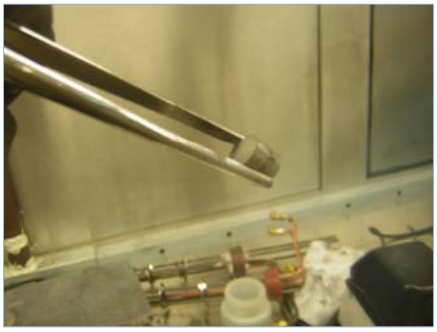

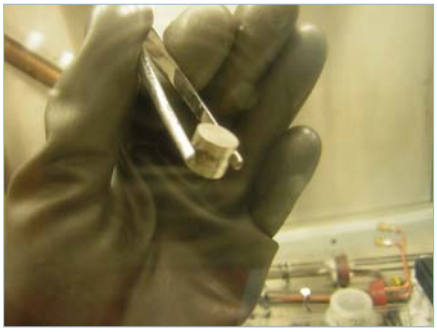

Representative DU-Zr Sintering

- Sintering in both phases much more rapid than for DU

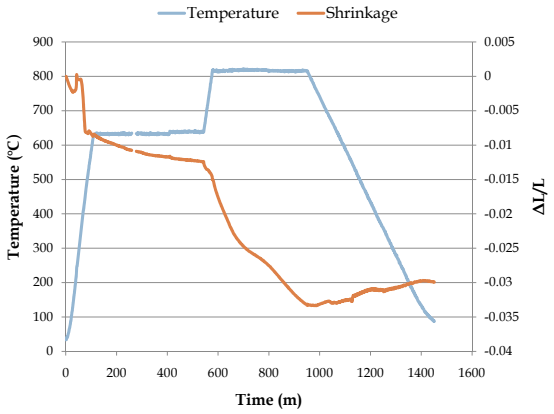

DU-10Zr Imaging

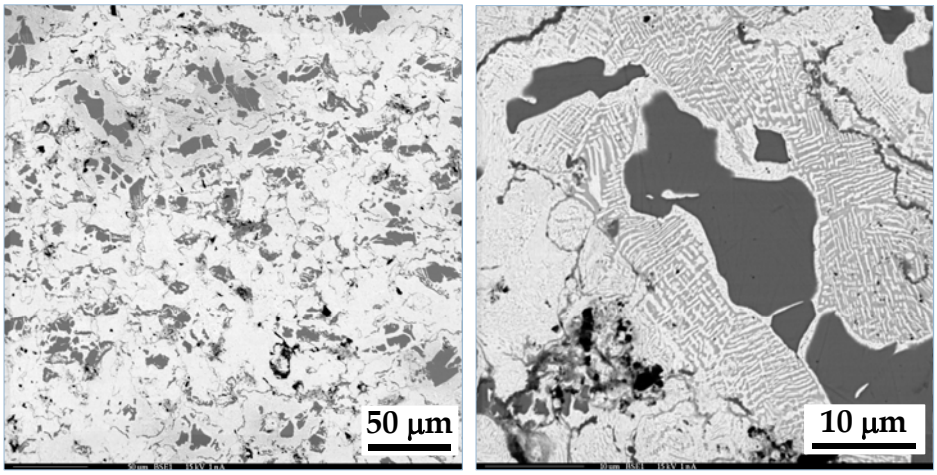

DU-10Zr Imaging

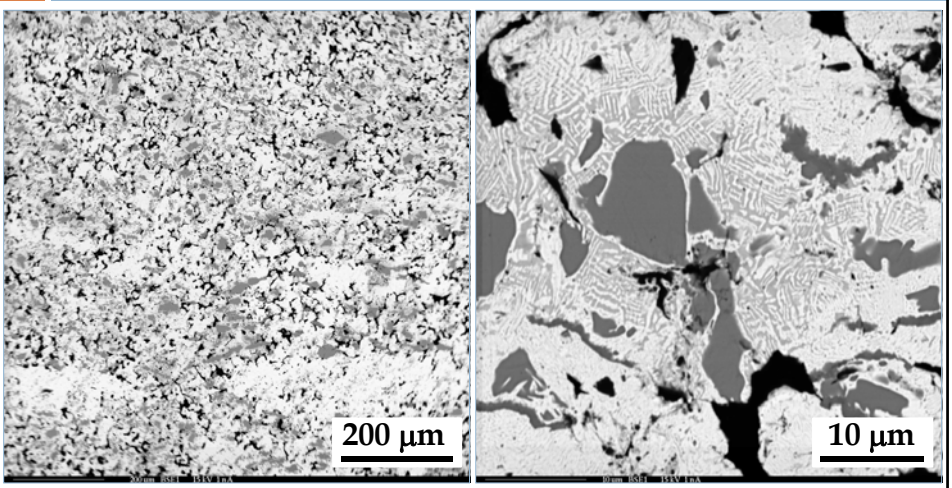

DU-5Zr Sintering

- Double compaction force of prior pellets
  - Sintered for 48 hours at 650°C
  - Previously observed difference in inner and outer porosity was not observed
  - Only pellet sintered exclusively in α-phase

Pellet 14– Imaging

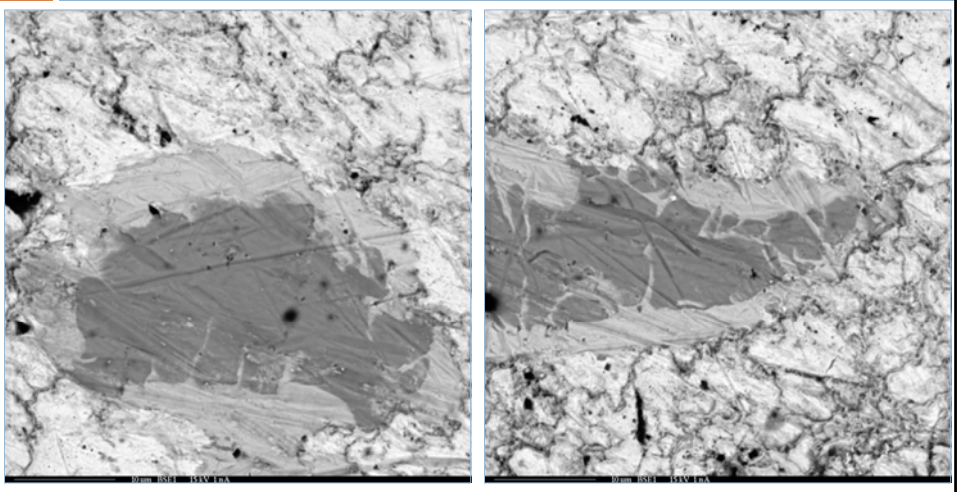

Determination of *n* for DU-10Zr

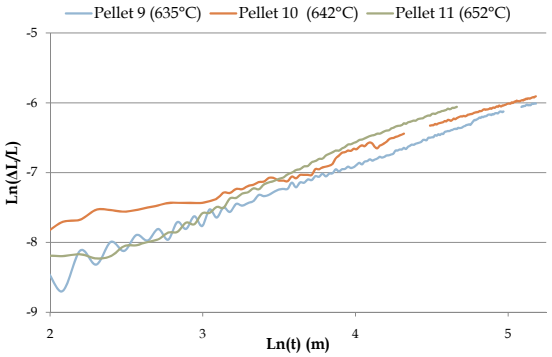

	α-Phase Temperature	Calculated n	R^2
Pellet 9	635°C	2.55	0.9871
Pellet 10	642°C	2.29	0.9855
Pellet 11	652°C	3.11	0.9876

Determination of *Q* for DU-10Zr

- Activation energy of 272 +/- 91 kJ/mol

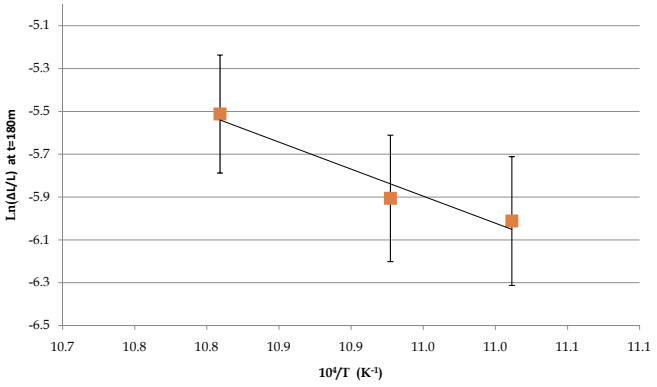

Summary of Results

Summary of Results

- A model for the initial phase of sintering for DU and DU-10Zr was developed based on isothermal shrinkage rates during sintering
- The effects of zirconium addition to uranium during sintering were measured
- The microstructure of sintered uranium-zirconium pellets was analyzed, indicating the presence of the alloyed $\alpha+\delta$ phase when sintered in the γ-phase and the presence of δ phase when sintered in the α-phase
- The uranium powder produced by the hydride/dehydride method was characterized to determine size distribution and morphology
- Previous issues with pellet cracking during cooling due to delamination were resolved by the use of controlled cooling and finer control over the quality of the uranium powder

Acknowledgements

- Dr. McDeavitt for his guidance and counsel throughout this project
- Dr. David Cecala and the Y-12 Plant at ORNL for supplying the DU used in this project
- Will Sames for designing apparatus and assisting in powder characterization
- Brandon Blamer for his assistance in sectioning and polishing samples
- David Garnetti for prior research in the FCML which formed the starting point of this project

References

1 - D. E. Burkes, R.S. Fielding, and D.L. Porter, Metallic Fast Reactor Fuel Fabrication for the Global Nuclear Energy Partnership, Journal of Nuclear Materials 392 (2009), 158-163.

2 - C.L. Trybus, J.E. Sanecki, S.P. Henslee, Casting of Metallic Fuel Containing Minor Actinide Additions, Journal of Nuclear Materials 204 (1993) 50-55.

3 – D. Garnetti, S.M. McDeavitt, Uranium Powder Production via Hydride Formation and Alpha Phase Sintering of Uranium and Uranium-Zirconium Alloys for Advanced Nuclear Fuel Applications. Masters Thesis, Texas A&M University, College Station, TX.

4 - R.M. German, Sintering Theory and Practice, John-Wiley & Sons, Inc., New York, (1996).

5 - Powder Metallurgy by Fritz V. Lenel, pg 211-268

6 – J.J. Carroll, A.J. Melmed, Field Ion Microscopy of Alpha Uranium, Surface Science 116 (1982) 225-239.

7 - W.D. Wilkinson, Uranium Metallurgy, John Wiley & Sons, Inc., New York (1962).

8 – L. Grainger, Uranium and Thorium, George Newnes Limited, London (1958).

9 – S.F. Pugh, Swelling in Alpha Uranium due to Irradiation, Journal of Nuclear Materials 4 (2) (1961) 177-199.

10 – J.J. Burke, D.A. Colling, A.E. Gorum, J. Greenspan, Physical Metallurgy of Uranium Alloys, Brook Hill Publishing Company, Columbus (1976).

11 - C.E. Stevenson, The EBR-II Fuel Cycle Story, La Grange Park, Illinois: American Nuclear Society Inc. (1987).

12 - P. Chiotti, B.A. Rogers (1950), The Production of Uranium and Thorium in Powder Form, United States Atomic Energy Commission, AECD-2974.

13 - S.M. McDeavitt (1992), Hot Isostatic Pressing of DU-10Zr Alloy Nuclear Fuel by Coupled Grain boundary Diffusion and Power-Law Creep. Doctoral Thesis, Purdue University, West Lafayette, IN.

14 - S.M. McDeavitt, A.A. Solomon, Hot-Isostatic Pressing of DU-10Zr by a Coupled Grain Boundary Diffusion and Creep Cavitation Mechanism, Journal of Nuclear Materials 228 (1996) 184-200.

15 - T. Hashino, Y. Okijima, Mechanism of the Reaction of Hydrogen with Uranium, Journal of Physical Chemistry 77 (1973) 2236-2241.

16 - C.R. Clark, M.K. Meyer, Fuel Powder Production from Ductile Uranium Alloys, Presented at the 1998 International Meeting on Reduced Enrichment for Research and Test Reactors, Oct. 18 - 23, 1998, Sao Paulo, Brazil.

17 - J. Bloch, The Hydriding Kinetics of Activated Uranium Powder Under Low (Near Equilibrium) Hydrogen Pressure, Journal of Alloys and Compounds 361 (2003) 130–137.

Appendices

Sintering Mechanisms

- Surface Transport
  - Evaporation Condensation
  - Surface Diffusion
  - Volume Diffusion
- Bulk Transport
  - Grain Boundary Diffusion
  - Volume Diffusion
  - Plastic Flow

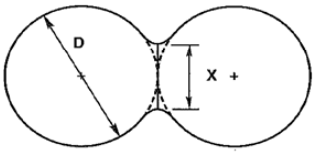

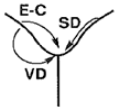

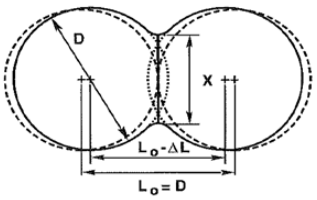

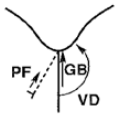

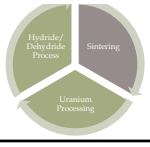

Heterogeneous Porosity

- Pellets pressed to 90.5 ksi had inner low porosity region and outer high porosity region
- Likely the result of density gradients during compaction
- Increasing compaction pressure to 181 ksi resulted in consistently low, even porosity

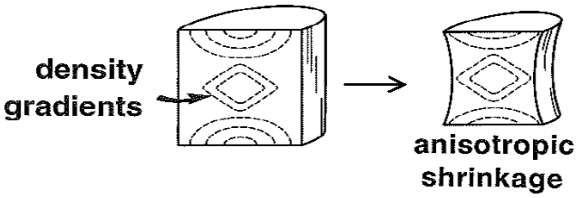

Uranium Metallurgy

- Three allotropes of uranium: α (T<667°C), β (667°C<T<772°C), and γ (772°C<T)
- α uranium possesses complex orthorhombic lattice structure
- Orthorhombic structure undergoes anisotropic expansion during cyclic heating and irradiation
- Addition of zirconium reduces anisotropic swelling issues

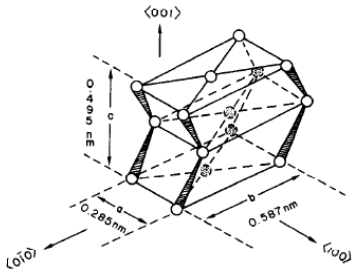

Powder Characterization

- Atmospheric Containment Vessel (ACV) used to transfer pyrophoric uranium powder outside glovebox
- Quartz viewing lens allowed imaging with Hirox KH-1300 Optical Microscope
- Particle size distribution based on ImageJ analysis

Uranium Powder Production Using a Hydride-Dehydride Process

Department of Nuclear Engineering, Texas A&M University
Grant Helmreich, William Sames, David Garnetti, and Dr. Sean M. McDeavitt

As part of the Department of Energy's Advanced Fuel Cycle Initiative, research is being conducted on the use of Advanced Fast Reactors to use uranium efficiently and provide a forum for the transmutation and destruction of the transuranic elements Pu, Np, Am, and Cm. Metal fuels have been demonstrated as effective fuels for fast reactor systems, however the injection casting method used to fabricate alloy nuclear fuels has limitations when applied to Am and Np due to vaporization. We are exploring the use of alpha phase uranium sintering and hot extrusion of uranium metal powders in order to develop alternative methods for fabricating U-TRU-Zr alloy fuels. (Mg is used as a surrogate for TRU elements in these experiments)

Large Argon Atmosphere Glovebox

Hydride Rig In Glovebox

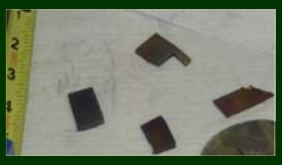

DU at various stages of Oxidation

Tube Furnace at bottom of well

Hydride-Dehydride Process

Background

- A methodology has been developed to produce fine, high purity uranium powder for use in metallic uranium fuel fabrication studies.

Process

- Slugs of depleted uranium (DU) are washed in a nitric acid solution to remove the outer oxide coating.
- The DU slugs are then loaded onto a SS wire mesh in a yttria crucible
- The DU is then hydrided by heating to ~235°C in an Ar-5%H_2 environment.
- The decreased density of the hydrided uranium results in spallation and the formation of a fine UH_3 powder, which falls through the wire mesh to the bottom of the crucible.
- The reaction vessel is evacuated after completion of the hydriding step and heated to ~335°C to decompose the UH_3 , leaving high purity DU metal powder.

Image Collection

Image Collection

- High resolution pictures were taken with a Hirox MX-5040SZ Microscope.
- The powder was contained in an ACV (see inset) to prevent oxidation.

Image Analysis

- Image analysis was performed using ImageJ software (version 1.38x 2007).
- Grayscale threshold image analysis was used to determine the particle diameter and volume based on the assumption of spherical particles.

Powder Characterization

Results

- Current results confirm that particles produced using a hydride-dehydride method are ~40 µm, as previously reported in literature.
- Reaction vessel is currently capable of producing ~50 grams of powder in a 24 hour period, with approximately 50% conversion efficiency.

Future Work

- Further work will be done to fully characterize the rate of hydriding reaction and to assess the effect of input parameters on powder quality.
- Temperature, time, and gas pressure will be varied in the hydride process to determine rate dependencies.

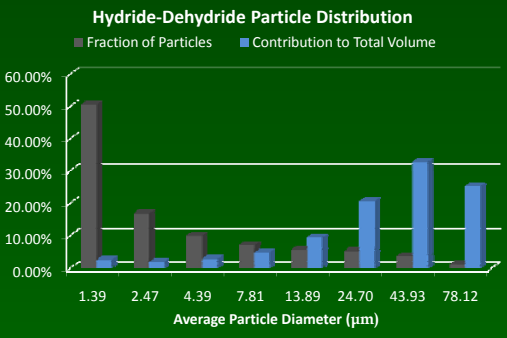

Uranium Powder at 800x

Atmosphere Containment Vessel (ACV) with alternate nipple size

Uranium slugs loaded into Yttria crucible before hydriding

Uranium powder after removal from the reaction vessel

APPENDIX C

Fuel cycle research and development undergraduate materials and poster presentation

URANIUM METAL POWDER PRODUCTION, PARTICLE DISTRIBUTION ANALYSIS, AND REACTION RATE STUDIES OF A HYDRIDE-DEHYDRIDE PROCESS

An Honors Fellows Thesis

by

WILLIAM JAMES SAMES V

Submitted to the Honors Programs Office
Texas A&M University
in partial fulfillment of the requirements for the designation as

HONORS UNDERGRADUATE RESEARCH FELLOW

April 2011

Major: Nuclear Engineering

URANIUM METAL POWDER PRODUCTION, PARTICLE DISTRIBUTION ANALYSIS, AND REACTION RATE STUDIES OF A HYDRIDE-DEHYDRIDE PROCESS

An Honors Fellows Thesis

by

WILLIAM JAMES SAMES V

Submitted to the Honors Programs Office
Texas A&M University
in partial fulfillment of the requirements for the designation as

HONORS UNDERGRADUATE RESEARCH FELLOW

Approved by:

Research Advisor: Sean M. McDeavitt
Associate Director of the Honors Programs Office: Dave A. Louis

April 2011

Major: Nuclear Engineering

ABSTRACT

Uranium Metal Powder Production, Particle Distribution Analysis, and Reaction Rate Studies of a Hydride-Dehydride Process. (April 2011)

William James Sames V
Department of Nuclear Engineering
Texas A&M University

Research Advisor: Dr. Sean McDeavitt
Department of Nuclear Engineering

Work was done to study a hydride-dehydride method for producing uranium metal powder. Particle distribution analysis was conducted using digital microscopy and grayscale image analysis software. The particle size was found to be predominantly in the 40 μm range, which agreed with previous work. The effects of temperature, pressure, and time on the reaction fraction of powder were measured by taking experimental data. The optimum hydride temperature for the system was found to be 233.4°C. Higher gas pressures resulted in higher reaction fractions, over the range studied. For the sample parameters studied, a time of 371 minutes was calculated to achieve complete powderization. System design parameters for commercialization are proposed.

DEDICATION

This work is dedicated my parents for their unending support of everything that I do.

ACKNOWLEDGMENTS

I would like to thank my parents, family, friends, and teachers for their support of my pursuit of an education.

I would like to thank Dr. Sean McDeavitt for his support and guidance in this research.

I would like to thank all the students in the Fuel Cycles and Materials Laboratory for help, advice, and camaraderie along the way.

I would like to thank David Garnetti for his work in developing the hydride-dehydride system used in this research.

I would like to thank Grant Helmreich for his work in particle analysis, nitric acid chemistry, and teaching me about the hydride-dehydride process.

I would also like to thank Dr. D. Cecala and the Y-12 plant in Oak Ridge, Tennessee for providing the depleted uranium used in this project.

NOMENCLATURE

FCML	Fuel Cycle and Materials Laboratory
ORNL	Oak Ridge National Laboratory
NERI	Nuclear Energy Research Initiative
AFCI	Advanced Fuel Cycle Initiative
ACV	Atmosphere Containment Vessel
TRU	Transuranic
H_2	Hydrogen Gas
U	Uranium
UH_3	Uranium-Hydride
GC	Growth Center
P	Pressure
T	Temperature
t	Time
α	Reaction Fraction

TABLE OF CONTENTS

Page

LIST OF FIGURES

FIGURE Page

CHAPTER I

INTRODUCTION AND BACKGROUND

Different forms of nuclear fuel are used in different reactor designs. One fuel type, metal fuel, is of particular interest for fast reactor systems. These fuels frequently involve varying compositions of Uranium, Plutonium, and Zirconium (U-Pu-Zr). Transuranic (TRU) wastes are produced during the use of nuclear fuel. These waste products can be transmuted, or eliminated, by incorporation in fast reactor fuel in a Uranium-Transuranic-Zirconium (U-TRU-Zr) fuel. Powder metallurgy and injection casting are current methods of manufacturing metal fuels. Powder metallurgy requires metal powders that are pressed and sintered into fuel pellets. Powder metallurgy of uranium metal is under investigation at Texas A&M University for its potential to solve problems of transuranic volatility in U-TRU-Zr fuel manufacture. The production of uranium powder from larger pieces of uranium is necessary to make this process work. One method of powderizing uranium metal is to hydride the metal at elevated temperatures and then dehydride the hydride powder to produce uranium metal powder. This powder can then be blended with other metal or transuranic powders to create the desired composition for a fast reactor fuel pellet.

This thesis follows the style of *Journal of Nuclear Materials*.

Description of hydride

Uranium metal (U) forms uranium-hydride (UH_3) when subjected to temperatures greater than 150°C and hydrogen gas (H_2). [1] The temperature dependence of the reaction is shown in Figure 1 at constant pressure. The peak H_2 consumption corresponds to the peak reaction temperature at ~225°C. [2] This reversible reaction proceeds according to Eq. 1.

$$U + \frac{3}{2}H_2 \leftrightarrows UH_3 \quad (1)$$

The uranium metal usually has a thin oxide (UO_2) layer present on the surface. This oxide layer can be between 10-100 nm thick and still allow for the progression of the hydride reaction. [3] Thicker oxide layers can impede or prevent the reaction. The H_2 diffuses through the oxide layer to react with the U surface. [4] The difference in the density of uranium (18.9 g/cc) and UH_3 (10.3 g/cc) facilitates the formation of powder. [5] The corresponding increase in volume can lead to the precipitation of UH_3 blisters as shown in Figure 2. [4, 5, 6]

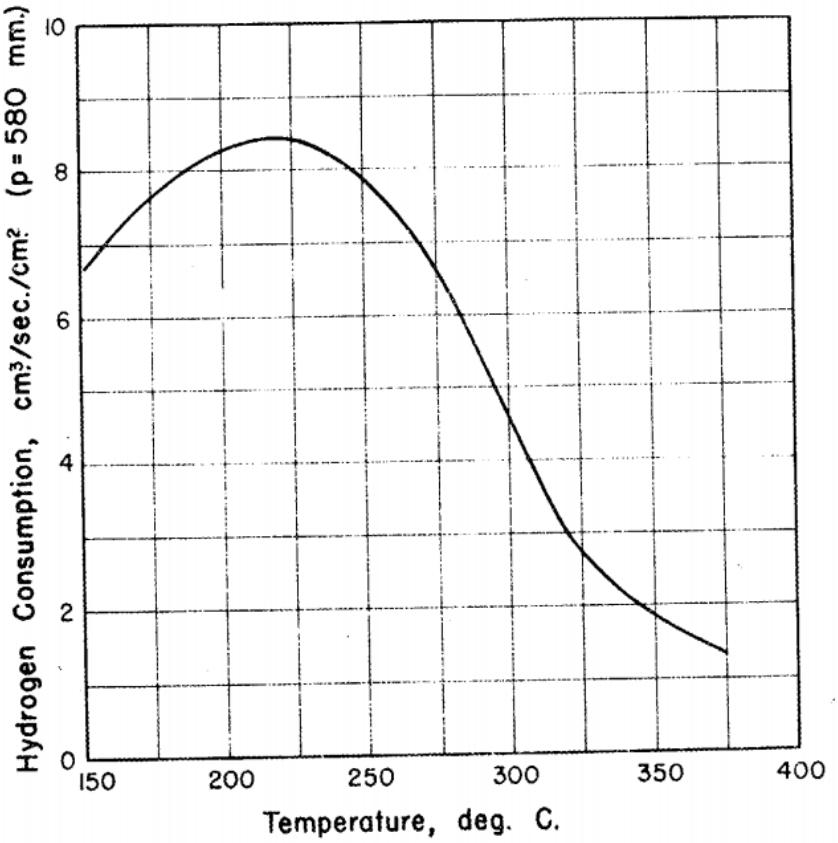

Figure 1. Temperature dependence of the hydride reaction. [2]

The hydrogen reacts at nucleation sites that are located beneath a small oxide layer as shown in Figure 2. Initial nucleation sites are small, on the order of a few nm. [3] Nucleation sites remain small, unless locate near a defect in the oxide layer. The growth of the blister near the defect can lead to the fracture of the oxide layer, and the continuance of the hydride reaction [3] A site at which this fracture occurs is described as a Growth Center (GC). [3] Approximately 77% of the nucleation sites were observed near grain or twin boundaries of the uranium metal by Bingert. [4] In the case of no oxide layer, nucleation occurs at the metal surface and continues unimpeded by an oxide

layer. As volume swelling breaks down the lattice structure, powder forms on the surface of the slug. Depending on the system, fluid or other motion can mechanically remove the powder layer, further exposing more uranium metal for reaction. It is also possible for continued hydrogen diffusion. If the powder layer sits on the uranium metal piece, the reaction rate will be impeded by the reduction in reactive surface area.

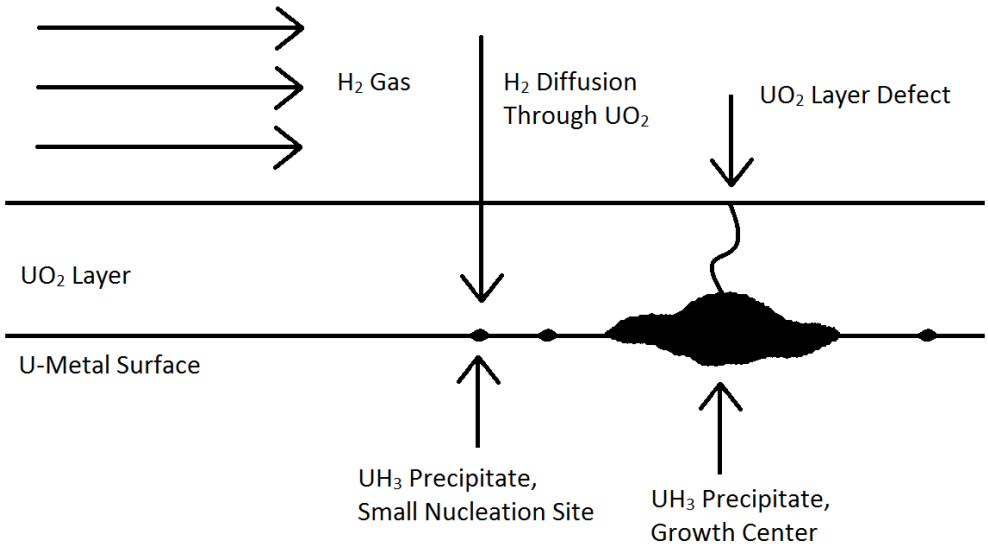

Figure 2. Sketch showing formation of UH_3 precipitate on a microscopic level.

Bingert's results show that hydrogen will diffuse through a layer of uranium dioxide (UO_2) on uranium metal to react and form uranium-hydride (UH_3). [4] The formation results in the formation of a "blister" at the metal-oxide interface. The blister formation is due to the change in volume associated with the formation of UH_3. An observation

made of this phenomenon is shown in Figure 3 (blister figure). The thickness of the UO_2 layer is proposed to be important to the formation of UH_3.

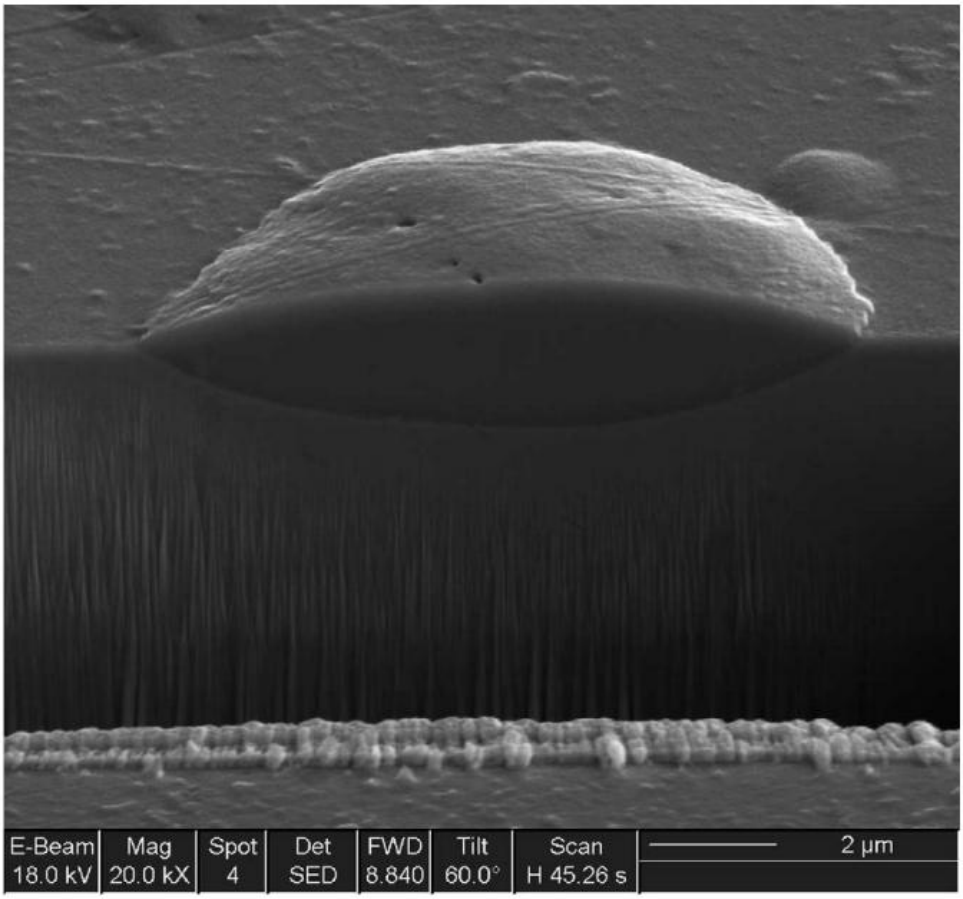

Figure 3. UH_3 blister formation at the oxide-metal interface. [4]

Description of dehydride

Uranium-hydride (UH_3) dissociates to uranium metal (U) and hydrogen gas (H_2) when subjected to temperatures above 430°C at atmospheric pressure. [2] The dissociation occurs at lower temperatures, for lower pressures. The relationship between temperature and pressure is exponential and is shown in Figure 4. The dehydride reaction is the reverse of the hydride reaction and proceeds according to Eq. 1 as well.

$$U + \frac{3}{2}H_2 \leftrightarrows UH_3 \quad (1)$$

Starting with uranium-hydride powder, the reaction leaves behind uranium metal powder. Work by Garnetti shown in Figure 5 shows a rise in the pressure of a reaction vessel system under vacuum from the dehydride process. The rise in pressure is associated with the release of hydrogen gas from the UH_3 powder. This reaction was shown to usually complete within 20 minutes, but in one case took a little over 25 minutes. [7]

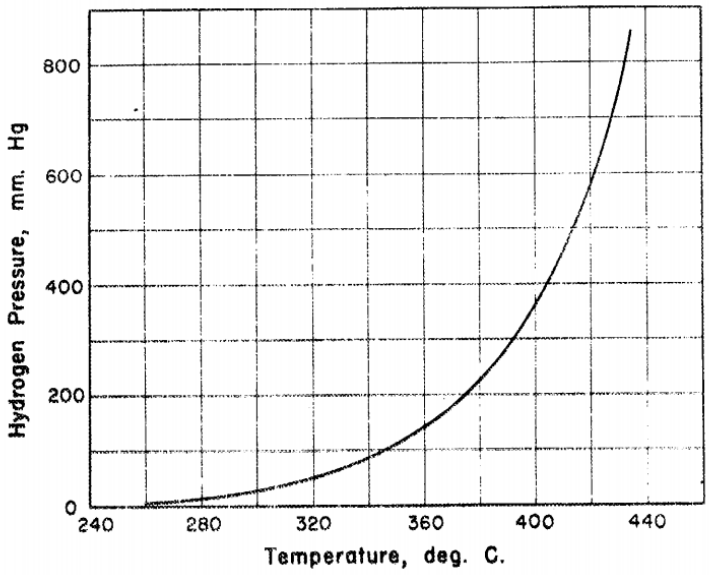

Figure 4. Pressure vs. temperature of dissociation for the dehydride reaction. [2]

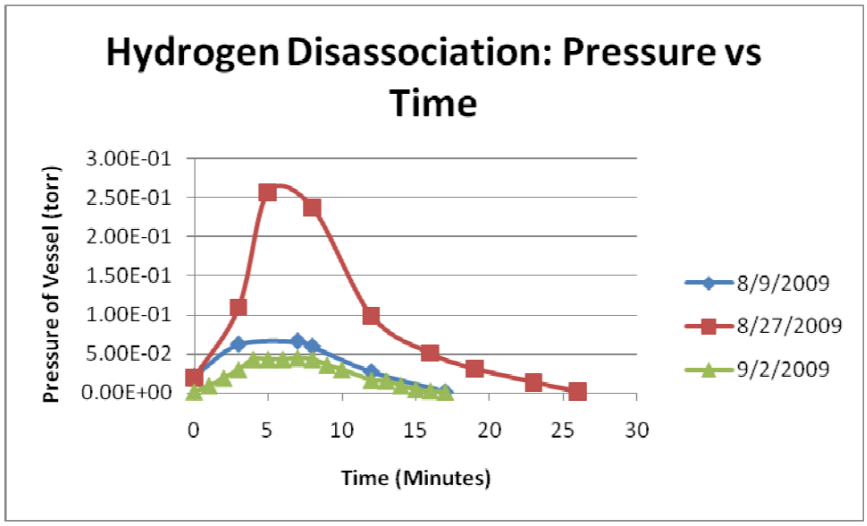

Fig. 4-13 Pressure vs Time during the dehyride step

Figure 5. The time scale of dehydride under varying vacuum pressures and the pressure increase associated with the release in hydrogen gas. [7]

Description of uranium powder

The powder that is produced is of interest because its properties will affect the quality of the pellets that are produced from it. Full powderization of uranium metal pieces is desired, and the size distribution of particles is of particular interest. Previous work by Bloch and by Condon found particle sizes to be ~40 μm. [5,8] In the process of interest uranium powder is pressed using a hydraulic or extrusion. Work by Helmreich has been performed that demonstrated these capabilities. [1]

The powder that was produced in this experiment was analyzed in an Argon atmosphere so as to obtain distributions for the metal powder, and not an oxide powder. In order to accomplish this, an Atmosphere Containment Vessel (ACV) was developed using fittings designed for glovebox use. An o-ring and clamp system allowed for powder to be placed in sample trays and sealed in with an Argon environment. The ACV is built on a 1.8 (0.75 in) cm tall, 6.35 cm (2.5 in) diameter nipple. A quartz, optical viewing port was selected to allow for optimal transmission of the visible light spectrum (>93%). The ACV is shown is Figure 6. The powder was analyzed a HIROX MX-5040SZ optical microscope. The microscope used allowed for resolutions of up to 800x and is shown in Figure 7.

Figure 6. The ACV with an alternate nipple size for viewing larger samples.

Figure 7. HIROX digital microscope used for powder imaging.

Description of process and facilities used

Uranium metal slugs were obtained from the Y-12 plant at Oak Ridge National Laboratory (ORNL) for use in this project as a part of the Nuclear Energy Research Initiative (NERI), under the Advanced Fuel Cycle Initiative (AFCI). These slugs are shown in Figure 8. They are stored in air, and have an oxide layer present on the surface. For the experiments performed in this work, these slugs were cutting using the diamond saw in Figure 9. The resulting cut samples are shown in Figure 10. After samples were cut, they were cleaned using an ultrasonic cleaner.

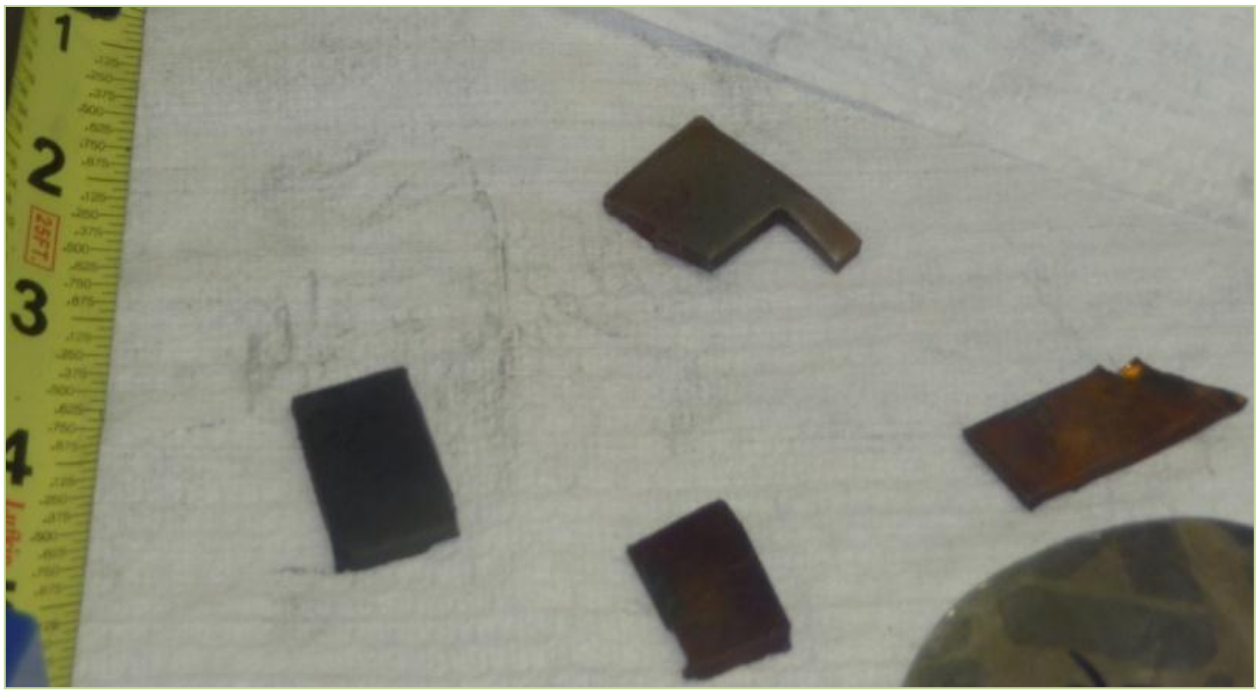

Figure 8. Uranium metal slugs from Y-12 in at ORNL. [7]

Figure 9. Diamond saw used for cutting uranium metal slugs into smaller sample sizes.

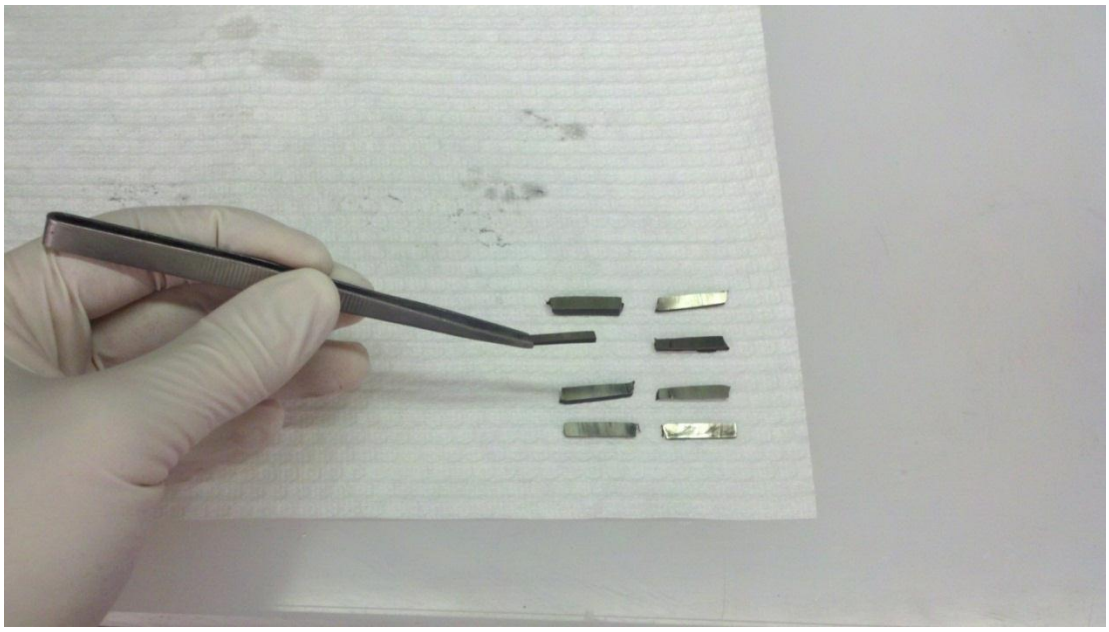

Figure 10. Cut uranium metal samples after being cut with the diamond saw and cleaned using an ultrasonic cleaner.

In order for the hydride reaction to proceed, the oxide layer must be removed from the uranium slugs. This is done by using a nitric acid wash, which removes the oxide layer based on Eq. 2. [9] The nitric acid used is a 35% by volume solution with water. The nitric acid process is conducted over ~10 minutes, and the uranium is removed once the oxide layer has been removed. If the uranium metal is left too long in the nitric acid solution, the nitric acid will begin to react with the uranium metal itself. This process is performed in an Argon atmosphere glovebag, shown in Figure 11. The uranium metal slugs were rinsed with deionized water after the nitric acid wash, let dry, rinsed with ethanol, and then let dry a second time. The ethanol rinse is to clean the surface and is conducted in a separate tray from the nitric acid as a safety precaution to prevent nitric acid-ethanol reaction.

$$UO_2 + 4HNO_3 \rightarrow U^{+4} + 2H_2O + 4NO_3^- \quad (2)$$

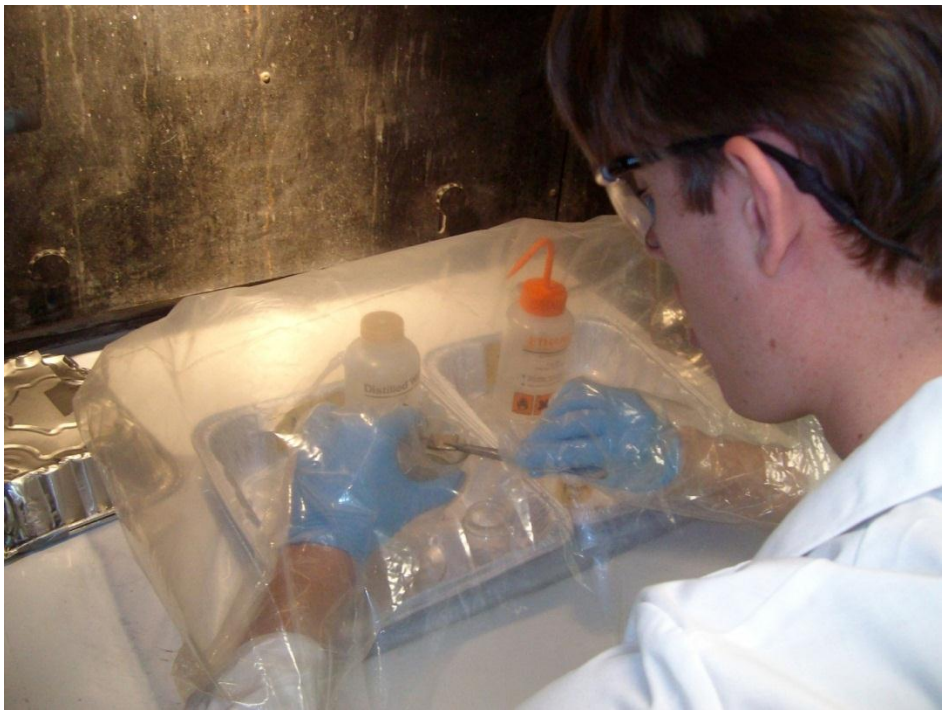

Figure 11. Acid wash station located inside a glovebag under argon atmosphere to reduce sample oxidation.

After the acid wash, the uranium slugs were transported to the glovebox in an argon filled container. The slugs were then used to make hydride-dehydride powder production runs.

The hydride-dehydride process used in this investigation was designed and developed by David J. Garnetti. [7] The reaction is contained within an aluminum-oxide crucible, held in a rig at the bottom of a furnace well as shown in Figure 12. The outside of the furnace system and furnace controls are shown in Figure 13. The whole system is held within an Argon atmosphere glovebox, shown in operation in Figure 14. Preliminary experiments

by Helmreich found that the reaction vessel used is capable of producing ~50 grams of powder in a 24 hour period, with approximately 50% conversion efficiency. The conversion efficiency of the reaction vessel has since been demonstrated to fully convert uranium metal to uranium metal powder.

Figure 12. Aluminum oxide crucible located at the bottom of the hydride-dehydride rig.

Figure 13. Furnace and furnace controls used in hydride-dehydride process.

Figure 14. Glovebox in operation, working at the hydride-dehydride station.

The aluminum-oxide reaction vessel is subjected to temperatures ~225°C and an argon-5%-hydrogen gas mixture for the hydride reaction. Gas flow to the furnace reaction chamber is cut off, a vacuum of 0.1 Pa (1E-3 Torr) is pulled on the chamber, and the furnace temperature is increased to temperatures around 325°C to dehydride the powder. For the reaction rate studies performed in this work, the mass of the sample was measured before the reaction and after completion. The mass of the remaining uranium metal slug was measured, as was the mass of the remaining slug and powder. This allowed for a determination if the powder was fully dehydrided. For both the hydride and dehydride reactions, the dwell time on the furnace was set. This means that the time of reaction was actually the measured time (dwell time) and the time required to heat up to the dwell temperature set (the temperature reported for each run).

Powder production runs were made to study the distribution of particle sizes and the hydride reaction rate. The hydride reaction rate was study with respect to temperature, gas pressure, and surface area. The dehydride reaction rate was not studied, and the same times and temperatures of dehydride were used for all experimental runs. This choice was made, as the dehydride reaction occurs over a much quicker timescale, and has little effect of the amount of powder produced. The dehydride reaction parameter of interest is the timescale required to fully dehydride the uranium-hydride powder produced.

CHAPTER II

PREVIOUS WORK AND MODELS

Thermal Properties

The pressure dependent heats of formation of uranium hydride were calculated by Abraham and are given in Figure 15. [10]

Condon reported models for calculating the Gibbs' free energy and the standard enthalpy of formation for uranium-hydride as shown in Figure 16. Rate constant dependence on surface area, position on phase diagram, thermal history and other variables prevented Condon from fully characterizing these values. [11]

HEATS OF FORMATION OF UH_3, UD_3 AND UT_3 AT 25°

Expt. no.	$-\Delta H_f$ (cal./mole) UH_3	UD_3	UT_3
1	30,346	31,014	31,170
2	30,362	31,039	31,114
3	30,347	31,011	31,140
Mean	30,352	31,021	31,141
Est. error	±30	±30	±50

Figure 15. Heats of formation of uranium hydride. [10]

$$\Delta G_f^\circ(\mathrm{UH_3}, T)/\mathrm{J\ mol^{-1}} = 720.7(T/\mathrm{K}) - 182.6 \times 10^{-3} - 70.34(T/\mathrm{K})\ln(T/\mathrm{K}),$$
$$\sigma/\mathrm{J\ mol^{-1}} = 0.26(T/\mathrm{K}) \approx 180,$$
$$\Delta H_f^\circ(\mathrm{UH_3}, T)/\mathrm{J\ mol^{-1}} = 182.6 \times 10^3 + 70.34(T/\mathrm{K}), \qquad \sigma/\mathrm{J\ mol^{-1}} = 117 \text{ to } 620,$$
and
$$\Delta C_p^\circ/\mathrm{J\ K^{-1}\ mol^{-1}} = 70{,}37, \qquad \sigma/\mathrm{J\ K^{-1}\ mol^{-1}} = 5.6.$$

Figure 16. Models developed by Condon for the Gibbs' free energy and the standard enthalpy of formation for uranium-hydride. [11]

Albrecht and Mallett

The primary result of work by Albrecht was the formation of linear rate Eq. 3,

$$r = 4.11 * 10^{-3} p^{\frac{3}{4}} \exp\left(-\frac{1820}{RT}\right) \tag{3}$$

where r is the linear rate in ml/cm^2*sec, p is in mm Hg, R is the gas constant in cal/K*mol, and T is temperature in K. Eq. 3 is valid for temperatures from 96-250°C. Albrecht also notes variations on Eq. 3 with temperature and pressure. [12]

Bloch

Work by Bloch focused on the development of linear reaction rate constants for the uranium-hydride reaction. [5] The linear kinetic constant, k_L is defined as Eq. 4,

$$k_L = \frac{d\alpha(t)}{dt} \tag{4}$$

where $\alpha(t)$ is the time dependent reaction and t is time. [5] The temperature and pressure dependence of the linear kinetic constant are addressed in Eq. 5,

$$k_L(P,T) = k_{L0}(T)\left(\frac{P}{P_0} - 1\right)^2 \quad (5)$$

where P is the hydrogen pressure, P_0 is the absorption equilibrium pressure, T is temperature, and k_{L0} is the pressure-independent linear rate constant. Bloch quantified the temperature dependence of $k_{L0}(t)$ in Figure 17. Bloch quantified the quadratic relationship between the rate constant and pressure in Figure 18. [5] This work by Bloch forms a strong basis for ideal, lab scale experiments.

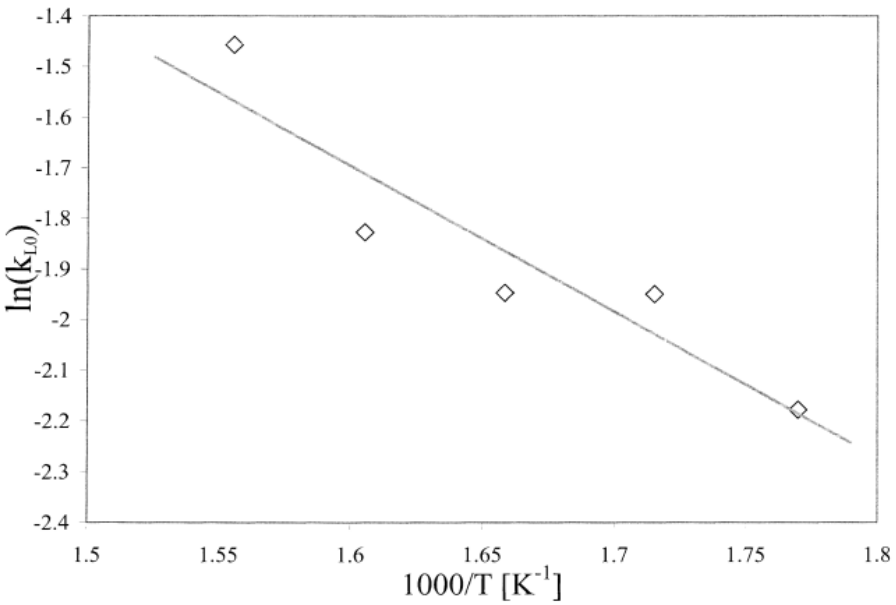

Figure 17. Temperature dependence of the pressure-independent linear rate constant. [5]

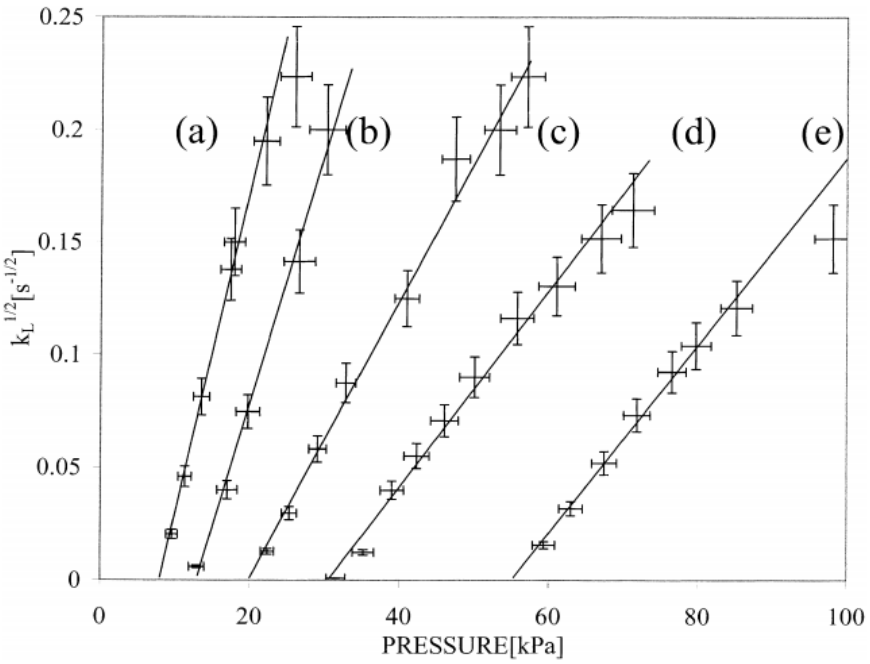

Figure 18. Pressure dependence of the square root of the linear hydriding rate constant for (a) 294°C, (b) 313°C, (c) 332°C, (d) 352°C, and (e) 371 °C. [5]

Condon

Work by Condon was done to quantify the diffusion of hydrogen into a uranium sample. This work was based on the diffusion Eq. 6,

$$D\frac{\partial^2 C}{\partial x^2} = \frac{\partial C}{\partial t} - a\frac{\partial U}{\partial t} \tag{6}$$

where D is the diffusion coefficient, C is the atomic concentration (in mole fraction) of hydrogen, U is uranium content expressed as a mole fraction, t is time, and a is the stoichiometric ratio for the reaction (=3). [13] Further definition is given in Eq. 7,

$$-\frac{\partial U}{\partial t} = k_1 C U \tag{7}$$

where k_1 is the rate constant. [13] The following values are defined as a function of Temperature:

$$k_1 = 10.4 * \exp\left(\frac{1592}{T}\right) \sec^{-1} * (mole\ fraction\ of\ H)^{-1} \tag{8}$$

$$D = 1.9 * 10^{-6} \exp\left(-\frac{5820}{T}\right) \tag{9}$$

where D is in units of m^2/sec and T is the temperature in K. [13] The initial atomic concentration is set as a boundary condition for the solution and is given by

$$C_0 = 5.58 * 10^{-4} \exp\left(-\frac{894}{T}\right) P^{\frac{1}{2}} * (mole\ fraction\ of\ H) \tag{10}$$

where P is pressure in Pa. This model is then further explored, and the proposed inclusion of a constant for dehydriding is discussed. This is a useful model for determining the depth of penetration and the reaction fraction as a function of depth. [13]

CHAPTER III

RESULTS

Powder characterization

The powder produced in a preliminary run was analyzed using ImageJ (version 1.38x 2007) image analysis software. The software allowed for gray scale image analysis and the calculation of particle size distributions by determining the number of pixels in each particle, and relating that to the scale of the image taken. Spherical particles were assumed, and reported values are given in terms of calculated diameter and spherical volume. Particle boundaries were identified, and analysis was carried out on a 5895 particle set. The results of this run are shown in Figure 19 and an example of a characteristic powder image at 800x is shown in Figure 20. [14] The main contribution to the volume of the powder sample was of particles in the 25-78 μm range, with a peak ~44 μm. These results fit with previous experiments by Bloch and Condon which found the characteristic size ~40 μm. [5,8]

Run #1 (as detailed in the Appendix) was conducted and shown to have particles within the same order of magnitude as the previous run. An image of this run is shown in Figure 21. After this, further particle distribution analysis was concluded.

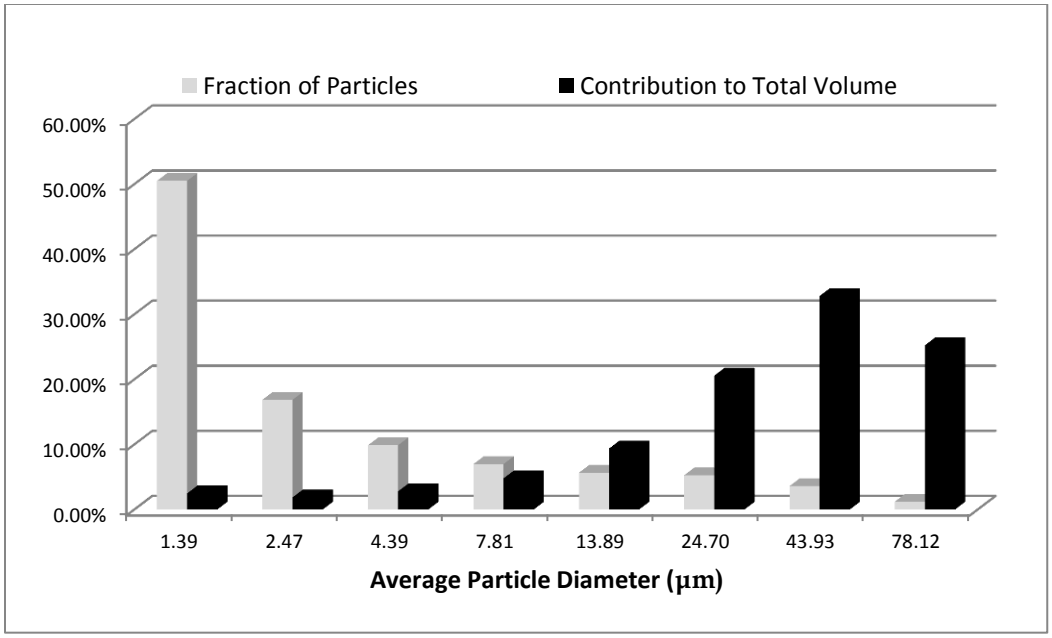

Figure 19. Results from image analysis of a preliminary run. [14]

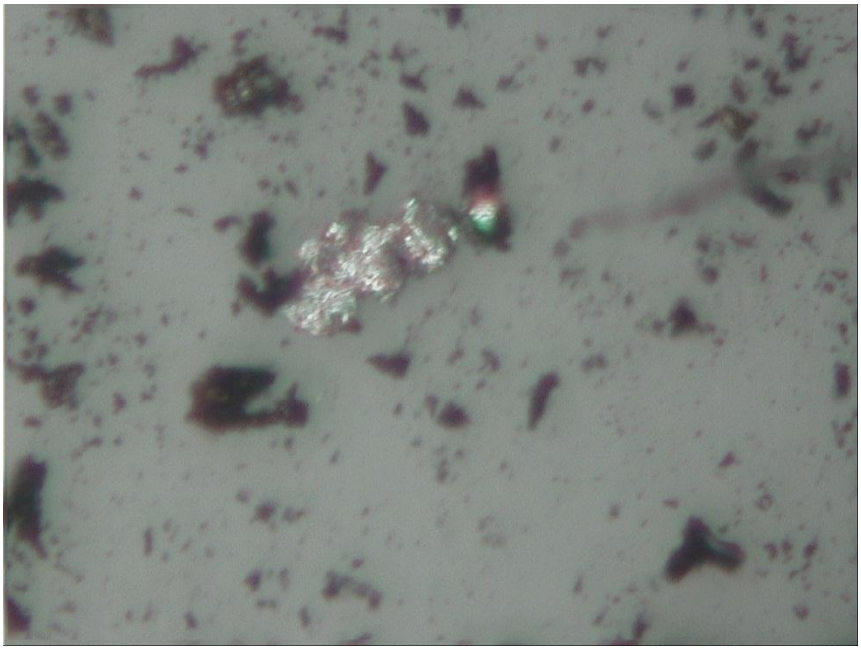

Figure 20. Image of powder from preliminary calculations at 800x.

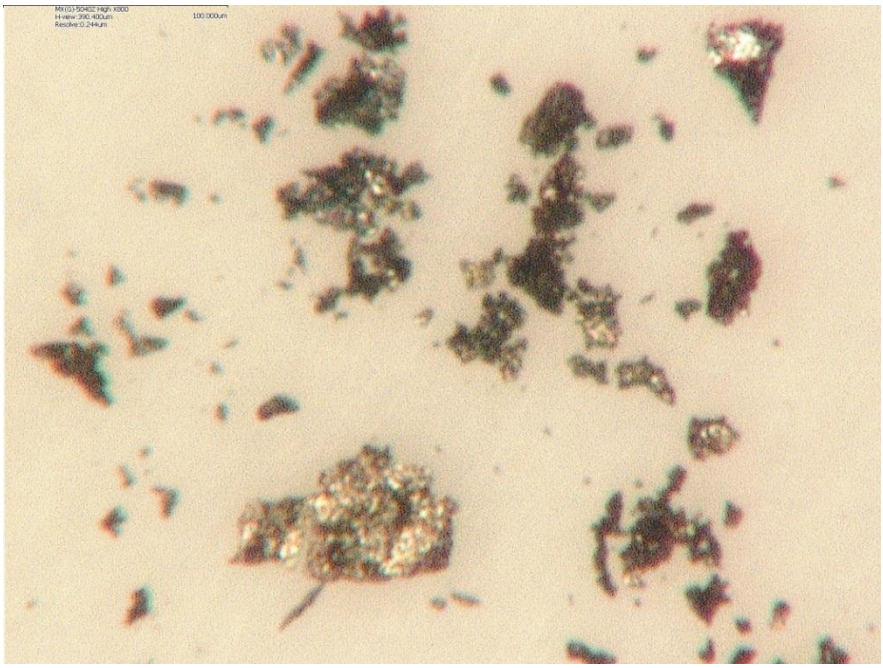

Figure 21. Image of powder from Run #1 at 800x.

Reaction dependence studies

The rate of reaction was determined by holding system pressure constant at 5 psig, hydride temperature constant at 250°C, and dehydride temperature at 325°C. Other variables held constant are given in the Appendix A. An S-curve shape appears, as expected based on previous work. [5] The S-curve shape of the data occurs due to an initial lag in reaction rate due to breakdown of the initial oxide layer and a relatively smooth initial reaction surface. The reaction speeds up due to increases in reaction surface area, but eventually slows down as the amount of uranium metal to react

becomes smaller than the amount of powder produced. The Avrami Equation can be used to model such a reaction. The Avrami Equation is given by

$$\alpha = 1 - \exp(-kt^n) \quad (11)$$

where α is the reaction fraction (powder yield), t is time in seconds, and k and n are constants. When ln(ln(1/(1- α))) is plotted versus ln(t), the slope is the constant n and the intercept is ln(k). These values are plotted in Figure 22 for the uranium hydride reaction rate as calculated from the data in Appendix B. The Avrami Equation constants were found to be k= 3.783E-6 and n=2.1294. The experimental data from Appendix B and the fitted Avrami Equation are plotted in Figure 23.

The Avrami Equation approaches complete powderization as time approaches infinity. To reach 99% powderization, a time of 562 minutes is required. This value, an approximate time for most of the powder to react, should only be used for only small changes in system parameters, but as long as the same pressure and temperatures are used, it may be scalable (depending on the result of future surface area calculations).

The reaction characteristics with respect to temperature were studied for runs at 5 psig, 270 minute hydride, and 325°C dehydride. The data was graphed and fit with an exponential curve as shown in Figure 24. The fit resulted in Eq. 12,

$$\alpha(T) = -0.00077631 * T^2 + 0.78654162 * T - 198.68740459 \quad (12)$$

where α is the reaction fraction (powder yield) and T is temperature in Kelvin. This parabolic relationship with temperature was demonstrated previously by Bloch. [5] Eq. 12 should be only be used for temperatures close to the range of temperatures used to calculate it and care should be given to the extrapolation of this equation to other pressures. The derivative of Eq. 12 was set equal to zero to determine the maximum. The maximum powder yield occurred at a temperature of 233°C.

The reaction characteristics with respect to pressure were studied for runs at 270 minute hydride, 250°C hydride, and 325°C dehydride. The data was graphed and fit with an exponential curve as shown in Figure 25. The fit resulted in Eq. 13,

$$\alpha(P) = -0.00437970 * P^2 + 0.08883989 * P - 0.01002987 \qquad (13)$$

where α is the reaction fraction (powder yield) and P is pressure in psig. This gauge pressure is the pressure resulting from the argon-5%-hydrogen gas flowing through the reaction chamber. Previous work has supported the modeling of pressure dependence based on fractional exponents. [10,12] The quadratic relationship was used to fit the data due to its good fit and based on the presumption that at some point additional gas pressure could impede the reaction. More data at higher pressures is needed to better determine the behavior of this pressure dependence.

Data was collected to determine the effect of surface area on the reaction. The data is presented in Figure 26. The surface area was calculated by adding the area of all but one side of the cut metal slug, which approximates a rectangle. One of the bottom sides was not included, as the sample was set on this side in the aluminum oxide crucible. This blocked the reaction area of that side. The blocked side was always one of the largest surface area sides (dimension y by dimension z in the Appendix). More data needs to be collected with respect to surface area to try and find a correlation. The data presented here does not appear to show a correlation, but errors in measurement could account for this.

The powder yield in each run was measured after a dehydride reaction was run on the hydride powder. The dehydride reaction was run for 20 minutes of dwell time.

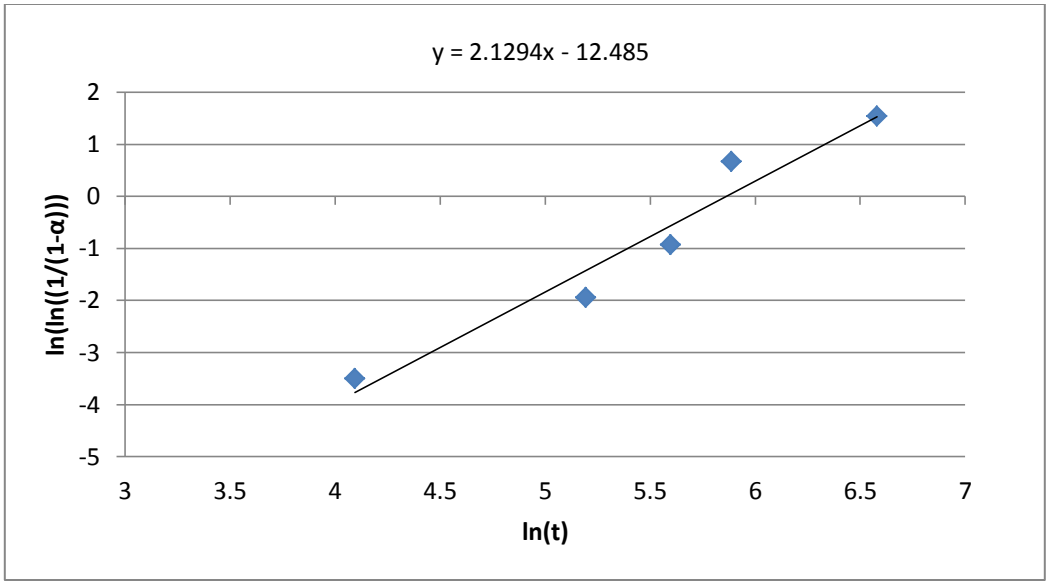

Figure 22. ln(ln(1/(1- α))) vs. ln(t) for runs at 5 psig, 250°C hydride, 325°C dehydride used for calculation of the parameters k and n for the Avrami Equation.

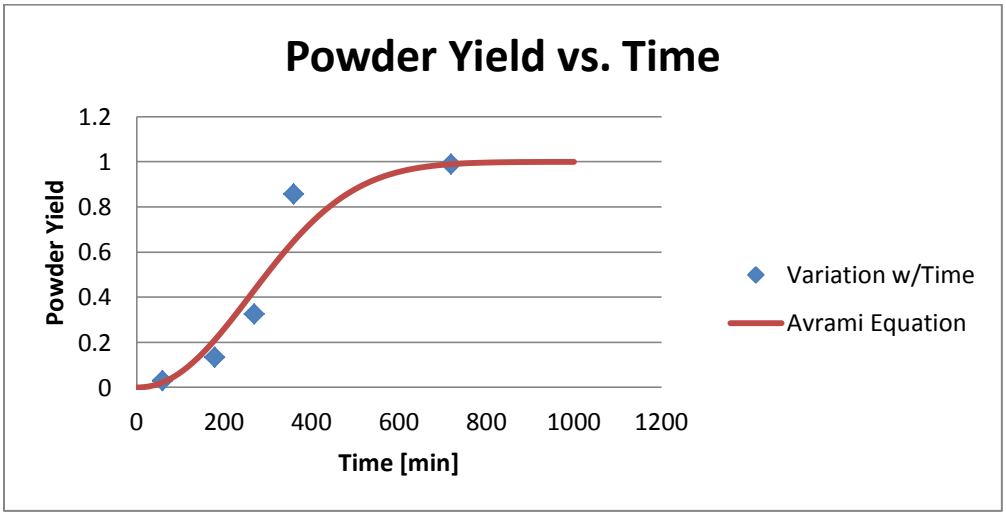

Figure 23. Powder Yield vs. Dwell Time for runs at 5 psig, 250°C hydride, 325°C dehydride.

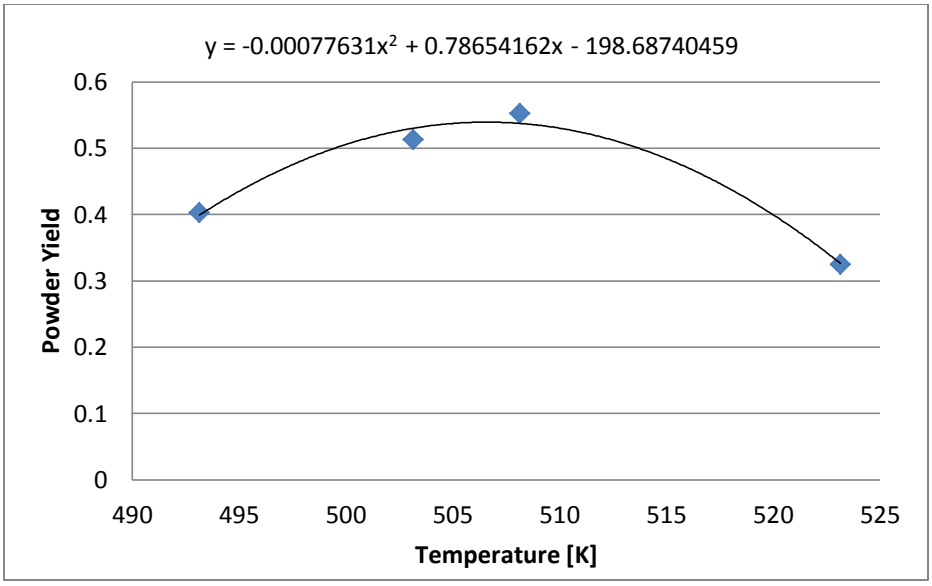

Figure 24. Powder Yield vs. Temperature for runs at 5 psig, 270 minutes, 325°C dehydride.

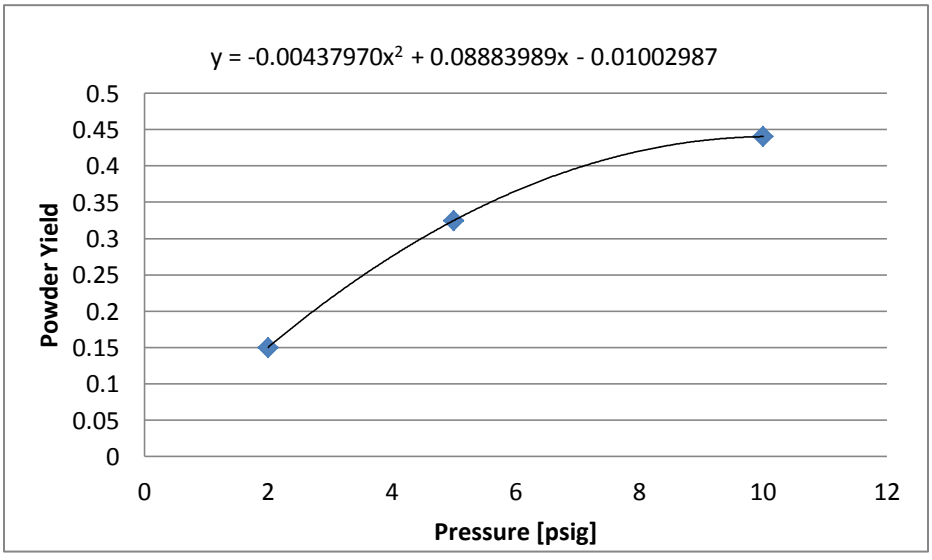

Figure 25. Powder Yield vs. Pressure for runs at 270 minutes, 250°C hydride, 325°C dehydride.

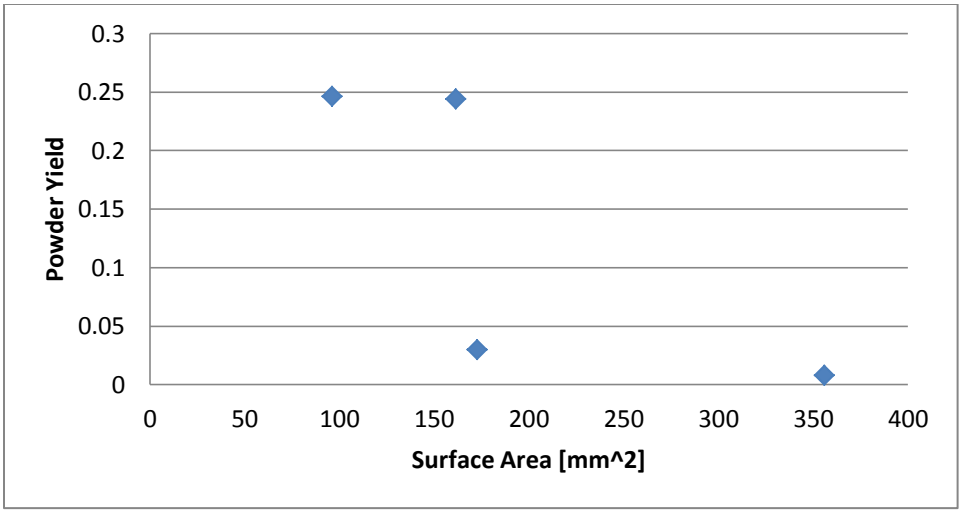

Figure 26. Powder Yield vs. Surface Area for runs at 60 minutes, 5psig, 250°C hydride, 325°C dehydride.

Sources of error

Several practicalities of experiment operation may have introduced error or uncertainties into this analysis. The time required to heat each sample up to the desired hydride temperature would vary between different temperatures and contribute to error in comparing temperature runs where time was meant to be held constant. The process of separating the unreacted metal slug from the uranium powder produced may have led to small losses of powder before mass measurement. Incomplete dehydriding of reacted powder may have added mass to some of the reported final masses. Of the potential sources of error, accounting for the start-up heat transient could be accounted for with a different measurement of reaction time. Incomplete dehydride of reacted powder could be accounted for by dehydriding at a higher temperature, increasing the time of dehydride, or a combination of both.

CHAPTER IV

CONCLUSIONS

Process optimization

The reaction rate studies conducted of the hydride-dehydride process in use at Texas A&M in the FCML have produced the following recommendations for process optimization:

- Maximize the reaction vessel pressure
- Run the hydride process near 233 °C
- Run the dehydride process at a minimum of 325 °C under a vacuum of 0.1 Pa for at least 25 minutes. Higher temperatures can be used, but should remain below 400 °C in order to reduce sample self-sintering. [7]
- To ensure complete powderization, Eq. 11 or similarly derived equations should be used to determine the run time necessary. For the parameters used in this experiment, 562 minutes was calculated to produce complete powderization.

The laboratory scale process used in this work is not the most effective way of producing large amounts of uranium powder. For process commercialization, a different system should be used. In order to allow for process heating and maximization of reaction surface area a rotary kiln would be an efficient system for powder production.

A rotary kiln is a kiln that spins during operation. The spinning action is desired to separate powder from the surface of uranium slugs, which allows for continued reaction of the uranium slug to form uranium-hydride powder. A rotary kiln designed at ORNL for the powderization of uranium dioxide using voloxidation is shown in Figure 27. Voloxidation powderizes used nuclear fuel (UO_2 + fission products) by reacting UO_2 with O_2 at increased temperatures. This rotary kiln was still considered laboratory scale, as it could handle a limit of 20 kg of processing per year. The design allowed for single pass or recirculation of gas flow, rotational speeds up to 10 RPM, and an operational temperature range of 200-600°C. [15]

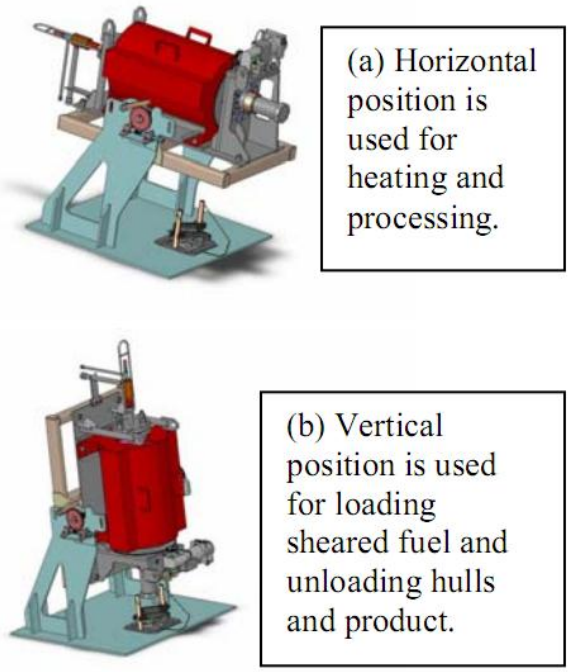

Figure 27. Rotary Kiln designed at ORNL for use in Voloxidation. [15]

Optimal design characteristics for a commercial scale hydride process:

- Gas recirculation
- Ability to use same vessel for hydride and dehydride process
- Inert operation environment
- Furnace capabilities up to at least 400 °C
- Ability to draw a vacuum on the system
- Method for removal of powder layer from metal slugs (rotary kiln suggested)

Future work

Work still needs to be done to relate the microscopic models developed by previous work to macroscopic models published in this work. The diffusion model of Condon, the linear kinetic constants of Bloch, and the work of others present a wealth of knowledge on this process, but appear to be limited to lab scale experiments. While the work published here was done for small sample sizes, it represents progress towards macroscopic system quantification oriented at system optimization.

REFERENCES

[1] G.W. Helmreich, M.S. Thesis, Texas A&M University (2010).

[2] P. Chiotti and B.A. Rogers, United States Atomic Energy Commission, AECD-2974 (1950).

[3] J. Bloch and M.H. Mintz, International Atomic Energy Commission (IAEC) Annual Report (2001) 53-75.

[4] J.F. Bingert, R.J. Hanrahan Jr., R.D. Filed, P.O. Dickerson, J. Alloys and Compounds 365 (2004) 138-148.

[5] J. Bloch, Journal of Alloys and Compounds 361 (2003) 130–137.

[6] J.B. Condon, J. Less-Common Met. 73 (1980) 105.

[7] D. J. Garnetti, M.S. Thesis, Texas A&M University (2009).

[8] J.B. Condon, E.A. Larson, J. Chem. Physics, 59 (2) (1973) 855-865.

[9] G.W. Helmreich, Verbal Description of Nitric Acid Chemistry (2011).

[10] B.M. Abraham and H.E. Flotow. J. Am. Chem. Soc. 77 (6) (1955) 1446–1448.

[11] J.B. Condon, J. Chem. Thermodynamics (1980) 1069-1078.

[12] W.M. Albrecht and M.W. Mallet, J. Electrochemical Society, 103(7) (1955) 404-409.

[13] J.B. Condon, J. Phys. Chem. 79 (1975) 392.

[14] G.W. Helmreich, W.J. Sames, D.J. Garnetti, and S.M. McDeavitt, Trans. of the Am. Nuclear Society, 102 (2010).

[15] B. B. Spencer, G. D. Del Cul, E. C. Bradley, R. T. Jubin, T. D. Hylton, and E. D. Collins, Trans. of the Am. Nuclear Society, 98 (2008) 103-104.

APPENDIX A

EXPERIMENTAL DATA

Run #	mass_start [g]	mass_slug_final [g]	mass_total_final [g]	Overall Mass Change [g]	mass_powder [g]	Yield of Powder [mass of powder/mass initial]	P [psi]	Flow Rate [scfh]	T_hydride [°C]	T_dehydride [°C]	t_hydride [min]	t_dehydride [min]	Dimension x [mm]	Dimension y [mm]	Dimension z [mm]	Surface Area [mm^2]
1	1.5384	1.3082	1.513	-0.0254	0.2048	0.13312533	5	3	250	325	180	20	1.62	3.57	15.93	120.0501
2	1.436	0.1973	1.4272	-0.0088	1.2299	0.85647632	5.4	3	250	325	360	20	1.61	3.57	15.89	119.3885
3	1.5222	1.4767	1.5219	-0.0003	0.0452	0.02969386	5.2	3	250	325	60	20	1.46	3.6	16.03	115.0276
4	1.3761	0	1.3629	-0.0132	1.3629	0.99040767	5	3.3	250	325	720	20	1.32	3.61	15.82	108.4054
5	1.2757	1.0101	1.3214	0.0457	0.3113	0.24402289	5	3	250	325	60	20	1.11	3.62	16.22	102.7612
6	1.4017	1.0113	1.4664	0.0647	0.4551	0.32467718	5	3	250	325	270	20	1.34	3.62	15.95	110.1866
7	1.3802	0.703	1.4659	0.0857	0.7629	0.55274598	5	3	235	325	270	20	1.33	3.57	15.87	108.3663
8	1.3785	0.8929	1.4485	0.07	0.5556	0.40304679	5	3	220	325	270	20	1.35	3.53	16.08	109.7094
9	0.04062	0.4003	0.4103	0.36968	0.01	0.24618415	5	3	250	325	60	20	0.86	3.5	10.34	59.9948
10	2.4785	2.1538	2.5259	0.0474	0.3721	0.15013113	2	3	250	325	270	20	1.99	3.54	18.82	155.6156
11	5.4344	5.403	5.4454	0.011	0.0424	0.00780215	5	3.1	250	325	60	20	3.84	4.24	20.02	271.2016
12	1.7569	0.941	1.8427	0.0858	0.9017	0.51323354	5	3	230	325	270	20	1.28	3.78	19.05	130.4538
13	1.953	1.1414	2.0015	0.0485	0.8601	0.44039939	10	3	250	325	270	20	1.45	3.78	19.59	141.8232

APPENDIX B

DATA FOR CALCULATION OF AVRAMI EQUATION CONSTANTS

t [min]	α	ln(t)	lnln(1/(1- α))
60	0.029694	4.094345	-3.50178
180	0.133125	5.192957	-1.94588
270	0.324677	5.598422	-0.93505
360	0.856476	5.886104	0.663335
720	0.990408	6.579251	1.536177

CONTACT INFORMATION

Name:	William James Sames V
Professional Address:	c/o Dr. Sean McDeavitt Department of Nuclear Engineering MS 3133 Texas A&M University College Station, TX 77843
Email Address:	will.sames@gmail.com
Education:	B.S., Nuclear Engineering, Texas A&M University, May 2011 Latin Honors Honors Undergraduate Research Fellow University Honors Foundation Honors Engineering Scholars Program Alpha Nu Sigma

Characterization of Alpha-Phase Sintering of Uranium and Uranium-Zirconium Alloys

Department of Nuclear Engineering, Texas A&M University
Grant Helmreich, David Garnetti, and Dr. Sean M. McDeavitt

As part of the Department of Energy's Advanced Fuel Cycle Initiative, the alpha phase sintering of uranium and uranium-zirconium alloys was characterized to provide a scientific background for a hot extrusion powder metallurgy approach to U-TRU-Zr metal fuel fabrication. By operating in the alpha phase, this approach will circumvent potential issues arising from the potential vaporization of americium, neptunium, and curium. Alpha phase sintering was characterized by quantifying the rate of sintering for uranium and uranium-zirconium pellets and analyzing the sintered microstructures by SEM.

Large Argon Atmosphere Glovebox

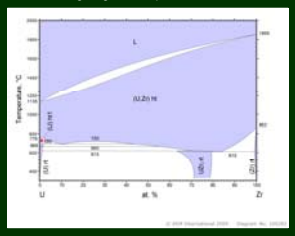

T. Ogawa, U-Zr Phase Diagram, ASM Alloy Phase Diagrams Center

Compacted DU-Zr Pellet

Sintered DU-Zr Pellet

Sectioned DU-Zr Pellet

Experimental Procedures

Pellet Fabrication

- Depleted uranium (DU) powder was produced inside of a glovebox using a hydride/dehydride process.
- DU and DU-10Zr pellets were compacted using a dual-action. punch and die with a pressure of 90.5 ksi held for 15 seconds.

Pellet Sintering

- Compacted pellets were sintered in an inert argon atmosphere.
- Sintering was performed in the alpha and gamma phases.
- Uniaxial sintering shrinkage was measured *in situ* via LVDT.

Sintering Analysis

- Shrinkage data was analyzed using a fundamental sintering model.
- Cross-sections of sintered pellets were imaged by SEM to identify sintered phases and microstructure.

SEM Imaging

Sintered Porosity

- Interior low porosity and exterior high porosity regions were consistently observed due to compaction density gradients.
- Increasing compaction pressure resulted in uniform porosity.
- Addition of zirconium to the pressed powder mixture resulted in increased sintering rates and higher final densities.
  - This was attributed to sintering enhancement by U-Zr interdiffusion.

Uranium-Zirconium Microstructures

- Zirconium rich phase contained virtually no uranium.
- Mixed U-Zr phase formed around pure zirconium phases.
  - U-Zr samples sintered in the γ-phase developed lamellar α(U)+δ(UZr_2) structure.
  - U-Zr samples sintered in the α-phase developed pure UZr_2 δ-phase.
- Uranium rich phase contained dispersed zirconium precipitates.

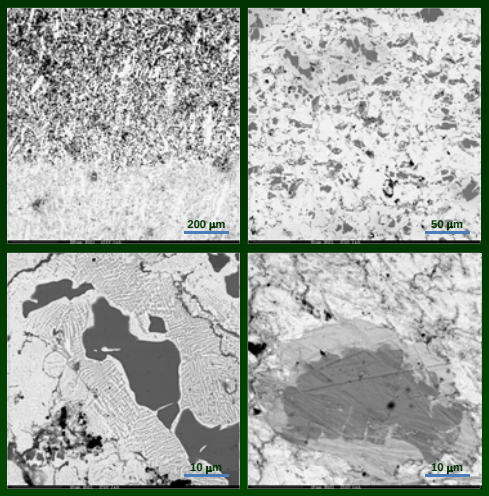

Sintered DU showing high and low porosity regions (upper left), sintered DU-Zr (upper right), sintered DU-Zr showing lamellar α+δ microstructure (bottom left), sintered DU-Zr showing pure δ-phase between uranium and zirconium rich regions (bottom right).

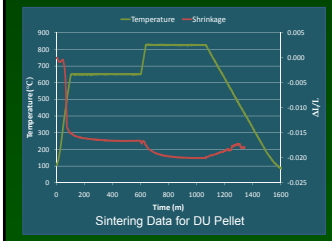

Sintering Data for DU Pellet

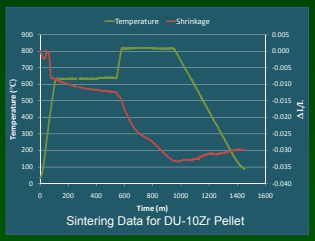

Sintering Data for DU-10Zr Pellet

Sintering Modeling

$$\left(\frac{\Delta L}{L}\right)^{2/n} = \frac{B_0 \cdot t}{Z^{n} \cdot D^{eff}} \cdot e^{-Q/RT}$$

R.M. German, Sintering Theory and Practice, John-Wiley & Sons Inc., New York, (1996)

DU Sintering

- Steady, slow shrinkage in both α-phase and γ-phase.
- α-phase Q=340 +/- 41 kJ/mol, higher than previously observed for γ-phase.
- *n*=3.92 +/- 0.41, indicates bulk diffusion controlled sintering process.

DU-10Zr Sintering

- Rapid shrinkage in both phases, hump in γ-phase indicative of alloying interaction
- α-phase Q=272 +/- 91 kJ/mol, *n*=2.59 +/- 0.40
- Reduced Q and *n* due to U-Zr interdiffusion enhanced sintering.

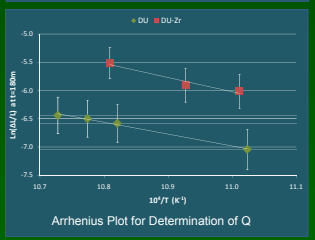

Arrhenius Plot for Determination of Q